ULTRAFAST SPIN DYNAMICS IN ADVANCED MAGNETIC STRUCTURES FOR APPLICATIONS IN SPINTRONICS

Thesis submitted for the degree of

Doctor of Philosophy (Science)

in

Physics (Experimental)

By

Soma Dutta

Department of Physics

University of Calcutta

2024

Dedicated to my mother, father & elder brother……

ABSTRACT

Spintronics is a burgeoning area of research focused on developing advanced nanoelectric devices that aim to lower power consumption while enhancing memory and processing capacities for future generations. A comprehensive understanding of ultrafast magnetization dynamics and its effective control across a wide range of timescale in magnetic thin films and heterostructures has recently attracted significant attention from the scientific community due to its promising applications in modern data storage and memory technologies. This doctoral thesis presents an investigation into ultrafast magnetization dynamics within various ferromagnetic (FM) thin films and heterostructures, spanning timescales from femtoseconds to nanoseconds. A comprehensive study has been conducted on the effects of different internal and external factors, including film thickness, laser fluence, external magnetic field strength, the in-plane orientation of the external magnetic field, and interfacial spin-orbit coupling on magnetization dynamics. We employed time-resolved magneto-optical Kerr effect (TR-MOKE) magnetometry, utilizing an amplified femtosecond laser system, to measure ultrafast spin dynamics. We have studied different phenomena like ultrafast demagnetization, fast remagnetization, slow remagnetization with magnetization precession and damping in FM thin film, nonmagnet (NM)/FM, 2D-transition metal dichalcogenides (TMD)/FM, Weyl semi-metal (WSM)/NM heterostructures. The results of ultrafast demagnetization were analyzed using a phenomenological three-temperature model (3TM), while the damped precessional oscillations were modelled through the macrospin formalism based on the Landau-Lifshitz-Gilbert equation. The impact of NM layer, in-plane magnetic anisotropy in the FM, and layer-dependent characteristics of TMDs and perpendicular magnetic anisotropy (PMA) in magnetization dynamics has been thoroughly examined. Through the investigation of the correlation between ultrafast demagnetization time and damping constant, we have delved into the primary mechanism underlying ultrafast demagnetization. Furthermore, the inverse correlation between demagnetization time and damping has allowed us to extract the spin chemical potential at the interface of heterostructures such as Ta/CoFeB, $WS_2(n_{ML} = 2,4)$/CoFeB, and Co_2MnGa/Pt. The Co_2MnGa/Pt heterostructure exhibits the highest intrinsic spin-mixing conductance ever reported. Additionally, PMA-controlled ultrafast demagnetization has been studied in HM/CoFeB/MgO heterostructures.

Our study aims to enhance the understanding of spin dynamics and explore the possibility of controlling parameters in thin film heterostructures, thereby promoting their potential application in on-chip power supply and other energy-efficient spintronic and spin-orbitronic devices.

LIST OF PUBLICATIONS:

A. Published/Submitted in Journals

- Included in the thesis:

1. "Role of Spin Transport through the β-Ta/$Co_{20}Fe_{60}B_{20}$ Interface on its Ultrafast Demagnetization: Implications for Ultra-High-Speed Spin-Orbitronic Devices", **S. Dutta**, S. N. Panda, J. Sinha, S. Chowdhury, and A. Barman. *ACS Applied Nano Materials,* **5**:17995-18003 (2022)
2. "Ultrafast Demagnetization and Gilbert Damping in Electrodeposited CoP Film", **S. Dutta**, A. Samanta, S. N. Panda, S. Roy, and A. Barman. *Journal of Material Sciences,* **58**:14817–14830 (2023)
3. "Manipulating Ultrafast Magnetization Dynamics of Ferromagnet using two-dimensional Transition Metal Dichalcogenides", **S. Dutta**, S. Hussain, P. Kumar, N. K. Gupta, S. Chowdhury, P. Svedlindh, and A. Barman. *Nanoscale*, **16** (8), 4105-4113 (2024)
4. "Role of Spin Transport on Ultrafast Spin Dynamics in Magnetic Weyl Semimetal (Co_2MnGa)/Pt Heterostructures with High Spin-Mixing Conductance", **S. Dutta,** S. N. Panda, A. Markou, C. Felser, E. Lesne and A. Barman. *Advanced Functional Materials, doi: https://doi.org/10.1002/adfm.202413194*
5. "Magnetic Anisotropy Controlled Ultrafast Demagnetization in Heavy Metal/CoFeB Heterostructures with Varying CoFeB Thickness", **S. Dutta** *et al.* (*Manuscript to be submitted*)

- Not included in the thesis:

1. "Structural Phase-Dependent Giant Interfacial Spin Transparency in W/CoFeB Thin-Film Heterostructures", S. N. Panda, S. Majumder, A. Bhattacharya, **S. Dutta**, S. Chowdhury, and A. Barman. *ACS Applied Materials & Interfaces,* **17**, 20875-20884 (2021).

ACKNOWLEDGEMENTS

I would like to express my heartfelt appreciation to my PhD supervisor, Prof. Anjan Barman, for his unwavering support and exceptional guidance during my entire PhD journey. His guiding principle of "Hope for the best, prepare for the worst" instils in me a sense of perseverance and helps me maintain a calm and relaxed outlook on life. I find myself recalling this advice whenever I encounter obstacles. His dedication to upkeeping his world-class laboratory is truly remarkable. Additionally, his exceptional time management skills serve as a great inspiration to me.

I express my gratitude to my esteemed senior, Dr. Surya Narayan Panda, for imparting comprehensive knowledge regarding the time-resolved magneto-optical Kerr effect magnetometry setup and its alignment procedures. His assistance was invaluable during the lockdown period in 2020, which marked the early phase of my PhD journey, as he provided me with research papers and guidance in analyzing experimental data for the first time. I am thankful to Prof. Jaivardhan Sinha for his support during the review process of my initial research project and recommending me for the IEEE Summer School in Taiwan. His humility is truly admirable and leaves a positive impression on everyone he encounters. Additionally, I extend my sincere thanks to the exceptionally polite and humble senior Dr. Bivas Rana for discussion regarding collaborative research work. Also, I am thankful to my senior colleagues-cum-friends Dr. Sucheta Mondal, Dr. Samiran Choudhury, Dr. Arpan Bhattecharya, Dr. Santanu Pan, Dr. Anulekha De, Dr. Kartik Adhikary, Dr. Avinash Kumar Chaurasiya, Dr. Sourav Sahoo, Dr. Amrit Kumar Mondal, Dr. Kaustuv Dutta, Mr. Sudip Majumdar, Ms. Arundhati Adhikary, Mr. Pratap Kumar Pal for their support and valuable discussions during my PhD tenure. Also, I thank my lab batchmate Ms. Sreya Pal and junior colleagues Ms. Suchetana Mukhopadhyay, Mr. Chandan Kumar, Mr. Bikram Baghira, Mr. Sayan Mathur, Ms. Sayanti Mondal for designing a very friendly and cheerful environment in the lab. I would like to acknowledge our collaborators, Prof. Saibal Roy and Mr. Arindam Samanta from Tyndall National Institute, Ireland; Dr. Sajid Hussain and Prof. Peter Svedlindh from Uppsala university; Prof. Sujeet Chaudhury and Dr. Nanhe Kumar Gupta from IIT Delhi; Edouard Lesne, Claudia Felser and Anastasios Markou from Max Planck Institute, Germany.

I extend my gratitude to the University Grants Commission for their financial assistance and to the academic section of S. N. Bose National Centre for Basic Sciences (SNBNCBS) for their invaluable support. I would also like to thank my juniors, seniors, and colleagues at SNBNCBS for fostering a welcoming atmosphere on campus. My appreciation goes to the SNB-mess cooking team for consistently providing nutritious meals each day, as well as to the members of the institute canteen for their delightful evening snacks.

I would like to express my heartfelt gratitude to my family for their unwavering support, which has been instrumental in my modest achievements. I hold deep admiration for my mother, Mrs. Sandhya Dutta, my father, Mr. Brajendra Kumar Dutta, and my elder brother, Mr. Sandip Kumar Dutta, whose boundless love and faith in me have been the cornerstone of my success. Although my late grandmother, Mrs. Snehalata Dutta, and my late maternal uncle, Mr. Dilip Dutta, were with me for a brief period, their inspiration left a significant impact on my life. My

interest in physics was initially sparked by my elder brother and has since been nurtured by the esteemed faculty of the Visva-Bharati Physics Department, including Rajkumar da, Arani da, Manas da, Swarup da, Aditya da, the late Somnath da, Sudipta di, Subhashis da, Swapan da, Tarapada da, Tapas da, Srikantha da, Biswajit da, Biplab da, and Bikash da. I am also grateful to my higher secondary teacher, Sakur sir, for fostering my passion for mathematics, and to my chemistry teacher, Manoj sir, for his invaluable guidance till now. Additionally, I extend my thanks to my headmistress and all the teachers at Nalhati High School for Girls for their guidance. All of them have fostered in me a curiosity to explore the world further, which has significantly influenced my passion for research. This thesis serves as a tribute to their contributions.

Soma Dutta

S N Bose national Centre for Basic Science

Kolkata, India

TABLE OF CONTENTS

LIST OF ABBREVIATIONS

AFM: Atomic force microscopy

AHE: Anomalous Hall effect

ANE: Anomalous Nernst effect

AOS: All-optical switching

BBO: Barium Beta-borate

BWD: Band-width detector

CPA: Chirped pulse amplification

DC: Direct current

DMI: Dzyaloshinskii-Moriya interaction

DW: Domain wall

EDX: Energy dispersive x-ray

EY: Elliott-Yafet

FFT: Fast Fourier transform

FM: Ferromagnet

FMR: Ferromagnetic resonance

FWHM: Full width at half maximum

GMR: Giant magnetoresistance

GVD: Group velocity dispersion

HM: Heavy metal

IMA: In-plane magnetic anisotropy

IP: In-plane

KLM: Kerr-Lense mode-locking

LCP: Left circularly polarized light

LLG: Landau-Lifshitz-Gilbert

LL: Landau and Liftshitz

ME: Magnetoelastic

ML: Monolayer

MRAM: Magnetic random-access memory

MSHG: Magnetic second harmonic generation

MTJ: Magnetic tunnel junction

NDM: Negative dispersion mirror

NM: Nonmagnet

NTA: Naphthalene trisulfonic acid

OBD: Optical bridge detector

OISTR: Optical inter-site spin transfer

OOP: Out-of-plane

PC: Pockel cell

PEM: Photoelastic modulator

PMA: Perpendicular magnetic anisotropy

PRP: Pulsed-reverse plating

PSSW: Perpendicular standing spin wave

RA: Regenerative amplifier

RCP: Right circularly polarized light

REE: Rashba-Edelstein effect

RF: Radio frequency

RR: Retro-reflector

SDG: Synchronization and delay generator

SFS: Spin-flip scattering

SHE: Spin Hall effect

SHG: Second-harminic generator

SLD: Scattering length density

SML: Spin memory loss

S-MOKE: Static magneto optical Kerr effect

SOC: Spin-orbit coupling

SOT: Spin-orbit torque

SPM: Self-phase modulation

SST: Super-diffusive spin transport

ST: Spin transport

ST-FMR: Spin-torque ferromagnetic resosnance

SW: Spin-wave

TMDs: Transition metal dichalcogenides

TME: Transient magnetic enhancement

TMS: Two-magnon scattering

TR-MOKE: Time-resolved magneto-optical Kerr effect

VPUF: Verdi pumped ultra-fast

VSM: Vibrating sample magnetometer

WSM: Weyl semimetal

XRD: X-ray diffraction

XRR: X-ray reflection

2D: Two-dimensional

3TM: Three-temperature model

LIST OF FIGURES

CHAPTER 1

Introduction

In traditional electronics, the charge property of electron is employed to generate and control electric current with external electric or electromagnetic fields. From the first transistor to advanced microprocessors in computer, almost all electronic devices use circuits that express data as zeros and ones represented by absence and presence of electric charge. The growth of microelectronics is described in Moore's law that the number of transistors or the power of the microprocessor per chip will double within every 18 months [1]. However, the size of the transistors and other components have reached nanoscale dimensions [2] and further reduction in size would lead to the heating problem making the circuit inoperable. On the other hand, another intrinsic quantity of angular momentum of electron, spin was utilized solely through its macroscopic manifestation, specifically the magnetization of a ferromagnet in magnetic recording before the invention of giant magnetoresistance (GMR) in 1988 [3,4]. The discovery of GMR paved the way to control the motion of electron by manipulating spin i.e., the orientation of magnetization of magnetic multilayers. To make the technological devices smaller, faster and efficient; physicist have employed 'spin' of the electron, developing a new field of research and technology, called 'spintronics' [5]. The spin-based devices can replace and aid several electronic devices very well with better performance such as higher data processing speed, integration densities and lower power consumption. However, to successfully integrate spin into semiconductor technology, efficient injection, transmission, manipulation and identification of spin polarization and spin current is necessary.

1.1 Magnetic length scales

Spin polarization is transmitted either by conduction electron or propagation of spin-waves throughout the local magnetic moments within an insulating material. The dipolar field or the demagnetizing field emanating from the edges of the samples, significantly influences the breakdown of magnetization into domains in bulk magnets [6]. The size of the domain ranges from the decades of nanometres (nm) to micrometres (μm) or even millimetres (mm) depending on the materials. The domain wall width is determined by balancing the exchange energy (defined by the stiffness constant: A) and the anisotropy energy. The exchange interaction becomes the predominant factor leading to a single-domain state when the system size is significantly decreased. Then the complete magnetization is oriented with the global easy axis, considering the shape anisotropy. From the perspective of electronic transport, there are two important length scales: one is the elastic mean free path that refers to the distance an electron can travel in a magnetic material without undergoing scattering, and this distance is influenced by the electron's spin and ranges from a fraction of nm to few tens of nm. Another one is the spin-diffusion length that refers to the distance travelled by an electron keeping its spin memory. This length varies from a nm with high spin-orbit coupling (SOC) to a few hundred of nm or more in nonmagnetic materials with low SOC.

If the length of the device is shorter than the spin-diffusion length, the electron spin will remain intact. When the length scale is significantly less than the electron's mean free path, the momentum of the electron will be conserved during transport. Now magnetic storage media, ranging from magnetic tapes to hard disk drives, consist of granular ferromagnetic materials where the grains are single domains and remain largely independent. The binary data, represented by 0s and 1s, are stored as magnetic domains (bits) that are magnetized either in alignment or in opposition along the magnetic easy axis. Each domain consists of a cluster of tens or hundreds of grains. The areal density of these media has been increased by reducing the grain size from μm in audio tape to a few nm in modern hard disc drives. The maintenance of thermal stability for the magnetization of each grain is required. Magnetic random-access memory (MRAM) is made of magnetic tunnel junction (MTJ). Each bit is represented by a single tunnel junction. The storage layer of each MTJ in contemporary MRAM typically ranges in thickness from 1.4 nm to 2 nm.

1.2 Importance of thin films and heterostructures

Magnetic thin films possess magnetic properties that differ from their bulk form due to their reduced dimensionality and surface/interface phenomena, with a thickness of around nm or less, even down to atomic monolayers [7-10]. The limited dimensionality combined with inherent anisotropy facilitates the emergence of phenomena that are intriguing for the fundamental understanding of magnetic systems and significant for modern technological applications, which include magnetic storage devices and sensors. The primary motivation for investigating magnetic thin films stemmed from their ability to increase data storage capacity, especially at high and ultra-high densities. The manipulation of the magnetization in these films allows for the encoding and retrieval of information in the form of magnetic bits. In this regard, perpendicular magnetic anisotropy (PMA) has been recognized for providing the smallest bit dimension and the greatest storage capacity. As a result, magnetic thin films have been engineered to serve as the active layer in magnetic recording material and magnetic memory devices [11]. Recently, there has been an increasing interest in exploring innovative materials aimed at enhancing magnetic thin-film technology. The investigation of new materials, morphologies, and interfacial interactions has led to the discovery of new properties and distinctive behaviours, thereby creating new technological opportunities. Magnetic thin films have become essential elements in magneto-optic, magnetoelectronic, and spintronic devices. They are employed in spin valves, MTJs, and spintronic sensors, where their unique magnetic characteristics are crucial for the manipulation of electron spins and the detection of magnetic fields. To achieve superior magnetic properties, such as increased magnetic anisotropy, diminished magnetization noise, and improved thermal stability, various materials, including magnetic alloys, multilayers, heterostructures and nanostructured films, are currently under investigation.

Heterostructures refer to a stratified arrangement consisting of a nonmagnetic (NM) material and a ferromagnetic (FM) material that have recently garnered significant interest due to their potential uses in energy-efficient magnetic data storage and memory devices. When the NM layer exhibits a high SOC strength, these heterostructures can manifest pronounced spin-orbit phenomena, including spin pumping [12], spin Hall effect [13], inverse spin Hall effect [14], interfacial Dzyaloshinskii-Moriya interaction [15], spin caloric effects [16], Rashba-Edelstein effect [17], and inverse Rashba-Edelstein effect [18], among others. These effects are crucial for the advancement of spin-orbitronic devices. Such spin-based phenomena can facilitate the generation and utilization of pure spin currents [19] for information storage and processing, where the overall charge flow is negligible. Devices that operate on pure spin currents exhibit minimal unwanted power loss due to Joule heating and the Oersted field effect, rendering them more efficient and less power-intensive [20]. To effectively harness pure spin currents within an electronic circuit, it is essential to establish a source of spin imbalance, often referred to as a spin battery, alongside a dissipation-free conductor, an external manipulator, and a detector. In 2002, A. Brataas *et al*., introduced the notion of a "spin battery," wherein pure spin currents are generated through magnetization precession in a FM layer and subsequently transported to the adjacent NM layer due to the chemical potential differences that arise within these heterostructures [21]. This process is termed "spin pumping." The theoretical framework and experimental confirmation of the spin pumping mechanism were further elaborated by Y. Tserkovnyak *et al*. in the same year [22]. Spin pumping has been extensively studied and is recognized as an effective method for generating pure spin currents in NM/FM heterostructures, as it operates without a net charge flow across the NM/FM interface, thus avoiding issues related to impedance mismatch [23,24].

Fe, Co, Ni, CoFe, $Co_{20}Fe_{60}B_{20}$ (CoFeB), Permalloy ($Ni_{80}Fe_{20}$, Py), ferromagnetic Heusler alloys etc. are commonly used in conjunction with various NM materials to produce pure spin current through spin pumping. CoFeB and Py are particularly popular choices due to their characteristics such as low coercivity, minimal magnetostriction, small magnetic anisotropy, high spin polarization, and significant tunnel magnetoresistance. These properties make them ideal candidates for magnetic recording head sensors and high-frequency transformers [25,26]. A wide variety of NMs, including heavy metals (like Ta, W, Pt, Pd, Cu, Ru etc.), two-dimensional materials like graphene and transition metal dichalcogenides (TMDs), semiconductors, superconductors, topological insulators, metal oxides etc., have been studied for spin pumping applications.

1.3 Spin current in heterostructures

The spin current produced in NM/FM heterostructures through spin pumping is utilized in spin-torque-based devices, leading to the emergence of spin-orbitronics [27]. However, the effectiveness of the spin-orbit torque (SOT) is heavily reliant on the quality of the NM/FM interface, which can be assessed through parameters such as interfacial spin transparency [28], spin-mixing conductance, and spin backflow factor. The interface governs the transport of spin current from one layer to another. Various other factors, such as spin memory loss [29], interfacial band hybridization [30], interfacial spin-orbit coupling [31], two-magnon scattering [32], and proximity-induced effects [33], may also manifest in NM/FM interfaces, impacting spin current transport. To facilitate the fabrication of efficient spin current-based devices, it is crucial to enhance the efficiency of spin transfer across NM/FM interfaces by minimizing interfacial losses. The dissipation of pure spin current applies a torque to the precession of the magnetization within the FM layer, ultimately modulating the Gilbert damping parameter of the composite system. If the NM/FM interface lacks transparency, the extent of damping modulation can be significantly affected by interfacial losses. Therefore, the NM/FM interface plays a pivotal role in the efficient transport of pure spin current for utilization in SOT devices.

Up till now, mainly electrical excitation and detection methods like non-local spin injection in lateral spin valves, spin-torque ferromagnetic resonance (ST-FMR), spin Hall magnetoresistance, second-harmonic generation, inverse spin Hall effect measurement, etc., have been employed to study the spin pumping effect. These electrical detection techniques require precise and complex sample fabrication techniques, leading to potential artifacts due to electrical contacts, impurity scattering centres, and large area averaging. The values of dynamic parameters such as the Gilbert damping parameter are often inflated due to the presence of these external artifacts. Recently, the all-optical time-resolved magneto-optical Kerr effect (TR-MOKE) technique [34] has emerged as a reliable and non-invasive method for accurately determining the modulation of Gilbert damping parameter, particularly useful in investigating spin pumping-induced pure spin current transport in NM/FM bilayers. This technique allows for the direct extraction of the Gilbert damping parameter from the decay profile of the damped precessional oscillation, offering an advantage over traditional electrical techniques. Additionally, TR-MOKE is a local technique that reduces contributions from defects and inhomogeneities through small area averaging. In this doctoral thesis, we will utilize the all-optical TR-MOKE technique to analyze the ultrafast magnetization dynamics in various NM/FM heterostructures across femtosecond to nanosecond timescales.

1.4 Objective of this thesis

The primary aim of this doctoral research is to clarify the ultrafast spin dynamics that occur over an extensive timescale, from femtoseconds to nanoseconds, in various ferromagnetic thin films and heterostructures. This study intends to address several critical issues within the realm of spintronics, particularly the relationship between various microscopic processes associated with ultrafast magnetization dynamics, which are influenced by factors such as film thickness in FM and NM thin films, laser fluence, the orientation of in-plane magnetization, controlling the interfacial SOC as well as the effect of odd-even layer dependence of TMDs on magnetization dynamics of FM.

The studied systems can be categorized as follows:

I. **Role of spin transport in NM/FM thin film heterostructures:** Chapter 4 describes the study of ultrafast demagnetization, remagnetization and damping in β-Ta(t)/$Co_{20}Fe_{60}B_{20}$(d)/SiO_2(2 nm) thin film heterostructures by systematically altering both the Ta and $Co_{20}Fe_{60}B_{20}$ thicknesses. By correlating the ultrafast demagnetization and damping, the role of spin transport in magnetization dynamics as well as the role of NM thickness in the interfacial spin accumulation, is comprehensively studied.

II. **Dependence of magnetization dynamics on in-plane magnetization orientation in electrodeposited CoP film:** In chapter 5, we have investigated the in-plane magnetic orientation dependent ultrafast magnetization dynamics of electrodeposited cobalt phosphorus (CoP) alloy and the role of anisotropic SOC on ultrafast demagnetization, precession frequency and damping.

III. **Odd-even layer dependence of TMDs on magnetization dynamics of FM:** Chapter 6 demonstrates the odd-even layer dependence of WS_2 layer number in response to spin-valley coupling by measurement of ultrafast magnetization dynamics in WS_2/Co_3FeB thin film heterostructures. Fluence-dependent magnetic damping measurements indicate the presence of broken inversion symmetry and various band scattering mechanisms. Furthermore, it elaborates on the distinct microscopic mechanisms contributing to ultrafast demagnetization for varying WS_2 layer number.

IV. **Magnetization dynamics of Weyl semi-metal ferromagnet in heterostructures:** Chapter 7 illustrates the magnetization dynamics of Weyl semi-metal Heusler FM (Co_2MnGa) as well as spin transport in Co_2MnGa/Pt interface. Various parameters such as spin mixing conductance, Pt spin-diffusion length, and interface transparency have been determined.

V. **Effect of interfacial SOC on ultrafast demagnetization:** In chapter 8 we have investigated the impact of magnetic anisotropy on laser-induced ultrafast demagnetization. A reduction in FM thickness results in a shift of the magnetic easy axis from in-plane (IP) to out-of-plane (OOP), leading to a doubling of magnetic quenching. Notably, a faster demagnetization process is observed in OOP-oriented samples when compared to those at the thickness transition point from OOP to IP, as well as the IP samples.

CHAPTER 2

Theoretical Background

2.1 Ferromagnetism

Throughout history, the term ferromagnetism has been utilized to describe any material capable of displaying spontaneous magnetization, means having magnetic moment without any magnetic field. This characteristic is found in specific materials, such as iron, resulting in a noticeable magnetic permeability and coercivity, enabling the material to become a permanent magnet. Ferromagnetic materials are visibly attracted to magnets due to their substantial magnetic permeability. In the field of physics, various types of material magnetism have been identified, with ferromagnetism (as well as the related effect of ferrimagnetism) being the most powerful form of magnetism and we encounter in our daily lives. Other types of magnetism, such as paramagnetism, diamagnetism, and antiferromagnetism, elicit weaker responses from substances. Ferromagnetism plays a crucial role in industrial settings and advanced technologies, serving as the foundation for electrical devices. While the exchange interaction maintains spin alignment, it does not dictate a specific direction. In the absence of magnetic anisotropy, the spins within a magnet will alter direction unpredictably in reaction to thermal variations, resulting in super-paramagnetism.

2.2 Magnetic energies

The magnetic properties of materials are greatly influenced by various energy terms such as exchange energy, magnetostatic self-energy (demagnetizing energy), Zeeman energy, and magnetic anisotropy energy. When in equilibrium, the system naturally seeks to minimize the total free energy. This section provides a concise overview of the key energy contributions.

2.2.1 Zeeman energy

The relationship between the magnetization ($\boldsymbol{M}$) of the sample and an externally applied magnetic field ($\boldsymbol{H_{ext}}$) is demonstrated by this equation:

$$E_{Zeeman} = \mu_0 \int_0^V \boldsymbol{M} \cdot \boldsymbol{H_{ext}} dV \tag{2.1}$$

Here, V represents the total volume occupied by the magnetic specimen, while dV denotes the volume element, and μ_0 signifies the permeability of free space. This indicates that when subjected to a magnetic field, the magnetization tends to orient itself along $\boldsymbol{H}_{ext}$ in order to minimize its energy.

2.2.2 Exchange energy

The short-range magnetic ordering in magnetic materials is a result of quantum-mechanical properties, particularly through exchange interaction. This interaction plays a significant role in ferromagnets, ferrimagnets, and antiferromagnets by aligning neighbouring magnetic ions either parallel or antiparallel to each other. The origin of this interaction can be attributed to the Coulombic interaction energy and Pauli exclusion principle, which are described phenomenologically by the Heisenberg exchange Hamiltonian.

$$H_{ex} = -\sum_{i \neq j} j_{ij} \boldsymbol{S}_i \cdot \boldsymbol{S}_j \tag{2.2}$$

In the equation above, $\boldsymbol{S}_i$ and $\boldsymbol{S}_j$ represent the spin operators of the i-th and j-th atoms, while j_{ij} denotes the exchange integral between them. The material can be categorized as either a ferromagnet or an antiferromagnet based on the polarity (sign) of j_{ij}. When considering the continuum model, the equation can be expressed as:

$$E_{ex} = A \int_0^V (\nabla m)^2 dV \tag{2.3}$$

Here, the magnetic moment (m) is regarded as a continuous vector quantity, while A is referred to as the exchange stiffness constant, which can be represented as:

$$A = \frac{2JS^2}{a} \tag{2.4}$$

The lattice constant, denoted as ' a ', is considered in the context of isotropic exchange (J) in the FM medium. This exchange interaction, known as direct exchange interaction, involves the interaction of electrons from magnetic atoms with their nearest neighbours. However, indirect exchange interactions can also occur, coupling magnetic moments over larger distances. Several examples of indirect exchanges are provided below.

I. RKKY exchange: Metallic ions are connected by itinerant electrons in this scenario.
II. Super-exchange: The magnetic cations' spins are exchange-coupled through various non-magnetic anions in this scenario.
III. Anti-symmetric (or anisotropic) exchange: The Dzyaloshinskii-Moriya interaction (DMI), is characterized by the significant influence of spin-orbit interaction and super-exchange, which frequently results in the slight canting of spins.

2.2.3 Magnetic dipolar interaction

The interaction between two magnetic dipoles is present in all materials, regardless of whether they are ferromagnetic or not, although the strength may vary. The energy term associated with this interaction is expressed as:

$$E_d = \frac{\mu_0}{4\pi r^3}\left[m_1 \cdot m_2 - \frac{3}{r^2}(m_1 \cdot r)(m_2 \cdot r)\right] \tag{2.5}$$

The permeability in free space is denoted by μ_0, while m_1 and m_2 represent the moments of the two magnetic dipoles. The vector r connects the two dipoles, which are influenced by the magnetic field generated by each other. Equation 2.5 above illustrates that the energy decreases with the third power of their separation, r. In the case of ferromagnets, this interaction may not directly impact magnetic ordering, but it significantly influences various phenomena like domain formation, demagnetizing field distributions, and the characterization of spin waves in the long wavelength range.

2.3 Magnetic anisotropy

Magnetic systems exhibit certain preferred orientations that make it easier to magnetize the sample. These orientations are referred to as easy axes, and this phenomenon is recognized as magnetic anisotropy. There are several types of magnetic anisotropy:

I. **Magneto-crystalline anisotropy:** The magnetization of a crystal is influenced by its atomic structure, which creates specific orientations. The presence of spin-orbit coupling (SOC) is crucial in determining the crystallographic axes that display magneto-crystalline anisotropy.

II. **Shape anisotropy:** In a confined magnetic structure, when the shape of the element is not completely spherical, the demagnetizing field will vary across different directions, resulting in the formation of one or more preferred axes to attain a state of minimal energy.

III. **Surface and interface anisotropy:** The presence of broken symmetry at the surfaces and interfaces of magnetic thin films and multilayers frequently results in the creation of an effective anisotropy within the system. Within a ferromagnetic thin film, the energy associated with this anisotropy per unit volume can be mathematically represented as:

$$E_{ani} = K^{eff} sin^2\theta \tag{2.6}$$

$$K^{eff} = K_v^{eff} + \frac{2K_s^{eff}}{d} \tag{2.7}$$

Where, d is the thickness of the ferromagnet, K_v^{eff} is the volume anisotropy constant including magneto-crystalline as well as the demagnetizing term and K_s^{eff} is the effective surface or interface anisotropy constant. Surface roughness alters the magneto-crystalline surface anisotropy by disrupting symmetry near the atoms on that plane. This anisotropy tends to orient the magnetization of the sample out-of-plane (OOP).

IV. **Strain Induced anisotropy:** When a magnetic system is subjected to strain, it gains anisotropy energy as a result of changes in magnetoelastic (ME) energy. Strain in films can be caused by various factors, such as intrinsic strain from the deposition process, strain due to mismatched lattice parameters of adjacent layers/substrate, and thermal strain resulting from differences in thermal expansion coefficients. The fabrication of ultrathin films/multilayers can lead to significant strain, particularly when epitaxial growth occurs on a substrate with varying lattice parameters (i.e. lattice mismatch between the materials of two consecutive layers).

V. **Perpendicular Magnetic Anisotropy:** The orientation of magnetic moments in ultrathin magnetic films and multilayers can be significantly different from bulk materials due to factors such as planar interfaces, surfaces, choice of materials, and layer thickness. These elements can lead to tailored magnetic anisotropy, with the most intriguing result being the change from in-plane to perpendicular magnetization direction, known as perpendicular magnetic anisotropy (PMA), which can enhance the thermal stability of nanomagnets at room temperature. PMA is observed when electron orbitals in an FM material are deformed in the direction perpendicular to the film interface. When the magnetization vector (**M**) of the specimen is maintained along the OOP direction, the effective magnetic field (H_{eff}) of the system is substantially increased due to SOI. However, there is no effect of SOI when the **M** lies in-plane. PMA can also be observed at the interfaces between 3d transition metal FMs (Co) and heavy nonmagnetic metals (W, Au, Pt, Pd). Heterostructures made from CoFeB and MgO have drawn particular attention due to their lower damping constant and high tunnelling magnetoresistance (TMR) ratio at room temperature.

2.4 Magnetization dynamics

Magnetization dynamics refers to the study of how the orientation and strength of magnetization in a material change over time in response to external stimuli. This field of research is crucial for understanding the behaviour of magnetic materials in various applications, such as data storage devices and magnetic sensors. Therefore, in order to gain a comprehensive understanding of various magnetic properties exhibited by a material, it is essential to comprehend the static as well as dynamic spin-based properties of the material. Magnetization dynamics can manifest across a broad spectrum of time scales. The fundamental exchange interaction is the fastest process, occurring within 10 fs. Spin-orbit coupling and spin-transfer torque take place within the time frame of 10 fs to 1 ps. Laser-induced ultrafast demagnetization occurs within a few hundred fs. The fast remagnetization period subsequent to ultrafast demagnetization spans from 1 to 10 ps. Magnetic writing, achieved through spin reversal, operates within a time scale of a few ps to a few hundred ps, while vortex core switching ranges from a few tens of ps to ns. Magnetization precession lasts from a few ps to a few hundred ps, with the associated damping occurring from sub-ns to tens of ns. Spin waves in ferromagnetic materials can propagate from a few hundred ps to tens of ns before dissipating. The most slow process is the movement of domain walls, with a timescale ranging from a few ns to hundreds of μs.

In TR-MOKE measurements, a fs laser pulse excites the magnetic material and the subsequent magnetization dynamics is studied. The laser photon's coherent interaction with electron and spin degrees of freedom in magnetic material results in rapid thermalization of these particles, leading to a sudden decrease in magnetization. This process is known as the ultrafast demagnetization [35]. Ultrafast demagnetization is succeeded by a dual-phase restoration of the chaotic magnetic structure via fast remagnetization (taking place in less than 10 ps due to the transfer of energy from the electron and spin systems to the lattice) and slow remagnetization (taking place in less than 100 ps due to energy dissipation from the lattice to the environment or substrate). The slow remagnetization procedure is intertwined with a damped precessional oscillation around a specific magnetic field orientation lasting for a few ns [34].

2.3.1 Ultrafast demagnetization

Beaurepaire *et al*. [35] used 60 fs laser pulses to measure transient transmittivity and linear MOKE of a 22 nm thick Ni film. They estimated an electron thermalization time of 260 fs and an electron temperature decay constant of 1 ps from the three-temperature model. The spin temperature attained its maximum around 2 ps, suggesting different electron and spin dynamics. The magnetic second harmonic generation (MSHG) experiment by Hohlfeld *et al*. [36] showed alike electron thermalization time of 280 fs, but there is no delay between electron excitation and magnetization loss. The results showed that ultrashort laser pulses led to ultrafast heating of the electronic system. However, questions arose about the explanation of the experimental findings, such as whether the magneto-optical behaviour exhibited from a nonequilibrium system is directly related to the magnetization. A study on Cu/Ni/Cu wedges [37] showed that the dynamic progression of Kerr ellipticity and rotation did not align, resulting in a disruption of the proportional relationship between magnetization and the Voigt vector. Over time, numerous independent theories have been suggested to elucidate various experimental findings on ultrafast demagnetization. Despite the multitude of proposed models and mechanisms, the precise microscopic processes responsible for this rapid decline in magnetization have continued to be a topic of debate.

- **Phenomenological Three-temperature model (3TM)**

Since the inception of the initial laser-induced magnetization dynamics experiments, it has been evident that the ensuing demagnetization is a complex process, involving various constituents of the system that engage in different relaxation processes. The interactions within such a system can be depicted qualitatively through a single model comprising three distinct yet interconnected reservoirs - electrons, lattice, and spins, see Figure 2.1(a). These reservoirs are linked by interactions of varying origins and efficiencies, with each reservoir being assigned a specific effective temperature. The 3TM elucidates the temporal progression of the system through three interlinked differential equations:

$$C_e(T_e)\frac{dT_e}{dt} = -G_{el}(T_e - T_l) - G_{es}(T_e - T_s) + P(t) \tag{2.8a}$$

$$C_s(T_s)\frac{dT_s}{dt} = -G_{sl}(T_s - T_l) - G_{es}(T_s - T_e) \tag{2.8b}$$

$$C_l(T_l)\frac{dT_l}{dt} = -G_{sl}(T_l - T_s) - G_{el}(T_l - T_e) \tag{2.8c}$$

Where, G_{ij} is the coupling between the ith and jth bath, C_i represents the specific heat, T_i describes the temperature of the ith bath and $P(t)$ is the laser source term. Electronic specific heat is proportional to the electron temperature, i.e., $C_e = \gamma T_e$, where γ is dictated by the electron density of states in the vicinity of the Fermi level. The magnetization of a system at a specific time delay can be determined by solving equations (2.8a-2.8c) in conjunction with the mean-field theory of ferromagnetism. This approach allows for the calculation of the evolution of electron, spin, and lattice temperatures over time delays, as well as the determination of specific heat values and coupling constants. Based on this model, following the excitation from the pump laser pulse, the photon energy from the laser beam is absorbed by the electron heat reservoir, resulting in the production of hot electrons that exceeds the Fermi level. This is clearly indicated by the sudden rise in electron temperature as shown in Figure 2.1(b). Throughout this increase in electron temperature, the total spin angular momentum of the system remains conserved due to dipole approximation. Additionally, the redistribution of majority and minority spins through scattering leads to an increase in spin temperature after a certain time delay. This rise in spin temperature subsequently causes rapid magnetization loss in the sample. Subsequently, energy from the electron and spin baths is dissipated in the lattice, leading to a fast remagnetization. After a few ps, all three heat baths reach an equilibrium state. The 3TM was additionally resolved analytically by Dalla Longa et al. in 2007 [38] under particular boundary conditions, including negligible specific heat, immediate rise in electron temperature following laser stimulation, and so forth. This analytical resolution is extensively employed within the scientific realm for calculating the ultrafast demagnetization time and rapid remagnetization time based on the ultrafast demagnetization information.

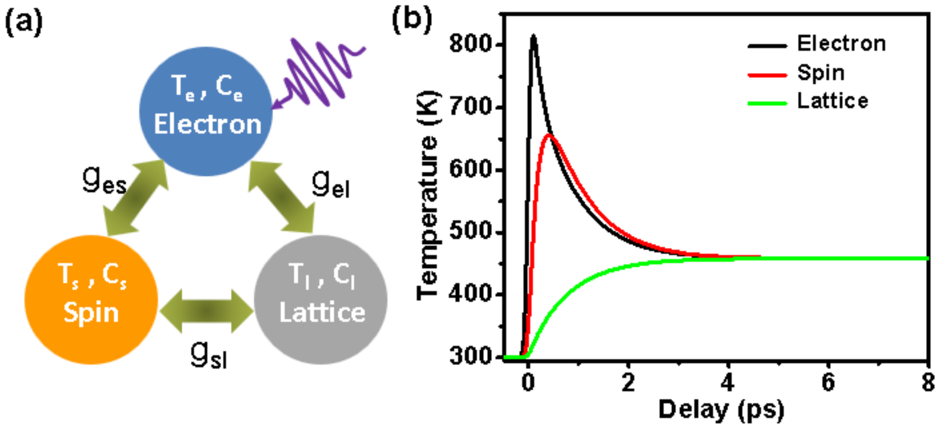

Figure 2.1: (a) Schematic of 3TM, (b) temporal evolution of electron, spin and lattice temperatures.

2.3.1.1 Mechanisms responsible for ultrafast demagnetization

The 3TM provides a phenomenological explanation for ultrafast demagnetization and subsequent fast recovery. However, it lacks consideration for the underlying microscopic mechanisms involved in the ultrafast demagnetization phenomenon, such as energy transfer processes from laser photons to ordered ferromagnetic systems and angular momentum transfer mechanisms between different heat baths. Additionally, the model fails to explain the two-step demagnetization process observed in rare-earth ferrimagnets, consisting of a sub-ps demagnetization followed by a slow few ps magnetization loss. Various microscopic mechanisms have been proposed over time to address these discrepancies in the 3TM, which is discussed in the subsequent sections.

2.3.1.1.1 Spin-photon interaction

In 1997, Hubner and Zhang proposed that ultrafast demagnetization is a result of the interplay between exchange interaction and SOC [39]. Zhang and Hübner have contended that ultrafast demagnetization is a collaborative outcome of the laser field and the SOC of a magnetic material [40]. Their research revealed that without SOC, a femtosecond laser pulse alone is incapable of demagnetizing a ferromagnetic sample. With the introduction of SOC, the spin angular momentum of a magnetic material triggers a measurable orbital angular momentum. This orbital angular momentum is highly susceptible to lattice fluctuations and deformations. Consequently, there is a reduction in spin angular momentum as electrons fail to keep up with the spin motion, resulting in ultrafast demagnetization. Moreover, under the influence of SOC, singlet and triplet states blend together and lose their distinctiveness. This blending can transform various prohibited spin states into permissible states. Furthermore, diverse laser-induced spin transitions explore these permissible states, causing a sudden decline in system magnetization.

In 2004, Beaurepaire *et al*. [41] discovered that the ultrafast demagnetization process is linked to the generation of terahertz pulses. Following excitation by a pump laser, various spin-flip scattering events take place within a magnetic system due to its SOC. These spin-flip events in the electron relaxation process are facilitated by SOC, which does not lead to complete demagnetization as observed in experiments. Additionally, the relaxation of electron spins between majority and minority sub-bands, aided by photon emission in the far infrared range, contributes to the demagnetization process. This explanation serves as an expansion of a previously proposed model that considers the coherent interaction between photons and electrons [40].

2.3.1.1.2 Spin-flip scattering

In a ferromagnetic metal, there exists four primary mechanisms by which an excited electron can change its spin orientation. These include: a) Stoner excitation, which is most effective at higher energy levels [42], b) inelastic electron-spin-wave scattering, which is effective when the photon energy for excitation is relatively low [43,44], c) spin-flip scattering (SFS) resembling single-particle behavior involving impurities or phonons, known as the Elliott-Yafet (EY) mechanism [45,46], and d) electron-electron scattering based on Coulomb interaction [47].

a) **Stoner excitation:** The spin-flip probability in metals is significantly influenced by the band structure, which separates electronic bands for spin-down and spin-up electrons.

When the Fermi level is positioned between these bands, the lower-energy spin-up states are filled, whereas the higher-energy spin-down states remain unoccupied. This difference results in a net spin polarization of the conduction electrons. Exchange-split bands also present a unique single-particle magnetic excitation, called a Stoner excitation, where an electron undergoes spin reversal.

b) **Electron-magnon scattering:** Stoner excitations, involving spin reversal, are considered magnetic excitations at the single-particle level in itinerant-electron magnets. When the electronic bands have a large exchange splitting at low energy and wave vector, individual Stoner excitations are not allowed. Instead, a collective magnetic excitation known as a spin wave can be produced through a coherent superposition of virtual excitations characterized by wave vector q at low energy [44]. In areas of energy-momentum space where individual Stoner excitations are almost permitted, there will be a coupling between the spin waves and Stoner modes, resulting in heavily damped spin waves. Therefore, in the low-energy region, spin waves are expected to dominate over Stoner excitations. This phenomenon is observed in the majority of experiments involving laser-induced magnetization dynamics using near-infrared wavelengths around 800 nm, corresponding to a photon energy of 1.5 eV. It is important to note that on-site spin flips do not require a finite q vector, yet low-energy excitation is made possible by many-body effects.

c) **Elliot-Yafet mechanism:** In 2010, Koopman *et al*. [48] introduced a microscopic model that utilized phonon-mediated EY scattering to elucidate the ultrafast demagnetization mechanism. This model is capable of accounting for both the ultrafast sub-picosecond single-step demagnetization process in transition metals ferromagnets (Type-I demagnetization) and the slower two-step demagnetization process of rare earth ferrimagnets (Type-II demagnetization). The model operates under the assumption that there exists a finite probability for a spin to undergo flipping through a scattering event, which is referred to as the spin-flip probability. During a scattering event, electrons transfer a portion of their angular momenta to the phonons, resulting in the band-mixing of minority spin-down and majority spin-up states with similar spin states near the Fermi level. This process also alters the likelihood of locating the scattered electron in its previous spin state (either spin-up or spin-down). According to this theory, the spin-mixing due to the phonon-mediated SFS is contingent upon the number of minority spin-down and majority spin-up states at the Fermi level. The temperature evolution of the electron, lattice, and magnetization can be described by three interconnected differential equations as per this model:

$$C_e(T_e)\frac{dT_e}{dt} = \nabla_z(k\nabla_z T_e) + g_{el}(T_l - T_e) \tag{2.9a}$$

$$C_l\frac{dT_l}{dt} = g_{el}(T_e - T_l) \tag{2.9b}$$

$$\frac{dm}{dt} = Rm\frac{T_l}{T_C}\left(1 - m\coth\left(\frac{mT_C}{T_e}\right)\right) \tag{2.9c}$$

Where k is the thermal conductivity of electron, m represents the normalized magnetization and, T_l, T_e and T_C are the lattice, electron and Curie temperature respectively. Furthermore,

$$R = \frac{8a_{sf}g_{el}K_B T_C^2 V_{at}}{(^{\mu_{at}}/_{\mu_B})E_D^2} \tag{2.10}$$

Here, a_{sf}, g_{el}, V_{at}, μ_{at} and E_D are the spin-flip probability, electron-lattice coupling parameter, atomic volume, atomic magnetic moment and Debey energy, respectively. It has been noted that the R-value is significantly lower for rare earth materials such as Tb and Gd, compared to transition metals like Ni and Fe. This observation enables researchers to suggest that a lower R-value may result in a two-step slow demagnetization process, with spin-lattice relaxation playing a significant role in the demagnetization process.

d) **Coulomb interaction:** Krauβ *et al*. have shown that a mechanism similar to that of EY, which relies on electron-electron scattering facilitated by the Coulomb interaction, has the capability to elucidate the extremely ultrafast demagnetization process in materials with high SOC strength [47]. This scattering mechanism provides a larger phase space for electrons to transition from minority spin bands to majority spin bands compared to electron-phonon scattering. When excited by an ultrashort laser pulse, nonequilibrium electron distribution is created, leading to inter-band and intra-band Coulomb scattering. The ultrafast demagnetization is then succeeded by fast remagnetization as energy is transferred to the lattice heat bath.

2.3.1.1.3 Relativistic spin-photon interaction

Bigot *et al*. [49] put forward a theory in 2009 that is rooted in relativistic spin-photon interaction, offering an explanation for the ultrafast demagnetization mechanism. According to this theory, the material's polarization, brought about by the photon field, coherently interacts with the spins. This mechanism is derived from relativistic quantum electrodynamics, going beyond the spin-orbit interaction that involves the ionic potential. Furthermore, this coherent interaction is distinctly separate from the incoherent ultrafast demagnetization linked to the spins' thermalization.

2.3.1.1.4 Super-diffusive spin current transport

The majority of theories developed to comprehend ultrafast demagnetization have concentrated on the angular momentum transfer process. These suggestions are grounded on the idea that the femtosecond laser interacts directly with perfectly aligned spins and initiates various avenues for angular momentum dissipation. None of these hypotheses consider any spin transport phenomenon to elucidate the ultrafast demagnetization mechanism. Nevertheless, in 2008 Malinowski *et al*. [50] noticed that the spin transport of hot electrons within a synthetic antiferromagnet hastens its demagnetization process. Subsequent to this experimental observation, Battiato *et al*. [51] introduced a semiclassical model in 2010 to support the significance of spin transport in the demagnetization process. In this model, they illustrated that the laser-induced demagnetization process can be clarified without assuming the generation of any spin-flip channels, but merely through super-diffusive spin transport (SST) theory. As per this theory, there is a spin-dependent transport of electrons within a magnetic system where the electrons with majority up-spin orientation led to quicker diffusion into the substrate compared to the electrons with minority down-spin orientation. Post laser excitation, electrons in d-bands are stimulated by absorbing energy from the laser photons to the s-bands or p-bands that are present above the Fermi level. The mobility of these stimulated s-bands and p-bands is significantly higher in contrast to the initial d-bands, rendering these electrons highly mobile. These mobile electrons move at a very high speed in various directions and undergo multiple spin-conserving scattering events. These successive scattering events generate a flow of hot electrons. The electron flux produced through laser excitation can be expressed by the transport equation:

$$\frac{\partial n^{tot}}{\partial t} + \frac{n^{tot}}{\tau} = \left(-\frac{\partial}{\partial z}\hat{\varphi} + \hat{I}\right)\left(\hat{S}n^{tot} + S^{ext}\right) \tag{2.11}$$

Here, $\hat{\varphi}$ and $\hat{I}$ represent the flux and identity operator. n^{tot}, S^{ext} and τ are the electron density, electron source term and lifetime of spin respectively. $\hat{S}n^1 = S^2$, where n^1 and S^2 are the electron density of the initial generation and the excitation term of the subsequent generation. The lifetime of electrons with majority and minority spins varies, leading to a gradual decrease in the majority spins within the magnetic layer. This reduction in majority carriers results in a decrease in the net magnetization of the system, ultimately causing ultrafast demagnetization. The diffusive motion of particles can be described by the variance of the displacement (σ^2). In the case of a particle distribution exhibiting diffusive transport, the relationship for σ^2 can be written as $\sigma^2 \propto t^n$, where n = 1. Conversely, for Ballistic transport, n = 2, meaning that $\sigma^2 \propto t^2$. It is important to note that super diffusive spin transport does not fall under either ballistic or diffusive categories. In this scenario, the value of n is subject to change over time, ranging from n = 2 for a shorter lifetime to n = 1 for a longer lifetime.

Another emerging mechanism in this context is the optical inter-site spin transfer (OISTR) effect [52], which also produces a pure spin current. The OISTR process becomes important when the photon energy of an ultrashort infrared femtosecond pump pulse can cause a resonant transition between elemental subsystems of an alloy.

- **Ultrafast Einstein–de Haas effect**

Despite the intense controversy surrounding the microscopic mechanism of this process, the 2019 study by Dornes *et al*. [53] utilized femtosecond time-resolved X-ray diffraction to demonstrate that the majority of the angular momentum lost from the spin system in spin-flip scattering mechanism during laser-induced demagnetization of ferromagnetic iron is transferred to the lattice on sub-picosecond timescales. This results in the initiation of a transverse strain wave that propagates from the surface into the bulk.

2.3.2 Precessional dynamics

In the lack of a magnetic field, electron spins in a magnetic material are randomly oriented. When a large enough magnetic field is applied, all spins try to align along the magnetic field direction to reduce the overall energy of the system. The ground state spin configuration is the minimum energy state where all spins are directed along the effective magnetic field direction. The total energy of the system is the sum of different energies like Zeeman, anisotropy, magnetoelastic, and exchange energy, which correspond to different applied magnetic field values. The vector that sums up all these fields is called the effective magnetic field. Before any external perturbation, the macrospin of a magnetic material is in equilibrium and oriented in the effective magnetic field direction. However, a femtosecond laser pulse or RF microwave field modifies the effective magnetic field, leading to it being directed along a non-equilibrium direction. This causes a damped spiral movement of the magnetization about the effective magnetic field, known as the precessional dynamics. This spiral motion can be explained by a phenomenological theory based on the Landau-Lifshitz-Gilbert (LLG) equation [54]. The LLG torque equation was initially introduced by Landau and Lifshitz in 1935 [55] and later revised by Gilbert, who added a modified damping term [56]. The theoretical formulation of the LLG equation is briefly outlined below:

Quantum mechanically, the relation between the torque (τ) experienced by an electron having spin angular momentum (S) can be written as

$$\tau = \frac{dS}{dt} \tag{2.12}$$

When a material with a net magnetic moment M is subjected to an effective magnetic field H_{eff}, it will undergo a torque

$$\tau = M \times H_{eff} \tag{2.13}$$

From equation 2.12 and 2.13, we can have

$$\frac{dS}{dt} = M \times H_{eff} \tag{2.14}$$

Here, the effective magnetic field, denoted as H_{eff}, is a combination of the external magnetic field, dipolar field, exchange field, and anisotropy field. The magnetic material's magnetic moment M is related to S through the specific equation

$$M = -\gamma S \tag{2.15}$$

Where γ is the gyromagnetic ratio. Substituting the value of S in equation 2.14, we will have

$$\frac{dM}{dt} = -\gamma\left(M \times H_{eff}\right) \tag{2.16}$$

The significance of this equation lies in the fact that the magnetization rotates around H_{eff} with a constant amplitude and frequency (known as Larmor frequency = γH_{eff}) without any energy loss. However, in practical situations, the rotational amplitude gradually diminishes over time. Therefore, to accurately represent the real rotational dynamics, the introduction of a damping term becomes essential. Consequently, Landau and Lifshitz (LL) proposed a dynamic equation that includes a damping term in addition to the rotational torque term. After that equation can be written as:

$$\frac{dM}{dt} = -\gamma\left(M \times H_{eff}\right) + \frac{\lambda}{M^2} M \times \left(M \times H_{eff}\right) \tag{2.17}$$

Here, the damping of the magnetization dynamics is represented by the term $\frac{\lambda}{M^2} M \times (M \times H_{eff})$. λ is the Landau damping parameter. The LL-damping was unable to account for the substantial non-eddy current-induced damping contributions. In order to overcome this constraint, Gilbert revised the theory to be more coherent and to include other important damping contributions. The revised LL-equation, referred to as the LLG-equation, is expressed as:

$$\frac{dM}{dt} = -\gamma(M \times H_{eff}) + \frac{\alpha}{M}\left(M \times \frac{dM}{dt}\right) \tag{2.18}$$

Where α is the dimensionless Gilbert damping parameter.

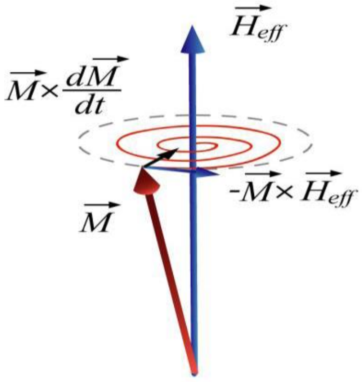

Figure 2.2: Precession of magnetization with damping about the effective magnetic field.

2.3.2.1 Kittel equation

Precessional dynamics leads to the concept of ferromagnetic resonance, which occurs when a ferromagnetic system absorbs power from an oscillating field under a stable bias field and an alternating magnetic field. This resonance occurs at a higher frequency than the Larmor precession frequency, known as ferromagnetic resonance (FMR) and its frequency (f). In 1948, C. Kittel derived the resonance condition by solving the equation of motion and defining the role of the demagnetizing field [57]. ω can be written as:

$$f = \frac{\gamma}{2\pi}\sqrt{[H + (N_y - N_z)M_s][H + (N_x - N_z)M_s]} \tag{2.19}$$

In this case, N_x, N_y, and N_z represent the x, y, and z components of the demagnetizing field tensor. The demagnetizing field tensor components and their respective resonance frequencies for several commonly used shapes are as follows:

1. For spherical shape: $N_x = N_y = N_z = 1/3$ and $f = \frac{\gamma}{2\pi} H$.

2. For planar film: $N_x = N_z = 0$, $N_y = 4\pi$ and $f = \frac{\gamma}{2\pi}\sqrt{H(H + 4\pi M_s)}$.
3. For a cylindrical shape: $N_x = N_y = 1/2$, $N_z = 0$ and $f = \frac{\gamma}{2\pi}(H + \frac{M_s}{2})$.

In addition to the demagnetizing field, the magnetic anisotropy of a system has an impact on the resonance frequency of a material. The equation (2.19) governing the resonance frequency can be adjusted by including various magnetic anisotropy terms. Several examples of resonance frequency expressions with different anisotropies include:

1. For an in-plane magnetized sample having uniaxial anisotropy (K_1 represents uniaxial anisotropy constant)

$$f = \frac{\gamma}{2\pi}\sqrt{\left(H + \frac{2K_1}{M_s}\right)\left(H + 4\pi M_s + \frac{2K_1}{M_s}\right)} \tag{2.20}$$

2. For an in-plane magnetized sample having cubic anisotropy (K_2 represents cubic anisotropy constant)

$$f = \frac{\gamma}{2\pi}\sqrt{\left(H + \frac{2K_1}{M_s} - \frac{4K_2}{M_s}\right)\left(H + 4\pi M_s + \frac{2K_1}{M_s} - \frac{4K_2}{M_s}\right)} \tag{2.21}$$

3. For out-of-plane magnetized sample ($K_\perp$ represents out-of-plane magnetic anisotropy constant)

$$f = \frac{\gamma}{2\pi}\sqrt{\left(H + \frac{2K_\perp}{M_s}\right)\left(H + 4\pi M_s + \frac{2K_\perp}{M_s}\right)} \tag{2.22}$$

2.3.2.1 Spin wave

In 1930, F. Bloch introduced the concept of spin waves to explain the decrease in saturation magnetization as the system temperature increases [58]. Initially, electron spins are aligned parallel to each other and oriented along the effective magnetic field. When the magnetic material is excited, the temperature rises in the excited region, causing an electron spin to flip. Due to the exchange interaction in a ferromagnet, the flipping of one spin leads to neighbouring spins flipping with a phase difference. This phase difference propagates as a wave in the magnetic system to minimize exchange energy, known as a spin wave. The quanta of this wave are called magnons [59]. In the case of uniform precessional motion, exchange-coupled spins precess in sync around the effective magnetic field, resulting in an infinite wavelength (λ) and a wavevector (k) approaching zero. However, in non-uniform precession, there is a finite propagation of phase difference leading to a finite wavelength and a non-zero k-value of the spin wave.

Spin waves can be categorized into two types based on their range of interaction and wavelength: exchange spin waves and dipolar spin waves [60]. Exchange-dominated spin waves are characterized by short wavelengths and are dominated by exchange interaction, while dipolar spin waves are identified by longer wavelengths and are dominated by dipolar interaction. Additionally, there are spin wave modes where both exchange and dipolar interactions play equal roles, typically appearing at a wavelength similar to the exchange length. The resonance frequency for dipole-exchange dominated spin waves in an FM system of infinite thickness can be expressed as:

$$f = \frac{\gamma}{2\pi}\sqrt{\left(H + \frac{2A}{M_s}k^2\right)\left(H + 4\pi M_s sin^2\theta + \frac{2A}{M_s}k^2\right)} \tag{2.23}$$

Here, the wavevector is denoted as k, while the exchange-stiffness constant is represented by A. The angle between the magnetization and the magnetic easy axis of the sample is denoted as θ.

Within a ferromagnetic material, the exchange-dominated spin waves have the ability to propagate through the thickness of the film, resulting in the formation of standing waves. The specific spin wave modes that emerge in the spectrum as a result of these standing waves are referred to as perpendicular standing spin wave (PSSW) modes. In this context, the resonance frequency can be expressed as:

$$f = \frac{\gamma}{2\pi}\sqrt{\left(H + \frac{2A}{M_s}\left(\frac{n\pi}{d}\right)^2\right)\left(H + 4\pi M_s + \frac{2A}{M_s}\left(\frac{n\pi}{d}\right)^2\right)} \tag{2.24}$$

Here, the PSSW mode's order is denoted by n, while the sample's thickness is represented by d.

Manipulating various spin waves can be achieved through external stimuli like femtosecond laser, spin-torque, or an external bias magnetic field. This control can potentially result in diverse structural modifications in magnon-based information processing tools. The focus of this doctoral research has been primarily on examining the uniform precessional motion ($k \approx 0$) and PSSW modes of varying orders in magnetic thin films and heterostructures.

2.3.3 Magnetic damping

During the precession of magnetization, there is always a certain amount of spin angular momentum dissipated through the lattice, leading to a gradual decrease in precessional amplitude over time. This phenomenon is known as magnetic damping. The precise control of the magnetic damping parameter is crucial in the magnetic data storage industry as it enables the acceleration of magnetization recovery to equilibrium during the magnetization reversal process. Moreover, a thorough understanding of the mechanisms underlying magnetic damping and its effective modulation through external means is essential for the development of advanced spintronics devices. High magnetic damping materials are sought after to eliminate the 'ringing' of magnetization (precession) in MRAM devices during the data-writing process. Conversely, low damping materials play a significant role in the spintronics field by reducing the write-current in spin-torque-based MRAM devices and facilitating long-distance spin-wave propagation in magnonic devices.

The classification of magnetic damping is based on the direction of energy transfer, resulting in indirect and direct magnetic damping categories [61]. Indirect damping occurs when the energy within the magnetic system is conserved, such as damping of spin waves by Stoner excitation or damping due to mode conversion. On the other hand, direct damping involves the conveyance of energy from the magnetic system to an adjacent nonmagnetic system and is further divided into intrinsic and extrinsic damping [34]. Intrinsic damping, determined by scattering from phonons, cannot be externally controlled as it is inherent to the system. Extrinsic damping, on the other hand, arises from additional magnon scattering from phonons and is influenced by external factors like defect density, magnetic anisotropy, temperature, sample geometry, and growth quality. Various contributions to damping can also be adjusted through spin current [12], eddy current [62], phonon-drag [63], capping [64], doping [65], introduction of strain [66], inversion symmetry breaking at the interface [67] etc. In the next section, we will briefly outline the mechanisms involved in both intrinsic and extrinsic damping.

2.3.3.1 Intrinsic damping

Various factors like intrinsic spin-orbit coupling of ferromagnets, eddy current, and phonon drag mechanisms play a significant role in intrinsic damping.

A. Intrinsic spin-orbit coupling

The relationship between the spin of an electron and its orbital angular momentum is referred to as SOC. This interaction is crucial in determining the electronic and magnetic properties of a material by influencing the electron flow, spin-flip scattering, magnetic anisotropy, spin relaxation time, and dissipation rate of the spin current in these devices. In the presence of SOC in a material, the spin magnetic moment is transformed into orbital magnetic moments, which are highly sensitive to lattice fluctuations. This results in a loss of the net magnetic moment of the system, leading to finite magnetic damping. V. Kambersky provided a detailed theoretical calculation in 1976 on the relationship between intrinsic damping and the strength of SOC using the torque-correlation model. According to this model, two processes significantly contribute to SOC-induced magnetic damping: i) phonon-mediated spin-flip scattering (explained by *s-d* exchange interaction) and ii) ordinary scattering (explained by the breathing Fermi surface model).

i) Phonon-mediated spin-flip scattering

In 1954, Elliott and Yafet introduced a phonon-mediated spin-flip scattering mechanism through the scattering theory approach for energy dissipation in ferromagnetic metals [45,46]. Two years later, Kittel and Mitchel provided the mathematical formulation of this mechanism based on the *s-d* relaxation mechanism [68]. According to this model, the SOC of a material enables spin-flip scattering via phonons between two spin sub-bands. In these materials, the localized *d*-electrons are connected to itinerant s-electrons through *s-d* exchange interaction, facilitating the transfer of spin angular momentum from *d*-electrons to *s*-electrons. This results in an incoherent spin-flip scattering of both *s*- and *d*-electrons, where the total spin angular momentum is not conserved. The α-value extracted from this model can be expressed as:

$$\alpha = D_F \left[\frac{\gamma\hbar^2(\delta g)^2}{4\tau M_s}\right] \tag{2.25}$$

In this context, D_F, τ^{-1}, and δg denote the density of states at the Fermi level, electron-phonon collision frequency, and deviation in the electronic g-factor, respectively. The relationship between α and D_F suggests that a higher density of states at the Fermi level will contribute to increased damping.

ii) Ordinary scattering

The ordinary scattering mechanism theory was presented as the Fermi surface model for breathing [69,70]. In this model, spin sub-bands with different wave vectors are considered to be distinct in the presence of SOC. Scattering within these sub-bands contributes finitely to the damping process. As the magnetization orientation changes continuously during precessional motion, the energy states of the various spin bands fluctuate randomly. Consequently, a spin state on one side of the Fermi level at a specific delay time may transition to the other side of the Fermi level at a different delay time. This transition can lead to the creation of an electron-hole pair, resulting in quicker dissipation of spin angular momentum. The damping contribution based on this model can be expressed as:

$$\alpha = \left[\frac{\gamma \xi^2 D_F \tau (\delta g)^2}{4M_S}\right] \tag{2.26}$$

The material's SOC strength, denoted as ξ, was observed to have been underestimated due to the failure of the breathing Fermi surface model to account for electron scattering caused by temperature variations in the system. It was later discovered that there are two types of contributions to damping, depending on the generation of electron-hole pairs [71]:

1. Intra-band electron-hole pair generation involves the occurrence of both electron and hole in the same band. Damping contributes significantly to conductivity (as it is directly proportional to the material's conductivity) and varies proportional to ξ^3. This phenomenon is predominantly observed at low temperatures.

$$\alpha \propto \sigma \tag{2.27}$$

2. Inter-band electron-hole pair generation occurs when the electron and hole are present in different bands. Damping plays a major role in resistivity (as it is directly proportional to the material's resistivity) and varies as ξ^2. This phenomenon is mainly valid at high temperatures.

$$\alpha \propto \rho \tag{2.28}$$

B. Eddy current mechanism

According to Faraday's principle, a voltage will be created as a result of a time-varying magnetic field. This voltage will resist any further alterations in the magnetic field being applied. The rotation of magnetization in a ferromagnetic material is akin to a time-varying magnetic field, capable of generating a voltage. This voltage can induce a finite electric current in the ferromagnetic material, known as an eddy current. In accordance with Faraday's principle, this eddy current opposes any changes in the orientation of magnetization with respect to the external magnetic field, leading to an increase in damping. The contribution of eddy currents to damping is more significant in highly conductive ferromagnetic materials with greater thickness, approaching or exceeding the skin depth of the microwave excitation field [72]. The modulation of damping resulting from this mechanism can be mathematically expressed as:

$$\alpha = \frac{(\gamma M_S)^2}{6}\left(\frac{4\pi}{c}\right)2\sigma d^2 \tag{2.29}$$

Here, the electrical conductivity of the FM material is denoted by σ, while c represents the speed of light in a vacuum, and d stands for the thickness of the FM material.

C. Phonon drag mechanism

In 1998, H. Suhl introduced a magnon-phonon scattering mechanism aimed at amplifying the damping process in magnetostrictive materials [73]. Phonons can dissipate their energy in two ways:

a. Direct energy dissipation to the lattice from uniform precessional oscillation.

b. Indirect energy dissipation through non-uniform spin-wave excitation.

The direct energy dissipation process is commonly referred to as the phonon-drag mechanism. The resulting damping from this mechanism can be expressed as:

$$\alpha = \frac{2\zeta\gamma}{M_S}\left[\frac{B(1+\sigma)}{Y}\right]^2 \tag{2.30}$$

In this system, ζ, σ, B, and Y symbolize the and phonon viscosity, Poisson’s ratio, magnetoelastic shear constant, Young’s modulus, respectively. The phonon-drag mechanism occurs exclusively in materials where the ferromagnetic resonance frequency is influenced by elastic waves propagating through the film thickness.

2.3.3.2 Extrinsic damping

Few external factors can have a significant impact on the damping parameter in a magnetic system, resulting in what is known as extrinsic damping. This extrinsic damping can stem from both local and nonlocal sources. Local damping occurs when energy is dissipated within the phonon and electron system of the magnetic material itself. For instance, defects and inhomogeneities in the sample can lead to the generation of non-uniform resonance modes alongside the uniform ones, thereby increasing the damping of the composite system. On the other hand, nonlocal extrinsic damping in a magnetic material occurs when another magnetic or nonmagnetic material is located adjacent to it. This additional damping is caused by spin-torques on the magnetic system resulting from spin current (via various spin-orbit effects) or the transfer of spin angular momentum out of the magnetic system (also referred to as spin pumping). The extent of this nonlocal damping is heavily influenced by factors such as layer thicknesses, the strength of SOC in materials, and the characteristics of the interface. In this overview, we discuss the popular extrinsic mechanisms that can impact the damping of uniformly precessing spins.

A. Magnetic impurity

Within a magnetic material, defects or impurities can serve as points of scattering for the spinning spins. The scattering phenomenon is inherently inelastic. These scattering points cause a loss of energy from the magnetic system by disrupting the precessional oscillation, ultimately resulting in an increase in α. The extent of magnetic damping due to this factor can be managed by reducing the defect density within the sample.

B. Inhomogeneous magnetic anisotropy

In the presence of magnetic anisotropy within a material, the system's magnetization shows a preference for specific directions [74]. When the sample exhibits sufficiently high magnetic anisotropy, the precessional dynamics can be altered, leading to a significant increase in magnetic damping. This increase in damping is more noticeable in lower applied fields, where spins are less tightly bound along the magnetic field direction, making them more susceptible to perturbations from the anisotropy field. The higher the anisotropy field relative to the external magnetic field, the greater the value of α. As the external magnetic field decreases, α experiences an exponential increase, reaching a peak at the anisotropy field.

C. Spin current induced torque

The magnetic damping of an FM material can undergo significant changes through spin current injection, which can be influenced by various spin-orbit effects such as the spin Hall effect (SHE) [75], Rashba-Edelstein effect (REE) [76], and other spin caloric effects [77]. The injected spin current introduces a torque on the precessing spins, affecting their energy dissipation process. In the case of a high strength NM material with strong SOC, the application of a charge current leads to the development of spin polarization along its transverse direction due to spin-dependent scattering, known as the SHE. This spin polarization, in the form of pure spin current, flows to the adjacent FM layer through the NM/FM interface, exerting a torque on the precessing magnetization of the FM. This torque can either increase (damping-like torque) or decrease (anti-damping-like torque) α of the composite NM/FM system. The REE is another mechanism for spin-charge conversion, which emerges in the presence of spin-polarized surface states. When a charge current flows through these spin-polarized surface states, a finite spin accumulation is observed at the interfaces. This spin accumulation acts as a spin current, influencing the magnetization dynamics. Alongside the SHE and REE, there exist several spin caloric effects like the spin Seebeck effect, spin Nernst effect, and spin Peltier effect, which can convert between thermal and spin current. In these cases, a temperature gradient can generate spin current and significantly modulate α.

D. Spin pumping

In an NM/FM heterostructure, an external stimulation leads to magnetization precession, resulting in the transfer of spin angular momentum from the FM layer to the NM layer in the form of pure spin current. This phenomenon, known as the spin pumping effect, is analogous to a physical pumping mechanism. As a consequence, the amplitude of precession experiences accelerated decay, leading to an increase in α. The spin pumping effect in NM/FM layered systems was initially proposed in 1988 by Hurdequint *et al.* to explain the findings of a spin resonance experiment [78]. The authors suggested that the precessing magnetization serves as the source of a nonequilibrium spin accumulation that diffuses out of the NM/FM interfaces into the adjacent NM layer, where it is dissipated by spin-flip processes. The enhancement in α induced by spin pumping was further explored in 1996 by Berger *et al.* in NM/FM/NM type spin valve structures [79]. Their expression for the modulation of α is dependent on the layer thickness and several material parameters. However, this modulation does not disappear with vanishing exchange splitting, raising doubts about its validity. In 2002, Y. Tserkovnyak and A. Brataas theoretically demonstrated this damping enhancement in NM/FM heterostructures using the time-dependent adiabatic scattering theory, which gained widespread acceptance in the scientific community [12,22,80]. Their study predicted that in the presence of an NM layer adjacent to the FM layer, spin current would be pumped from the FM layer to the NM layer and be partially or fully absorbed. The pumped spin current (I_s^{pump}) from the FM layer to the NM layer due to the spin pumping effect can be expressed as:

$$I_s^{pump} = \frac{\hbar}{4\pi}\left(g_r^{\uparrow\downarrow} M \times \frac{dM}{dt} - g_i^{\uparrow\downarrow}\frac{dM}{dt}\right) \tag{2.31}$$

The imaginary and real components of the spin-mixing conductance are represented by $g_i^{\uparrow\downarrow}$ and $g_r^{\uparrow\downarrow}$. When a large but finite NM reservoir is connected to one side of the FM, it is expected to create a non-vanishing spin accumulation at the NM/FM interface. The difference in chemical potential between spin-up and spin-down states perturbs these accumulated spins, causing them to be pumped out from the NM/FM interface and allowing them to relax through spin-flip scattering. With a slow enough variation of magnetization, this spin accumulation is anticipated to flow back into the FM layer, generating a spin backflow current (I_s^{back}). The spin backflow current is influenced by the spin accumulation at the NM/FM interface and is dependent on the spin backflow factor (β) of the NM layer. The most significant increase in damping occurs when there is no backscattered spin current, meaning that $\beta \rightarrow 0$. As I_s^{back} becomes more significant, the enhancement in damping decreases from its highest value. Conversely, when $\beta >> 1/g_r^{\uparrow\downarrow}$, the damping enhancement is insignificant. The spin current that is pumped into the NM layer is almost completely sent back to the FM layer.

In order to function as an effective spin sink, the NM layer thickness must exceed its spin diffusion length by several times. The increase in the Gilbert damping parameter is greater for NM layers with a higher spin-flip relaxation rate (r). NM layers possessing high r values have the potential to counteract the spin accumulation at the NM/FM interface. This r can be approximately defined as:

$$r \propto Z^4 \tag{2.32}$$

Where, Z represents the atomic number. The heavier elements with $Z \geq 50$ exhibit a significantly high r value, making them well-suited for utilization as spin sink material. Consequently, NM/FM heterostructures containing a heavy metal NM layer like W, Ta, Pt, or Pd are anticipated to have a substantial damping enhancement. Conversely, lighter materials with atomic number $Z \leq 50$, such as Cu, Ru, or Al, have a considerably smaller r, rendering them less effective as spin sink material.

E. Two-magnon scattering

The existence of magnetic imperfections and irregularities in the ultra-thin magnetic films can lead to the dispersion of the uniform precessional mode ($k = 0$) by non-uniform modes ($k \neq 0$). This phenomenon is commonly referred to as two-magnon scattering (TMS) [81-83]. It represents an inelastic scattering process where energy remains constant, but magnon momentum does not. The TMS contribution to precessional dynamics is primarily influenced by three factors:

i) Precessional frequency: The quantity of degenerate magnons accessible for scattering rises as the precessional frequency rises. This also suggests that the likelihood of magnon-magnon scattering increases with a higher frequency.

ii) The angle between the easy axis of the sample and the external applied magnetic field: As the angle between the sample's easy axis and the external applied magnetic field grows, magnon degeneracy diminishes slowly. Ultimately, the degeneracy disappears when the sample's magnetization aligns perfectly along the out-of-plane direction.

iii) The thickness of the magnetic film: The TMS contribution to the α demonstrates an inverse square dependence on the FM layer thickness.

$$\alpha_{TMS} = \beta_{TMS} t_{FM}^{-2} \tag{2.33}$$

F. Spin memory loss

The partial depolarization of the spin current produced by the FMR technique at the interface is caused by the spin memory loss (SML). This concept was initially introduced in 1933 by T. Valet *et al.* in their research on current perpendicular to-plane GMR [84]. As per this proposition, if J_s represents the quantity of spin current produced on the FM side, after excitation then only $(1 - \delta)J_s$ can traverse the NM/FM interface (where δ denotes the SML coefficient). During the absorption process at the interface, δJ_s is influenced by the interfacial spin-orbit coupling or defects. Various theoretical calculations and experimental investigations have validated that a current discontinuity emerges at the NM/FM interface due to SML, turning the interface into an ideal spin sink [29,85]. This loss impacts spin transport and enhances the α-value of a composite system by reducing the interface's transparency. To fabricate spin-based devices, it is advisable to minimize this impact in a composite structure by establishing a transparent, well-defined, and defect-free interface.

2.5 Correlation between ultrafast demagnetization and Gilbert damping

The synchronization of magnetization dynamics spanning from femtoseconds to nanoseconds poses a persistent challenge for the field of magnetism. A microscopic model was introduced by Koopmans *et al.* in 2005 to establish a connection between ultrafast demagnetization, a femtosecond event, and magnetic damping, a nanosecond process [86]. This model operates under the assumption that both ultrafast demagnetization and magnetic damping rely on spin-flip scattering to release energy to the lattice. Furthermore, it suggests that the primary angular momentum transfer pathways in both scenarios are identical. As per this model, when the temperature is significantly lower than the Curie temperature (T_C), the relationship between ultrafast demagnetization time (τ_m) and α can be expressed as:

$$\tau_m = \frac{\hbar}{4 k_B T_C \alpha} \tag{2.34}$$

Nevertheless, this model fails to account for these phenomena at elevated temperatures, where regular scattering takes precedence. Additionally, it is flawed in two ways: i) it oversimplifies the treatment of electronic spin-flip scattering by using only one effective parameter, and ii) it neglects the impact of band structure variation. Djordjevic *et al.* developed a micromagnetic model in 2007, suggesting an additional magnetic relaxation path, including instantaneous ultrafast demagnetization due to spin-flip scattering events and energy transfer between excited states and spin wave relaxation chains [87]. In 2008, Walowski *et al.* challenged the Koopmans model by revealing a discrepancy in the inverse relationship between τ_m and α for rare earth (Dy) doped ferromagnetic Py films [88]. This discrepancy is due to missing electron relaxation channels in the presence of rare earth metals. Only one spin relaxation channel was considered for both femtosecond and nanosecond time scales, which is not true in the presence of f-band electrons. Radu *et al.* also observed similar discrepancies against Koopman's model in Py films with Dy, Ho, Gd, and Tb impurities [89].

Later M. Fähnle *et al.* proposed a universal model to correlate τ_m and α, considering electronic band structure details and electronic transitions between states. The relation between τ_m and α can be proportional or inversely proportional depending on the dominant contribution to magnetic damping. A proportional relation occurs if the damping has a dominant conductivity-like contribution, which can be modelled using the "breathing Fermi surface" model of damping:

$$\tau_m = \frac{M}{\gamma p b^2 F_{el}} \alpha , \tag{2.35}$$

Where, M is the magnitude of magnetization vector $\mathbf{M}$, F_{el} is determined by the derivatives of the individual electron energies in relation to the orientation of $\mathbf{M}$, p represents a material-specific parameter and b^2 is the Elliot-Yafet spin-mixing parameter.

There will be an inverse relationship between τ_m and α, when the damping mechanism is dominated by a resistivity-like contribution. This resistivity-like contribution is a result of the inter-band relaxation of electrons and holes, and can be represented by the "bubbling Fermi surface" model of the damping. In such instances, the relationship between τ_m and α can be expressed as:

$$\tau_m = \frac{F'_{el}}{p b^2} \frac{1}{\alpha} , \tag{2.36}$$

The value of F'_{el} is calculated based on the electronic states, but it differs from F_{el}. F'_{el} is determined by the matrix elements formed by two distinct electronic wave functions, while F_{el} is determined by matrix elements formed by the same electronic wave functions. However, the model proposed by Fähnle *et al.* failed to account for the impact of spin transport effects.

Therefore, it is limited in its applicability to conventional ferromagnetic materials characterized by spin-flip scattering influencing both ultrafast demagnetization and damping. Tveten *et al.*, have recently made a theoretical prediction regarding the potential explanation of τ_m in relation to spin current-induced damping in NM/FM heterostructures using electron-magnon scattering theory [90]. Subsequently, Zhang *et al.*, experimentally showed that a direct correlation between τ_m and α would confirm spin-flip scattering as the primary factor in ultrafast demagnetization [91]. Conversely, an inverse relationship would indicate that spin current transport is the predominant microscopic mechanism driving the ultrafast demagnetization process [92]. Through this inverse correlation, one can derive the spin chemical potential (μ_s) for different NM/FM interfaces using the following equation:

$$\Delta \frac{1}{\tau_m} = \frac{\mu_s}{\hbar} \Delta\alpha. \tag{2.37}$$

where the demagnetization rate and modulation of damping is represented by ($\Delta \frac{1}{\tau_m} = \frac{1}{\tau_m}|_t - \frac{1}{\tau_m}|_{t=0}$) and ($\Delta\ \alpha = \ \alpha|_t - \ \alpha|_{t=0}$) respectively. μ_s quantifies the spin chemical potential at the interface of NM/FM. The femtosecond laser-generated spin current is extremely short-lived (sub-ps), whereas the spin current induced by spin pumping can persist for ns. Despite occurring at two distinct time scales, the physical characteristics of both spin currents are alike. The fs spin current enhances the demagnetization rate, while the spin pumping induced spin current enhances the magnetic damping.

2.6 Magneto-optical Kerr effect

The phrase "magneto-optics" describes the different event that occur when electromagnetic radiation strikes the materials that are magnetically polarized. Two significant magneto-optic phenomena are the Kerr effect and the Faraday effect. The Kerr effect is the rotation of the plane of polarization of a light beam when reflected from a magnetized sample [93]. Typically, the rotation is minimal (around tenths of a degree) and is influenced by both the magnitude and direction of magnetization. On the other hand, the Faraday effect causes the plane of polarization of a light beam to rotate as it passes through a magnetized sample [94]. In this scenario, the rotation can be more pronounced, reaching several degrees, as the radiation interacts more intensely with the sample compared to the Kerr effect. Nevertheless, the Faraday effect is only observable in thin samples with low attenuation, making it unsuitable for studying bulk samples.

Magneto-optical Kerr effect (MOKE) is proved as an efficient method for detecting the magnetization of a magnetic material. Currently, there is extensive utilization of it in the examination of the static and dynamic magnetic characteristics of various magnetic substances across a wide spectrum of length and time intervals.

2.4.1 Physical origin of MOKE

The physical origin of MOKE can be explained either from a macroscopic and microscopic point of view.

Macroscopic view:

Linearly polarized light can be separated into two opposite circular polarized lights. Circularly polarized beams consist of photons with equal magnitudes of angular momentum, which is 1. However, the angular momentum vector associated with right circularly polarized (RCP) light is oriented in the direction opposite to that of left circularly polarized (LCP) light. The magnetization of a magnetic substance can lead to a Zeeman splitting of the energy states. For instance, in the case where the atomic spin is 1/2, each state will divide into two levels, with a total spin of S = +1/2 and S = -1/2, respectively. It is essential to ensure the conservation of both angular momentum and energy when a photon stimulates an electron to move from a sub-level in level 1 to a sub-level in level 2. Consequently, only specific transitions are permissible in order to uphold the conservation of angular momentum.

$$S_1 = -\frac{1}{2} \quad \rightarrow \quad S_2 = +\frac{1}{2}, \quad \Delta L = +1.$$

$$S_1 = +\frac{1}{2} \quad \rightarrow \quad S_2 = -\frac{1}{2}, \quad \Delta L = -1.$$

The photon carrying angular momentum L = +1 stimulates an electron from the spin S = -1/2 state in level 1 to the spin S = +1/2 state in level 2. Likewise, the photon with angular momentum L = -1 stimulates an electron from the spin S = +1/2 state in level 1 to the spin S = -1/2 state in level 2. Therefore, photons with opposite polarizations result in distinct electronic transitions within the atom.

In level 1, there is a disparity in the electronic populations between the two spin states, with the lower-energy state accommodates a greater number of electrons statistically. Consequently, one of the circular polarizations is absorbed more than the other, leading to the phenomenon known as circular dichroism. Upon the combination of the final circular polarizations into a linearly polarized beam, a rotation of the plane of polarization is noted in comparison to that of the incoming beam. The phase difference that arises between the initial and final planes of polarization is referred to as circular birefringence.

Microscopic view:

MOKE is believed to have originated from the spin-orbit interaction. According to this theory, the motion of electrons influenced by the electric field of light impacts the spin-orbit interaction of the system. This alteration in spin-orbit interaction can be represented as: $S \times \nabla V$, where S and ∇V denote the spin angular momentum of an electron and the electric field acting on the electron, respectively. While this phenomenon is observable in both FM and NM materials, it is more pronounced in FM materials due to the disparity between up-spin and down-spin within them.

2.4.2 MOKE Geometries

MOKE geometries can be categorized into three distinct types: longitudinal, transverse, and polar geometries, which depend on the alignment of the magnetization vector with respect to the sample surface and the plane of light incidence. In the longitudinal geometry (Figure 2.3(a)), the magnetization (M) aligns with both the surface of the sample and the plane in which the light is incident. On the other hand, in the polar geometry (Figure 2.3(b)), M is perpendicular to the sample surface and parallel to the plane of light incidence. The Kerr rotation can be qualitatively explained by the interaction between the electric field (E) of the light and the material's magnetization[95]. In linearly polarized light (such as p-polarized light), the electrons within the sample oscillate in alignment with the E-field of the light, with the oscillation occurring in the plane of light incidence and the sample. When the light is reflected, there is a π phase change compared to the incident beam, resulting in the direction of E becoming opposite to the incident electric field. The Lorentz force (F_{Lor}) on the oscillating electrons generates an additional small vibrational component (k) perpendicular to the plane of light incidence. The electric field of the reflected light is the vector sum of the original electric field vector (r) and the Lorentz field vector (k). The reflected light's electric field, which is the vector sum, is rotated due to the sample's magnetization. S-polarized light, characterized by an electric field that is perpendicular to the plane of incidence, demonstrates a comparable Kerr rotation in relation to the polar effect. The longitudinal Kerr effect is not observed at normal incidence due to the cross-product being zero. However, for different incident angles, the longitudinal Kerr effect is detected in both p-polarized and s-polarized light. The third MOKE configuration is known as the transverse geometry, in which M is situated within the sample plane, but perpendicular to the plane of light incidence (refer to Figure 2.3(c)). Only p-polarized light exhibits the transverse Kerr effect. Under these conditions, the reflected beam retains its linear polarization without any Kerr rotation, although the amplitude is altered as the magnetization vector shifts from +M to -M.

The rotation angle within the polarization plane caused by the Kerr effect is identified as Kerr rotation (θ_k), while the induced ellipticity is termed Kerr ellipticity (ϵ_k). Both θ_k and ϵ_k are directly linked to the magnetization of the system (Figure 2.3(d)) and are interconnected through the equation:

$$\theta_k + i\epsilon_k = \frac{k}{r}, \text{ where } k \ll r \tag{2.38}$$

Here, k and r are the perpendicular and parallel components of the electric field vector (E) of the reflected beam, respectively.

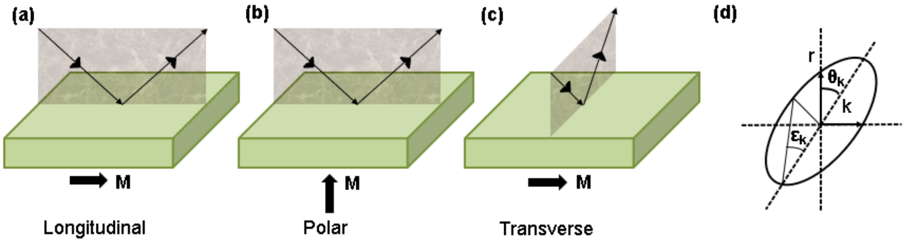

Figure 2.3: Schematic diagrams of (a) longitudinal, (b) polar and (c) transverse MOKE geometry. (d) Geometry of the Kerr rotation (θ_k) and Kerr ellipticity (ϵ_k) are demonstrated.

CHAPTER-3

Experimental Methods

3.1 Introduction

The production of high-quality samples with dimensions as small as the sub-nanometre range is crucial for future technological advancements. This process heavily relies on advanced engineering techniques that ensures precise growth of on-chip devices and the selection of optimal materials. To meet these requirements, scientist have developed various sophisticated fabrication methods to create thin film heterostructures and nanostructures with exceptional perfection and minimal defects. There are primarily two methods to create these desired samples: bottom-up chemical technique and top-down physical technique. The bottom-up method involves chemical reactions to synthesize nanowires, nanoparticles, and other nanostructures. While this method is cost-effective and easier to manage, controlling the deposition process can be challenging, especially when aiming for ordered crystalline structures and monodispersed samples. Conversely, the top-down approach allows for the efficient deposition of high-quality nanostructures, ultrathin films, and multilayers with precise structure and composition. In recent times, a combination of both bottom-up and top-down approach are utilized to fabricate high quality samples based on user convenience. The research presented in this thesis focuses on thin films and heterostructures deposited using RF/DC magnetron sputtering technique. This method enables the production of film with exceptional quality, sharp interfaces, and minimal structural defects on a substrate. Following the deposition of this thin films, various structural characterizations are conducted using techniques such as atomic force microscopy (AFM), X-ray diffraction (XRD), X-ray reflectivity (XRR), and Raman spectroscopy. The static magnetic properties are analyzed using static MOKE (S-MOKE) magnetometer and vibrating sample magnetometers (VSM). We have utilized a custom build non-collinear TR-MOKE magnetometer to investigate the magnetization dynamics. Subsequently, we will provide a brief overview of the operational principles behind these fabrication and characterization techniques.

3.2 Sample fabrication technique

There are several methods of depositing samples on a substrate: molecular beam epitaxy, chemical vapour deposition, thermal evaporation, pulsed laser deposition, magnetron sputtering, electron beam evaporation, and more. The quality of the samples can be controlled by selecting the appropriate technique for the desired material deposition and by controlling various deposition conditions to optimize the technique. Our thin films and heterostructures are deposited using magnetron sputtering technique, which offers distinct advantages over other techniques, such as:

i) The entire target surface act as the source in sputtering.
ii) Better adhesion to the substrate is achieved due to the high velocity of sputtered particles.
iii) Deposited materials exhibit higher melting temperature due to several cooling procedures.

3.2.1 Magnetron sputtering technique

Magnetron sputtering [96] is a highly versatile and efficient method of physical vapor deposition [97] for producing high-quality thin films and heterostructures. The sputtering chamber consists of four main components: the target (made of the material to be deposited), the substrate (where the deposition occurs), the sputter gun, and the plasma. Sputtering operates on the principle of momentum transfer through elastic collisions, resulting in the transfer of molecules from the target to the substrate. The negatively charged target is located at the bottom of the chamber, while the substrate, at ground potential, is positioned at the top (as shown in Figure 3.1). A high-voltage power supply ionizes the inert gas to create plasma containing electrons, ions, and neutral atoms within the chamber. The electrons in the plasma are repelled from the negatively charged target and collide with neutral atoms, generating secondary electrons and maintaining electron density. Positively charged ions are accelerated at high velocity toward the target, dislodging some of its atoms, which are then deposited onto the substrate. These processes occur within a vacuum of approximately 10^{-7} Torr or better. Argon is commonly used as the inert gas in sputtering chambers due to its heavier atomic weight compared to helium and neon, as well as its lower cost relative to krypton and xenon. During the deposition process, a powerful magnetic field is utilized to guide the secondary electrons along a helical path around the target. This results in a higher likelihood of ionization for the inert gas within the chamber, leading to improved sputtering efficiency, decreased impurity concentration, and the ability to lower the substrate temperature.

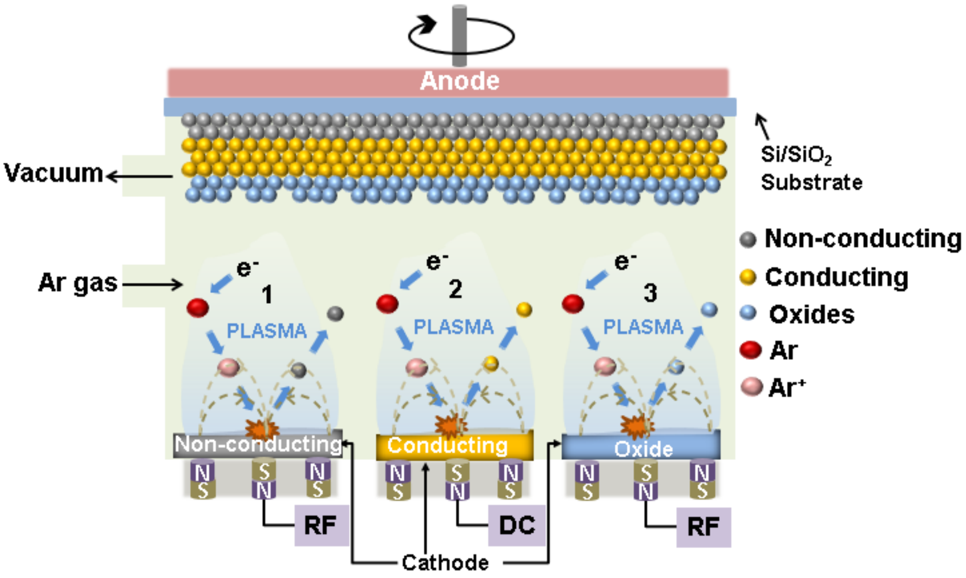

Figure 3.1: Schematic diagram of RF/DC magnetron sputtering.

There are two categories of sputtering, depending on the power supply used during the deposition: direct current (DC) sputtering and radio frequency (RF) sputtering. In DC sputtering, a DC voltage is applied between the electrodes during the deposition. While DC sputtering is an efficient and cost-effective method for depositing conductive materials such as metals (e.g. Ni, Co, Au, W, Ta, Cu, NiFe, CoFe, CoFeB), it is not suitable for dielectric or nonconducting materials such as insulators and oxides (Al_2O_3, SiO_2). Deposition of dielectric or nonconducting materials using this sputtering technique can generate a polarized charge near the target, leading to problems such as arcing and target poisoning. To avoid this issue, RF sputtering is employed, where the target material is continuously bombarded with positive and negative ions by changing the electrical potential of the target at radio frequencies. In conclusion, high-quality ultrathin films and multilayers can be grown using the sputtering technique by selecting the appropriate electrode voltage (DC or RF), controlling the deposition rate through a quartz crystal monitor, and optimizing pressure inside the sputtering chamber.

3.3 Static characterization techniques

3.3.1 X-ray diffraction

The X-ray diffraction (XRD) technique [98], proposed by Max von Laue in 1912, is utilized to investigate the crystalline properties of a material. This technique is widely used due to X-rays having a wavelength similar to the lattice spacing of crystalline materials. By diffracting X-rays from lattice planes separated by distance d, Bragg's law [99] states that $2dsin(\theta) = n\lambda$, where n is the order of diffraction and θ is the incident angle. In an XRD experiment, θ is incrementally changed in small steps, and the intensity of the diffracted X-ray beam at 2θ angle relative to the incident beam direction is recorded. Certain diffracted beams may negate one another; however, when the beams possess comparable wavelengths, constructive interference takes place. The diffraction peak positions provide information about the atomic planes reflecting X-ray beams and the spacing between these planes, aiding in identifying the elements present in the sample and their crystal structure. For the measurements conducted in this thesis work, a Cu-Kα X-ray source characterized by a wavelength of 1.54 Å was used.

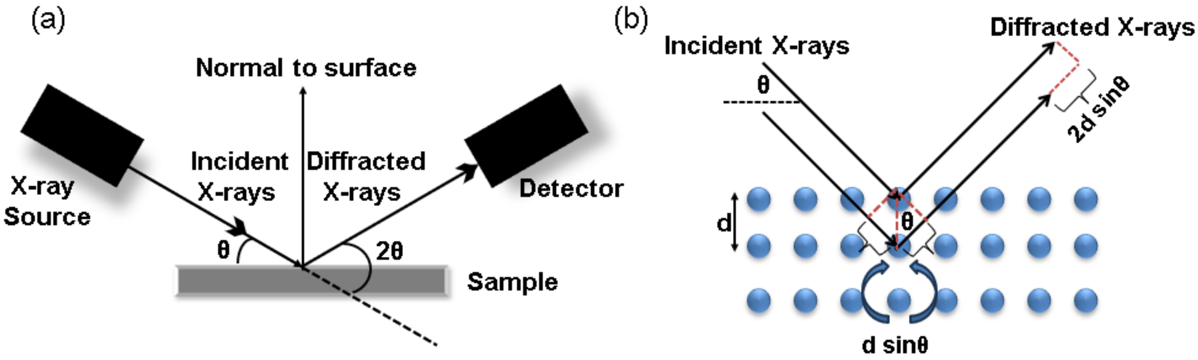

Figure 3.2: Schematic diagram of (a) X-ray diffractometer, (b) X-ray diffraction process.

3.3.2 X-ray reflectivity

The technique of X-ray reflectivity (XRR) is employed to examine the intensity curves of X ray reflections resulting from a grazing incident X-ray beam. This analysis facilitates the determination of various thin film parameters, such as thickness, density and surface or interface roughness. It is a method that does not require physical contact and does not cause damage when examining the quality of surfaces and interfaces. This technique was initially utilized in 1954 by Lyman G. Parratt to investigate the surface of a glass coated with copper [100]. This method includes the measurement of the X-ray intensity reflected based on the incident angle within a specific range close to the critical angle for total reflection. Beyond this critical angle, the intensity of specular reflection decreases, exhibiting a pattern that relies on the structural characteristics of the interface. A standard reflectivity curve comprises the Fresnel reflectivity (with a $1/Q^4$ relationship, where $Q = 4\pi \sin\theta/\lambda$) and an interference pattern (Kiessig fringes) resulting from scattering at various layers (such as in a thin film or multilayer).

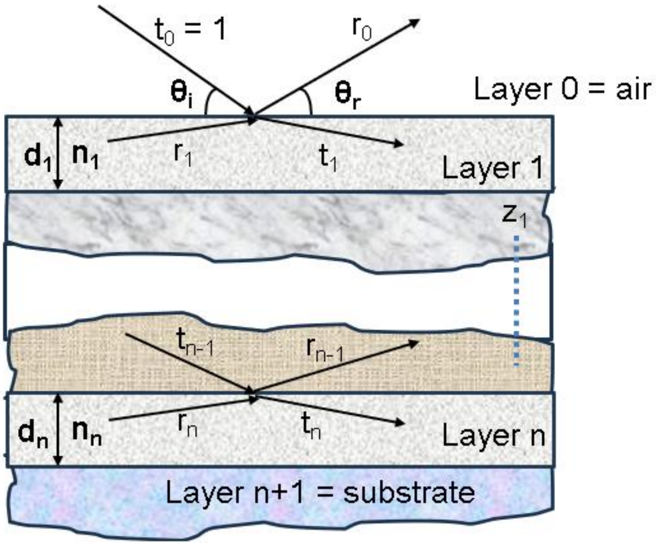

Figure 3.3: Diagram illustrating numerous reflections occurring within a multilayer film consisting of *n* layers on a substrate with *n*+1 interfaces.

3.3.3 Atomic force microscopy

The technique of atomic force microscopy (AFM) was initially developed by IBM in 1986 to examine the morphology and topography of a sample surface [101]. This type of microscopy can achieve a vertical resolution of 0.1 nm and a lateral resolution of approximately 20 nm under ambient conditions. The technique involves probing the atomic force between a cantilever tip and the sample surface, followed by imaging. It is capable of characterizing a wide range of materials, including polymers, ceramics, glasses, composite materials, thin films, and biological membranes. A multimodal AFM set-up consists of an optical head, a piezoelectric scanning stage, a mechanical cantilever with a sharp tip, and a controller connected to a computer (as shown in Figure 3.4). The optical head contains a laser and several photodetectors. The sample is positioned on a piezoelectric x-y-z scanning stage, enabling precise and accurate scanning with a resolution better than the optical diffraction limit. A sharp tip, coated with metals or doped diamond, is attached to a cantilever coated with Pt-Ir, Co-Cr, and is used to scan the sample surface. As the cantilever tip approaches the sample surface, it experiences various atomic forces such as capillary force, electrostatic force, force due to chemical bonding, magnetic force, and van der Waals force, causing deflections from the usual cantilever motion. This deflection is detected by sensitive photodetectors attached to the optical head, and the signal is collected via the controller in terms of voltage, forming a three-dimensional representation of the sample surface in the computer.

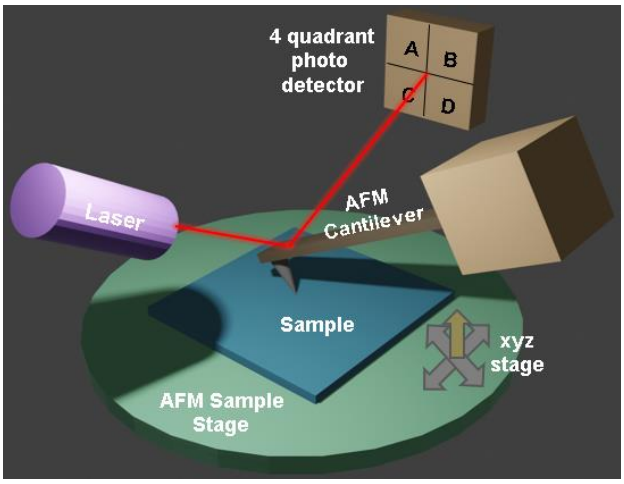

Figure 3.4: Schematic of atomic force microscopy.

Alteration in surface topography causes the cantilever tip to deflect, which can then be recorded on a three-dimensional image obtained through the controller. An AFM can function in three distinct modes: i) contact mode, ii) non-contact mode, and iii) tapping mode. In the contact mode, the cantilever tip is positioned very close to the sample surface (within a few Å distances), leading to a repulsive van der Waals force. To prevent any harm to the cantilever tip and the sample surface while scanning, these cantilevers are crafted from highly flexible materials. In the non-contact mode, the cantilever tip is maintained at a distance from the sample surface to experience an attractive van der Waals force. Tapping mode is the most favoured mode of operation for an AFM set-up. In this mode, the cantilever tip vibrates at its resonance frequency, causing the distance between the tip and the sample surface to oscillate between contact and non-contact modes. Near the sample surface, the tip encounters a repulsive force, leading to a reduction in the oscillation amplitude. As the distance between the tip and the sample surface increases, the strength of this repulsive force diminishes and eventually transforms into an attractive force at a specific distance. The final AFM image reflects the varying amplitude of the cantilever tip.

3.3.4. Raman spectroscopy

Raman spectroscopy is a non-invasive method for analyzing chemicals, offering in-depth insights into chemical composition, phase, structure, polymorphism, molecular interactions, and crystallinity. This technique relies on the interaction between light and chemical bonds present in a material. In a typical Raman spectroscopy procedure, the sample is exposed to photons of a specific wavelength (typically from a high-intensity laser) causing the sample molecules to scatter the incident light. The majority of the scattered light retains the same wavelength as the laser source (known as Rayleigh scatter resulting from elastic collisions), while a small portion scatters at different wavelengths. This discrepancy in energy levels is a result of inelastic collisions, where the photon interacts with the sample, leading to changes in the rotational and vibrational energy of the molecule. A Raman spectrum displays various peaks, indicating the intensity and wavelength position of the Raman scattered light. The intensity of peaks observed in the spectrum is directly corelated with the concentration of the species from which it was produced. A LABRAM HR Evolution instrument utilizing a solid-state laser, featuring a spectral resolution of 600 lines/mm is employed to accurately identify the number of WS_2 layers. We employed laser excitations at a wavelength of 532 nm, maintaining the laser power at 1.15 mW.

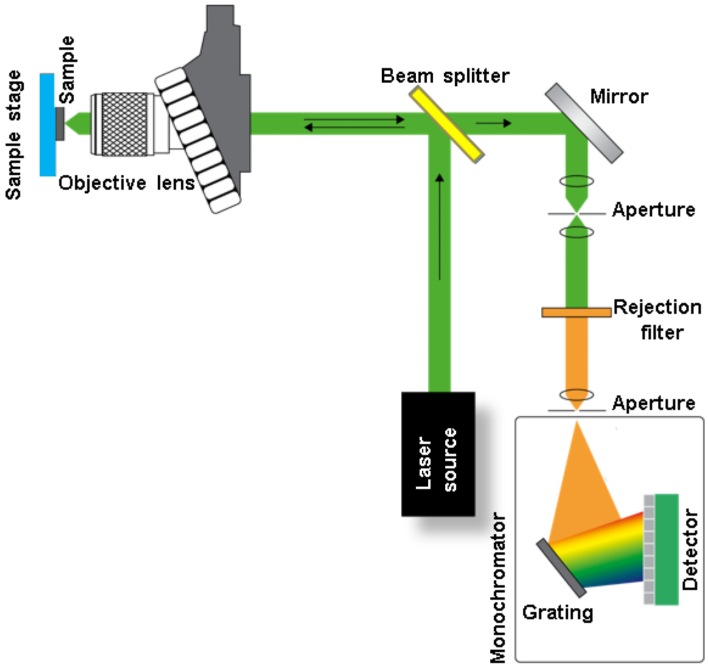

Figure 3.5: Schematic of Raman spectroscopy.

3.3.5. Vibrating sample magnetometry

Vibrating sample magnetometry (VSM) is a commonly utilized and effective inductive technique for analyzing the magnetic properties of a material in relation to the applied magnetic field and temperature. The method was discovered by Simon Foner in 1956 and has since then undergone enhancements in versatility and sensitivity. The fundamental concept of VSM measurement is rooted in Faraday's law of magnetic induction, which states that a variation in magnetic flux through a coil can produce an induced electromotive force (E) within that coil. This E can be written as:

$$E = -NA\frac{dB}{dt} \tag{3.1}$$

Here, A is the area of each coil, N is the number of turns in the coil, and B $(= H + 4\pi M)$ is the induced magnetic field. Using the value of B in equation 3.1, we have:

$$E = -4\pi NA\frac{dM}{dt} \tag{3.2}$$

Throughout the VSM measurement, the sample is affixed to a nonmagnetic plastic or quartz rod and suspended vertically between two magnetic pole pieces of an electromagnet (refer to Figure 3.6). The electromagnet will generate a consistent magnetic field around the specimen and attempt to align its spins in the direction of the field. A piezoelectric transducer is connected to the specimen rod, facilitating sinusoidal oscillation of the rod along the vertical axis. This vertical oscillation will introduce a disturbance to the external magnetic field, which will ultimately be detected by the coils. This disturbance will alter the magnetic flux passing through the coil and produce an electromotive force that can be expressed as:

$$E = -2\pi fmlANGN_c\cos(2\pi ft) \tag{3.3}$$

Where, f and A are the frequency and amplitude of the vibration, m is the DC magnetic moment, N_c and l are the number of pick-up coils and the length between the coils. The generated electromotive force is identified by a lock-in amplifier. The lock-in amplifier collects its reference signal from the piezoelectric transducer. By adjusting the external magnetic field, magnetic hysteresis loops can be obtained, while conducting a temperature-dependent magnetic measurement will reveal the Curie and Neel temperature of the sample.

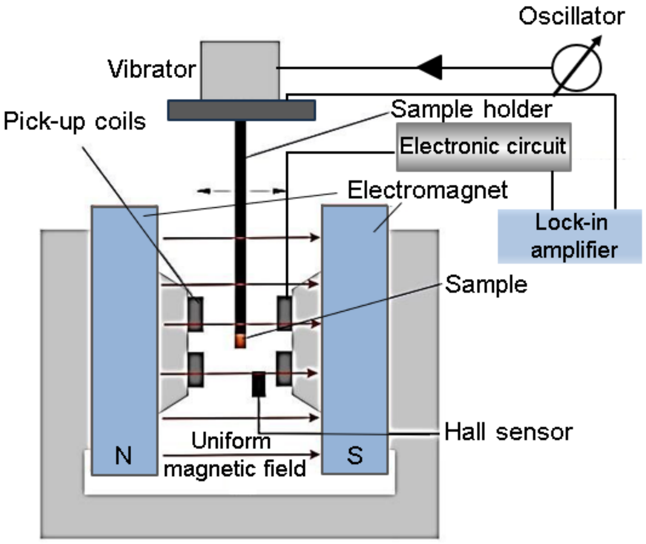

Figure 3.6: Schematic of vibrating sample magnetometry.

3.3.6. Static magneto-optical Kerr-effect magnetometry

The S-MOKE technique is a magneto-optical method utilized for measuring the magnetization of thin films and nanostructures through Kerr rotation or ellipticity [34]. This method is non-invasive and provides local measurements of magnetization. While S-MOKE can measure Kerr signal in all three MOKE geometries, this thesis primarily focuses on the longitudinal Kerr geometry, where the sample magnetization is parallel to both the incident plane and sample surface. A continuous-wave He-Ne laser operating at a wavelength of 632.8 nm is employed for detecting the Kerr rotation. Prior to exciting the sample, the laser beam passes through a polarizer to ensure that the incident beam is fully linearly polarized. An in-plane magnetic field is applied to the sample using an electromagnet. The reflected beam from the sample is directed towards an optical bridge detector (OBD) capable of detecting the rotation in the plane of polarization. The laser beam is modulated at a frequency of 1 kHz by a photoelastic modulator (PEM). The optical head of the PEM is connected to a controller unit via an electrical head. The frequency of the PEM serves as the reference signal for the lock-in amplifier. The output signal from the OBD is phase-sensitively measured using a lock-in amplifier (refer to Figure 3.7). For the measurement of magnetic hysteresis loop, the external in-plane magnetic field is varied from the positive direction to the negative direction, and vice-versa, and the change in the Kerr signal is monitored at each field value with the assistance of a LabView software.

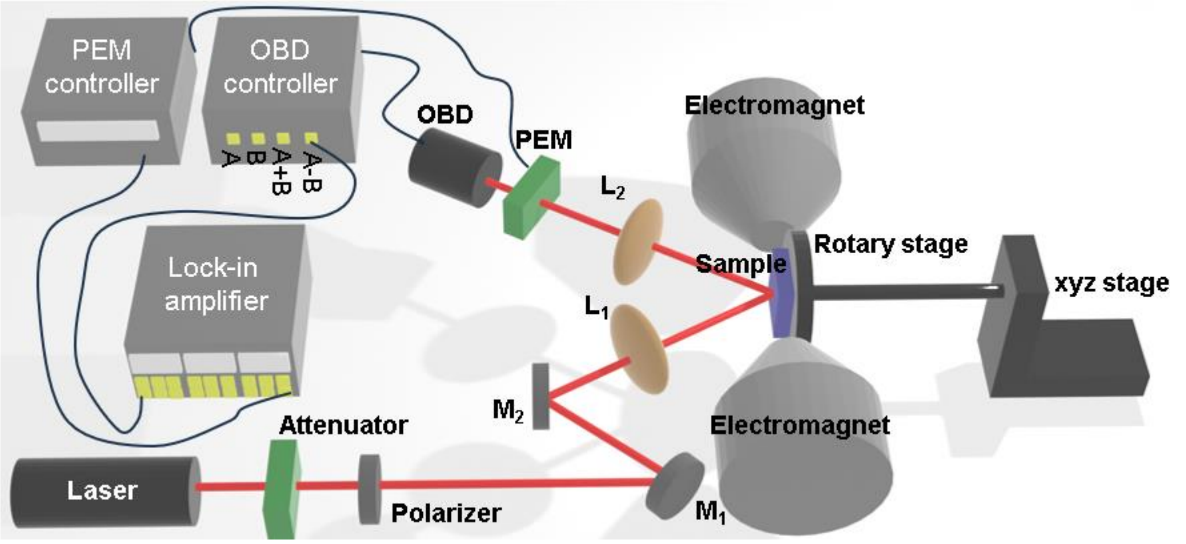

Figure 3.7: Schematic diagram of a static magneto-optical Kerr-effect magnetometry.

3.4 Dynamic characterization technique

In order to study the ultrafast spin dynamics of magnetic systems, a non-collinear TR-MOKE magnetometry technique was employed utilizing an amplified femtosecond laser system. This method involves a dual-beam pump-probe experiment [34,102]. As the pump-probe spectroscopy is utilized to study dynamical process, the physical system needs to be disturbed from its equilibrium state. A pump pulse initially stimulates the system being studied, followed by a probe pulse that measures the changes induced by the pump at various delay times. The interval between the pump and probe pulses is regulated by adjusting the difference in path length between them, in accordance with the equation dt = dx/c, where dx represents the path length difference and c denotes the speed of light. As an example, we examine the electron energy levels within an atom. When the pump pulse energy matches the energy gap between two levels, the atoms within the specimen will absorb photons from the pump pulse, leading to an increase in the electron population at the higher energy level. Subsequently, the probe pulse is detected after interacting with the sample. Monitoring the changes in the probe pulse post-interaction with the sample is crucial in determining the physical condition of the sample as it returns to an equilibrium state following the disturbance caused by the pump pulse. By examining a wide range of timescales, one can observe how the system evolves over time following the initial disturbance. The TR-MOKE magnetometry is capable of identifying various phenomena including ultrafast demagnetization (taking place within a few hundred femtoseconds), fast remagnetization (occurring within a few picoseconds), and slow remagnetization combined with damped precessional oscillation (taking place within a few nanoseconds). It has many advantages over its competing techniques such as FMR as below.

1. This measurement technique is entirely optical and non-invasive, and it is also unaffected by any electrical leakages.
2. There is no need for intricate microfabrication when utilizing this method to measure a sample.
3. This technique has an exceptional temporal resolution of approximately 35 femtoseconds.
4. This method is local technique with a spatial resolution of approximately 100 μm, resulting in minimal impact from extensive area averaging.
5. The TR-MOKE magnetometry utilizes an amplifier laser with a high average pulse energy of approximately 4.2 mJ/pulse. This allows for the delivery of high fluence values of around 100 mJ/cm^2. Additionally, the wavelength of the laser beam can be varied from 250 nm to 2200 nm using an optical parametric amplifier system.

In the following section, the experimental arrangements of this set-up will be thoroughly discussed.

3.4.1. TR-MOKE magnetometry

In this pump probe set up the fundamental laser beam having wavelength of 800 nm is split into two beams using a beam splitter. A portion of the beam is frequency doubled (400 nm) using a second-harmonic generator (SHG) to be used as a pump beam to excite the sample. The other portion of the fundamental laser beam is attenuated and aligned in order to be utilized as the probe beam to detect the dynamics. The pump beam strikes the sample at an angle, whereas the probe beam is incident on it perpendicularly. The reflected probe beam is then utilized to concurrently measure the time-dependent polar Kerr rotation and reflectivity signals. The process of creating an amplified femtosecond laser pulse is highly sophisticated and complex. The entire amplifier laser system consists of several parts as below [103].

1. A seed laser (Vitesee)
2. A pump laser (Evolution)
3. Regenerative cavity
4. Stretcher and compressor gratings
5. Synchronization and delay generator

3.4.1.1. Vitesse

The Vitesse laser is a Verdi-pumped ultrafast laser that is compact in size, generating mode-locked pulses of less than 100 femtoseconds pulse-width at a repetition rate of 80 MHz [104]. It delivers an average output power exceeding 200 mW at 800 nm. The laser system comprises a laser head and power supply linked by an umbilical cord. This cord includes fiber optic cables for transmitting light from the diode bar in the power supply to the laser head, as well as electrical cables for controlling and monitoring signals between the two components. The Vitesse laser head is equipped with a sealed optical cavity housing either (A) a 2- or 5-Watt, 532 nm Verdi laser head serving as the pump laser, (B) a Power Track mirror, and (C) the Verdi Pumped Ultra-Fast (VPUF) laser head. Additionally, beam steering mirrors are integrated into the laser head to ensure precise exit beam alignment, a feature that is standard across all Vitesse Laser Systems.

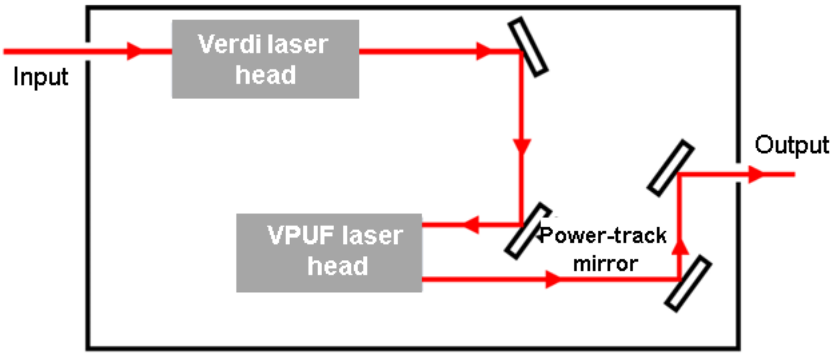

Figure 3.8: Schematic diagram of Vitesse laser head.

A. Verdi laser head

The primary optical components in the sealed pump laser head (Figure 3.9) consist of Nd doped Yttrium Vanadate serving as the gain medium, LBO (Lithium Triborate, LiB3O5) functioning as the doubling crystal, an etalon utilized for single-frequency optics, an optical diode, an astigmatic compensator, along with two pump mirrors and two end mirrors. All optical elements are mounted on Invar for strength and stability. The resonator assembly, permanently aligned, is housed in a clean-room environment within a sealed enclosure. Verdi's Nd: YVO_4 gain medium is stimulated by an 808 nm laser beam from the fibre array package, resulting in a robust single frequency beam of 1064 nm. This beam is then directed through the LBO crystal, producing a 532 nm beam through second-harmonic generation. The laser resonator undergoes unidirectional single-frequency oscillation with the help of an intra-cavity etalon and an optical diode. Single-frequency selectivity is improved by a temperature-stabilized Fabry-Pérot etalon, while the optical diode utilizes the "spatial hole burning" mechanism for unidirectional lasing. Thermal gradient within the laser resonator can lead to astigmatism due to thermal focusing, which can be mitigated through temperature optimization. Astigmatism caused by spherically curved mirrors inside the resonator cavity is corrected using a Brewster plate compensator. To ensure maximum efficiency of the Verdi laser head, the LBO crystal must meet a band matching condition where the fundamental beam and its second harmonics travel at the same speed within the crystal. This phase matching is achieved by adjusting the temperature of the LBO crystal, approximately 149°C for the 1064 nm fundamental laser beam. To prevent abrupt temperature changes that could harm the optical coating on the LBO crystal, a central processing unit continuously monitors the temperature. A gradual heater ramp-up cycle heats the LBO crystal, while a slow cool-down cycle cools it. In case of a sudden power outage, a battery backup circuit in the power supply ensures controlled cooling of the LBO crystal. The 532 nm output beam from the Verdi laser head is directed towards the VPUF laser head via the power-track mirror.

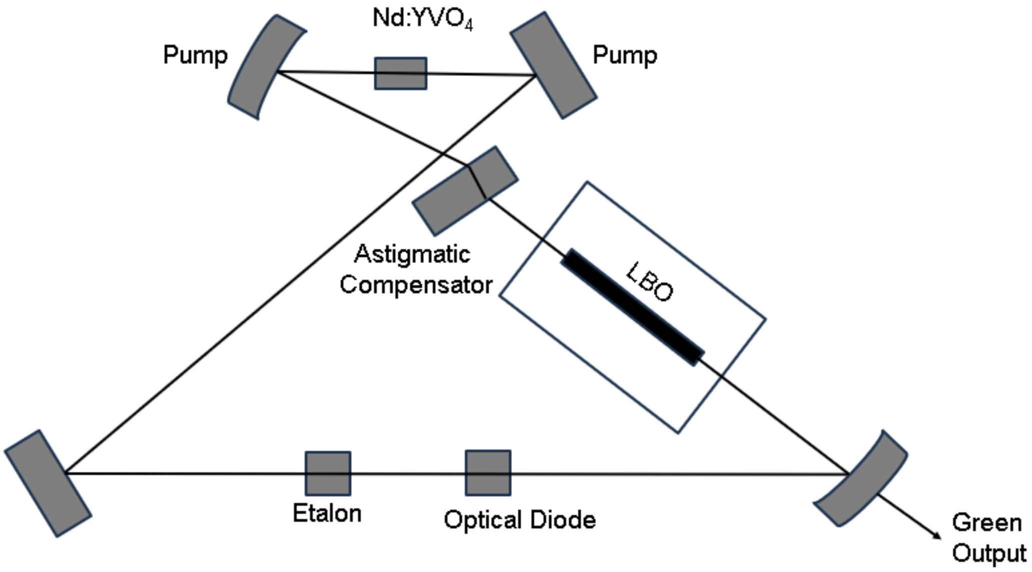

Figure 3.9: Schematic of optical pump (Verdi) laser head.

B. Power Track

The Power Track feature utilizes a Piezo-driven mirror to actively maintain the optimal alignment of the pump beam into the VPUF cavity, effectively reducing fluctuations in the ultrafast output power. These mirrors are connected to levers that enable scanning in the XY-plane by adjusting the tilt and pointing direction. Controlled by a piezoelectric transducer (PZT), the levers receive voltage from the PZT controller when the Vitesse system is activated, initiating raster scanning to change the pump beam position on the mirror. Following initial adjustments, the raster scan transitions into a smaller amplitude dither scan for precise alignment, with the system electronics able to differentiate between the two scans based on the change in PZT voltage. This distinction allows for fine-tuning of the pump beam alignment by optimizing the PZT voltage.

C. VPUF laser

The ultrafast laser VPUF (Figure 3.10) utilizes Ti-Sapphire as the gain medium. Negative Dispersion Mirrors (NDM) with proprietary technology are employed to achieve the necessary total negative dispersion compensation for generating sub-100 femtosecond pulses. Mode-locking is achieved through the Kerr-Lens mode-locking (KLM) technique, with an automatic starter triggering the initiation of mode-locking. The laser cavity is constructed on an invar plate to ensure mechanical strength and stability, and it is sealed to minimize environmental contamination. In the instance of a pulsed laser beam, the central region of the beam exhibits a higher intensity compared to the edges. As a result of the optical Kerr effect, the refractive index at the edges and the center of the pulsed laser beam will differ, creating a Kerr lens. This laser beam will converge, allowing only the intense portion to pass through. The resulting narrow beam is directed through a slit that permits only that specific portion of the beam to pass through unattenuated, serving as the driving force for mode-locking. Additionally, the laser beam interacts with various optical components possessing different refractive indices. This interaction alters the shape of the laser pulse and introduces spectral chirping (negative or positive), a phenomenon known as group velocity dispersion (GVD). Furthermore, Kerr lensing causes distinct phase shifts for different frequency components, potentially exacerbating the chirping and leading to pulse broadening, a phenomenon referred to as self-phase modulation (SPM). To mitigate the impact of GVD and SPM, a few negative dispersion mirrors, primarily Febry-Pérot etalons, are integrated within the cavity. Ultimately, a sub-100 fs pulsed laser output at 800 nm is derived from the VPUF laser head, which is subsequently utilized for amplification.

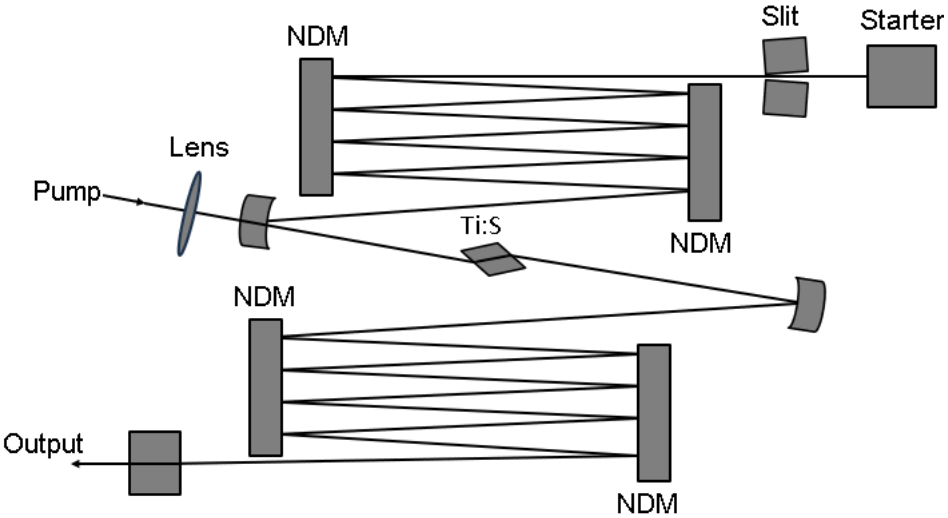

Figure 3.10: Schematic of Optical VPUF laser head.

3.4.1.2. Evolution

The Evolution-30 laser system is a diode-pumped, intra-cavity doubled, Q-switched Nd:YLF laser that can generate an average energy exceeding 20 mJ at 527 nm with repetition rates 1 kHz [105]. This laser system marks a notable progression within its category, providing high efficiency, minimal maintenance requirements, and superior beam quality made possible by laser diode pumping. The Evolution-30 laser system consists of four primary components: (A) optical laser bench assembly, (B) power supply assembly, (C) control computer, and (D) closed loop chiller.

A. Optical laser bench assembly

The Evolution-30 optical laser bench comprises a sealed monolithic aluminium chassis that houses integrated opto-mechanical, electrical, and cooling components, such as:

- A water-cooled, diode-pumped Nd:YLF laser head (pump chamber)
- An optical resonator
- Acousto-optical Q-switches
- A temperature-controlled oven with an LBO frequency-doubling crystal
- Safety shutter.

I. **Diode Lasers:** The Evolution-30 laser system utilizes a three-block arrangement with four AlGaAs diode laser bars to pump the laser gain medium. The diode laser bars are connected to a water-cooled heat sink for continuous temperature maintenance. These diode lasers are specifically used for pumping the Nd: YLF gain medium.

II. **Nd: YLF laser:** The Nd: YLF gain medium proves to be highly effective in producing high-energy pulses at a low repetition rate. This is attributed to its extended upper-state lifetime of around 470 µs, which facilitates efficient energy storage. The inherent birefringence and minimal thermal lensing of the medium contribute to preserving the beam quality. By utilizing an intra-cavity polarizer, users can select between 1047 nm and 1053 nm as the emission wavelength. Nevertheless, the Evolution-30 typically functions at a 1053 nm wavelength to minimize thermal lensing effects.

III. **Acousto-optic Q-switching:** When ultrasonic vibration interacts with an optically transparent material, it causes a connection between the material's refractive index and the strain field of the vibration. This phenomenon, known as the photo-elastic effect, transforms the optically transparent material into a grating. When a laser pulse hits this grating, it diffracts the laser beam in various directions due to different refractive indices, resulting in energy loss within the cavity and a decrease in the cavity's Q factor. Ultrasonic waves are generated from an electrical signal using a PZT. Turning off the PZT voltage stops the ultrasonic vibration in the optically transparent material, such as fused silica in our case, and allows tuning the laser cavity into a high Q factor state. Therefore, adjusting the voltage of this transducer emits a Q-switched laser pulse.

IV. **Frequency doubling component:** An LBO crystal with nonlinear properties is utilized as an output coupler to produce a frequency-doubled Q-switched beam, offering high-efficiency frequency conversion and a wide acceptance angle. To ensure maximum efficiency, a heater is employed to maintain the LBO crystal at a temperature of 327.4°F (164.1°C). The crystal can operate effectively within a temperature range of 157°C to 171°C, converting a 1053 nm input laser beam into a 527 nm beam. Additionally, the crystal is equipped with an anti-reflection coating to minimize reflection for both 1053 nm and 527 nm laser beams.

B. The power supply assembly

The primary purpose of the power supply assembly is to supply DC voltage to all electronic components. It is linked to the optical bench assembly via an umbilical cable. The key elements of the power supply assembly include master control electronics, diode power supply, LBO temperature controller, Q-Switch driver, and several accessory electronics.

C. Control computer

The "Evolution" LabView software on an external computer manages all operations within Evolution-30. The laser system is linked to this designated computer via a USB interface.

D. Closed-loop chiller

The Evolution-30 system is equipped with a closed-loop chiller unit designed to dissipate waste heat efficiently. This chiller unit plays a crucial role in maintaining the wavelength of the diode lasers and optimizing their absorption in the Nd: YLF gain medium. Operating at a temperature of 18.5°C and a pressure of 60 PSI, the chiller unit ensures the system functions at its peak performance.

3.4.1.3 Working principles of Libra

Various phenomena play a role in the regenerative amplification process within Libra i.e., (A) chirped pulse amplification (CPA), (B) pulse stretching and compressing, and (C) regenerative amplification. All of these phenomena are outlined in the subsequent section.

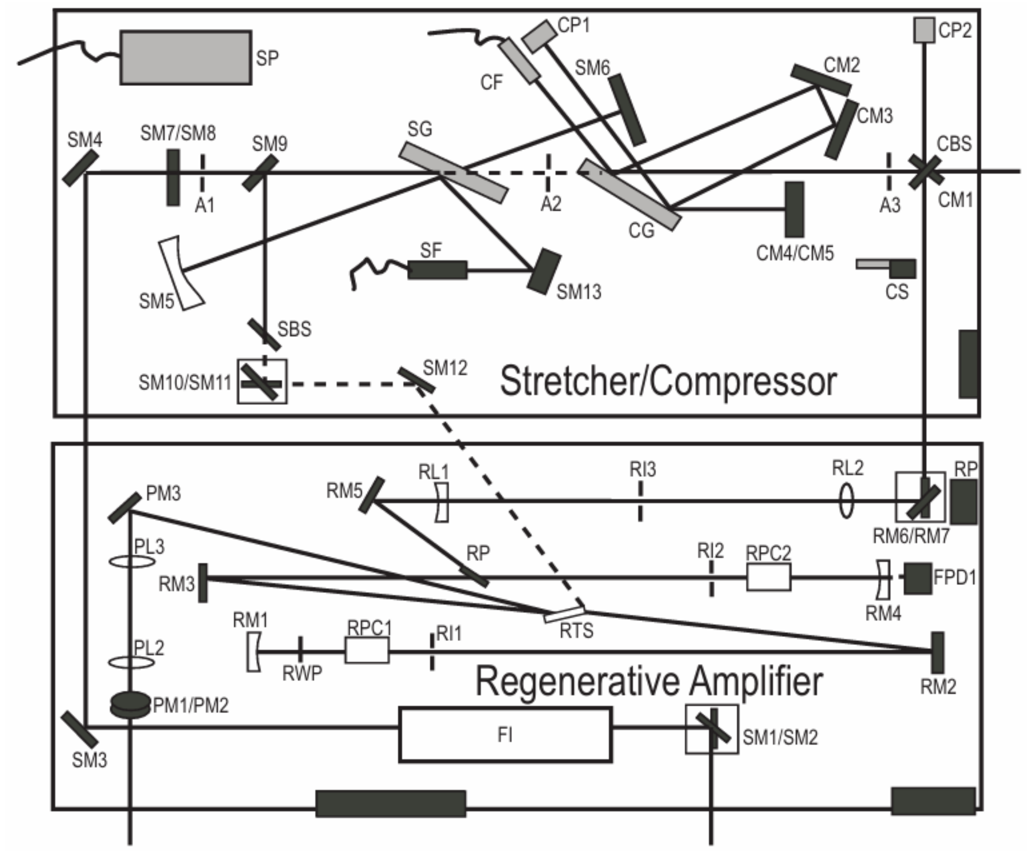

Figure 3.11: Schematic of regenerative amplifier and stretcher/compressor optical components.

A. Chirped pulse amplification (CPA)

CPA involves transforming an ultrashort low energy pulse into a high energy pulse. Prior to amplification, the laser pulse undergoes temporal stretching by a factor of approximately 10,000. This stretching is crucial in preventing energy loss caused by self-focusing, where a highly intense beam loses energy due to its short path length. Following stretching, the peak power of the laser pulse decreases significantly. The low-power pulse is subsequently amplified by a factor of around 106 using the regenerative amplifier. Post-amplification, the laser pulse is compressed back to its initial temporal duration.

B. Pulse stretching and compressing

Pulse stretchers and compressors are tools that can alter the timing of specific frequencies by directing them in different paths. These tools primarily consist of diffraction gratings, which elongate a short laser pulse and shorten a long laser pulse. Within the stretcher components, higher frequencies travel a longer path than lower frequencies, causing the lower frequencies to exit first and resulting in a stretched optical pulse due to positive group velocity dispersion. The resulting laser pulse is known as a positively chirped pulse. On the other hand, pulse compression reverses the process of pulse stretching. In this case, higher frequencies travers a shorter path in comparison to lower frequencies, leading to a negative group velocity dispersion. The output pulse is then referred to as a negatively chirped pulse. Despite the temporary stretching of the laser pulse after passing through the stretcher, it returns to its original temporal width after compression.

C. Regenerative amplification

Regenerative amplification involves the conversion of a low peak power laser pulse into a high peak power laser pulse. The process utilizes a Ti: Sapphire crystal, known for its high thermal-strain resistance, making it suitable for high-power optical pumping. The principle of operation for the regenerative amplifier (RA) is to amplify a confined single laser pulse by utilizing its polarization state, followed by dumping the cavity output. While the amplification factor in each pass through the Ti: Sapphire crystal is only 2-3 times, the overall amplification of 106 times is achieved by multi-passing the seed laser through the pumped Ti: Sapphire crystal, resulting in the amplification of a nano-Joule order laser pulse into a milli-Joule order pulse.

The optical elements (illustrated in Figure 3.11) utilized in the amplification procedure are outlined as follows:

1. During the stretching operation, the laser beam follows the path: SM1-SM2-FI-SM3-SM4-SM3-SG-SM5-SM6-SG-SM3-SM4-SM3-SG-SM7-SM8-SM9-SM10-RA cavity.

2. In the regenerative amplification operation, a "Z-fold configuration" is utilized within the regenerative amplifier cavity. The laser beam path for this operation is: RM1- RWP-RPC1-RI1-RM2-RTS-RM3-RP-RI2-RPC2-RM4.

Synchronization and delay generator and the Pockels cells: The Pockels effect is primarily observed in materials such as lithium niobate ($LiNbO_3$) due to their inversion symmetry breaking. These materials contain Pockels cells (PCs) that generate birefringence through the linear electro-optic effect when an electric field is applied. PCs are essential components of electro-optic modulators and function as voltage-controlled waveplates. In the regenerative amplification process, two PCs are utilized. By applying voltage, these PCs act as quarter-wave plates and rotate the polarization by 90° through a double-pass mechanism. The first PC confines the beam within the resonator cavity for regenerative amplification, while the second PC releases the amplified beam from the cavity. This confinement and release of beams must occur in a synchronized manner with a time interval of approximately 150 ns between them. Furthermore, the first PC must be synchronized with the pulse train of the Vitesse seed laser to permit only a single laser pulse into the resonator. These synchronization tasks are managed by the synchronization and delay generator (SDG) unit [106]. Additionally, the SDG introduces an optimal delay between the two PCs to achieve maximum gain during the multi-pass operation. The SDG is linked to the band-width detector (BWD) interlock system to safeguard the regenerative amplifier unit from any intense laser pulses that could potentially harm the unit.

3. During the compression process, the laser beam follows the path: CM1-CG-CM2-CM3-CG-CM4-CM5-CG-CM3-CM2-CG-Output.it.

The Libra laser system produces an 800 nm fundamental pulsed laser beam with a pulse width of approximately 35 fs, an average pulse energy of around 4.2 mJ, a repetition rate of about 1 kHz, and an output power of 4 W. To adjust the output pulse for daily use, a knob connected to the compressor grating and a few mirrors inside the Libra can be remotely tuned.

3.4.1.4 Verification of the cavity construction process within the Libra laser system

The effectiveness of the regenerative amplification process relies on the precise coordination among the Vitesse seed pulse, Evolution pump pulse, and amplifier PCs. The alignment procedures of the RA consist of three distinct steps: pre-alignment of optics using He-Ne laser (performed during installation), alignment of the Evolution pump beam, and alignment of the Vitesse seed beam. To enhance the RA cavity, the Ti: Sapphire crystal in the RA is pumped by the Evolution laser pulse. The pump beam is focused into the Ti: Sapphire crystal while maintaining a constant height of approximately 5 inches. Additionally, the stretched Vitesse seed laser pulse from the stretcher serves as an input to the RA. A portion of the mode-locked seed laser beam is directed towards a photo diode connected to an output line (regen build-up line) at the backside of the Libra chassis. This output line, along with a trigger from the front interface of SDG (sync out delay ns), is linked to a 1 GHz digital oscilloscope to monitor the intra-cavity build-up during system operation. The time base of the oscilloscope is set to 100-200 ns per division, producing a megahertz pulse train output. Each pulse represents the same laser pulse on multiple passes through the RA cavity. The photodiode signal is displayed without and with a well-aligned seed beam in Figures 3.12(a) and 3.12(b), respectively. In the well-aligned state, the delay time between two PCs is optimized through SDG to cavity-dump the amplified output pulse (as depicted in Figure 3.12(c)) and achieve maximum output power. Following the efficient generation of amplified pulse, the pulse width of the beam can be externally optimized by the user through fine-tuning the compressor delay stage. The stability of the RA cavity is maintained by carefully controlling the temperature, humidity, and dust level in the air.

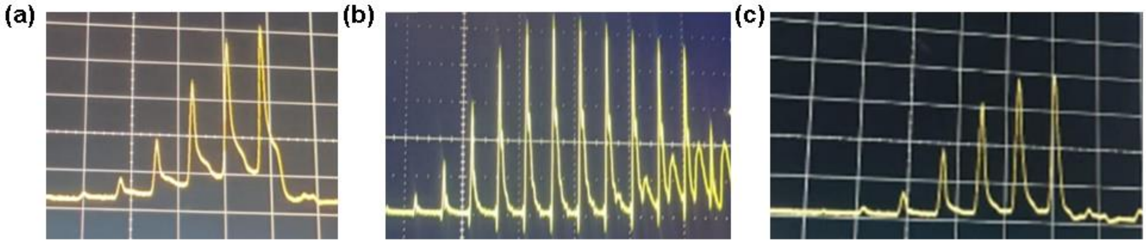

Figure 3.12: Photodiode signal at (a) unseeded, (b) seeded and (c) perfectly optimized condition of RA cavity.

3.4.1.5 Second-harmonic generator

In our experiment using a pump-probe setup, we utilize the 800 nm fundamental output beam from the Libra as the probe, while the second-harmonic beam at 400 nm wavelength serves as the pump. The second-harmonic generator (SHG) with the model number Harmonic, HGS-T, is responsible for producing this 400 nm second-harmonic beam for our experiment. Additionally, this model has the capability to generate a third harmonic beam with a deep ultraviolet wavelength. The operational principle of SHG relies on the nonlinearity found in the optical properties of dielectric materials. The dielectric materials' polarization and refractive index can exhibit both linear and higher-order nonlinear electric field terms. Within non-linear crystals, the generation of the second-harmonic beam occurs due to coherent dipole radiation, which is associated with the second-order polarization term. When dipoles of a non-centrosymmetric crystal are subjected to an oscillating electric field with frequency ω, the resulting radiation includes both the fundamental frequency ω and its second-harmonic frequency 2ω. The power of the second-harmonic output can be represented as:

$$P = \frac{l^2 P_\omega^2 \sigma^2 \varphi}{A} \tag{3.4}$$

Where, A is the beam spot size, l denotes the length of the non-linear crystal, P_ω is the input power, σ and φ are the non-linear and phase-matching coefficients, respectively. To enhance the power output of the second-harmonic beam, the beam spot size is reduced and collimated using a pair of lenses. The collimated beam is then tightly focused on the non-linear SHG crystal (specifically Barium Beta-borate (BBO) in this case), resulting in a horizontallypolarized frequency-doubled beam and a vertically-polarized residual of the fundamental beam. These two beams are separated by a prism that diffracts the second-harmonic beam onto another pair of prisms. This optical setup serves three main purposes: (i) aligning the second-harmonic beam parallel to the fundamental beam, (ii) maintaining a consistent output beam direction regardless of crystal orientation, and (iii) compensating for any induced ellipticity in the second-harmonic beam. Ultimately, both the fundamental and second-harmonic beams exit in parallel through two distinct output ports. To minimize temporal broadening caused by GVD, an extremely thin BBO crystal is utilized. Furthermore, to prevent moisture buildup within the crystal, it is enclosed in a sealed cylinder with an antireflection coating and filled with index-matching fluid.

3.4.1.6 Description of the non-collinear TR-MOKE magnetometry setup

The fundamental laser beam having s-polarization is directed through a series of mirrors after leaving the amplifier (Libra), and is then split into two equal parts using a 50:50 beam splitter (refer to Figure 3.13(a)). One part of this beam is used for frequency doubling in the SHG, resulting in the pump beam with a wavelength of 400 nm. The other part of the fundamental laser beam, with a wavelength of 800 nm, is heavily attenuated and a small portion is utilized as the probe beam. This probe beam is directed into a motorized scanning delay stage (Newport, with motion controller: model number-EPS301) with a retro-reflector (RR) to introduce a variable time delay (refer to Figure 3.13(b)). Before entering the RR, the probe beam is collimated using a pair of plano-convex lenses with focal lengths of 10 cm and 15 cm, and its beam-waist is reduced to approximately 5 mm. The probe beam emerging from the RR is directed to the sample using several mirrors before being focused onto the sample surface using

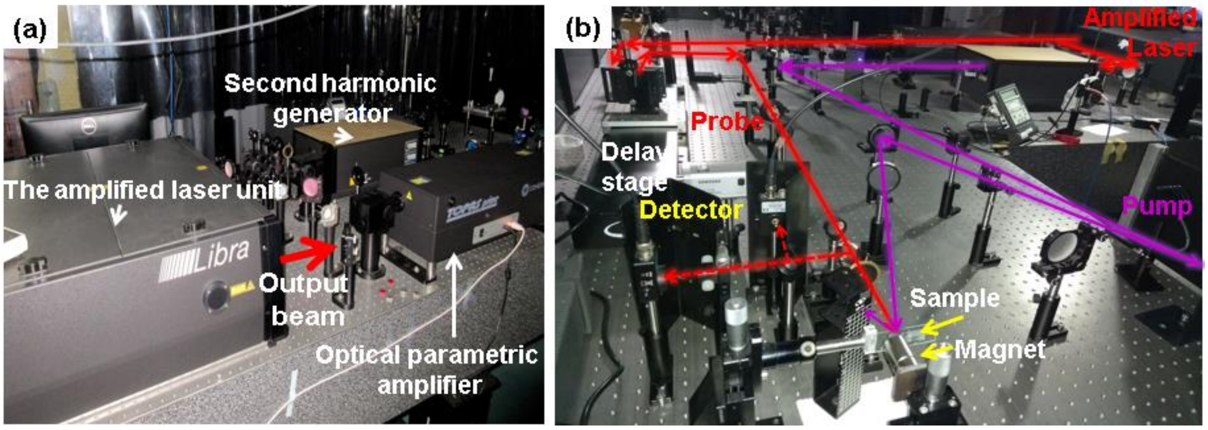

Figure 3.13: Photograph of (a) amplified laser system and (b) TR-MOKE magnetometry setup in our laboratory.

a plano-convex lens. A Glan-Thompson polarizer (GTH5M, Thorlabs) with an extinction ratio of 100000:1 is positioned in the path of the probe beam to make sure a high degree of polarization. Three Iris are placed in the path of the probe beam to regularly monitor its vertical and lateral shift.

The sample is placed on a holder that is linked to an x-y-z translational stage for precise positioning. The pump beam excites the sample at an angle of ~45° while the probe beam is incident on the sample perpendicularly. Both the pump and probe beams are intentionally made slightly out-of-focus on the sample plane to prevent any damage/degradation to the thin metallic film samples during the long measurement time. The diameter of the pump and probe beams are approximately 250 and 100 µm, respectively. The probe beam is centered within the pump beam to avoid probing any nonuniformly excited volume of the sample. The reflected pump beam from the sample is obstructed, whereas the reflected probe beam is divided into two sections using a beam splitter. One section is directed straight to a silicon photodetector to gauge the overall reflectivity of the sample. The other section goes through another Glan-Thompson polarizer (acting as an analyzer) before reaching a silicon photodetector to measure the Kerr rotation. The analyzer is set close to the extinction angle to only allow the Kerr-rotated probe beam to pass through with minimal reflective background. The readings from both silicon photodetectors are processed by two separate lock-in amplifiers (Stanford Research Systems, Model: SR830). An external magnetic field is applied in the desired geometry using a permanent magnet. The pump beam is intermittently blocked or chopped (chopper frequency ~ 373 Hz) by an optical chopper (Thorlabs, Model: MC2000B with a 10-slot chopper blade).

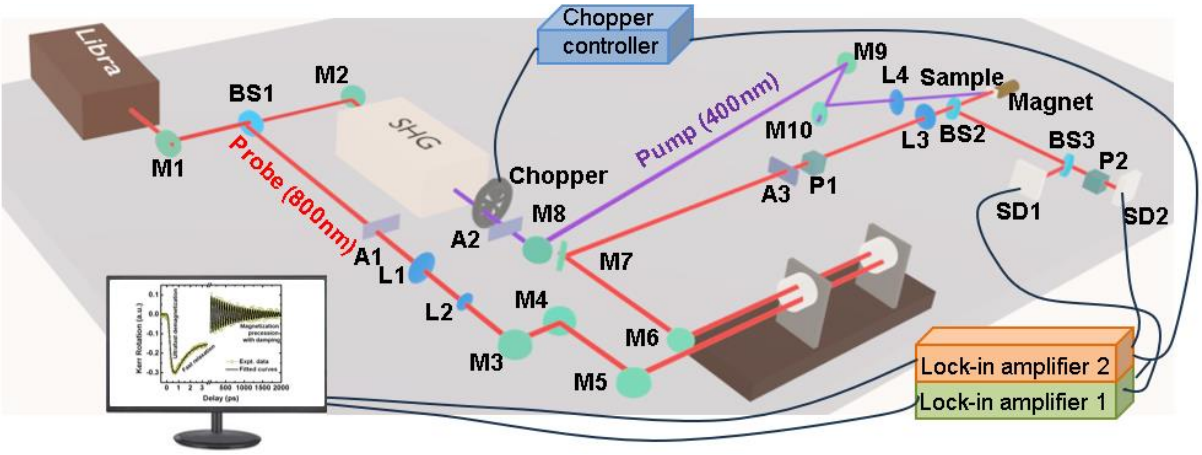

Figure 3.14: Schematic of non-linear TR-MOKE magnetometry setup.

The chopper frequency also serves as a reference frequency for the lock-in amplifiers to conduct a phase-sensitive analysis of both time-resolved reflectivity and Kerr rotation. The time-varying dynamic data are gathered through a custom-built LabView software. The humidity and temperature in the laboratory are maintained below 30% and 22°C, respectively. A schematic of TR-MOKE magnetometry setup is shown in Figure 3.14.

3.4.1.7 Standard protocols for measuring time-resolved magnetization dynamics

After maximizing the output power from the Libra amplified laser and the SHG, the probe and pump beam are maintained at an appropriate fluence for further fine-tuning of the TR-MOKE system. Typically, the total reflectivity signal of a reference silicon substrate is observed at various delay times by adjusting the motorized delay stage. The reflectivity data displays a sudden increase followed by an exponential decrease. The beginning of this abrupt rise of reflectivity can be pinpointed as the zero-delay position when there is perfect temporal overlap with no time delay between the probe and pump beam. The shape and decay time of the exponential decrease in the positive delay offer insights into the accuracy of pump-probe alignment. This alignment can be enhanced by modifying the mirrors positioned in the path of the pump beam. Following the optimization of the transient reflectivity signal, the magnetic samples are substituted for the silicon substrate and a magnetic field is applied in the desired direction using the permanent magnet. The reflectivity and Kerr rotation signal are recorded on the computer at various time delays through an automated process utilizing a home-built LabView program. The total delay time depends on the length of the delay stage, which is approximately 2 ns in our case.

CHAPTER 4

Role of Spin Transport Through the β-Ta/$Co_{20}Fe_{60}B_{20}$ Interface on its Ultrafast Demagnetization: Implications for Ultra-High-Speed Spin Orbitronic Devices

4.1 Introduction

For the growth of ultra-high-speed spintronics, it is imperative to gain deep understanding on the microscopic mechanisms behind spin manipulation in femtosecond to nanosecond timescale. Ultrafast demagnetization [35], one of the fastest known spin manipulation mechanisms, was first experimentally demonstrated by Beaurepaire *et al.* in 1996. Beyond which a flurry of reports on ultrafast demagnetizations in different materials came up [36,37,107]. However, the true microscopic mechanism behind this magnetization quenching, which is an important phenomenon involved in AOS [108-110], remains highly debatable. It is believed that when a femtosecond laser pulse is incident on a magnetic material, it changes the material's electronic configuration near the Fermi level followed by electron thermalization by electron-electron scattering and creation of so-called 'hot electrons'. According to the phenomenological 3TM by Beaurepaire *et al.,* these hot electrons transfer energy to coupled systems such as spins and lattice indicating fast increase in spin temperature which leads to demagnetization. In 1997, Zhang and Hübner argued that ultrafast demagnetization is an effect from exchange interaction and SOC [111] and then in 2000 they inferred that it is a collective effect of applied laser field and SOC of ferromagnetic layers [40]. Subsequently, various models have shown that the spin angular momentum of the excited electrons are modified by spin-flip scattering with other electrons [47], phonons [48], magnons [112], induction of direct laser [49] and the influence of relativistic effect [113]. In the Elliott-Yafet model [45], demagnetization occurs because, electron-phonon or electron-defect momentum-dependent scattering process changes the spin admixture. While according to Krauβ *et al.* [47], interband electron-electron Coulomb scattering is the driving force for demagnetization. Carpene *et al.* [44] claimed that hot electrons excite the magnons through a sudden reduction of magnetization. Further reports have suggested that demagnetization is a combined effect of electron-phonon scattering that transfers angular momentum from spin system to lattice and electron-magnon scattering which is responsible for disordering of magnetic system [114].

On the other hand, in 2010, Battiato *et al.* [51] proposed a new model on optically induced super-diffusive transport of spin polarized electrons for ultrafast demagnetization where they assumed electrons are excited from quasi-localized d band to mobilized sp-like bands by absorption of photon and the larger mobility of the sp-like electrons generates spin angular momentum conserving SST. Malinowski *et al.* [50] first experimentally showed that interlayer spin angular momentum transfer can speed up the demagnetization process irrespective of spin angular momentum conservation in a single layer ferromagnet. Moreover, using *s-d* model of ferromagnetism based on the transverse spin diffusion [115] and spin transfer [116] at interface, Tveten *et al*. [90] theoretically showed that relaxation of the imbalanced spin accumulation among itinerant electrons can provide a major channel for spin angular momentum dissipation from the combined electronic system in NM/FM heterostructures. An alternative report [117] demonstrated that unpolarized hot electrons can demagnetize ferromagnets indicating unavoidable local spin-angular momentum dissipation over SST in heterostructure. Some reports [118,119] have shown the evidence of SST with the indication of transient magnetization enhancement (TME) in layered structures by exciting the FM with femtosecond laser pulses. However, weakly efficient SST led to the ultrafast demagnetization, whereas SST with stronger efficiency is responsible for TME. Schmidt *et al*. [24] proposed that stronger SST occurs from lower electrical conductivity material to higher electrical conductivity material. Another emergent mechanism in this regard is OISTR [52] effect which also generates pure spin current. But the OISTR process is significant when photon energy of ultrashort infrared femtosecond pump pulse can make resonant transition between elemental subsystems of an alloy.

Efficient spin-based ultrafast devices demand a clear understanding of the involved mechanisms besides broad-range control over ultrafast demagnetization time (τ_m) which will be very helpful for future ultrahigh-speed spintronic devices such as tuning the switching time of AOS-based magnetic bits.

Other than τ_m, controlling the Gilbert damping constant (α) [120] is also an important and longstanding research interest in spintronics. Magnetic damping can have several intrinsic and extrinsic origins [22,34,121]. In 2005, Koopmans *et al.* [86] first derived an inverse relation between τ_m and α based on EY spin-flip scattering. Later Fähnle *et al*. [122,123] derived a directly proportional relationship between these two quantities based on the 'breathing Fermi surface model' with conductivity-like damping materials and an inversely proportional relationship based on the 'bubbling Fermi surface model' for resistivity-like damping.

Zhang *et al*. [91] first experimentally demonstrated that for multilayers and heterostructures a proportional relationship between τ_m and α represents the dominating behavior of local spin-flip scattering mechanism behind the ultrafast demagnetization, whereas also a direct relationship between the variation of the ultrafast demagnetization rate, $\Delta\,(1/\tau_m)$ and change in Gilbert damping $\Delta\alpha$ is caused by the spin currents [92] via interfacial spin chemical potential (μ_s). The deviation of mean free path of majority and minority hot electrons in ferromagnetic thin film generates super-diffusive spin currents on femtosecond time scale. Such spin currents dispersed at the interface of the heterostructure result in the non-equilibrium spin accumulation, i.e., spin chemical potential μ_s. On the other hand, flow of up and down spin electrons along opposite directions generates spin current which may lead to enhancement of α. Although the lifetime of femtosecond laser induced spin current is in the picosecond's regime, whereas spin pumping induced spin current lasts for nanoseconds, their physical natures are alike. The femtosecond laser induced spin current causes a reduction of the demagnetization time, while spin pumping induced spin current leads to increase in damping. However, for NM/FM heterostructures if the NM is not a perfect spin sink material, the accumulated spins can create a spin-current backflow [22] which reduces the net spin current followed by the reduction of α and $1/\tau_m$. Thus, understanding the influence of the NM layer on damping and ultrafast demagnetization in the adjacent FM layer in an NM/FM heterostructure is an important problem in ultrafast spin dynamics.

Creation of nonequilibrium spin polarized electrons at the interface due to interfacial spin-orbit effect in NM/FM heterostructure generates SOT which is an interesting topic, both for experimental [124] and theoretical [31] researchers. Since Ta has a strong SOC, this is a very potent material for energy-efficient memory and logic devices [125] as its magnetization can be efficiently controlled by SOT. Besides, Ta is a good spin sink material and very cost-effective in contrast to widely-used NM material like Pt. On the other hand, $Co_{20}Fe_{60}B_{20}$ (CoFeB) is a technologically important FM material because of its high spin polarization property, low intrinsic Gilbert damping, large tunnelling magnetoresistance, where Boron helps to create a sharp interface. Here, we have studied the ultrafast demagnetization and damping in β-Ta/CoFeB/SiO_2 thin film heterostructures by using all-optical TR-MOKE magnetometry. By systematic variation of the CoFeB and Ta layer thicknesses, we have established a direct relationship between $\Delta\,(1/\tau_m)$ and $\Delta\alpha$ which indicates the prevailing role of pure spin current behind the ultrafast demagnetization and damping. We have also shown that the Ta thickness plays a significant role in the accumulation of spin at the interface whose value is found to be

1.8 times smaller for $t \geq 7$ nm as opposed to that in $t < 7$ nm indicating spin-backflow current from NM to FM. While larger spin accumulation at the interface has slowed down the demagnetization process, lower spin accumulation has accelerated the demagnetization in these thin film heterostructures.

4.2 Experimental details

Sub/Ta(t)/CoFeB(d)/SiO_2(2 nm) thin film heterostructures, with t = 0, 1, 2, 3, 4, 5, 6, 7, 10, 15, and 20 nm and d = 1, 2, 3, 4, 6, 10, and 13 nm, were deposited using radio frequency (RF)/direct current (DC) magnetron sputtering on Si (100) wafers coated with 100-nm-thick SiO_2 (thermally oxidized) with high quality in terms of chemical composition as well as surface morphology and interface. RF power supply was used for Ta, SiO_2 deposition whether DC power supply was used for CoFeB deposition. The purpose of varying Ta thickness was to study two separate thickness regimes, i.e., above and below its spin diffusion length (λ). The deposition rate was kept at 2 Å/s at a base pressure of 4×10^{-7} Torr and Ar pressure of about 1 mTorr. Choice of very slow deposition rate was crucial for obtaining uniform thickness over the sample area even for very low thickness values. CoFeB were grown using a DC voltage of 380V while Ta and SiO_2 were deposited with RF power of 40 and 60 W, respectively. RF sputtering reduces the race track erosion on the surface of the target material (Ta) which can be observed during DC magnetron sputtering especially where the surface of the target material gets etched into a circular pattern. However, the width and depth of the race track is much less in RF sputtering due to the alternating nature of the RF discharge with electrons causing less confinement by the magnetic field and hence, the plasma spreads out more, resulting in a wider, larger and shallower race track. This makes more uniform and efficient utilization of the target. These sputtered deposited films were not annealed to avoid the presence of any magnetic dead layer. All other conditions during deposition were kept the identical for all samples.

We have used a TR-MOKE technique based on a two-color non-collinear pump-probe arrangement for measuring ultrafast spin dynamics in a polar Kerr geometry [34]. A large fraction of the fundamental laser beam (wavelength of 800 nm, pulse width of 40 fs, repetition rate of 1 kHz) from a femtosecond regenerative amplifier (Libra, Coherent Inc.) is passed through a second harmonic generator to produce the pump beam (wavelength of 400 nm, pulse width > 40 fs, repetition rate of 1 kHz) to excite the dynamics, while a small fraction of the remaining fundamental laser is used as a probe beam to measure the subsequent dynamics in femtosecond to nanosecond timescale. A time delay between the pump and the probe beam is introduced by steering the probe beam through a motorized variable delay generator. The power of the pump beam was chosen to be much stronger (~ 10 mW) than the probe beam (~ 1 mW) during all measurements. An external magnetic field is applied at ~10° tilt from the sample plane to introduce a finite demagnetizing field along the direction of the pump pulse. The in-plane component of this field is assigned to as the bias field (H). Modification of this field by the pump pulse launches a fast time-varying magnetic field inside the sample to trigger the precessional dynamics. The probe beam is focused to a spot diameter of ~ 100 μm and was incident normally on the sample plane. The pump beam is focused to a larger spot size of ~ 250 μm and was incident at 45° angle on the sample plane. The probe spot was aligned precisely at the center of the pump spot to detect the dynamics from a uniformly excited volume of the sample. This eliminates additional complications due to propagation of energy out of the uniformly excited region of the sample.

4.3 Results and discussions

Static Characterization:

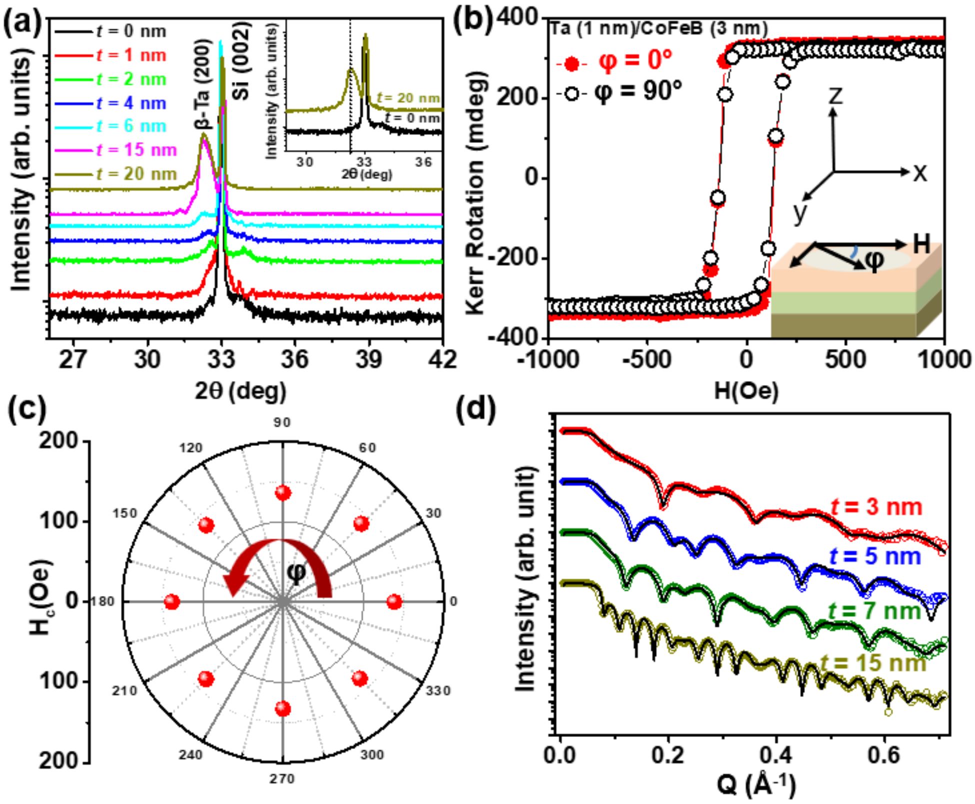

Figure 4.1: (a) X-ray diffraction patterns measured for Sub/Ta (t)/CoFeB (3 nm)/SiO_2 (2 nm) thin film heterostructures films with $t = 0, 1, 2, 4, 6, 15, 20$ nm. Peaks corresponding to β phase of Ta is marked in the plots. (b) Magnetic hysteresis loop from Sub/Ta (1 nm)/CoFeB (3 nm)/SiO_2 (2 nm) thin film heterostructures film for two different azimuthal angles ($\varphi = 0°$ and $\varphi = 90°$) obtained using static MOKE. (c) Angular dependence of H_c

for Sub/Ta (1 nm)/CoFeB (3 nm)/SiO_2 (2 nm). (d) X-ray reflectivity spectra for Sub/Ta (t)/CoFeB (3 nm)/SiO_2 (2 nm) thin film heterostructures films with t = 3, 5, 7, 15 nm.

The crystal structure of sputter-deposited Ta (t)/CoFeB (3 nm)/SiO_2(2 nm) thin films were characterized by XRD technique using 40 kV X-Ray source (Rigaku: SmartLab). Figure 4.1(a) shows the XRD-spectra for different Ta-thicknesses. These plots reveal that a very intense β (200)-peak [126] at 2θ angle of 32.5° for t = 20 and 15 nm. Intensity modulation on the left and right side of main β-Ta peak is attributed to crystal size effect (Laue function), as CoFeB is amorphous and is not expected to produce any sharp diffraction peak. With the decrease of t, the intensity of β (200)-peak decreases and we can see that a broad diffused peak shifts towards higher 2θ angles which is attributed to the presence of an amorphous layer. The small shoulder peaks observed for samples with 1 and 2-nm-thick Ta may have appeared due to the presence of this amorphous layer. Within our Ta-thickness regime, we have not observed any α to β phase transition. Therefore, we conclude that in all the studied samples Ta layer retains only the β phase without the appearance of any α phase of Ta.

The in-plane magnetic hysteresis loop is measured using static MOKE technique. Figure 4.1(b) shows the hysteresis loops for two different azimuthal angles ($\varphi = 0^\circ$ and $\varphi = 90^\circ$) of sample Sub/Ta (1 nm)/CoFeB (3 nm)/SiO_2(2 nm) with coercive field (H_c) of ~135 Oe both for the two perpendicular orientations. We do not expect significant effect of interfacial perpendicular magnetic anisotropy in these samples due to the insignificant modification of in-plane hysteresis loops for different Ta and CoFeB thicknesses. Figure 4.1(c) shows H_c vs. φ plot which reveals completely isotropic nature of the sample. The XRR-spectra of Sub/Ta (t = 3, 5, 7, 15 nm)/CoFeB (3 nm)/SiO_2(2 nm) thin film heterostructures are shown in Figure 4.1(d), which show well defined oscillations up to the scattering vector of 0.7 $Å^{-1}$ for all the thicknesses signifying their uniform deposition. The 'Reflex' software is utilized to analyze these spectra from where we have extracted the thickness, roughness and scattering length density (SLD) of all the layers. Here, SLD is proportional to the electron density of the material. The thicknesses of the layers obtained from the fits are found to be close to their nominal thickness values. The SLD and interfacial roughness values of Ta, CoFeB and SiO_2 are also tabulated in Table 4.1, which confirm relatively small roughness and SLD values are independent of layer thickness and near to the reported values in the literature [127,128].

Table 4.1: Various parameters obtained from XRR analysis:

Ta (3 nm)/CoFeB (3 nm)	**Layer**	**Thickness (nm)**	**Roughness (nm)**	**SLD (10^{-5}Å^{-2})**
	SiO$_2$	3.1	0.55	1.88
	CoFeB	3.7	0.28	5.10
	Ta	3.5	0.22	10.76
	SiO$_2$	-	0.36	1.88
Ta (5 nm)/CoFeB (3 nm)	**Layer**	**Thickness (nm)**	**Roughness (nm)**	**SLD (10^{-5}Å^{-2})**
	SiO$_2$	2.5	0.45	1.96
	CoFeB	4.3	0.33	5.55
	Ta	5.7	0.33	10.21
	SiO$_2$	-	0.24	1.88
Ta (7 nm)/CoFeB (3 nm)	**Layer**	**Thickness (nm)**	**Roughness (nm)**	**SLD (10^{-5}Å^{-2})**
	SiO$_2$	2.7	0.64	1.87
	CoFeB	4.3	0.34	5.40
	Ta	6.7	0.31	9.99
	SiO$_2$	-	0.25	1.88
Ta (15 nm)/CoFeB (3 nm)	**Layer**	**Thickness (nm)**	**Roughness (nm)**	**SLD (10^{-5}Å^{-2})**
	SiO$_2$	2.6	0.71	2.50
	CoFeB	4.2	0.32	5.85
	Ta	15.5	0.28	9.76
	SiO$_2$	-	0.29	1.62

TRMOKE Measurement of Laser-Induced Ultrafast Demagnetization and Gilbert Damping: We have performed the TR-MOKE measurements in polar Kerr geometry to obtain the ultrafast demagnetization time and Gilbert damping parameter. The schematic of TR-MOKE measurement geometry is shown in Figure 4.2(a). When a femtosecond laser pulse is incident on a ferromagnetic sample in its saturated magnetic state, its magnetization is either fully or partially lost in sub-picosecond time scale. This phenomenon is known as ultrafast demagnetization [35]. This is accompanied with a fast recovery of the magnetization within a few picoseconds (ps) and a slow recovery within a few hundreds of ps, known as the fast and the slow remagnetization process. The slow remagnetization is accompanied by a damped magnetization precession [129]. Figure 4.2(b) shows a typical TRMOKE trace for Sub/CoFeB (3 nm)/SiO_2 (2 nm) hetero nanostructure revealing above three temporal regimes.

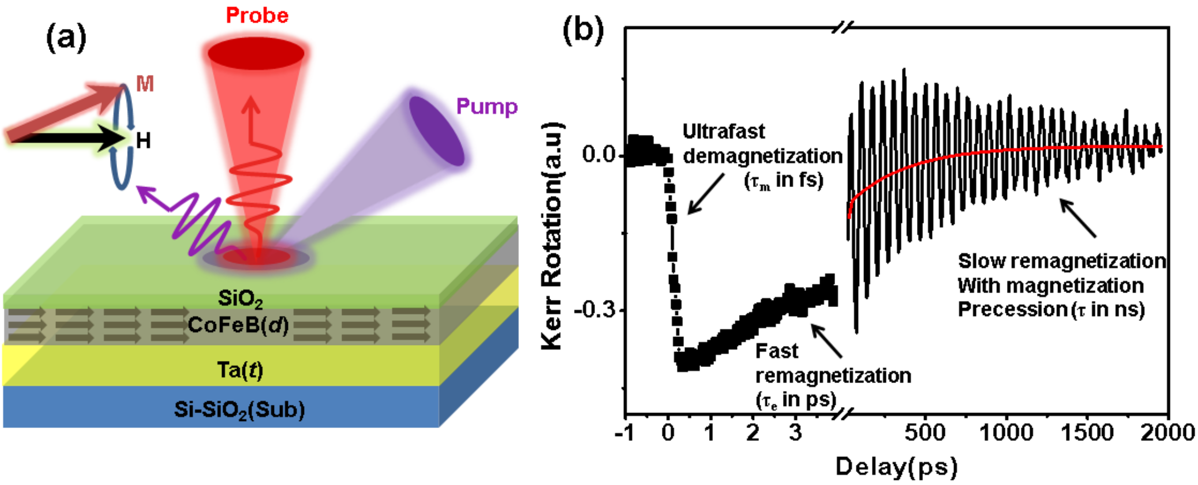

Figure 4.2: (a) Schematic of the experimental geometry and (b) a typical TRMOKE trace from the Sub/CoFeB (3 nm)/SiO_2 (2 nm) hetero nanostructure at H = 1.73 kOe. The three important temporal regimes are shown in the graph.

The ultrafast demagnetization and fast remagnetization part of the data can be fitted using a phenomenological equation derived from the 3TM [50]:

$$\frac{-\Delta \mathrm{M}}{\mathrm{M}} = \left[\left\{\frac{A_1}{(t/\tau_0+1)^{\frac{1}{2}}} + \frac{A_1\tau_m - A_2\tau_e}{\tau_e-\tau_m} e^{-t/\tau_m} + \frac{A_2\tau_e - A_1\tau_e}{\tau_e-\tau_m} e^{-t/\tau_e}\right\} H(t) + A_3\delta(t)\right] \otimes G(t) \qquad (4.1)$$

This is an approximate expression based on the assumption that the electron temperature increases instantaneously upon laser excitation to create hot electrons above the Fermi level. These electrons excite the spins by electron-magnon interaction resulting in a magnetization quenching [44]. Subsequently, the energy is distributed between three reservoirs: electron, lattice and spin due to which the quenched magnetization tries to reach its initial magnetization condition. In the above expression A_1 represents the value of magnetization state after equilibrium between electron, lattice and spin, A_2 is proportional to the initial maximum rise in electronic temperature and A_3 represents the magnitude of the state filling effect during pump-probe temporal overlap well established by a Dirac delta function ($\delta(t)$). τ_0 represents the cooling time by heat diffusion during electron-phonon interactions. $H(t)$ is the Heaviside step function and $G(t)$ is Gaussian function. The time scale of magnetization dynamics of ultrafast demagnetization time (τ_m) is described by the first exponential term, while the second exponential term dictates the electron-phonon interaction by fast relaxation time (τ_e). Figure 4.3(a) shows the ultrafast demagnetization curve for various CoFeB layer thicknesses, where the NM layer thickness is kept constant at 4 nm. Figure 4.3(b) shows the same for varying Ta thicknesses by keeping the CoFeB thickness constant at 3 nm. All these experimental data are fitted using equation 4.1.

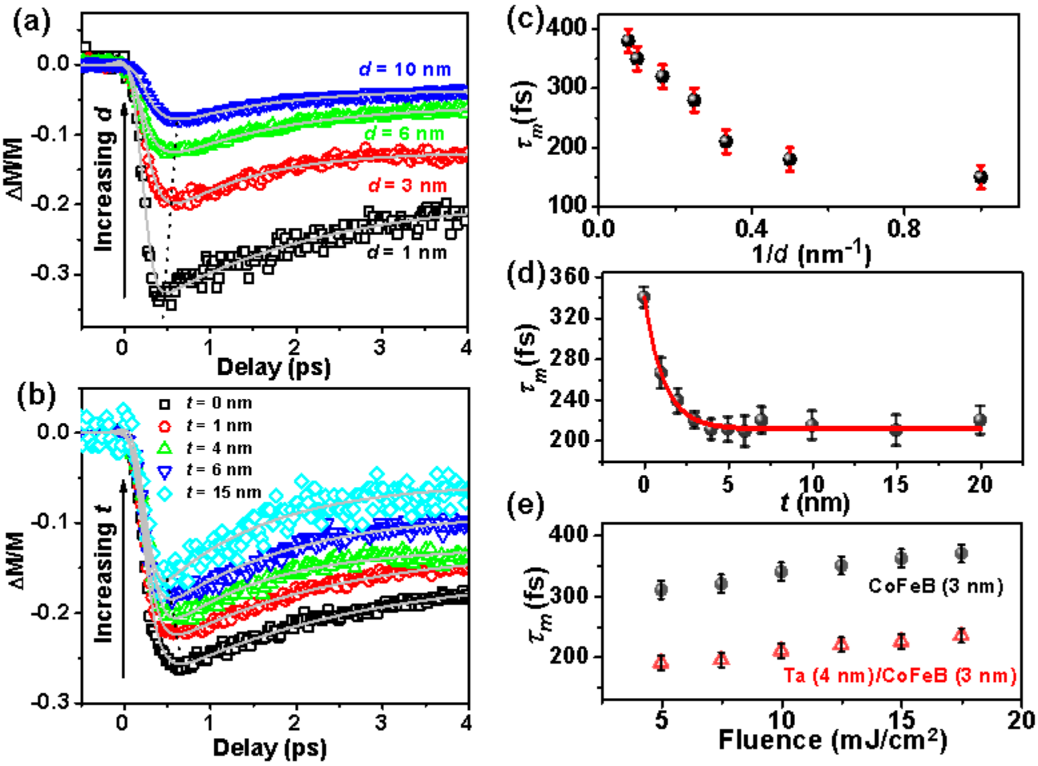

Figure 4.3: Time-resolved Kerr rotation showing ultrafast demagnetization and fast relaxation in Sub/Ta (*t*)/CoFeB (*d*)/SiO₂ (2 nm) thin film heterostructures with (a) varying CoFeB thickness at constant Ta thickness of *t* = 4 nm and (b) varying Ta thickness variation at constant CoFeB thickness of *d* = 3 nm. Here, the symbols are experimental data and solid lines are fits using equation 4.1. Evolution of demagnetization time (τ_m) with (c) (1/*d*) nm^{-1} and (d) *t* nm. Here, symbols are experimental results and solid lines are theoretical fits. (e) Variation of τ_m with pump fluence in thin film heterostructures with 4-nm-thick Ta (filled circle) and without Ta (open triangle).

Variation in τ_m for different CoFeB and Ta layer thicknesses are shown in Figure 4.3(c) and Figure 4.3(d), respectively. Clearly, τ_m increases with CoFeB layer thickness from 150 ± 20 fs for *d* = 1 nm to 380 ± 10 fs for *d* = 13 nm, while it decreases monotonically from 340 ± 15 fs for *t* = 0 to 210 ± 10 fs for *t* = 4 nm before nearly saturating for thicker Ta. A clear decreasing trend of magneto-optical quenching is observed for both cases on increasing thickness. This decrease in quenching with layer thickness can be ascribed to the increase in reflectivity and decrease in absorption of thicker metallic layer [130]. Figure 4.3(e) shows a clear decrement in τ_m (~ 62%) with the insertion of NM. In the absence of NM, the Elliot-Yafet like spin-flip scattering is believed to be primarily responsible for the rapid increment of spin temperature and the ensuing demagnetization. Whereas the presence of NM also brings the effect of spin transport (ST) into the picture for the enhancement of demagnetization rate. A slight change of τ_m is further observed with the laser fluence which can be caused by the enhancement of spin fluctuation at elevated temperatures [131]. The electrical conductivity of Ta (~ 0.004×10^6 Ω^{-1}cm^{-1}) does not differ too much from that of CoFeB (~ 0.007×10^6 Ω^{-1}cm^{-1}) [132]. Thus, ST although present in these samples but not high enough to cause TME.

To understand the microscopic mechanisms behind the ultrafast demagnetization better, we have also studied the precessional dynamics and damping of the same samples. Figure 4.4(a) shows the damped precessional oscillations for Sub/Ta (4 nm)/CoFeB (*d*)/SiO_2 (2 nm) and Sub/Ta (*t*)/CoFeB (3 nm)/SiO_2 (2 nm) thin film heterostructures. It is clear from the plots that the magnetization precession is significantly influenced by the thickness of the FM and NM layers. We have fitted the precessional data using a damped harmonic oscillation as below to extract the precessional decay time.

$$M(t) = M(0)e^{-\left(\frac{t}{\tau}\right)}\sin(2\pi f t + \phi) \tag{4.2}$$

where τ is the precessional decay time, ϕ is the initial oscillation phase and f is the precessional frequency.

To extract the value of the effective magnetization (M_{eff}), the bias field dependent f is fitted with the Kittle formula by neglecting the anisotropy energy, which is negligible in amorphous CoFeB (equation 4.3) [133].

$$f = \frac{\gamma}{2\pi}\left(H\left(H + 4\pi M_{eff}\right)\right)^{1/2} \tag{4.3}$$

Where $\gamma = g\mu_B/\hbar$ and g is the Landé g-factor. Subsequently, the extracted τ and M_{eff} values are used for finding the α using the following expression [134]:

$$\alpha = \frac{1}{\gamma\tau\left(H+2\pi M_{eff}\right)} \tag{4.4}$$

In addition to spin pumping several other extrinsic mechanisms such as two-magnon scattering, spin memory loss, interfacial band hybridization can also modulate the damping in NM/FM thin film heterostructures. These extrinsic mechanisms will be negligible in our case because as we have applied a strong enough external magnetic field to avoid them [135]. Therefore, the primary mechanism for the modulation of damping is identified as the spin current generation by the spin pumping mechanism [12]. Recent studies have confirmed that spin pumping is the prevailing mechanism for modulation of α in β-Ta/CoFeB thin film heterostructures [121].

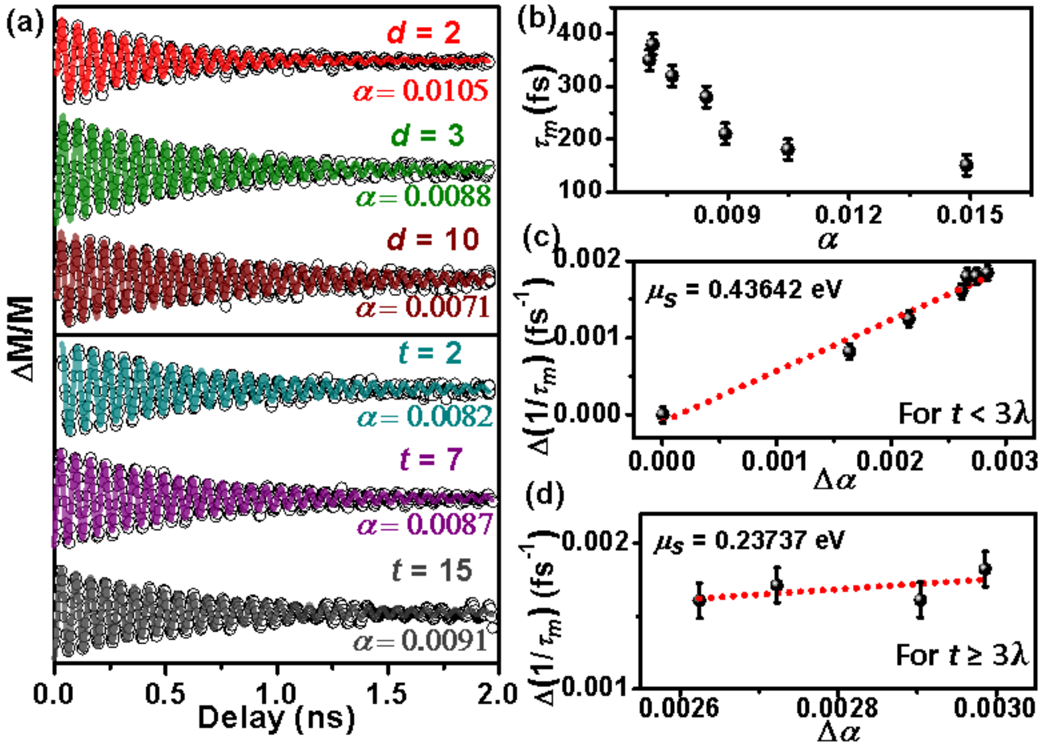

Figure 4.4: (a) Time-resolved Kerr rotation showing magnetization precession of Sub/Ta (4 nm)/CoFeB (*d*)/SiO$_2$ (2 nm) and Sub/Ta (*t*)/CoFeB (3 nm)/SiO$_2$ (2 nm) thin film heterostructures. The symbols are experimental data and the solid lines are fits with equation 4.2. (b) Plot of τ_m as a function of α for Sub/Ta (4 nm)/CoFeB (*d*)/SiO$_2$ (2 nm) thin film heterostructures. Variation of ultrafast demagnetization rate ($\Delta\ (1/\tau_m)$) in fs^{-1} as a function of modulation of damping ($\Delta\alpha$) for two different regimes of Sub/Ta (*t* nm)/CoFeB (3 nm)/SiO$_2$ (2 nm) thin film heterostructures: (c) *t* less than three times of spin diffusion length (3λ) and (d) *t* greater than 3λ. The symbols are experimental results while the dotted lines are fits with equation 4.6.

The modulation of damping due to spin pumping is given by [136]:

$$\Delta\alpha = \alpha - \alpha_0 = \frac{G_{\uparrow\downarrow}\left(1-e^{\frac{-2t}{\lambda}}\right)g\mu_B}{4\pi d M_s}. \tag{4.5}$$

Here M_s is the saturation magnetization, λ is the spin diffusion length, *d* is the FM layer thickness, *t* is the NM thickness and $G_{\uparrow\downarrow}$ is the intrinsic spin-mixing conductance. The spin-mixing conductance quantifies the conductivity of spin angular momentum through NM/FM interface. The value of $G_{\uparrow\downarrow}$ is found to be 7.2×10^{14} cm^{-2}.

Correlation between ultrafast demagnetization rate and Gilbert damping induced by spin pumping: The correlation between the ultrafast demagnetization time and damping has been used to identify their dominant underlying mechanisms for over a decade [86]. Based on the breathing Fermi-surface model [71] of damping, a proportional relationship [122] between τ_m and α indicates that the localized SFS mechanism dominates with conductivity-like damping, while based on the bubbling Fermi-surface model [137] non-local spin current mechanism dominates for inversely proportional relationship with resistivity-like damping.

Figure 4.4(a) shows the damped magnetization precessions for samples with different CoFeB and Ta thicknesses. Figure 4.4(b) shows the variation in τ_m with α for different CoFeB thicknesses. Clearly, τ_m shows an inverse dependence on α. This is an indication that spin current transport is a dominant mechanism behind the damping and the demagnetization process. The damping can therefore be considered as a sum of the spin pumping effect and the intrinsic damping of the CoFeB layer itself.

The injected spins due to magnetization precession from the CoFeB layer are accumulated at the interface of Ta/CoFeB, followed by diffusion associated with spin-flip scattering. This nonequilibrium spin accumulation is the difference between the chemical potential of up and down spins. When the Ta layer thickness is large enough then the spins can easily relax by spin flip processes, i.e., more spin current flows into the NM, causing faster demagnetization of CoFeB layer for higher Ta thickness. When injected spins cannot relax by spin-flip processes, small but finite spins accumulate at the interface [12].

This motivates us to find out NM thickness-dependent spin accumulation at the interface. To get better insight into the effect of NM, we have fitted the demagnetization rate ($\Delta\frac{1}{\tau_m} = \frac{1}{\tau_m}|_t - \frac{1}{\tau_m}|_{t=0}$) vs. modulation of damping ($\Delta\alpha = \alpha|_t - \alpha|_{t=0}$) induced by absorption and generation of spin current using equation 4.6.

$$\Delta\frac{1}{\tau_m} = \frac{\mu_s}{\hbar}\Delta\alpha \tag{4.6}$$

Where μ_s is the spin chemical potential which is proportional to the spin accumulation at the interface between different layers [92] (absence of spin accumulation in the FM is taken as reference) and ħ is the reduced Plank constant. This equation also gives further insight into the relationship between damping and demagnetization.

Spin accumulation at the interface follows the equation (derived in Appendix I).

$$\boldsymbol{\mu_s}(x = 0) = 4\pi\frac{\tau_{sf}/hNSt}{tanh(t/\lambda)}\boldsymbol{I_s} \tag{4.7}$$

where τ_{sf} is the spin-flip relaxation time, S is the area of the interface, N is the density of states in the film. This equation is showing that the spin chemical potential at the interface is NM thickness dependent.

We have divided the thickness regime into two parts $t < 3\lambda$ and $t \geq 3\lambda$. We have chosen 3λ as tanh(x) in equation 4.7 gets saturated at $x \approx 3$. From equation 4.6 we have extracted that for $t < 3\lambda$ spin accumulation is 0.436 eV, while for $t > 3\lambda$ the value is 0.237 eV as shown in Figure 4.4(c) and Figure 4.4(d). This shows that spin accumulation is thickness dependent. Besides, the resistivity also increases with the decreasing Ta layer thickness. Previous studies showed that it might affect spin pumping efficiency [138,139].

Based on the breathing Fermi-surface model and Elliot-Yafet relation for Gilbert damping and spin-relaxation time respectively, α and τ_m follow the relation [91]:

$$\tau_m = \frac{M}{\gamma F_{el} p b^2} \alpha \tag{4.8}$$

Taking the values of $\tau_m|_{t=0} = 340$ fs and $\alpha = 0.006$, $\alpha/\tau_m = 1.76 \times 10^{10}\ \mathrm{s}^{-1}$ is obtained. This value reasonably agrees with the calculated value for Ni by the breathing Fermi-surface model [122]. This indicates that the ultrafast demagnetization of bare CoFeB is primarily governed by the local spin-flip scattering process, while nonlocal spin current dissipated at the interface of CoFeB/Ta opens an additional channel to accelerate the ultrafast demagnetization and enhance the Gilbert damping.

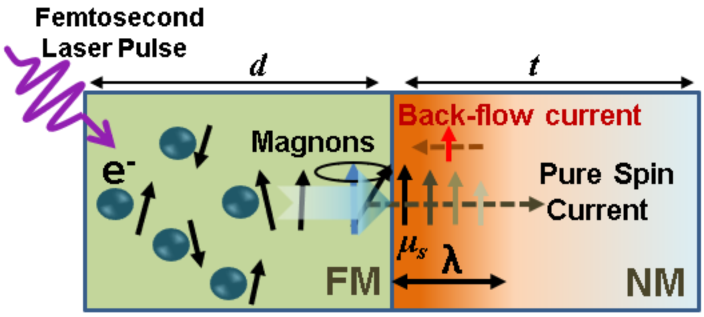

Figure 4.5: A schematic presenting the processes involved in ultrafast demagnetization and magnetic damping of NM/FM hetero nanostructure led by spin transport mechanisms.

In our study we have shown that photons of a femtosecond laser are absorbed by the electrons of the FM material and creates a non-equilibrium distribution (shown in Figure 4.5) that thermalizes through various scattering processes, including electron-magnon scattering. The electron-magnon scattering induces spin-flips influencing the net magnetization of the sample. However, the contribution of these scattering processes is minor and identical for all samples of varying thicknesses. On the other hand, super-diffusive spin transport plays a major role for the demagnetization mechanism on femtosecond timescale. On the other hand, magnetization precession transfers angular momentum by generating spin current from FM to NM through spin pumping that enhances the damping constant. In addition, the NM thickness also plays an important role for spin accumulation at the interface which is responsible for spin back-flow current. Thus, we can conclude that the demagnetization rate and damping both can be enhanced through spin transport in Ta/CoFeB bilayers system.

To have a deeper insight into the ultrafast demagnetization process, we have used the phenomenological 3TM and reproduced the experimental ultrafast demagnetization results obtained from TR-MOKE experiment. The corresponding three coupled differential equations are written as:

$$C_e(T_e)\frac{dT_e}{dt} = -G_{el}(T_e - T_l) - G_{es}(T_e - T_s) + P(t) \tag{4.9a}$$

$$C_s(T_s)\frac{dT_s}{dt} = -G_{sl}(T_s - T_l) - G_{es}(T_s - T_e) \tag{4.9b}$$

$$C_l(T_l)\frac{dT_l}{dt} = -G_{sl}(T_l - T_s) - G_{el}(T_l - T_e) \tag{4.9c}$$

Where T_e, T_s and T_l are electron, spin and lattice temperature, respectively. C_e is the electron specific heat and C_l, C_s are the lattice and spin contribution to the specific heat. G_{es}, G_{el} and G_{sl} and the electron-spin, electron-lattice and spin-lattice coupling strength constants which correspond to energy transfer rate from electron to spin, lattice and spin to lattice system. As the initial excitation occurs in the electronic bath, the laser source term $P(t)$ is added to equation 4.9a only.

In this numerical simulation, the initial temperature of three baths is set at room temperature and electron specific heat is taken proportional to the electron temperature ($C_e = \gamma T_e$, where $\gamma = 0.7\times10^3$ Jm^{-3}K^{-2}).

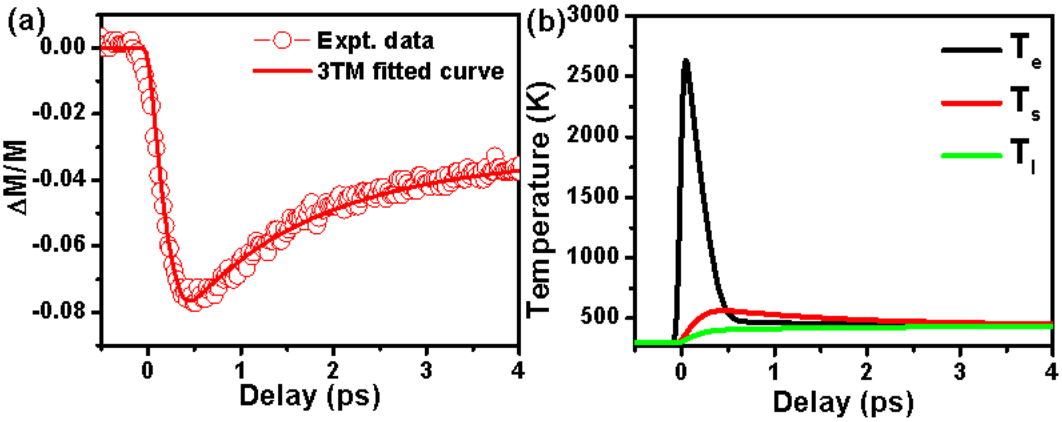

Figure 4.6: (a) Ultrafast demagnetization data fitted with 3TM and (b) temporal evolution of electron, spin and lattice temperature for Sub/Ta (4 nm)/CoFeB (10 nm)/SiO$_2$ (2 nm) thin film heterostructure.

Figure 4.6(a) shows the experimental ultrafast demagnetization results along with the results obtained from the 3TM and Figure 4.6(b) shows the temporal evolution of electron, spin and lattice temperatures for the Sub/Ta (4 nm)/CoFeB (10 nm)/SiO_2 (2 nm) thin film heterostructure. On the other hand, Figure 4.7(a) shows the experimental ultrafast demagnetization result along with the results obtained from the 3TM and Figure 4.7(b) shows the temporal evolution of electron, spin and lattice temperatures for the Sub/Ta (10 nm)/CoFeB (3 nm)/SiO_2 (2 nm) thin film heterostructure.

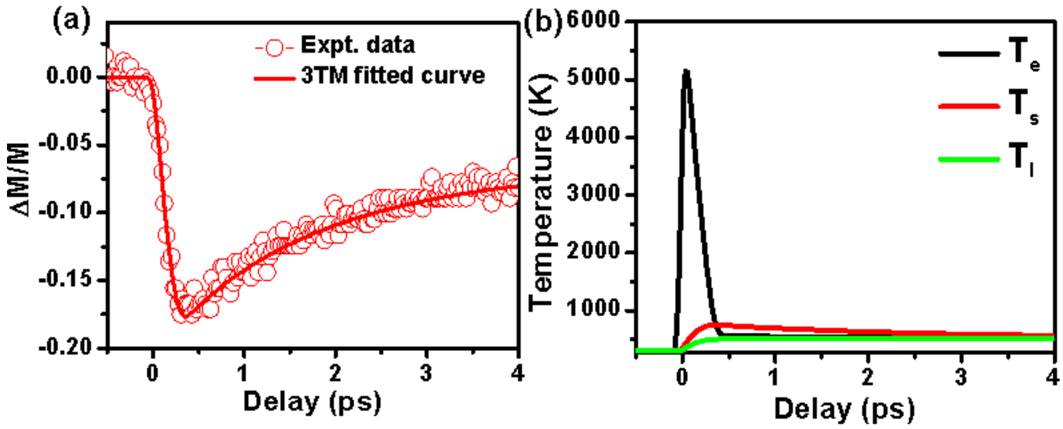

Figure 4.7: (a) Ultrafast demagnetization data fitted with 3TM and (b) temporal evolution of electron, spin and lattice temperature for Sub/Ta (10 nm)/CoFeB (3 nm)/SiO_2 (2 nm) thin film heterostructure.

We have listed the influence of different parameters obtained from 3TM on ultrafast demagnetization in Table 4.2 (for the CoFeB thickness series) and Table 4.3 (for the Ta thickness series) below.

Table 4.2: Parameters obtained from 3TM of ultrafast demagnetization results for samples with varying CoFeB thickness:

d **(nm)**	**C_s (× 10^6 $Jm^{-3}K^{-1}$)**	**C_l (× 10^6 $Jm^{-3}K^{-1}$)**	**G_{es} (×10^{17} $Wm^{-3}K^{-1}$)**	**G_{el} (×10^{17} $Wm^{-3}K^{-1}$)**	**G_{sl} (×10^{17} $Wm^{-3}K^{-1}$)**
1	7.39	85.1	32	250.5	0.7
2	6.09	51.8	29	138	0.7
3	5.99	36.2	28	103	7.7
4	5.29	32.2	26	84	6.7
6	5.29	32	24	53	4.7
10	4.59	20	23	34	8.7
13	4.49	14	22	26	7.7

Table 4.3: Parameters obtained from 3TM of ultrafast demagnetization results for samples with varying Ta thickness:

t **(nm)**	$\mathbf{C_s}$ **(× 10^6 $Jm^{-3}K^{-1}$)**	$\mathbf{C_l}$ **(× 10^6 $Jm^{-3}K^{-1}$)**	$\mathbf{G_{es}}$ **(×10^{17} $Wm^{-3}K^{-1}$)**	$\mathbf{G_{el}}$ **(×10^{17} $Wm^{-3}K^{-1}$)**	$\mathbf{G_{sl}}$ **(×10^{17} $Wm^{-3}K^{-1}$)**
0	4.79	29	23	92	1.7
1	4.99	34	25	105	0.7
2	5.59	33.5	26	89	1.7
3	6.09	38	27	92	4.7
4	5.99	38	28	101	5.7
5	5.99	44	28	101	5.7
6	5.99	45	28	105	6.7
7	5.99	44	28	106	3.7
10	5.99	57	28	112	3.7
15	5.99	68	28	114	3.7
20	5.99	39	28	105	5.9

As expected, G_{es} mainly determines the ultrafast demagnetization time followed by excitation of the spin population via electron-magnon interaction. The present results clearly corroborate that (Figure 4.8). The higher electron-spin coupling strength corresponds to enhancement of the demagnetization rate. G_{el} determines the decay of the electron temperature whereas G_{sl} the decay of spin temperature. C_s should be proportional to T_s and thus to G_{es}. The tabulated results clearly indicate these. The higher lattice specific heat C_l at lower CoFeB thickness probably

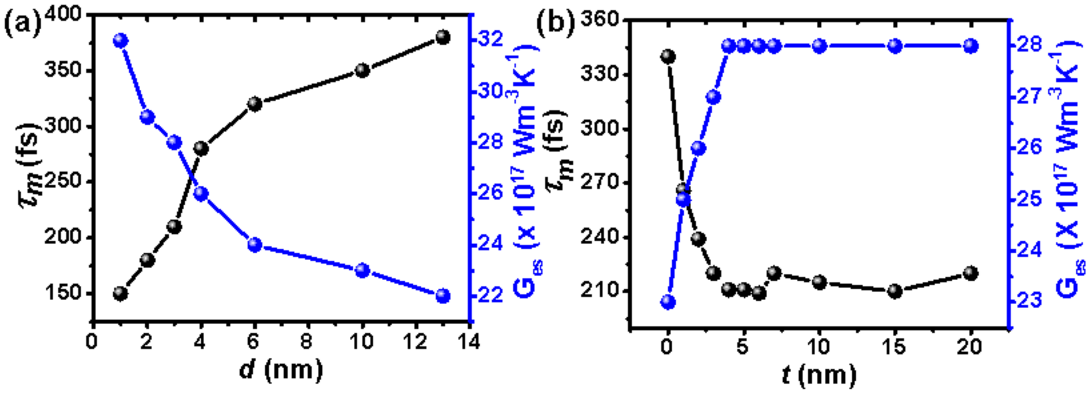

Figure 4.8: Variation of τ_m and G_{es} with (a) CoFeB (*d* nm) and (b) Ta (*t* nm) thickness variation.

stems from the high atomic vibration energies of the surface atoms. Time dependent density function theory from first principles calculation may give a better understanding but is beyond the scope of this article [140-142].

4.4 Conclusion

In conclusion, we have experimentally measured the time-resolved spin dynamics to investigate ultrafast demagnetization and magnetization precession in β-Ta/CoFeB thin film thin film heterostructures. Our main aim is to find out the dominating mechanism behind the ultrafast demagnetization for such thin film heterostructures. Therefore, we have correlated the ultrafast demagnetization and damping in these samples for different CoFeB layer thicknesses. The proportional relationship between the demagnetization rate ($\Delta \frac{1}{\tau_m}$) with the modulation of damping ($\Delta\alpha$) indicates that the spin transport effect is the dominating factor here. From this correlation we have obtained the spin chemical potential for two different Ta thickness regimes. We have found that spin accumulation is higher (μ_s = 0.436 eV) for lower NM thickness (< 3λ) as they cannot diffuse completely through the Ta layer, whereas the spin accumulation is lower (μ_s = 0.237 eV) for higher t values, i.e., $t \geq 3\lambda$ as in this regime Ta can act as a better spin sink material. Therefore, our study has enlightened the understanding of the underlying microscopic mechanisms behind ultrafast demagnetization and damping in technologically important β-Ta/CoFeB thin film heterostructures which will help to design spin-based devices with higher energy efficiency and faster operating speed.

Appendix

If the normal metal is a perfect spin sink, then all the spins ejected by $\boldsymbol{I_s^{pump}}$ through precession from FM to NM relax through spin-flip processes and the total spin current across the interface is approximated as $\boldsymbol{I_s} = \boldsymbol{I_s^{pump}}$, assuming negligible spin back-flow current of spin minority electrons from the neighboring layer ($\boldsymbol{I_s^{back}} \approx 0$). However, when the NM layer is not a perfect spin sink, then spin minority electrons due to lower velocity builds up at the interface at dynamic equilibrium. Then the spin accumulation driven current $\boldsymbol{I_s^{back}}$ contributes to I_s as; $\boldsymbol{I_s} = \boldsymbol{I_s^{pump}} - \boldsymbol{I_s^{back}}$ [12].

Spin accumulation-driven spin back-flow current ($\boldsymbol{I_s^{back}}$) through an interface can be expressed as:

$$\boldsymbol{I_s^{back}} = \frac{1}{8\pi}[2g_r^{\uparrow\downarrow}\boldsymbol{\mu_s}(x=0) + 2g_i^{\uparrow\downarrow}\boldsymbol{m} \times \boldsymbol{\mu_s}(x=0) + (g^{\uparrow\uparrow} + g^{\downarrow\downarrow} - 2g_r^{\uparrow\downarrow})[\boldsymbol{m} \cdot \boldsymbol{\mu_s}(x=0)]\boldsymbol{m} \tag{4.A1}$$

Where $\boldsymbol{m}$ is the magnetization and $g^{\uparrow\downarrow} = g_r^{\uparrow\downarrow} + ig_i^{\uparrow\downarrow}$, where $g^{\uparrow\downarrow}$ is the interfacial mixing conductance that governs the spin pumping through the NM-FM interface.

The total spin current can be written as:

$$\boldsymbol{I_s} = \boldsymbol{I_s^{pump}} - \frac{\beta}{2}[2g_r^{\uparrow\downarrow}\boldsymbol{I_s} + 2g_i^{\uparrow\downarrow}\boldsymbol{m} \times \boldsymbol{I_s} + (g^{\uparrow\uparrow} + g^{\downarrow\downarrow} - 2g_r^{\uparrow\downarrow})[\boldsymbol{m} \cdot \boldsymbol{I_s}]\boldsymbol{m}] \tag{4.A2}$$

where is the “backflow” factor β which governs returning spin current into the ferromagnet,

$$\beta = \frac{\tau_{SF}\delta_{SD}/h}{\tanh(t/\lambda)} \tag{4.A3}$$

τ_{SF}^{-1} is the spin-flip rate, an energy level difference of the states participating in the SFS events, λ is the spin diffusion length $\delta_{SD} = (NS\lambda)^{-1}$ for $t >> \lambda$ and $\delta_{SD} = (NSt)^{-1}$ for $t << \lambda$, t is the NM thickness and h is the Plank’s constant.

From equations (4.A1) and (4.A2),

$$\boldsymbol{\mu_s}(x=0) = 4\pi\beta\boldsymbol{I_s}$$

$$\text{or, } \boldsymbol{\mu_s}(x=0) = 4\pi\frac{\tau_{SF}\delta_{SD}/h}{\tanh(t/\lambda_{SD})}\boldsymbol{I_s} \tag{4.A4}$$

CHAPTER 5

Ultrafast Demagnetization and Gilbert Damping in Electrodeposited CoP Film

5.1 Introduction

High frequency nano-structured magnetic films are essential for cutting edge applications including the superior performance of high-frequency integrated micro-inductors, coupled inductors, micro-transformers having multi-nanomagnetic-layered cores, as part of on-chip power supply (DC-DC switch mode power conversion) for next generation microprocessors' power delivery [143,144], energy efficient switching of MRAM bits [133,145] and future high-speed spin-based devices. However, most of the high-frequency integrated magnetic devices suffer from eddy current losses, a common dissipation mechanism in magnetic materials, which transfers the excitation eventually into heat. To reduce eddy current losses (particularly in thicker magnetic materials to achieve reasonable power density), hysteresis losses and ferromagnetic resonance (FMR) losses for use in integrated inductors operating in the MHz-GHz range, highly resistive magnetic materials are required with high saturation magnetization, low coercive field and moderate anisotropy field (H_K) [146,147]. FMR loss is due to the spin motion, which arises due to the combination of direct relaxation to the lattice and indirect relaxation via excitation of non-uniform magnetization modes, i.e., spin waves [73]. Therefore, to develop a GHz-level integrated magnetic device working properly near the FMR frequency regime, one needs to design and model such devices particularly to study the spin dynamics and relaxation at that frequency regime [73,147].

Previously, electroplated inductors have been developed with multi-nano-layered structures in CoP thin film, where, phosphorous (P) was added to increase the resistivity and simultaneously achieve amorphousness in materials for integrated circuits [148]. Relatively, thicker nano-structured high-frequency magnetic materials are of paramount importance to achieve high power densities for use in cutting-edge applications. Additionally, the utilization of the electrodeposition technique for developing such films is of foremost importance as it is a low-cost, high-yield process and lends itself around patterned complex nano-topologies [149]. Though thin films of Cobalt Phosphorus alloys (CoP) have been prepared by electrodeposition technique, and have been extensively studied by several groups [150-158] including its dynamic property [155-157,159], the ultrafast magnetization dynamics of CoP thin film has never been reported so far. However, in addressing those aforementioned challenges and enhancing the performance of high-frequency integrated inductors, power delivery systems, energy efficient switching of MRAM bits and future high-speed spin-based devices, it is essential to study the ultrafast dynamics of magnetic materials, including their response to external stimuli and the relaxation processes of the magnetization, which provide a significant insight about their performance at high frequencies.

Optical control of magnetization in ultrafast regime by femtosecond (fs) laser pulse gives two important magnetization dynamics, namely: the ultrafast demagnetization [35] and laser induced magnetization precession. The precessional dynamics allows to explore different anisotropic magnetic properties through the frequency of different dynamical modes such as, the uniform Kittel mode, the PSSW mode, other dispersive modes in a continuous thin-film as well as the damping of the magnetic material. Ultrafast spin dynamics is the key spin manipulation mechanisms relevant for high-speed storage of information. It occurs when a femtosecond laser pulse is incident on a magnetic material and causes transient perturbation of its electron, spin and lattice systems giving rise to an exciting research field called femtomagnetism [160]. The system responds through a rapid quenching of magnetization within sub to few hundreds of femtoseconds, called the ultrafast demagnetization. Subsequently, a fast relaxation occurs through the energy transfer from electron and spin to the lattice subsystem by the phenomenological 3TM. Different mechanisms such as electron-magnon interaction [44], SFS [86], spin-photon interaction [49] and the role of SOC [40,111] were proposed to describe ultrafast demagnetization involving local dissipation of spin angular momentum. Later, a new mechanism based on SST was introduced to explain the enhanced quenching of magnetization in ferromagnetic/nonmagnetic (FM/NM) bilayer systems after laser irradiation [51]. More recently, a mechanism based on optical inter-site spin transfer has been proposed in multi-sub-lattice alloys and multi-layered systems [52]. Although the core mechanism behind ultrafast demagnetization has remained debatable, the co-existence of multiple mechanisms [92,161] has been demonstrated in different systems.

An increase in the lattice temperature after the fast relaxation causes a rapid change in the magneto-crystalline anisotropy triggering the precession of magnetization around an effective magnetic field. The precessional dynamics allows to explore different anisotropic magnetic properties through the frequency of different dynamical modes such as, the uniform Kittel mode, the PSSW mode, and other dispersive modes in a continuous thin-film [129] as well as the damping of the magnetic material [34]. Kittel mode is a coherent SW mode (wavevector, k = 0) that acts as the dominant coherent channel for magnetization relaxation in thin films. For relatively thicker samples (larger than optical penetration depth), SWs excited by a laser pulse propagate through the sample thickness and reflect back from the substrate to form PSSW modes. SWs act as one of the several channels to relax from a highly excited state to equilibrium [162]. The natural relaxation of the precession of magnetization is expressed by the Gilbert damping parameter (α) according to the well-known LLG equation [54,163]. Origin of the intrinsic damping lies in the SOC and band-width of the d band of 3d ferromagnets [164]. Various other intrinsic and extrinsic mechanisms such as eddy current [62], phonon drag [63], capping [22] or doping [65] with another material, two-magnon scattering [165], spin current injection [136] can influence the damping. From an application point of view, lower damping is important for the propagation of spin waves over long distances and energy-efficient switching of MRAM bits [133], while higher damping is useful for the elimination of ringing after magnetic switching [166]. Therefore, the Gilbert damping constant is a very crucial parameter for spintronics applications. Design and control of this parameter are imperative for device engineering. Therefore, the investigation of ultrafast demagnetization as well as spin relaxation and precessional dynamics in soft magnetic materials is a subject of intense interest due to the inherent physical mechanism as well as their potential applications for the development of future high-speed spin-based devices.

By understanding the ultrafast dynamics of magnetic materials, one can gain insights into the underlying mechanisms that affect their behaviour in high-frequency regimes, which can be leveraged to optimize the design and performance of aforementioned emerging technologies. For example, studying the spin dynamics and relaxation processes at ultrafast timescales can provide information on the behaviour of magnetic materials under rapid switching or dynamic conditions, which are prevalent in high-frequency operations. Such understanding can guide the selection of magnetic materials with properties such as high saturation magnetization, low coercive field, and moderate anisotropy field and steer the engineering design for following on highly miniaturized device topologies, which are desirable for minimizing losses at and achieving efficient performances at relatively higher operational frequencies.

As in the relatively lower frequency (sub-MHz – MHz level), the operational frequency is not only limited by the eddy current losses or losses due to the domain wall (DW) movement/rotation but also by spin losses and a decrease of the permeability, as we reach higher frequencies, such as GHz level. Additionally, any inhomogeneities of the magnetic ordering present in the material can result in the coexistence of the different dynamical processes, such as DW assisted dynamical responses and FMR assisted dynamical responses, independent of the orientation of the driving field. Moreover, from practical device applications point of view, study of the lifetime of the spin wave modes is also crucial because the presence of the eddy currents not only restricts the lifetime of the wave but also significantly alters its effective dispersion relation. Hence, to identify the exact nature of the dynamical processes for such highly miniaturized devices operating at ultrahigh frequencies, one needs to understand comprehensively the high-frequency dynamics for accurate evaluation of the spin losses of the system as well.

Here, we have simultaneously measured ultrafast demagnetization and magnetization precession in a soft ferromagnetic CoP alloy by using an all-optical TR-MOKE magnetometry. By systematically varying the in-plane magnetization orientation (φ) with respect to an externally applied magnetic field we have found that the precessional frequency follows a dominant two-fold anisotropy superposed with a moderate four-fold anisotropy, while Gilbert damping coefficient shows a strong four-fold anisotropy. In contrast, ultrafast demagnetization is found to be almost invariant with φ. Our results indicate that the anisotropic variation of precession frequency may stem from the variation of SOC with φ, while the four-fold variation of damping with high value of it has been attributed to the dephasing of the Kittel-like precessional mode with the PSSW and other dissipative modes. For the highly nonequilibrium spin dynamics followed by the laser excitation, role of anisotropic SOC is negligible in its contribution to the ultrafast SFS process [167]. The higher damping is key to reduce the resonance response of power supplies and any associated noise, ringing or oscillations produced by them.

5.2 Experimental details

The following chemicals and reagents [155] are used for preparing smooth, shiny, amorphous CoP thin film utilizing the electrodeposition technique at room temperature (293K): Phosphorus acid (3.30), Phosphoric acid (5.90), Cobalt chloride hexahydrate (18.87), Cobalt carbonate (1.55), Glycine (1.15), Saccharine (1.51), naphthalene trisulfonic acid (NTA) (1.52); values in the parenthesis are amount of the chemicals in g/100 mL. The pH of the bath was ~ 0.72 – 0.86. Initial instability of the electrolytic bath causes somewhat stressed and rough films developed by the electrodeposition, with the other possibility being the high surface tension between the working electrode and the electrolyte. A surface tension-reducing agent, glycine, stress-relieving additives, NTA and saccharine [168,169] have been added to the solution to stabilize the bath and to reduce the surface tension between the working electrode and the electrolyte. Consequently, stress-free, smooth, glossy films are developed. The electrodeposition of amorphous CoP film of 3.173 μm thickness using pulsed-reverse plating (PRP) on 2 × 2 cm^2 Si-wafer with a top conducting seed layer of 20 nm titanium and 200 nm gold has been carried out utilizing CHI 660B potentiostat. Forward and reverse currents have been utilized to develop the sample with PRP.

The elemental characterization and surface topography of the electrodeposited film are investigated using energy dispersive x-ray (SEM-EDX) spectroscopy and AFM. The crystallinity and amorphousness of this electrodeposited sample is characterized by the XRD technique. In-plane magnetic hysteresis loop measurements have been carried out using a hysteresis loop tracer (ShB Instruments, USA; Model: MESA 200).

To study the ultrafast demagnetization and precessional magnetization dynamics of the sample, we have exploited the TR-MOKE technique in polar Kerr geometry based on a two-colour non-colinear pump probe set-up. A part of the fundamental laser beam (wavelength = 800 nm, pulse width = 35 fs, repetition rate = 1 kHz) from a femtosecond regenerative amplifier (Libra, Coherent Inc.) is passed through a second harmonic generator to generate the pump beam (wavelength = 400 nm, pulse width > 35 fs, repetition rate = 1 kHz) for the excitation, while another small part of the fundamental laser beam is used as the probe beam to detect the magnetization dynamics. A time delay between the pump and probe beam is generated by passing the probe beam through a motorized variable delay stage. The fluence of the pump beam is kept much stronger (~ 10 mJ/cm^2) than the probe beam (~ 1.5 mJ/cm^2) during the measurements. An external magnetic field is applied at ~ 30° tilt (indicated as ξ in Figure 2(a)) to the sample plane which is suitable for this sample to introduce a finite demagnetizing field. This tilt of the magnetization is further modified by the pump pulse to launch the precessional dynamics in the sample. The probe beam is incident on the sample normally with a spot size of diameter ~ 100 μm, whereas the pump beam is slightly defocused with a spot diameter of ~ 250 μm and incident obliquely at around ~ 45° angle to the sample plane keeping a proper spatial overlap with the probe spot. We have used an optical chopper to chop the pump beam at 373 Hz frequency and the dynamic signal in the probe beam is detected through the Si detector by using a lock-in amplifier in a phase-sensitive manner. In our experiment we have used 4 ps and 2 ns time windows (time window corresponds to the total duration of measurement of the time-resolved signal), to probe the ultrafast demagnetization (temporal resolution = 25 fs) and damped precessional motion (temporal resolution = 5 ps), respectively.

5.3 Results and discussions

Static Characterization:

In determining the crystallinity or the amorphousness of CoP thin film, phosphorous content plays a key role. Therefore, it is important to study the qualitative and quantitative analysis of phosphorous in the electrodeposited thin film. The energy dispersive x-ray (EDX) spectrum for the electrodeposited Si/Ti (20 nm)/Au (200 nm)/CoP (3.173 μm) sample as shown in Figure 5.1(a) confirms different Co and P peaks. For example, the Co- L_{α} peak originates at 0.77 keV, K_{α} originates at 6.93 keV, and K_{β} is at 7.64, while the 2.13 keV peak is for the P- K_{β} peak. The EDX analysis confirms the presence of Co and P entities in the sample with ~ 87 % and ~ 13 %, respectively. EDX's premium software program, APEX is used for collecting and analysing energy dispersive spectroscopic data and the compositional characterization of the material. It uses ZAF-corrected (Z: atomic number, differences in deceleration of primary electrons; A: absorption, absorption of primary emitted characteristic x-rays; F: secondary fluorescence, generation of secondary x-ray fluorescence by characteristic radiation) spectral analysis for quantitative compositional information. Details of the EDX spectra are listed in Table 5.1.

Table 5.1: Ratio obtained from EDX analysis:

Element	Wt %	At %	K-Ratio	Z	A	F
P-K	7.45	13.28	0.0423	1.1010	0.5148	1.0017
Co-K	92.55	86.72	0.9155	0.9910	0.9982	1.0000
Total	100.00	100.00				

The surface topography of the electrodeposited film is investigated using AFM as shown in Figure 5.1(b). From the AFM image, we have extracted the average roughness of the surface as ~ 6.56 nm. The surface roughness is slightly higher than typical films deposited by physical vapor deposition techniques, but it is substantially small relative to the film thickness (3.173 μm) signifying the efficacy of the bath chemistry (proportion of stress relieving additives etc.) in the plating process.

The crystal structure of this electrodeposited sample is characterized by XRD technique using a 40 kV x-ray source (Rigaku: SmartLab) as shown in Figure 5.1(c). Four characteristic peaks can be observed at 2θ values of 38.2°, 44.6°, 61.7° and 69.1° which could be assigned to Au (111)[170], Co (111)[171], Si (004) [172] and Si (004) [173] plane, respectively. The very small standard diffraction peak of Co suggests mainly the face-centred cubic (*fcc*) structure of Co [171]. This peak is not sharp because of the amorphous nature of the material in the presence of P. Therefore, the system could be considered as a nano-hetero-structured system where tiny nanocrystalline Co-fcc phases are embedded in the amorphous CoP phase.

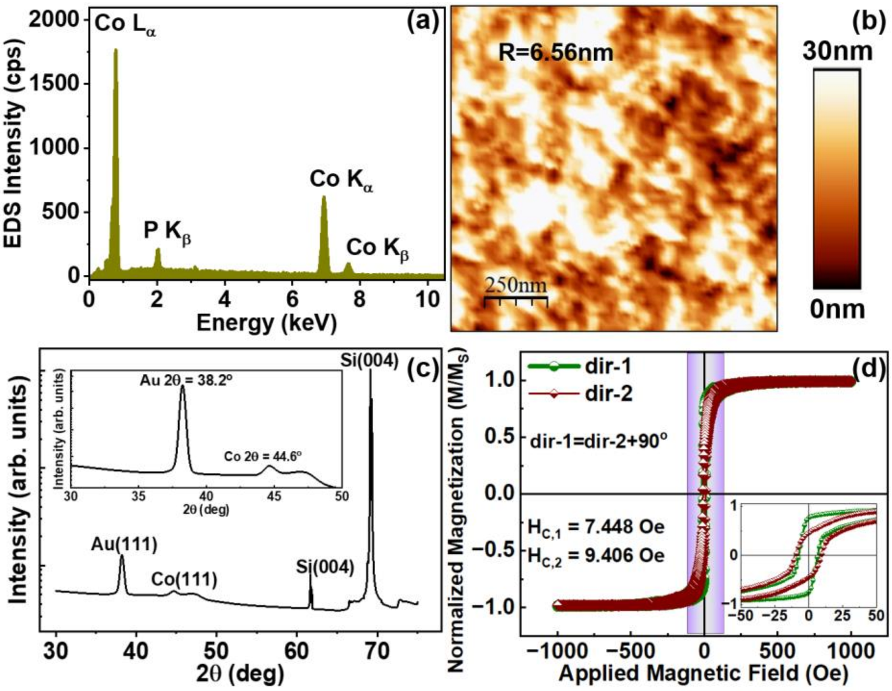

Figure 5.1: (a) Typical EDX spectrum of the sample at room temperature showing the presence of Co and P. (b) AFM image showing the surface topography of the sample. (c) X-ray diffraction pattern showing the amorphous property with nanocrystalline Co-fcc phase. (d) Typically measured static in-plane hysteresis loop at two different in-plane directions showing anisotropic nature of the sample, here, dir.-2 = dir.-1+90°. Inset: magnified hysteresis loop.

TRMOKE Measurement of Ultrafast Spin Dynamics:

The ultrafast spin dynamics of this electrodeposited film has been measured using an all-optical TR-MOKE magnetometry [34] in a non-collinear optical pump-probe geometry. The experimental measurement geometry in polar TR-MOKE configuration is shown in Figure 5.2(a). The optical pump-probe technique uses femtosecond (fs) laser pulses (pump) to excite the sample and to probe the ensuing dynamics in terms of the polar Kerr rotation (θ_k) of the sample as a function of the time delay between the pump and probe pulses. In the polar Kerr geometry, θ_k is proportional to the change of the out-of-plane component of the magnetization.

Figure 5.2(b) shows a typical TR-MOKE trace from CoP containing three different temporal regimes. When a femtosecond laser is incident on a ferromagnetic sample placed in an external magnetic field, a rapid quenching of magnetization is observed just after the zero delay (i.e., when pump and probe beams are incident simultaneously on the sample). This phenomenon is known as ultrafast demagnetization. This is followed by a fast remagnetization within a few picoseconds (ps) due to spin-lattice relaxation. Change in the lattice temperature changes magneto-crystalline anisotropy which acts as a pulsed magnetic field and triggers the precession of magnetization of the sample. The heat diffusion from lattice to surroundings corresponds to longer relaxation within hundreds of ps time range. In this timescale the magnetization precession damps out.

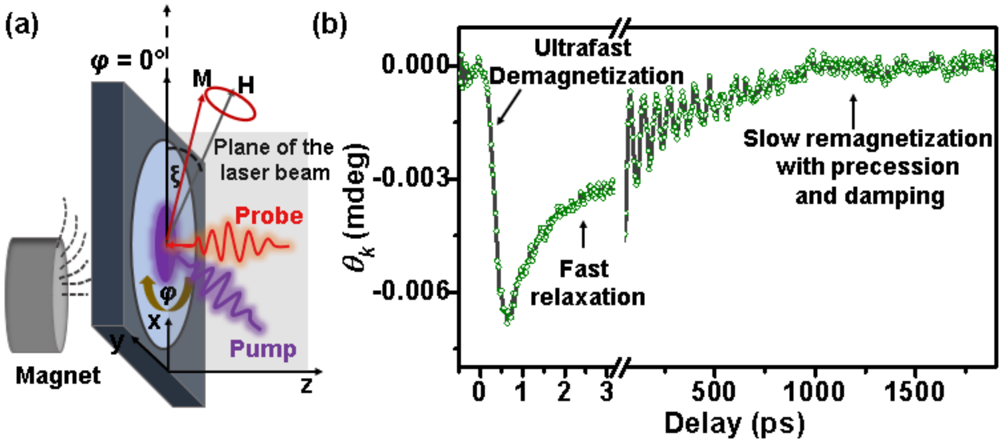

Figure 5.2: (a) Schematic of experimental geometry, sample is in x-y plane and x-z is the plane of the laser beam and (b) typical TR-MOKE data from Si/Ti (20 nm)/Au (200 nm)/CoP (3.173 μm) sample at an external bias magnetic field of 1.35 kOe. The three important temporal regimes at pump fluence of 17.5 mJ/cm^2 are indicated in the graph.

After subtraction of a bi-exponential background from the precessional oscillation in the Kerr rotation data, we obtain a damped oscillatory motion. Figure 5.3(a) shows the damped Kerr oscillation in the polar Kerr geometry at an external magnetic field of 1.35 kOe for three different in-plane angles of 15°, 60° and 135° w.r.t. the x-axis along the x-y sample plane in the clock-wise direction. The precessional oscillation is fitted to the equation,

$$\theta_k = \sum_{i=1}^{n} A_i e^{-t/\tau_i} \sin\left(2\pi f_i t + \delta_i\right) \tag{5.1}$$

Where n is the number of modes, and A_i, τ_i, f_i and δ_i are initial precessional amplitude, decay time, resonance frequency and initial phase shift of the i^{th} mode. When there is more than one clear SW modes ($1 \leq n \leq 3$), this expression is used to fit the time-resolved magnetization curves. The frequency of precession can be extracted by performing the fast Fourier transform (FFT) of the Kerr rotation data. Figure 5.3(b) shows the FFT spectra containing the magnetic modes corresponding to those three different in-plane angles. From these three angles we can see that there is a clear frequency shift in magnetic modes from one angle to another. This gives a signature of the existence of magnetic anisotropy in the system. Also, we observed that FFT spectrum for 15º and 60º orientation contain a single clear peak whereas the other angle (135º) contains two dominant peaks.

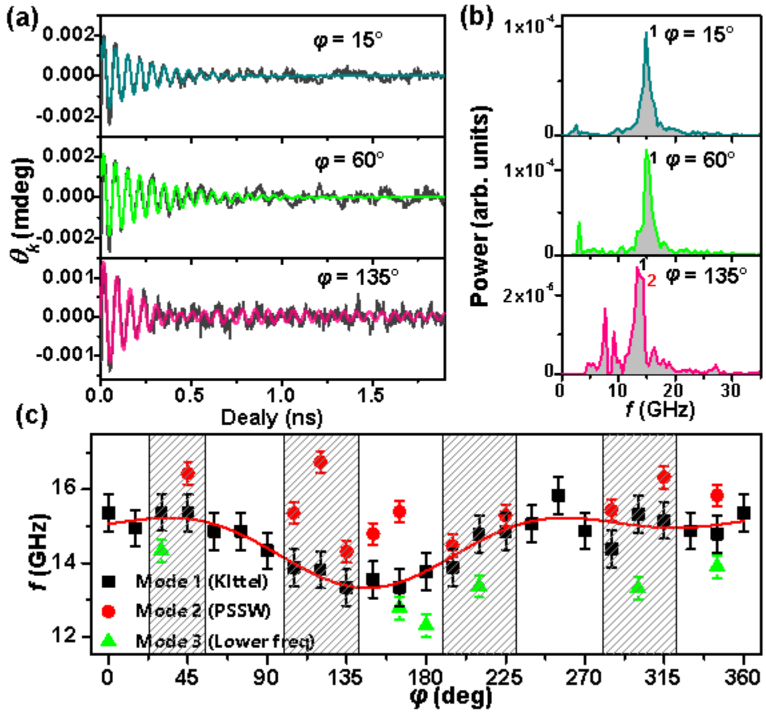

Figure 5.3: (a) Background subtracted time-resolved Kerr rotation data for external magnetic field of 1.35 kOe applied along three different in-plane angles (15º, 60º and 135º, respectively w.r.t. the x-axis along x-y plane) at a fixed pump fluence of 10 mJ/cm^2. The solid-coloured lines are fitted curves using the damped sine function. (b) FFT spectra corresponding to three different angles showing the magnetic modes. (c) In-plane angle dependent precessional frequency at the same external magnetic field of 1.35 kOe. The solid line is fitted the Kittel mode. i.e., equation 5.2.

To investigate the anisotropic magnetic behaviour more precisely, we have investigated the magnetic modes by continuously rotating the in-plane bias-field angle (φ) at 15º interval at an external magnetic field of constant magnitude of 1.35 kOe at a pump fluence of 10 mJ/cm^2. Figure 5.3(c) displays that the most dominated precessional mode shows a combination of two-fold and four-fold anisotropy terms. Thus, we have fitted its frequency (f) variation with φ using the following equation [174]:

$$f = \frac{\gamma}{2\pi}\left\{\left[H + \frac{2K_2}{M_s}\cos 2\varphi - \frac{4K_4}{M_s}\cos 4\varphi + \frac{2A}{M_s}\left(\frac{n\pi}{d}\right)^2\right] \times \left[H + 4\pi M_s + \frac{2K_2}{M_s} cos^2 2\varphi - \frac{4K_4}{M_s}(3 + \cos 4\varphi) + \frac{2A}{M_s}\left(\frac{n\pi}{d}\right)^2\right]\right\} \qquad (5.2)$$

Where f is the precessional frequency, $\gamma = \frac{g\mu_B}{\hbar}$ =1.76 ×10^7 rad/(s.G) is the gyromagnetic ratio, H =1.35 kOe is the bias magnetic field and M_s is the saturation magnetization. K_2 and K_4 indicate the two-fold and four-fold anisotropy constants. A, d and n are exchange stiffness constant, thickness of the film and order of PSSW mode, respectively. Here, we have fixed $n = 0$, since the most dominating mode here is the uniform Kittel mode. The estimated value of M_s is obtained as ~1350 emu/cc, which matches closely with the reported value for bulk Co [175]. We have cross checked this value from another independent measurement of the magnetic hysteresis loop measured along the hard axis of the sample and obtained the value of M_s as ~1129 emu/cc. The slightly lower value of M_s obtained from the hysteresis loop tracer can be attributed to the errors in evaluating the sample volume. The value of uniaxial anisotropy constant is found to be 1.1×10^5 erg/cc superposed with a weaker four-fold anisotropy constant of 0.3×10^5 erg/cc. Subsequently, we have fitted the magnetic field dispersion of the precessional frequencies for three different values of φ, i.e., 45°, 90° and 150° as shown in Figure 5.3(b) using the same equation, i.e., equation 5.2. In this case we have fitted f as a function of H, keeping the in-plane angle φ fixed at particular value, i.e., 45°, 90° or 150°. We have kept the value of sample thickness, d = 3.173×10^{-4} cm as constant parameter and K_2, K_4 are fixed at the obtained value from the fit as given above. Mode 1 is fitted with $n = 0$ and by leaving g and M_s as fitting parameters. While g is found to be constant at 2.0 ± 0.1 and M_s is ~1350 ± 50 emu/cc for three different angles. With the same $M_s$value for three different angles, mode 2 can be fitted for $n = 1$.

Additionally, the value of uniaxial anisotropy, K_2 can be calculated from the hard-axis hysteresis loop using the expression: $K_2 = \frac{1}{2} H_S M_S$. Here the saturation field, H_S~ 200 Oe and saturation magnetization M_S~1129 emu/cc. The value of K_2 is calculated to be ~ 1.13×10^5 erg/cc, in good agreement with the value obtained from the fit.

The magnitude of bias magnetic field is systematically varied to obtain field dispersion of the precessional frequencies for three different values of φ, i.e., 45°, 90° and 150° at a fixed pump fluence of 10 mJ/cm^2. The number of peaks varies with the magnitude and orientation of the bias field. The FFT power spectra of the time-resolved Kerr rotation traces for varying bias field at φ = 45° is shown in Figure 5.4(a). Two to three modes with reasonable power are observed in the spectra whose frequencies decrease with decreasing field. The evolution of f with bias field strength for three different values of φ are plotted in Figure 5.4(b) which are fitted using equation 5.2 while M_s, K_2 and K_4 are fixed at the values obtained from the fit. From

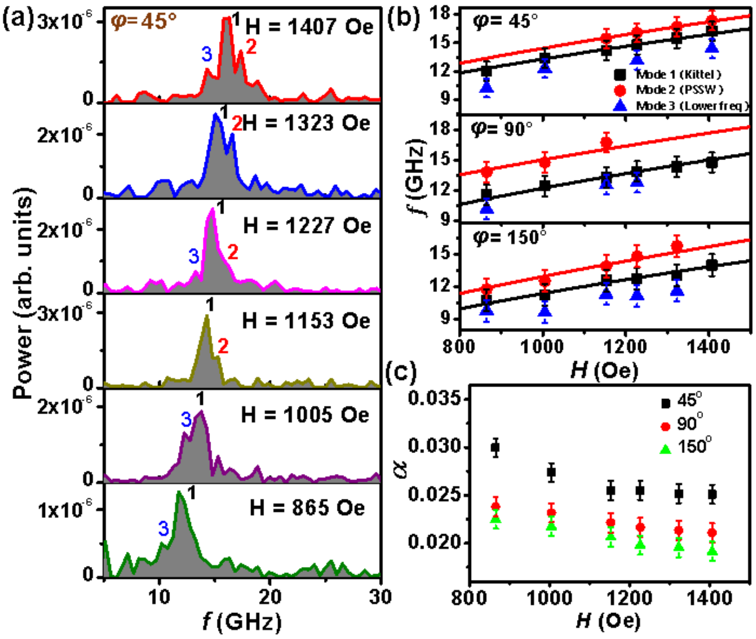

Figure 5.4: (a) FFT power spectra of time-resolved Kerr rotation traces at different strengths of the applied bias field at a fixed pump fluence of 10 mJ/cm^2 for φ = 45°. (b) Bias magnetic field dependent frequency of precessional modes at φ = 45°, 90° and 150°, black and red solid lines are the fitted results with equation 5.2 for n = 0 and n = 1, respectively. (c) Bias field dependent Gilbert damping constant of the Kittel mode at φ = 45°, 90° and 150° reveals the suppression of extrinsic effects at higher field.

the fit, we understand that mode 1, i.e., the most intense mode, is the uniform Kittel mode (n = 0), while mode 2 is the first order PSSW mode (n = 1). The value of the exchange stiffness constant A is found to be 1.9×10^{-6} erg/cm from the fit of PSSW mode, which agrees reasonably well with the previously reported values of crystalline Co [176,177]. At some values of φ, the dominant Kittel mode supresses other precessional modes. We have also observed a low frequency mode adjacent to the Kittel mode. The systematic variation of the mode frequencies with bias magnetic field confirms the magnetic origin of these modes. The magnetic field dispersion of the lowest frequency mode could not be fitted well with Kittel equation having reasonable magnetic parameters probably because of its origin in the magnetic inhomogeneity of the system. This magnetic inhomogeneity may lead to TMS [32] causing an enhancement of damping.

We have extracted the effective Gilbert damping (α) coefficient of the Kittel mode by using the expression:

$$\alpha = \frac{1}{\gamma\tau(H+H_1+H_2)} \tag{5.3}$$

Where $H_1 = \frac{K_2}{M_s}\cos 2\varphi - \frac{2K_4}{M_s}\cos 4\varphi$ and $H_2 = 2\pi M_s + \frac{K_2}{M_s}cos^2 2\varphi - \frac{2K_4}{M_s}(3+\cos 4\varphi)$. Here τ is the decay time of the magnetization precession and other parameters have their usual meaning. The effective damping consists of both intrinsic and extrinsic contributions. The damping as a function of H is plotted in Figure 5.4(c) for three different values of φ. Effective α is found to decrease with increasing frequency and becomes nearly constant for $H > 1.15$ kOe, as reported previously. This means a field above 1.15 kOe is high enough to supress all extrinsic effects contributing to the damping. At $\varphi = 45°$ (Figure 5.5(a)), the higher frequency precessional mode is found to be supressed in the low field regime, and the lower frequency mode and the Kittel mode dominate. Thus, the enhancement of α in the lower field regime can occur due to dominant TMS effect. For other two angles, the PSSW mode is present in the lower field regime too. However, we found it to be nontrivial to isolate different contributions to the damping, including TMS, in this study.

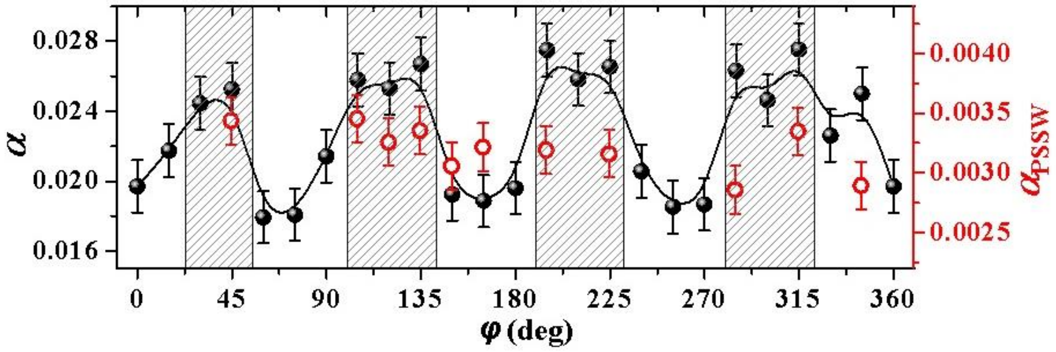

Figure 5.5: The variation of α of Kittel modes (solid black scattered points) and PSSW modes (open red scattered points) with different in-plane angles at an external bias magnetic field of 1.35 kOe with the pump fluence of 10 mJ/cm^2. Black solid line is guide to eye.

To investigate the anisotropic behaviour of damping, the angular dependence of effective damping was extracted, as shown in Figure 5.5 corresponding to the Kittel mode and the PSSW mode of Figure 5.3(c). Large in-plane four-fold anisotropic behaviour of damping is observed for the Kittel mode. Angular regimes with higher damping value are marked by black shade in Figure 5.5, those regimes are containing richer number of modes along with the Kittel mode (Figure 5.3(c)). Enhancement of α at some angles is found to be due to the mutual dephasing of PSSW and the low frequency mode with the Kittel mode (shown in Figure 5.6) which opens up additional energy dissipation channels [162]. The damping parameter corresponding to the PSSW mode (α_{PSSW}) wherever present is shown in Figure 5.5 with open circle symbol. The anisotropic behaviour of α has been theoretically predicted previously based on breathing Fermi-surface model [178,179]. This has been shown experimentally not only in ferromagnetic metals [180], but also in alloys [74]. From the ratio of K_2 and K_4, it can be found that the electrodeposited CoP film shows ~80% two-fold and ~20% four-fold anisotropy in precession frequency coupled with a four-fold anisotropic damping. Such anisotropic GHz-frequency precessional dynamics can be crucial for various high-frequency applications such as frequency selectivity can be achieved without replacing the magnetic film and only by rotating the film for any input information for radio frequency signals and spintronic resonators [181]. Moreover, anisotropy of damping will enable to design future spintronic devices. The higher damping of the CoP film will be useful for increasing the switching speed for high-speed magnetic recording devices and to reduce the noise in power supply devices.

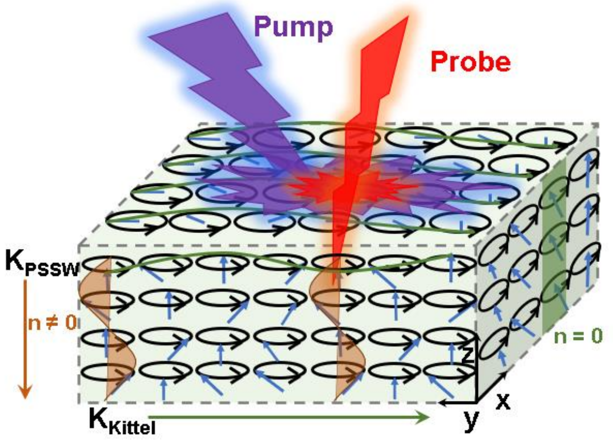

Figure 5.6: A schematic representing the formation of standing wave along the thickness of the sample and the mutual dephasing of PSSW and low frequency mode with the Kittel mode.

To understand the faster dynamics, i.e., ultrafast demagnetization and its dependence on the in-plane angle of bias magnetic field, we have explored the time-resolved Kerr rotation in the CoP film as a fixed pump fluence fixed of 10 mJ/cm^2, bias field strength of 1.35 kOe and by rotating the sample at 15° interval w.r.t. the bias field orientation. A phenomenological expression obtained from the well-known 3TM [50] is used to fit the ultrafast demagnetization and the fast remagnetization in the time-resolved Kerr traces as given below:

$$\frac{-\Delta \mathrm{M}}{\mathrm{M}} = \left[\left\{\frac{A_1}{(t/\tau_0+1)^{\frac{1}{2}}} + \frac{A_1\tau_m - A_2\tau_e}{\tau_e-\tau_m} e^{-t/\tau_m} + \frac{A_2\tau_e - A_1\tau_e}{\tau_e-\tau_m} e^{-t/\tau_e}\right\} H(t) + A_3\delta(t)\right] \otimes G(t) \qquad (5.4)$$

The assumption behind this expression is instantaneous increase of electron temperature upon laser excitation to generate hot electrons. By electron-magnon interaction hot electrons excite spins and quench the magnetization [44]. Following that, the quenched magnetization tries to recover its magnetization by distributing energy between three reservoirs, i.e., electron, spin and lattice subsystems. In the above expression A_1 represents the value of recovered magnetization after fast remagnetization, A_2 represents amount of magnetization quenching which is proportional to the initial rise in electron temperature and A_3 represents the magnitude of state filling effect during pump-probe overlap established by a Dirac delta function ($\delta(t)$). τ_0 is the cooling time by heat diffusion during the electron-phonon interactions. $H(t)$ and $G(t)$ are the Heaviside step function and Gaussian function. The first exponential term describes the time scale of ultrafast demagnetization time (τ_m) while the second exponential term indicates the electron-phonon interaction by fast remagnetization time (τ_e).

As shown in Figure 5.7(a), τ_m is nearly invariant for all in-plane bias-field orientation φ, revealing an isotropic behaviour. Conventionally, ultrafast demagnetization is described by EY type electron-phonon SFS led by spin-mixing due to SOC. Unlike the FM/NM heterostructures, here there is no interface and the ensuing difference in spin chemical potential [92], and hence super diffusive spin transport will not be responsible for ultrafast demagnetization [161]. Although the actual explanation behind isotropic ultrafast demagnetization is not well understood, the possible mechanism can be EY-like electron-electron coulomb scattering, proposed by Krauβ *et al*. [47] which is not (quasi)elastic scattering unlike electron-phonon or electron-defect scattering. This inelastic scattering diminishes the dependence of SF probabilities on the spin-mixing and anisotropic SOC, resulting isotropic ultrafast demagnetization. Moreover, recent photoemission spectroscopy in Ni [182,183] has revealed that highly non-equilibrium transient phase transition contributes a crucial role through sufficient energy transfer from optical excitation to the spin systems within a shorter timescale than ultrafast demagnetization. Over a longer time both experimental and theoretical works [184,185] have suggested that low energy magnon generation in femtosecond timescale by hot electrons provide a significant contribution in ultrafast SF processes, i.e., ultrafast demagnetization. Therefore, ultrafast demagnetization may have no dependence on the

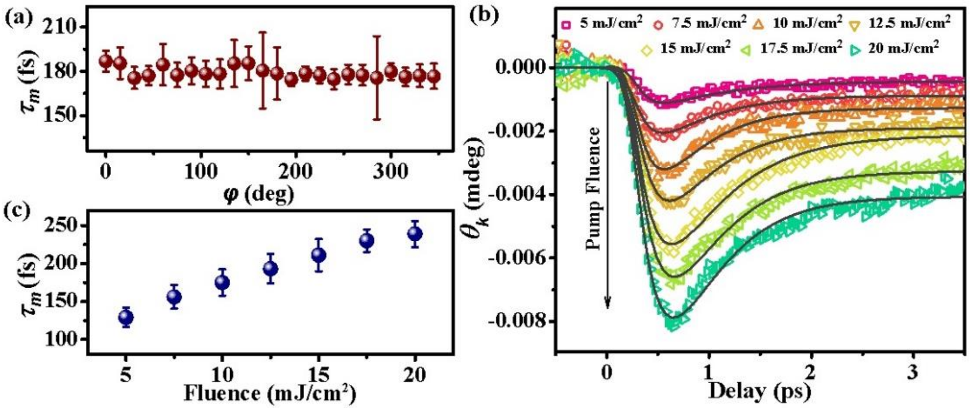

Figure 5.7: (a) Variation of τ_m with the in-plane angle φ of bias magnetic field at a fixed pump fluence of 10 mJ/cm^2 showing isotropic behaviour. (b) Time-resolved Kerr rotation traces containing ultrafast demagnetization and fast remagnetization. (c) Variation of τ_m with pump fluence.

anisotropic SOC of equilibrium state and shows nearly isotropic behaviour. Figure 5.7(b) shows the ultrafast demagnetization curve with varying pump fluence ranging from 5 mJ/cm^2 to 20 mJ/cm^2, while the probe fluence is kept constant at 1 mJ/cm^2. All the experimental data are fitted using equation 5.4. We observe that the demagnetization time increases linearly with fluence, as shown in Figure 5.7(c), due to the enhancement of spin fluctuation at elevated temperature [131].

We have numerically solved the phenomenological 3TM and reproduced the experimental data at different pump fluences obtained from the TR-MOKE magnetometry to have further insights about the ultrafast demagnetization phenomenon. The three phenomenological coupled differential equations are written as:

$$C_e(T_e)\frac{dT_e}{dt} = -G_{el}(T_e - T_l) - G_{es}(T_e - T_s) + P(t) \tag{5.5a}$$

$$C_s(T_s)\frac{dT_s}{dt} = -G_{sl}(T_s - T_l) - G_{es}(T_s - T_e) \tag{5.5b}$$

$$C_l(T_l)\frac{dT_l}{dt} = -G_{sl}(T_l - T_s) - G_{el}(T_l - T_e) \tag{5.5c}$$

Where T_e, T_s and T_l are temperature of electron, spin and lattice bath, respectively. Initial temperatures are kept at room temperature, i.e., 300 K. C_e, C_l and C_s are the electron, lattice and spin contribution to the specific heat. Electronic specific heat is proportional to the electron temperature, i.e., $C_e = \gamma T_e$, where γ = 0.7×10^3 Jm^{-3}K^{-1}. G_{el}, G_{es} and G_{sl} are the electron-lattice, electron-spin and spin-lattice coupling strength constant, which reciprocate energy transfer rate from electron to lattice, spin and spin to lattice system. Initial electronic excitation is expressed by adding the laser source term, $P(t)$ to equation 5.5a only. The spin temperature is then fed into the mean-field theory to reproduce the transient change in magnetization as obtained in the experiment. The modelled result and temporal evolution of three different baths at 7.5 mJ/cm^2 fluence are shown in Figure 5.8(a) and Figure 5.8(b), respectively.

We have enlisted different parameters obtained from 3TM in Table 5.2 below.

Table 5.2: Parameters obtained from 3TM as a function of pump fluence:

Fluence (mJcm^{-2})	**C$_s$ (× 10^5 Jm^{-3}K^{-1})**	**C$_l$ (× 10^6 Jm^{-3}K^{-1})**	**G$_{el}$ (×10^{17} Wm^{-3}K^{-1})**	**G$_{es}$ (×10^{17} Wm^{-3}K^{-1})**	**G$_{sl}$ (×10^{17} Wm^{-3}K^{-1})**
5	2.1	1.5	5.5	8.4	0.65

7.5	1.8	1.3	4.6	8	0.4
10	1.2	1.1	4.5	7.5	0.4
12.5	1.15	1.1	4.4	6.6	0.4
15	1	1.2	4.1	6.3	0.35
17.5	0.9	0.95	4	5	0.5
20	0.85	0.95	3.2	4.4	0.6

The results clearly demonstrate that (Figure 5.8(c)) faster ultrafst demagnetization at low pump fluence corresponds to higher electron-spin coulping strength (G_{es}). With the increase of fluence the electronic temperature increases which follows higher spin fluctuation, reducing the electron-spin coupling strength and demagnetization rate. G_{el} and G_{sl} determine the decay of electron and spin temperature to the lattice.

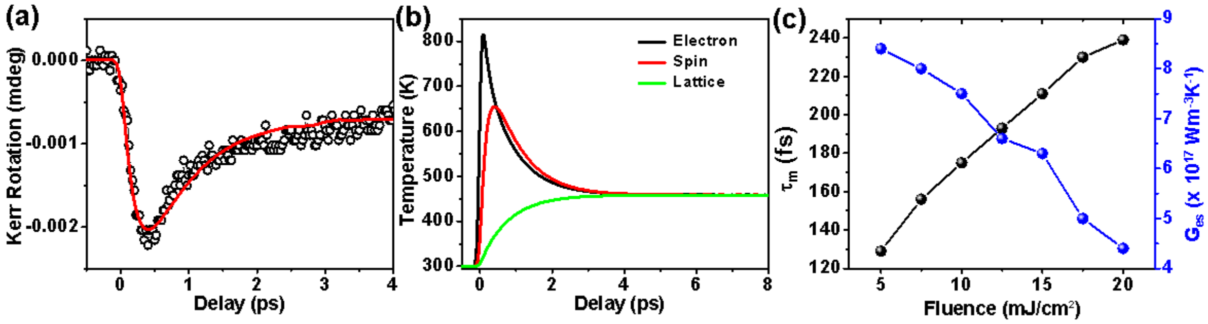

Figure 5.8: (a) Ultrafast demagnetization data fitted with 3TM and (b) temporal evolution of electron, spin and lattice temperature at 7.5 mJ/cm^2 fluence for Si/Ti (20 nm)/Au (200 nm)/CoP (3.173 μm) film heterostructure. (b) Variation of τ_m and G_{es} with pump fluence variation.

5.4 Conclusion

In conclusion, we have experimentally investigated the time-resolved spin dynamics in electrochemically deposited CoP alloy film using the all-optical TR-MOKE magnetometry to explore possible anisotropy in magnetization precession and damping as well as ultrafast demagnetization w.r.t. in-plane magnetization orientation of the sample. The magnetization precession frequency obeys a stronger two-fold anisotropy superposed with a weaker four-fold anisotropy, while the Gilbert damping follows a four-fold anisotropic nature. This typical anisotropic precession may stem from the variation of SOC at equilibrium. The strong four-fold anisotropic Gilbert damping can be attributed to the additional dissipation channel due to the presence of the PSSW mode and another lower-frequency mode along with the Kittel mode, which causes mutual dephasing of precession. The ultrafast demagnetization time is found to be nearly invariant with the in-plane magnetization orientation, indicating that the role of anisotropic SOC is negligible in a highly nonequilibrium state after laser excitation. Our work provides important experimental results regarding to ultrafast demagnetization and Gilbert damping in a new soft magnetic system for possible future applications and opening new avenues for further investigation.

CHAPTER 6

Manipulating Ultrafast Magnetization Dynamics of Ferromagnets using the Odd-Even Layer of Two-Dimensional Transition Metal Dichalcogenides

6.1 Introduction

Despite countless fascinating characteristics of graphene, the lack of intrinsic spin-orbit coupling in graphene has led to the discovery of two-dimensional (2D) TMDs MX_2, where M is a transition metal and X is a chalcogen atom. Different TMDs have rapidly emerged during the last decade due to their potential for a wide range of applications and rich physics. Among them, the group-VI TMDs (M = W, Mo and X = S, Se, Te) have shown unique electronic band structure properties depending on the layer number [186-189]. A monolayer (ML) of a TMD corresponds to half a unit cell of the bulk crystal, implying that the mirror inversion symmetry is broken in odd number of layers. The top of the valence band and the bottom of the conduction band consist of two inequivalent Q valleys in addition to the splitting at K and K′ points of the hexagonal Brillouin zone [187] in TMDs. Due to the lack of inversion symmetry in odd number of layers, the charges on the M and X atoms generate local in-plane electric fields and cause spin-orbit interaction which is strong enough to orient the spins in the bands perpendicular to the ML. Thus, this effect imitates a perpendicular magnetic field causing a giant Zeeman splitting of valleys that become fully spin polarized [190]. Based on the possibility to manipulate this valley degree of freedom, the concept of valleytronics [191] has emerged providing alongside with the SOC due to the *d* orbitals of the heavy metal atom, a way for spin manipulation. These effects lead to spin and valley coupled physics (spin-valleytronics), such as the valley Hall effect accompanied by the spin Hall effect [192,193], suppression of spin and valley relaxation [194] etc. Rather than the widely used electrical [195,196] and magnetic [197] methods, joint theory-experiment reports have shown that the spin-valley polarization and intervalley coupling of excitonic states in different valleys can be accessible through optical excitations [198]. Several theoretical [194,199] and experimental [200] reports have drawn attention to the combination of 2D TMDs with strong SOC with a 3*d* FM to modify the magnetic properties of the FM layer and to promote layer number dependent properties of the heterostructure [161]. This layer number dependence is one of the unique characteristics of

TMDs, which is however not yet been fully explored. Thus, it is essential to carry out a comprehensive study of the magnetization dynamics (via optical excitation) at ultrafast timescales of the layered TMDs as a function of the layer number. Previous reports suggest that the strong SOC promotes transfer of spin angular momentum within the spin system and plays important role in manipulating the ultrafast demagnetization time (τ_m), spin switching and spin-wave propagation [35,50,92,161,201].

An all-optical study of magnetization dynamics using a pump-probe technique based on TR-MOKE microscopy is one of the best tools that can provide a detailed understanding of the role of TMD materials on a FM at the time scale of one billionth of a second [35] and magnetization precession associated with damping from picoseconds to sub-nanosecond timescale. Due to broken inversion symmetry [202] interband optical transitions will have a strong impact on magnetic damping [203] vis-à-vis ultrafast demagnetization. During the optical excitation in the TMDs, valley dependent charge [204] transfer is the mechanism underpinning AOS [205] and hence ultrafast demagnetization. However, the microscopic mechanism and the role of spin valley coupling has not been studied in detail for TMD based heterostructures.

In this work, we report the fluence dependent ultrafast demagnetization (τ_m) and damping (α) in WS_2 (n_{ML}= 0, 1, 2, 3, 4, 5)/Co_3FeB (6 nm)/Al (4 nm) thin film heterostructures by using the all-optical TR-MOKE technique. Compared to other TMDs, WS_2 has high spin-orbit coupling, better thermal stability, high field effect mobility [206]. Their foremost stability with strong in-plane bond and ability to form hybrid interfaces without any lattice matching make them potential 2D materials for magnetic information storage to atomically thin limit. From the modulation of damping with pump laser fluence for different WS_2 layer number, it is observed that the broken inversion symmetry for odd number of layers leads to interband transitions, whereas even layers are governed by intraband transitions. We have extracted the dominant contributions for the ultrafast demagnetization by correlating τ_m and α. In case of n_{ML}= 0 (bare FM layer), both the ultrafast demagnetization and damping are governed by the SFS of the $3d$ itinerant electrons by impurities or quasiparticles. For odd number of layers, SFS dominates for the entire fluence range, while for even number of WS_2 layers, spin pumping dominates at low fluences but with the increase of laser fluence SFS overshadows spin pumping. This study provides detailed understanding of the magnetization dynamics as well as enabling a non-volatile control of the ultrafast relaxation based on the layer number.

6.2 Experimental details

Controlled WS_2 layers were prepared by the combined process of ion beam sputtering and subsequent plasma sulphurization of W films on thermally oxidized Si substrates. A detailed sulphurization recipe can be found in other reports [207]. After growth of the WS_2 films, the samples were transferred back to the ion beam sputtering chamber for growth of 6-nm-thick Co_3FeB thin films at room temperature. The details related to the deposition of Co_3FeB can be found in a previous report [203]. Following that a 4-nm-thick Al layer was deposited as a capping layer to prevent the surface from degradation. Thus, the heterostructure stacks consist of the following layers from bottom to top: Sub//WS_2 (n_{ML}= 0,1,2,3,4,5)/Co_3FeB (6 nm)/Al (4 nm), where the nominal thicknesses are given in the parentheses. For simplicity, the heterostructures are described as WS_2 (n_{ML})/Co_3FeB throughout the manuscript. The film thickness and roughness were obtained by XRR measurements and a ML of WS_2 corresponds to ~ 9Å thickness and WS_2 layer numbers are confirmed by Raman spectroscopy shown in Supplementary Information.

The static magnetic properties (see Supplementary Information) of the samples were measured using a VSM, whereas the magnetization dynamics were investigated using a two colour non-collinear pump-probe based TR-MOKE technique. The TR-MOKE set-up consists of a femtosecond regenerative amplified laser system with a central wavelength of 800 nm, pulse width of ~35 fs and repetition rate of 1 kHz. A part of this fundamental laser beam is passed through a second harmonic generator to double its frequency and generate the pump laser of wavelength 400 nm, pulse width of >35 fs with identical repetition rate. The magnetization dynamics is excited by an intense pump beam (fluence between 2.5 and 15 mJ/cm^2) whereas a small part of the rest of the fundamental laser beam (fluence of 1 mJ/cm^2) is used as a probe beam to measure the magnetization dynamics by detecting the transient Kerr rotation signal. In our TR-MOKE experiment, the pump beam is incident at 45° angle to the sample plane and focused to a spot having diameter of ~250 μm. The probe beam is tightly focused to a spot of diameter ~100 μm and is incident normally on the sample plane located at the centre of the pump spot to detect the dynamics only from a uniformly excited region of the sample. The probe beam is polarized and chopped at a frequency of 373 Hz using an optical chopper right before reaching the sample. The transient Kerr rotation is detected in the probe beam through an analyzer and a Si detector by using a lock-in amplifier in a phase sensitive manner. The output frequency from the optical chopper is used as the reference frequency for the lock-in amplifier. An external magnetic field (titled by ~10° out of the sample plane) is applied to introduce a finite out-of-plane demagnetizing field, which is modulated by the pump beam to induce precessional dynamics in the samples.

6.3 Results and discussions

Static characterization

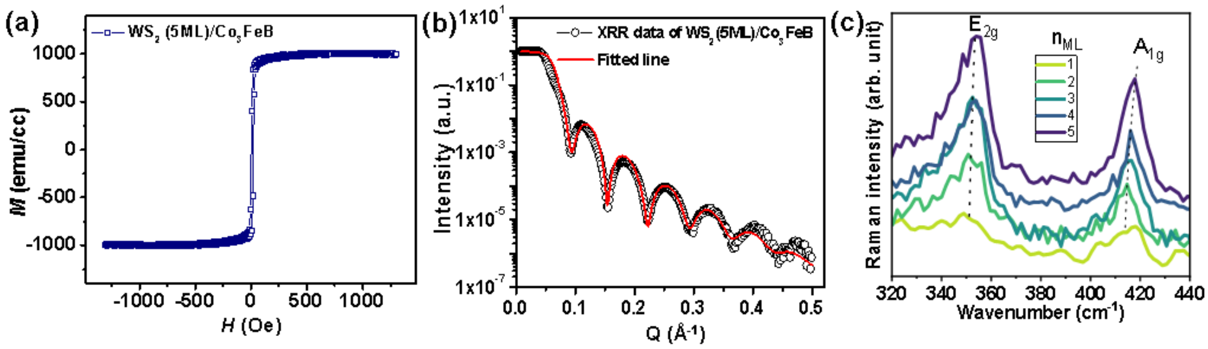

Figure 6.1: (a) Static in-plane magnetic hysteresis loop, (b) x-ray reflectivity spectrum from WS_2 (5 ML)/Co_3FeB (6 nm) heterostructure and (c) Raman spectra of WS_2 for 1 - 5 layers. Dotted lines indicate the peak shift with layer numbers.

A room temperature IP magnetic hysteresis loop of the WS_2 (5 ML)/Co_3FeB heterostructure, measured using VSM (Quantum Design PPMS, Dynacool-9T system), is shown in Figure 6.1(a). The small value of the saturation field is evidence of an IP magnetic easy axis with negligible OOP configuration. The small value of the coercive field, $H_c \sim 1.4$ Oe indicates the soft ferromagnetic nature of the heterostructure.

Figure 6.1(b) shows the XRR spectrum of WS_2 (5 ML)/Co_3FeB heterostructure measured using a 1.54 Å Cu-Kα x-ray source. The XRR spectrum exhibits well defined oscillations up to a scattering vector of 0.5 Å^{-1} signifying uniform deposition. The ‘Reflex’ software was used to analyze the XRR spectra from where we have extracted the thickness, SLD and roughness of the different layers. The SLD is proportional to the electron density of the material. The values of the layer thicknesses obtained from the fits are found to be close to their nominal thickness values. The interfacial roughness and SLD obtained from the fits are tabulated in Table 6.1.

Table 6.1: Parameters obtained from the XRR analysis of WS_2 (n_{ML})/Co_3FeB heterostructures.

Heterostructure	**Layer**	**Thickness (nm)**	**Roughness (nm)**	**SLD (10^{-5}Å^{-2})**
Co_3FeB	Al	5.5	1.1	2.635
	Co_3FeB	6.3	0.5	8.087
	Sub	-	0.17	2.067
WS_2(1ML)/Co_3FeB	Al	5.1	1.2	2.112
	Co_3FeB	6.2	0.3	8.588

	WS_2	1	0.4	4.817
	Sub	-	0.9	2.014
WS_2(2ML)/Co_3FeB	Al	4	0.4	2.112
	Co_3FeB	8	0.4	8.588
	WS_2	1.8	0.3	4.066
	Sub	-	1.9	2.014
WS_2(3ML)/Co_3FeB	Al	4.6	0.9	2.379
	Co_3FeB	8	0.4	8.85
	WS_2	2.8	0.2	4.434
	Sub	-	0.3	2.492
WS_2(4ML)/Co_3FeB	Al	4.3	0.38	2.635
	Co_3FeB	4.7	0.1	8.088
	WS_2	3.8	0.3	7.15
	Sub	-	0.45	2.067
WS_2(5ML)/Co_3FeB	Al	4	1.12	2.635
	Co_3FeB	4.2	0.3	6.869
	WS_2	4.44	1.3	7.15
	Sub	-	0.57	2.067

Raman spectroscopy has been performed to accurately identify the number of WS_2 layers using a solid-state laser based LABRAM HR Evolution instrument with 600 lines/mm spectral resolution. We used 532 nm laser excitations, keeping the laser power 1.15 mW at all times. A_{1g} mode blueshifts with the increase of WS_2 layer number (Figure 6.1(c)) that is consistent with the increase of restoring force caused by the interlayer van der Waals interactions. The low intensity peak at low wavenumber corresponds to the out-of-plane acoustic phonon mode. The blueshift of A_{1g} and redshift of E_{2g} are the proof of the formation of 1, 2, 3, 4, 5 ML. Observation of Raman peaks in all samples is indicative of the crystalline nature of WS_2.

TR-MOKE measurements:

A schematic of the TR-MOKE set up is depicted in Figure 6.2(a) along with the sample stack shown in Figure 6.2(b). A typical laser induced time resolved magnetization dynamics is shown in Figure 6.2(c) for the WS_2 (n_{ML}= 4)/Co_3FeB sample measured with pump fluence of 10 mJ/cm^2 under an in-plane bias magnetic field of 1.56 kOe. The applied magnetic field is large enough to reach saturation magnetization (Figure 6.1(a)). The transient Kerr rotation drops within sub-picosecond timescale followed by a recovery process. The ultrafast demagnetization [35] and fast remagnetization follow the expression derived from the phenomenological 3TM [50],

$$\frac{-\Delta M_z}{M_z} = \left[\left\{\frac{A_1}{(t/\tau_0+1)^{\frac{1}{2}}} + \frac{A_1\tau_m - A_2\tau_e}{\tau_e-\tau_m} e^{-t/\tau_m} + \frac{A_2\tau_e - A_1\tau_e}{\tau_e-\tau_m} e^{-t/\tau_e}\right\} H(t) + A_3\delta(t)\right] \otimes G(t). \qquad (6.1)$$

The 3TM is a thermodynamic model describing the spin fluctuations based on the energy transfer between three different subsystems: spin, electron, and lattice. Upon laser excitation, instantaneously created hot electrons are thermalized by electron-electron interactions. Shortly after that, spins also thermalize by electron-magnon interaction followed by ultrafast demagnetization. Then electron and spin start to relax by exchanging their energy with lattice via electron-phonon interaction. This is called the fast remagnetization time (τ_e). Here, A_1 represents the restoring value of $-\Delta M_z/M_z$ after equilibration of the different subsystems. A_2 represents the rise of the initial electron temperature, while A_3 represents the state filling effects due to pump-probe temporal overlap, described by a Dirac delta function ($\delta(t)$). $H(t)$ is the Heaviside step function and $G(t)$ is the Gaussian laser pulse. This model is useful to analyze the experimental data and extract quantitative information of timescales of ultrafast demagnetization and fast remagnetization.

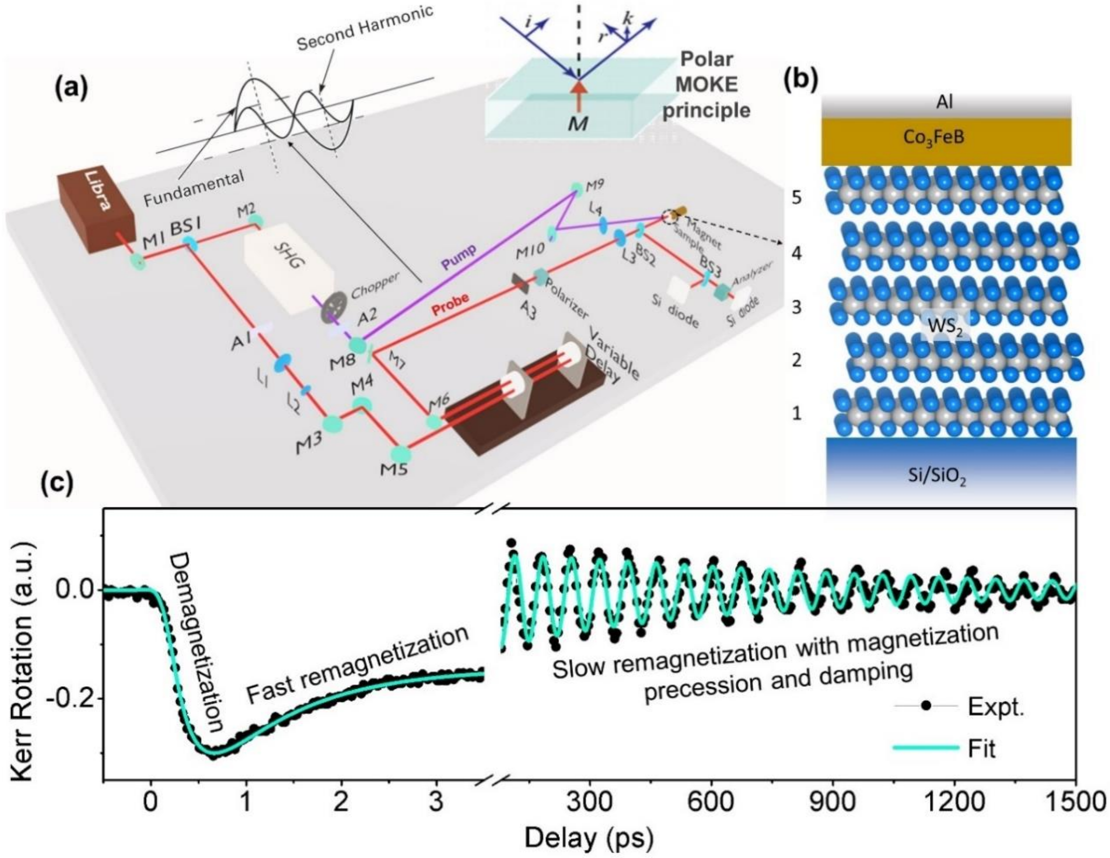

Figure 6.2: (a) TR-MOKE experimental setup. (b) Layer schematic of WS$_2$/Co$_3$FeB/Al heterostructure. (c) Recorded data on WS$_2$ (n_{ML}= 4)/Co$_3$FeB sample at an external bias magnetic field of 1.56 kOe and pump fluence of 10 mJ/cm^2. The three important temporal regimes are indicated in the graph. The green solid lines are fit to equation 6.1 and 6.2.

Fast remagnetization is followed by a slow remagnetization process occurs within few hundreds of ps timescale. In this timescale heat diffuses across the temperature gradient from ferromagnet to substrate via the intermediate layer i.e., WS$_2$, called the slow remagnetization time (τ_1). Exponentially decaying slow remagnetization superimposed with magnetization precession and damping can be fitted with an exponentially damped sinusoidal function,

$$M_z(t) = M_z(0)\left(Ae^{-\left(\frac{t}{\tau_1}\right)} + Be^{-\left(\frac{t}{\tau}\right)}\sin(2\pi f t + \phi)\right) \tag{6.2}$$

The precession frequency f is extracted from the FFT, while the decay time τ and the initial phase of the precession ϕ are fitting parameters.

The slow remagnetization time is the time (τ_1) to dissipate heat across the temperature gradient from ferromagnet to substrate via WS$_2$. Variation of τ_1 on odd-even layer numbers of WS$_2$ is shown in Figure 6.3

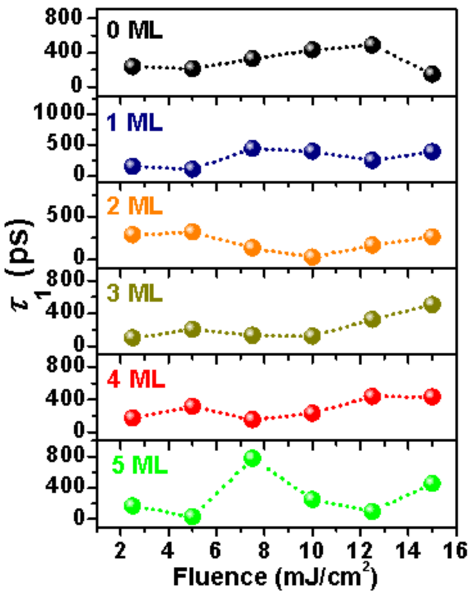

Figure 6.3: Variation of τ_1 with pump fluence for different number of layers of WS$_2$.

Experimental and numerical studies have shown that thermal transport in TMDs is phonon mediated [208]. The lattice specific heat (C_p) and thermal conductivity (κ) play dominant roles for thermal time constant in thermal dissipation. It is notable that both the IP and cross-plane κ contribute for this kind of layered materials [209]. While the IP κ increases with WS$_2$ layer number and helps for heat dissipation, cross-plane κ hinders the vertical heat flow due to the weak interlayer van der Waals interaction. Due to the balancing between IP and cross-plane κ, we have not observed any layer dependence of slow remagnetization time.

The effective magnetization (M_{eff}) can be extracted by fitting the bias field (H) dependent f using Kittel's formula neglecting the anisotropy energy in amorphous Co$_3$FeB [133],

$$f = \frac{\gamma}{2\pi}\left(H\left(H + 4\pi M_{eff}\right)\right)^{1/2}, \tag{6.3}$$

where $\gamma = g\mu_B/\hbar$; g, μ_B and ħ are the Landé g-factor, Bohr magneton and reduced Plank's constant, respectively. The extracted values of τ and M_{eff} from equation 6.2 and 6.3 are used to find the effective damping parameter at a particular bias field using the expression [134],

$$\alpha_{eff} = \frac{1}{\gamma\tau\left(H+2\pi M_{eff}\right)}. \tag{6.4}$$

The magnetization precession in a magnetic field of 1.56 kOe field (Figure 6.4(a)) is fitted with equation 6.2 and 6.3 is used to fit f vs. H for different WS$_2$ (n_{ML})/Co$_3$FeB samples at a pump fluence of 10 mJ/cm^2; results are shown in Figure 6.4(b). The extracted M_{eff} values for different layer number of WS$_2$ (Figure 6.4(c)) show a decreasing trend following previous results for TMD/FM heterostructures [203,207]. Here, the 5*d* electrons of W are strongly hybridized with the 3*d* electrons of Co/Fe at the interface reducing the magnetization at the interface. A finite *pd* hybridization between Co/Fe and S may also contribute in reducing the effective magnetization [207].

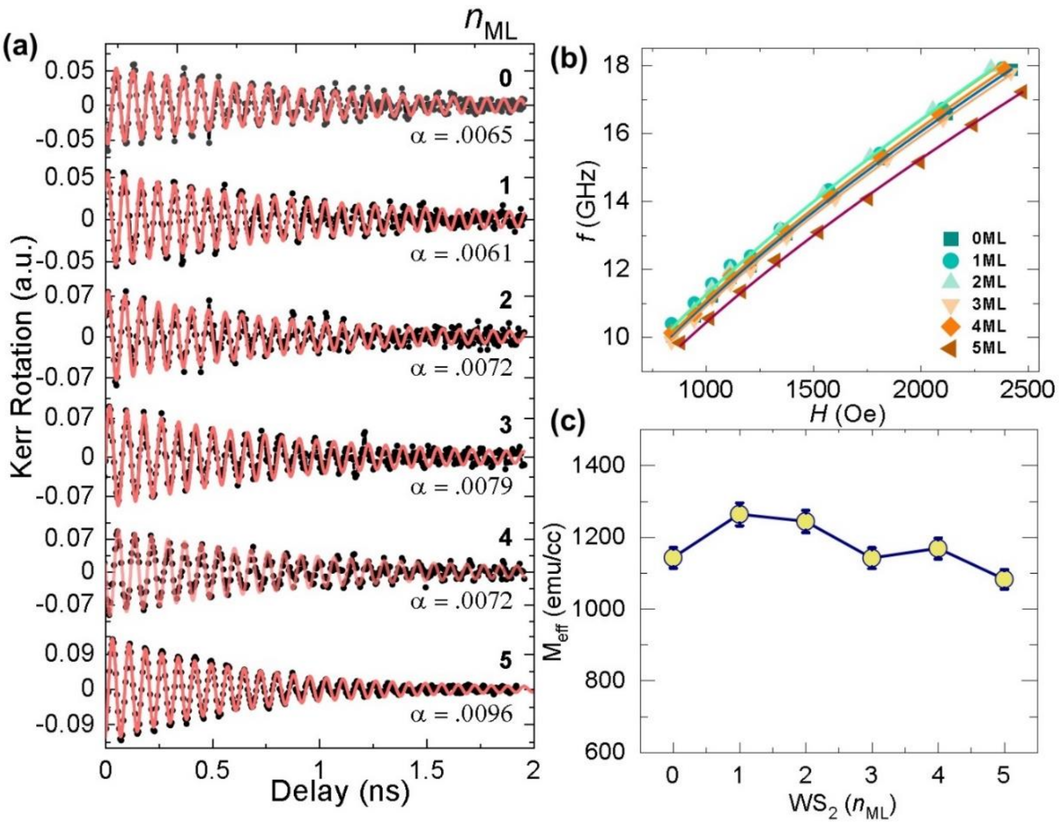

Figure 6.4: (a) Time resolved Kerr rotation showing the damped magnetization precession of WS$_2$ (n_{ML})/Co$_3$FeB thin film heterostructures measured with a pump fluence of 10 mJ/cm^2 at an external bias field of 1.56 kOe. The symbols are the experimental data points, and the solid lines are fits to equation 6.2. (b) Corresponding precession

frequency f of WS_2 (n_{ML})/Co_3FeB as a function of H. Solid lines are the Kittel fits. (c) Dependence of M_{eff} on layer number of WS_2 as extracted from Kittel fits.

Using equation 6.4, the effective damping parameter is calculated for the field range of ~ 840 Oe to ~ 2480 Oe (Figure 6.5(a)). The magnetic damping includes both intrinsic and extrinsic contributions. Extrinsic contributions arise from magnetic inhomogeneities and TMS [210,211]. Inhomogeneities in Co_3FeB thin film may induce variation of spin orientation via local magnetic anisotropy fields giving rise to a dephasing effect and an enhancement of the damping parameter when the applied field is not strong enough to align all spins [212]. TMS occurs when two spin waves interact at an impurity or discontinuity site ($k \neq 0$) in such a way that they transfer energy between the two spin waves and dissipates some of their energy at the site of the impurity. The scattering strength depends on the interfacial roughness that gives rise to interfacial magnetic anisotropy fluctuating field leading to TMS. Thus, a strong enough applied field can suppress the extrinsic contributions [135]. For all the layers of WS_2, the effective damping (α_{eff}) decreases gradually and reaches a nearly saturated value at higher H indicating that the inhomogeneous magnetic distribution is suppressed at large external magnetic fields. The experimental data is fitted with an exponentially decaying function, $\alpha_{eff} = \alpha + \alpha_{ex} exp(-H/H_0)$, where α corresponds to the intrinsic damping parameter and $\alpha_{ex} exp(-H/H_0)$ is the extrinsic part of the damping [92,213]. The variation of intrinsic damping α (as high field suppresses the extrinsic contributions) with pump fluence for WS_2 (Figure 6.5(b)) shows two opposite characteristics for odd and even number of WS_2 layers. The gradual enhancement of the background possibly emerges from the interlayer scattering for more than 2ML however the layer number dependence is remarkable in all samples [214].

The pump fluence increases the electronic temperature (T_e) up to thousands of Kelvins [215], which can be related to the absorbed laser energy per unit volume (E_a) according to the following relation,

$$E_a = C_e(T_e^2 - T_0^2)/2, \tag{6.5}$$

where C_e is the electronic specific heat of the sample, $T_0$is the initial electronic temperature (room temperature) and E_a depends on the pump fluence as,

$$E_a = F(1 - e^{-d/\psi})(1 - R)/d, \tag{6.6}$$

where F is the applied pump fluence, d is the ferromagnet thickness, ψ is the optical penetration depth and R is the reflectivity of the sample. The calculated E_a and T_e are estimated in the Table 6.2.

In the absence of WS_2, the damping parameter is nearly constant with pump fluence for bare Co_3FeB. This is to some extent consistent with a previous study, where the damping parameter was found to be temperature independent [216]. A temperature dependent damping parameter has been reported for several FM Heusler compounds [217,218], where the temperature dependence is explained by inter- and intraband scattering of electrons. The interband scattering contribution enhances the damping with increasing temperature known as resistivity like damping, while intraband scattering shows opposite behaviour, referred to as conductivity like damping [71]. It should be noted that the temperature dependence of the intrinsic damping is still being debated; a theoretical model [219] claims that the Gilbert damping should be independent of temperature. Thus, in a single Co_3FeB layer, we have not seen any signatures of the inter- and intraband electron scattering mechanisms. However, there is significant evidence of inter- and intraband electron scattering in the damping for the WS_2 (n_{ML}= 1, 2, 3, 4, 5)/Co_3FeB thin film heterostructures. The damping parameter increases with the increase of pump fluence for odd numbers of WS_2 layers (n_{ML} = 1, 3 and 5), indicative of interband electron scattering or resistivity like damping, while for even number of WS_2 monolayers (n_{ML} = 2, 4), intraband electron scattering dominates [203]. According to Kambersky's SFS mechanism, α depends on the SOC [220]. Further, Park *et al.* have shown that for 2D materials, the SOC strength is a function of temperature and the spin-orbit splitting factor ($\mathrm{SOC} = \frac{\hbar^2 k_0 \eta}{m^*}$, where η is the temperature dependent spin-splitting parameter) [221]. Moreover, inversion symmetry breaks for 2D TMD materials with an odd number of TMD layers generating additional spin splitting. These features will provide important implementation in spin-valleytronic devices. The layers showing higher damping would be useful for magnetic switching application to suppress the ringing effect, while the layers with lower damping would be useful to reduce write current in STT-MRAM/SOT-MRAM devices and magnonic devices where longer propagation of spin waves is desirable. In addition to that temperature dependent damping will provide another route to modulate damping by externally tuning the temperature of the system in place of heterostructure replacement. So, these heterostructures will be very useful to miniaturize electronic devices where temperature plays an important role.

Several mechanisms such as cooperative effects of SOC and exchange interaction [111], SOC and applied laser field [40], phonon mediated spin-flip scattering [48,86,114], electron-magnon scattering [44], electron-electron scattering [47] have been suggested to explain the ultrafast demagnetization. In 2008, Malinowski *et al.* first showed that the laser induced spin transport can speed up the ultrafast demagnetization process and increase magnetic quenching in

NM/FM heterostructures [50]. Local spin-flip scattering and nonlocal spin current transport are the two key mechanisms to explain ultrafast demagnetization [130,222]. An elegant method to extract the dominant contribution to ultrafast demagnetization is the simultaneous investigation and correlation of both the ultrafast demagnetization time (τ_m) and damping parameter (α) [91,92].

The normalized ultrafast demagnetization for WS_2 (n_{ML})/Co_3FeB thin film heterostructures is shown in Figure 6.5(c); the experimental results were analysed by fitting to equation 6.1. Here it appears that even numbers of WS_2 (n_{ML}= 2, 4) layers reduce the demagnetization time (τ_m), indicating a spin-pumping mechanism, while odd numbers of layers enhance τ_m. This can be attributed to the broken inversion symmetry causing an extra spin-splitting in valleys for odd number of layers contributing to relaxation of the spins and/or due to the uncompensated spins in the odd layer. However, a monolayer of WS_2 shows a different behaviour than the other odd

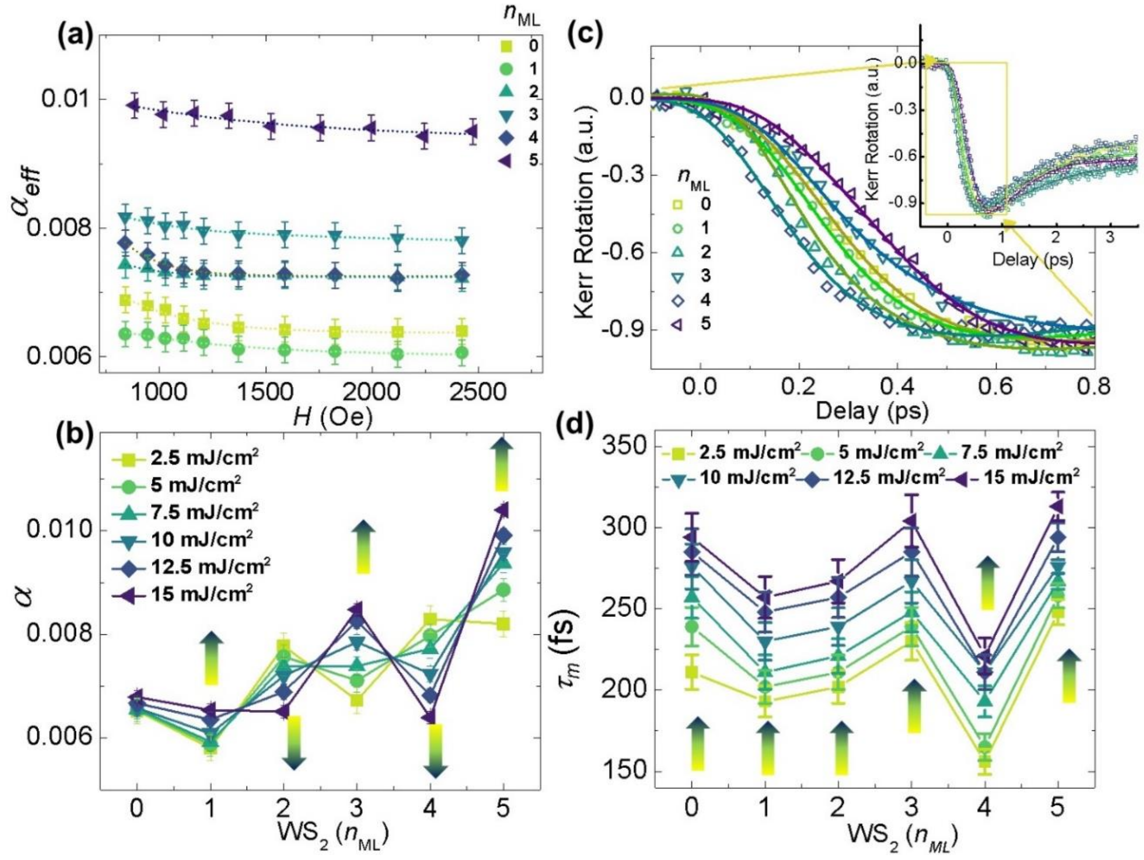

Figure 6.5: (a) Dependence of the effective damping parameter α_{eff} on the magnetic field H for WS_2 (n_{ML})/Co_3FeB at a fixed pump fluence (10 mJ/cm^2). Dotted lines correspond to fits to exponentially decaying functions. (b) Variation of α with n_{ML} at various pump fluences (2.5-15 mJ/cm^2) at an external bias field of 1.56 kOe. Coloured arrows indicate the increment of fluence. (c) Ultrafast demagnetization curves of WS_2 (n_{ML})/Co_3FeB. Inset shows the time-resolved Kerr rotation over longer time scale. Solid lines are fits to equation 6.1. (d) Variation of τ_m with n_{ML} at different pump fluences (2.5-15 mJ/cm^2). Coloured arrows indicate the increment of fluence.

numbers of layers, i.e., a lower τ_m value than for the bare Co3FeB layer. This is probably due to the absence of spin splitting in the electronic band structure in monolayer WS2 (ref. [203]). The τ_m as a function of WS2 layer number for different pump fluences ranging from 2.5 mJ/cm^2 to 15 mJ/cm^2 is shown in Figure 6.5(d). Unlike α, for all samples, τ_m is increasing with pump fluence due to larger spin fluctuations at elevated temperature [131].

Variation of α and τ_m with pump fluence are shown in Figure 6.6.

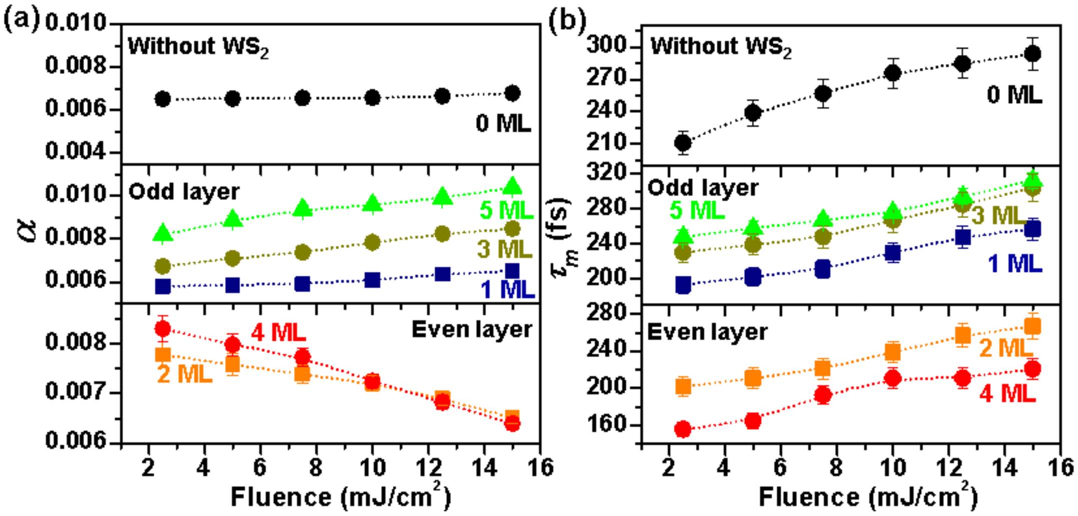

Figure 6.6: Variation of (a) α and (b) τ_m with pump fluences in absence of WS2, and for odd and even number of layers of WS2.

We have modelled the experimental ultrafast demagnetization data of Co3FeB (6 nm) thin film obtained from TR-MOKE magnetometry at different pump fluences using 3TM [35]. The three coupled differentail equations can be written as:

$$C_e(T_e)\frac{dT_e}{dt} = -G_{el}(T_e - T_l) - G_{es}(T_e - T_s) + P(t) \tag{6.7a}$$

$$C_s(T_s)\frac{dT_s}{dt} = -G_{sl}(T_s - T_l) - G_{es}(T_s - T_e) \tag{6.7b}$$

$$C_l(T_l)\frac{dT_l}{dt} = -G_{sl}(T_l - T_s) - G_{el}(T_l - T_e) \tag{6.7c}$$

Where C_e, C_s and C_l are the electron, spin and lattice specific heats. Electronic specific heat is proportional to the electron temperature, i.e., $C_e = \gamma\, T_e$, where $\gamma = 0.7\times10^3$ Jm^{-3}K^{-1}. T_e, T_s and T_l are temperature of electron, spin and lattice bath, respectively. Initial temperatures are kept at room temperature, i.e., 300 K. G_{el}, G_{es} and G_{sl} are the electron-lattice, electron-spin and spin-lattice coupling strength constant. Initial electronic excitation is expressed by adding the laser source term, $P(t)$ to equation 6.7a only. The temporal evolution of the spin temperature is then fed into the mean field theory to reproduce the similar change in magnetization that is observed in the experiment. Curie temperature (T_c) of Co_3FeB is ~1313 K [223].

We have enlisted the value of absorbed energy (E_a) and rise of electronic temperatures (T_e) using equation 6.6 and 6.7 of the manuscript and different parameters obtained from 3TM at different pump fluences for Co_3FeB (6 nm) thin film in Table 6.2 below.

Table 6.2: Estimation of different parameters obtained from equation 6.6, 6.7 and 3TM for Co_3FeB (6 nm) film.

F (mJ/cm^2)	E_a (mJ/cc)	T_e (K)	C_l (× 10^6 $Jm^{-3}K^{-1}$)	C_s (× 10^6 $Jm^{-3}K^{-1}$)	G_{el} (×10^{17} $Wm^{-3}K^{-1}$)	G_{es} (×10^{17} $Wm^{-3}K^{-1}$)	G_{sl} (×10^{17} $Wm^{-3}K^{-1}$)
2.5	0.67×10^6	1416	3.8	2.3	7	29.2	8
5	1.34×10^6	1979	4.2	3.5	6	29	13
7.5	2.01×10^6	2415	4.5	3.68	6	28.5	14
10	2.67×10^6	2778	5.3	3.8	11	28	10
12.5	3.34×10^6	3104	5.5	3.95	11	27	12.5
15	4.01×10^6	3398	7	4.05	14	26	9

We have observed an increase in both C_l and C_s with pump fluence that corresponds to the rise of their respective bath temperatures. G_{es} is showing a decreasing trend with fluence indicating that the higher fluence weakens the strength of coupling between electron and spin followed by an increase in τ_m.

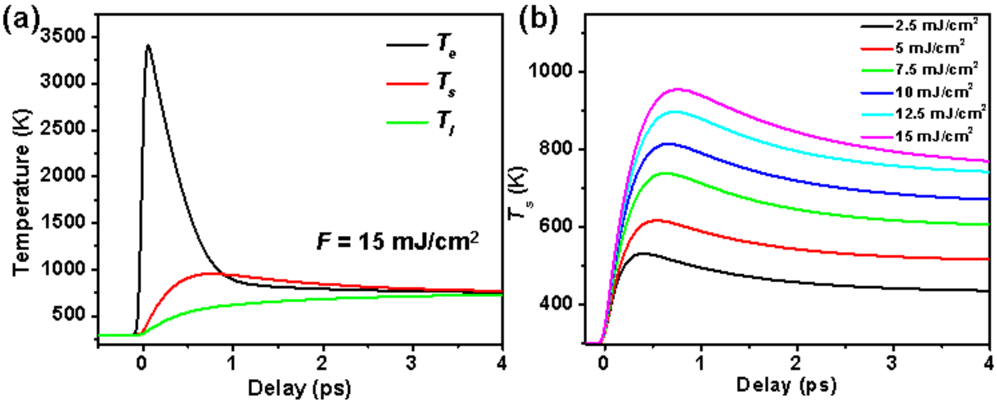

Figure 6.7: (a) Temporal evolution of electron temperature (T_e), spin temperature (T_s) and lattice temperature (T_l) at 15 mJ/cm^2 fluence and (b) variation of T_s as a function of time delay at different pump fluence for Co_3FeB (6 nm) thin film.

Relationship between ultrafast demagnetization time and damping parameter: Non-volatile control

The relationship between the ultrafast demagnetization time and the effective damping parameter can be used to extract the dominant microscopic mechanism behind these phenomena. The theoretical model by Koopmans *et al.* [86] predict an inverse proportionality between τ_m and α based on EY-type spin-flip scattering. Later, based on the 'breathing Fermi surface model' and the 'bubbling Fermi surface model', Fähnle *et al.* [122,123] derived both inverse and direct proportionalities between τ_m and α associated with resistivity-like and conductivity-like damping, respectively. More recently Zhang *et al.* proposed a model by incorporating spin transport through the interface of a FM/NM heterostructure [91,92] giving rise to a direct proportionality between τ_m and α when the dominating mechanism is local spin-filp scattering and an inverse proportionality when interface spin transport dominates.

The correlation between τ_m and α is depicted in Figure 6.8. In case of odd n_{ML} (Figure 6.8(a) and (b)) at the lowest and highest pump fluence used in our experiments the results indicate a linear relationship between τ_m and α as prescribed by the breathing Fermi surface model and the EY relation [122],

$$\tau_m = \frac{M}{\gamma p b^2 F_{el}} \alpha , \tag{6.8}$$

where M is the magnetization, F_{el} contains the derivatives of the single-electron energies with respect to the orientation of the magnetization M, p is a material specific parameter and b^2 is the EY spin-mixing parameter. The values α/τ_m = 4.55 × 10^{10} s^{-1} and 9.24 × 10^{10} s^{-1} are obtained for odd numbers of layers at the lowest and highest pump fluence, respectively. At the highest fluence, even n_{ML} also indicates a linear relationship (Figure 6.8(d)) and the obtained value of α/τ_m is 0.56 × 10^{10} s^{-1}. These values agree well with the previous reported values [92,123,161] indicating that the main governing mechanism behind the ultrafast demagnetization is the local spin-flip scattering. On the other hand, for even n_{ML} at the lowest pump fluence (Figure 6.8(c)) an inverse correlation occurs

$$\tau_m = \frac{\tilde{F}_{el}}{p b^2} \frac{1}{\alpha} , \tag{6.9}$$

where $\tilde{F}_{el}$ is also determined from the electronic states but it is different from the F_{el}. $\tilde{F}_{el}$ can be expressed by the matrix elements formed by the two different electronic wave functions whereas F_{el} contains matrix elements formed by the same electronic wavefunctions. This indicates the dominance of spin current transport. In even n_{ML}, the absence of broken inversion symmetry causes WS_2 (n_{ML}= 2, 4)/Co_3FeB to act like a normal NM/FM heterostructure. Due to the high SOC of WS_2, it absorbs the spin angular momentum from Co_3FeB and enhances the demagnetization rate through spin-pumping [22]. The demagnetization rate ($\Delta \frac{1}{\tau_m} = \frac{1}{\tau_m}|_t -$

$\frac{1}{\tau_m}|_{t=0}$) versus modulation of damping ($\Delta\,\alpha = \alpha|_t - \alpha|_{t=0}$) at lowest fluence for even n_{ML} has been used to find out the spin chemical potential using the relation [92],

$$\Delta\frac{1}{\tau_m} = \frac{\mu_s}{\hbar}\Delta\alpha. \tag{6.10}$$

Here, the spin chemical potential (μ_s) quantifies the spin accumulation at the WS_2/Co_3FeB interface, which generates a spin backflow current and reduces the spin pumping. We have extracted μ_s to be 0.53 eV for even n_{ML} at low fluence, which enhances the demagnetization rate and the damping factor. This value is reasonable for a 2D material/FM heterostrcuture as it is in close proximity with the reported values for graphene/CoFeB heterostructure [128,224,225]. This implies that with an increase of pump laser fluence, spin-flip scattering dominates over the spin pumping contribution for even number of layers. Unlike for NM/FM heterostructures, the direct proportionality observed for odd n_{ML} is due to the interpaly between the SOC and the spin-valley splitting caused by the broken inversion symmetry, which interrupts the generation and transport of spin current via interband transitions (Figure 6.8(e)). In reciprocal space, valley seperation is so large that the valley index is robust against the scattering of phonons and deformation [226]. So the effect of valley splitting on magnetization dynamics will make TMD/FM heterostructures as a promising candidate for next generation spintronic devices with high storage density and low power consumption.

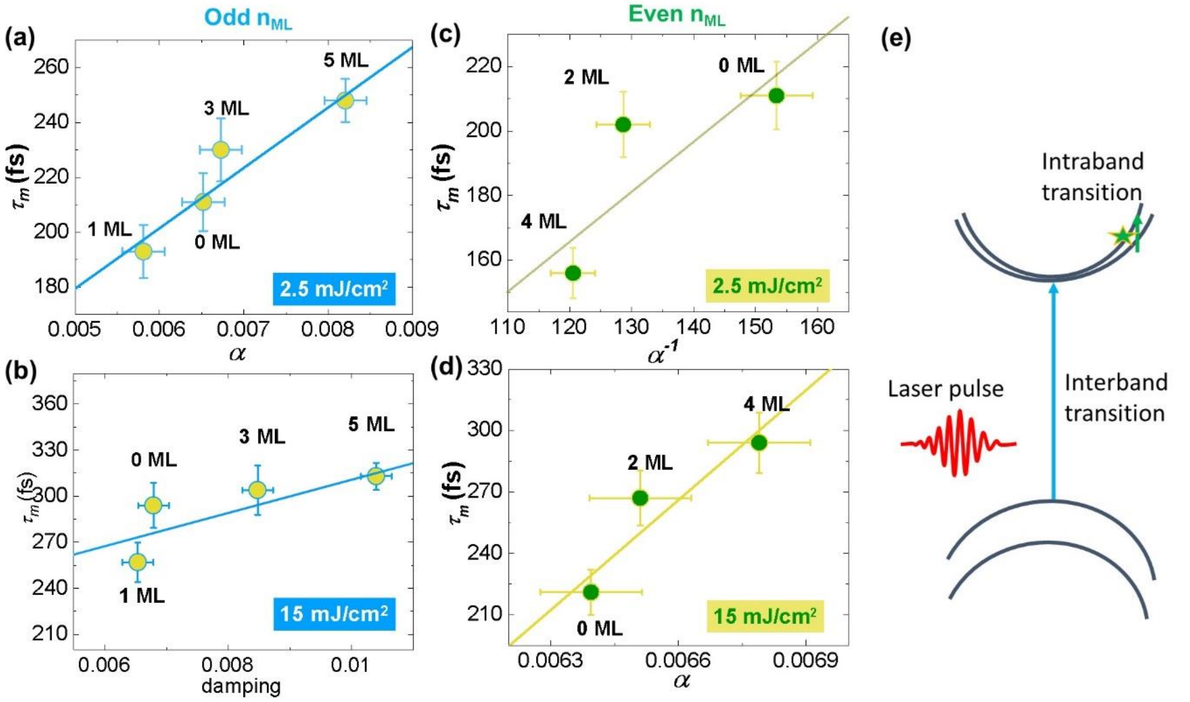

Figure 6.8: Variation of τ_m as a function of α for (a),(c) lowest pump fluence and (b),(d) highest pump fluence for odd n_{ML} and even n_{ML}, respectively. Lines in (a),(c),(d) are fits to the equation 6.8, while in (b) the line is a fit to equation 6.9. (e), Cartoon of laser pulse interaction resulting in inter- and intraband transitions in WS_2.

6.4 Conclusion

In summary, we have systematically investigated the magnetization dynamics from femtosecond to nanosecond timescales in $WS_2(n_{ML})/Co_3FeB$ thin film heterostructures using time-resolved magneto-optical Kerr effect magnetometry. An odd-even WS_2 layer number (n_{ML}) dependence is evidenced from measurements of the damping parameter (α). The α exhibits a laser fluence dependent character due to interband electron scattering because of broken inversion symmetry, while in heterostructures with even n_{ML} intraband electron scattering explains the fluence dependence. In contrarst, τ_m does not show any odd-even layer dependence with fluence, confirming that electron scattering plays no significant role on femtosecond timescales. Moreover, by correlating τ_m and α, the microscopic mechanisms involved in ultrafast demagnetization have been revealed. We have found that spin current transport is generally responsible for ultrafast demagnetization at temperatures near room temperature in heterostructures with even n_{ML}. However, with an increase of pump fluence, the SFS starts playing a dominating role. On the other hand, in heterostructures with odd n_{ML} the ultrafast demagnetization is dominated by the SFS mechanism for all fluences used in this study. The understanding of how the spin-valley coupling governs the odd-even layer dependence in two-dimentional materials is an important milestone for future fundamental research and applications.

CHAPTER 7

Role of Spin Transport on Ultrafast Spin Dynamics in Magnetic Weyl Semimetal (Co_2MnGa)/Pt Heterostructures with High Spin-Mixing Conductance

7.1 Introduction

Weyl semimetals (WSMs) [227-238] have stimulated the scientific curiosity as a new frontier of materials science due to the presence of Weyl fermions, which are spin-$\frac{1}{2}$ massless quasiparticles described by a simplified Dirac relativistic wave equation, omitting the mass term [239] . The scientific interest in WSMs is not only due to their unique electronic dispersion relation and Fermi-arc type surface states [228,229], but also because of their technologically attractive magneto-transport properties, such as nonlocal transport [240,241], high mobility [242], large magnetoresistance [243], chiral anomaly effect [244-246], anomalous Hall effect (AHE) [247,248], and anomalous Nernst effect (ANE) [249,250].

In WSMs, the valence and conduction bands cross linearly in three-dimensional (3D) momentum space via Weyl points, the emergent Berry flux between a pair of Weyl points with opposite chiralities, which act as source and sink of the Berry curvature [251]. In WSM which break time-reversal symmetry, the intrinsic part of the proximity of the Weyl points to the Fermi level govern the intrinsic part of the AHE [247] and yield the intrinsic SHE [252]. Among all Weyl semimetals, Co-based ferromagnetic Weyl full Heusler compounds are of particular interest in part due to their high spin polarization and topologically protected band crossings at high symmetry points of the Brillouin zone, making them potentially relevant for a wide variety of electronic device applications. According to recent literature, WSM Co_2MnSi-based MTJs show high tunnel magnetoresistance at low temperatures [253], with Co_2FeSi and Co_2FeAl MTJs utilized for tunnel magneto-Seebeck effect [254,255] for their high spin-Seebeck coefficient. Furthermore, theoretical investigations imply that these novel class of quantum materials with topologically non-trivial band structures have the potential to demonstrate rapid spin-to-charge interconversion and faster magnetization switching[108], making them suitable for spin-orbit torque-based devices [256,257]. Belopolski *et al.* first elucidated, by means of angle-resolved photoemission spectroscopy, the electronic band structure of Co_2MnGa (CMG) and confirmed that it exhibits both nodal line band-crossings and Weyl crossings at distinct points in momentum space, which leads to exotic electronic properties such as chiral fermions and topological surface states [258]. Later, CMG was the subject of numerous studies, which revealed that it exhibited substantial ANE [250,259,260] and a thickness-dependent AHE [261-264] from the bulk to thin film limit, originating from a sizeable intrinsic reciprocal-space Berry curvature, and displayed a strong potential for use as spintronics terahertz emitters [265-267] . For spintronic applications, a basic understanding of magnetization dynamics [268], as well as the microscopic mechanisms behind femtosecond to nanosecond spin phenomena, is necessary to enable a next-generation switchable device. In particular, understanding the underlying phenomena of femtosecond processes such as ultrafast demagnetization (a key mechanism responsible for all-optical switching) and the nanosecond spin-dissipation and spin transport process, which are characterized by the Gilbert damping parameter (analogous to the Rayleigh energy dissipation function) is crucial. Despite the uniqueness of Weyl semimetals, the processes involved in ultrafast demagnetization and spin transport across (magnetic) Weyl-based heterostructures are still largely unknown and require further exploration.

In this work, we present an all-optical investigation of femtosecond to nanosecond spin dynamics in cubic CMG thin films and subsequent spin transport across CMG/Pt interfaces. TR-MOKE [129] magnetometry is used to excite and detect the magnetization dynamics over a broad timescale [269] where the ultrafast demagnetization time (τ_m) and damping constant corresponding to the uniform Kittel mode (α) and perpendicular standing spin wave (PSSW) mode (α_{PSSW}) [270] as a function of Pt thickness (t) are extracted. By correlating the demagnetization rate ($\Delta\frac{1}{\tau_m}$) with the modulation of damping ($\Delta\alpha$), we have inferred the dominant role of spin transport phenomenon [51,128,161] as a microscopic mechanism behind ultrafast demagnetization and extracted the spin chemical potential (μ_s) at the interface during spin transport [92]. We conducted a thorough investigation of spin pumping in CMG/Pt heterostructures, in which the precessional motion of magnetization within the CMG layer results in a finite electrochemical potential at the CMG/Pt interface due to the asymmetric accumulation of majority spins. This non-equilibrium spin build-up works as a reservoir for spin current, which diffuses into the Pt layer and increases the damping of the composite system. The efficiency of this spin pumping mechanism is primarily determined by the spin-mixing conductance and interfacial spin transparency. Using the ballistic spin transport model [271,272], we have extracted an ultrahigh spin-mixing conductance and interfacial spin transparency for the CMG/Pt interface, indicative of an efficient spin transport across this interface. Additionally, to isolate the other possible interfacial effects, if present in the modulation of damping, a control experiment has been performed by inserting a thin copper (Cu) spacer layer between CMG and Pt which confirmed that spin pumping is playing the dominating role in the modulation of damping in our system. Overall, this thorough study of femtosecond to nanosecond magnetization dynamics identifies this magnetic Weyl semimetal as a promising candidate for future directions in both spin-electronics and ultrafast optoelectronics.

7.2 Experimental details

Sample fabrication

Co_2MnGa films, with a thickness of 42 nm, were grown epitaxially on (001)-oriented MgO single-crystal substrates by employing a BESTEC UHV magnetron sputtering system. Magnetron sources (mounted with 5.08 cm in diameter targets) of Co, and $Mn_{50}Ga_{50}$, as well as Mn (to achieve the desired stoichiometric Co_2MnGa compound), were used in confocal geometry during the sputtering deposition, with DC power of 34 W, 20 W and 6 W, respectively. The target-to-substrate distance was maintained at 20 cm to ensure optimal sputtering conditions. Before initiating the deposition process, the chamber was evacuated to a base pressure less than 5×10^{-9} mbar, whereas the process gas (Ar 5 N) pressure was set to 3.0×10^{-3} mbar. The substrate was rotated at 20 rpm to promote spatial uniformity of the resulting film. The films were grown at a temperature of 640 °C and subsequently subject to *in situ* post-annealing for an additional 30 min to enhance the chemical ordering. Subsequently, the nonmagnetic Pt layer of varying thicknesses (t = 2, 4, 6, and 8 nm) were grown on top of the Co_2MnGa at room temperature by applying a DC power of 40 W to a Pt source. In the reference sample (without the Pt layer), a protective Si capping layer was deposited at 60 W RF power to protect the Co_2MnGa film from oxidation. In another set of samples, a thin 2-nm-thick Cu spacer layer was inserted between the Co_2MnGa and Pt layers. This Cu spacer layer was deposited at room temperature using a DC power of 30 W. The conditions for deposition were meticulously optimized and maintained at nominally identical levels across all samples.

Structural, electrical and magnetic characterizations

Symmetric and asymmetric XRD scans were carried out using a Panalytical XPert^3 XRD diffractometer with Cu Kα_1 radiation (λ = 1.5406 Å). The interface roughness and thickness of different layers were determined by XRR measurements. Surface topography was studied using AFM with an MFP-3D origin microscope from Asylum Research (Oxford Instruments). For longitudinal resistivity measurement, we employed a PPMS Quantum Design cryostat with a low frequency AC excitation and a lock-in detection method of the corresponding voltage drop. We resorted to contacting the corners of the square samples by ultrasonically bonded aluminium wires, in the van der Pauw geometry. Magnetometry measurements were conducted utilizing a Quantum Design (MPMS SQUID-VSM) magnetometer.

Time-resolved Magneto-optical Kerr effect

The measurement of magnetization dynamics was performed using a custom-built TR-MOKE magnetometer [34] in a two-colour optical pump-probe geometry with an 800 nm probe beam and a 400 nm pump beam with a pump-probe cross-correlation width of ~100 fs. An amplified laser system (Libra, Coherent Inc.) with a chirped-pulse regenerative amplification technique creates 35 fs laser pulses. The fundamental laser beam of 800 nm from the amplifier is split into two beams using a beam splitter and one part is frequency doubled using a second harmonic generator to create the pump beam (wavelength = 400 nm, pulse width > 35 fs and repetition rate ~ 1kHz), for excitation of the sample. The other part (wavelength = 800 nm, pulse width = 35 fs and repetition rate ~ 1kHz) is time-delayed using a motorized delay stage with a retroreflector to probe the ensuing magnetization dynamics due to excitation by the pump beam. A noncollinear pump-probe geometry is utilized in which the pump beam is obliquely incident with a spot diameter of ~300 μm on the sample surface and the probe beam is normally incident with a spot diameter of ~100 μm carefully aligned at the centre of the pump spot to detect the change in the polar Kerr rotation locally. For the entire measurement, the pump fluence was set to 10 mJ.cm^{-2} and the probe fluence was set to 1 mJ.cm^{-2} . One Glan-Thompson polarizer is used in the probe path for having high degree of polarization before being incident on the sample, while another is used to analyze the polar Kerr rotation of the reflected probe beam from the sample. The detection is made by two Si-photodetectors which are connected to lock-in amplifiers (Stanford research system, Model: SR830) for measuring the total reflectivity and Kerr rotation. The pump beam is periodically chopped at 373 Hz frequency by an optical chopper (Thorlabs, Model: MC2000B with 10 slots chopper blade) which provides the reference frequency to the lock-in amplifiers. An external magnetic field of 290 mT is applied at ~10° tilt from the sample plane to trigger the magnetization precession. An external magnetic field of is applied at a small title angle of ~10° from the sample plane. This tilt creates a finite demagnetizing field along the direction of the pump pulse, which shifts the equilibrium orientation of the magnetization and induces precession around this new equilibrium position [57]. The in-plane component of the magnetic field is referred to as the bias magnetic field (*H*).

7.3 Results and discussions

Thin film fabrication and characterization

The CMG thin films were grown epitaxialy on (001)-oriented MgO single-crystal, at elevated temperatures, by magnetron sputtering, following the procedure detailed in the Methods section, while the Pt overlayers were sputtered *in vacuo*, at room temperature. We have conducted systematic X-ray diffraction measurements, including 2θ-ω scan, rocking curve (ω-scan), and azimuthal (ϕ) scan in order to characterize the films' structure, crystallinity, and heteroepitaxial relation with the substrate. Figure 7.1(a) depicts the crystal structure of the $L2_1$-ordered cubic full Heusler CMG. In Figure 7.1(b), the XRD spectra of CMG films in the presence and absence of a Pt overlayer are displayed. Alongside the (002) reflection of the MgO substrate, the samples display only the (002) and (004) reflections of the cubic CMG, which signifies the presence of (001)-oriented single-crystalline films. In the presence of Pt, we additionally observe a pronounced diffraction peak at 2θ = 44.3° and a faint one at 2θ ≈ 107.2°, corresponding to the (002) and (004) reflections of a (001)-textured Pt film.

The temperature-dependent measurements of the longitudinal resistivity were conducted on 42-nm-thick CMG and 6-nm-thick Pt film, respectively, of nominally identical thickness to those used in the CMG/Pt heterostructure. Figure 7.1(c) depicts the temperature-dependent longitudinal resistivity at zero field for the CMG and Pt thin films. Both films display a metallic behaviour, characterized by a continuous decrease in longitudinal resistivity as the temperature is lowered, with a residual resistivity of 220 μm.cm and 17 μm.cm at 10 K for CMG and Pt, respectively. We note an upturn of longitudinal resistivity for the CMG film below 35 K, which is attributable to a particle-hole electron-electron interaction mechanism [273].

In order to gain insight into the surface topography of our CMG films, we resorted to AFM. The topographical map was acquired on a nominally identical 42-nm-thick CMG film, but without any capping layer. In Figure 7.1(d), the AFM topography of 42-nm-thick CMG reveals an average topographical (root mean square) roughness of 3.85 nm. However, there are no indications of non-uniformity, discontinuity, or dislocations in our films.

This high topographical roughness can be due to initial oxidation of these uncapped films. The interfacial roughness obtained from XRR in the presence of the Pt layer is approximately 0.43 nm, while in its absence, it is around 1.40 nm. This indicates that the interfacial roughness of

Co_2MnGa/Pt thin films are small and closely follows the Co_2MnGa surface topography, even at the ultrathin Pt thicknesses used in this study.

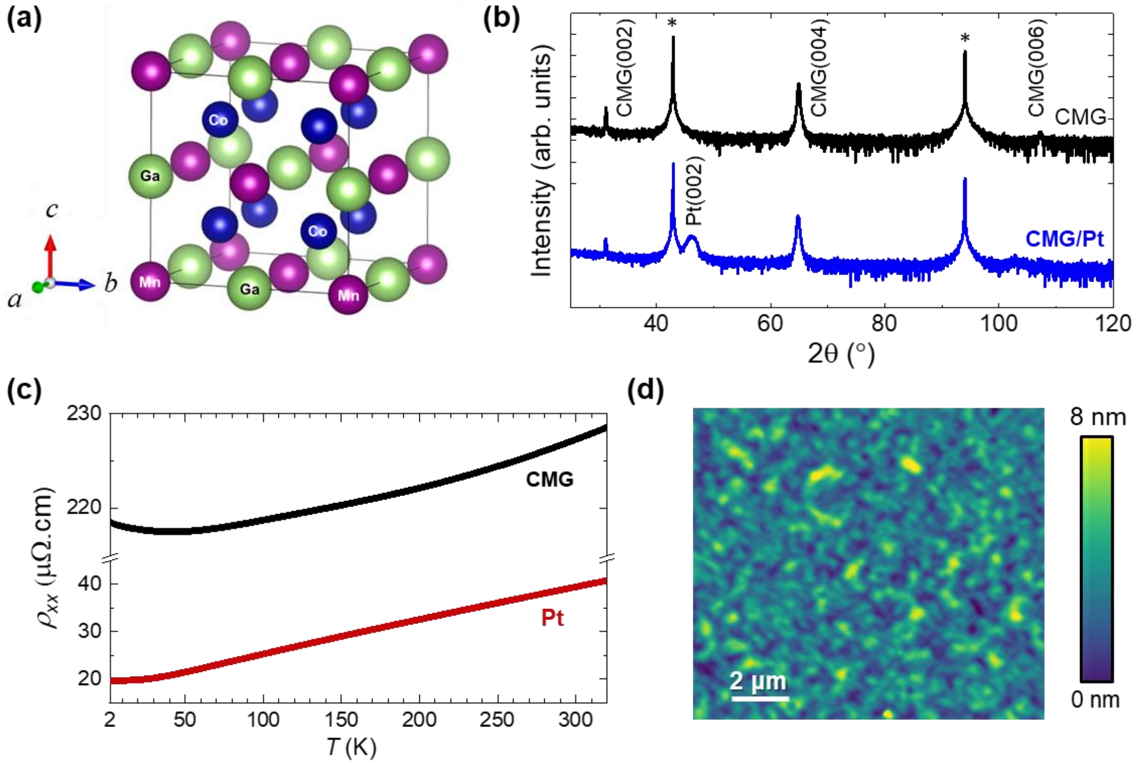

Figure 7.1: (a) Schematic of $L2_1$-ordered cubic crystal structure of Co_2MnGa. (b) XRD pattern of the Co_2MnGa (CMG) thin films in the presence and absence of Pt overlayer. Bragg diffraction peaks of the films are labelled by their Miller indices, and those corresponding to the MgO (001) substrate are marked by asterisks. (c) Longitudinal resistivity as a function of temperature for CMG (42 nm) and Pt (6 nm) films. (d) AFM image of uncapped CMG film showing the surface topography with relatively low roughness.

Figure 7.2(a) illustrates the ϕ-scan patterns of the {202} planes for both the CMG film and the MgO substrate. The CMG reflections exhibit a four-fold symmetry at 90° intervals, indicating the presence of single crystalline epilayers with a well-defined in-plane orientation. A comparison between the diffractions of the film and the substrate reveals a 45° in-plane rotation of the CMG unit cell in relation to the MgO substrate. The crystal quality of the CMG films was assessed by examining the full width at half maximum (FWHM) values of rocking curves measured around the (004) reflection. The obtained small FWHM of 0.47° [Figure 7.2(b)] indicates that our films have state-of-the-art high crystalline quality with low mosaicity, comparable to our previous work [263].

The characteristics of Heusler compounds are significantly influenced by the occupation of crystallographic sites. To ascertain the degree of chemical ordering of the films in the ordered full Heusler $L2_1$-type structure, the identification of superstructure (111) or (113) reflections, otherwise forbidden in chemically disordered compounds, is crucial. In Figure 7.2(c), 2θ-ω scans of the asymmetric (113) Bragg reflection for CMG thin films are presented. A quantitative analysis of the integrated intensities for all Bragg reflections, for similarly grown Co_2MnGa epitaxial films has set an upper bound of 10% on the B2-type disorder [263]. The clear (113) peak reported in our films reveal that they crystallize with almost fully chemically $L2_1$-ordered Heulser phase, in line with previous works [260,263].

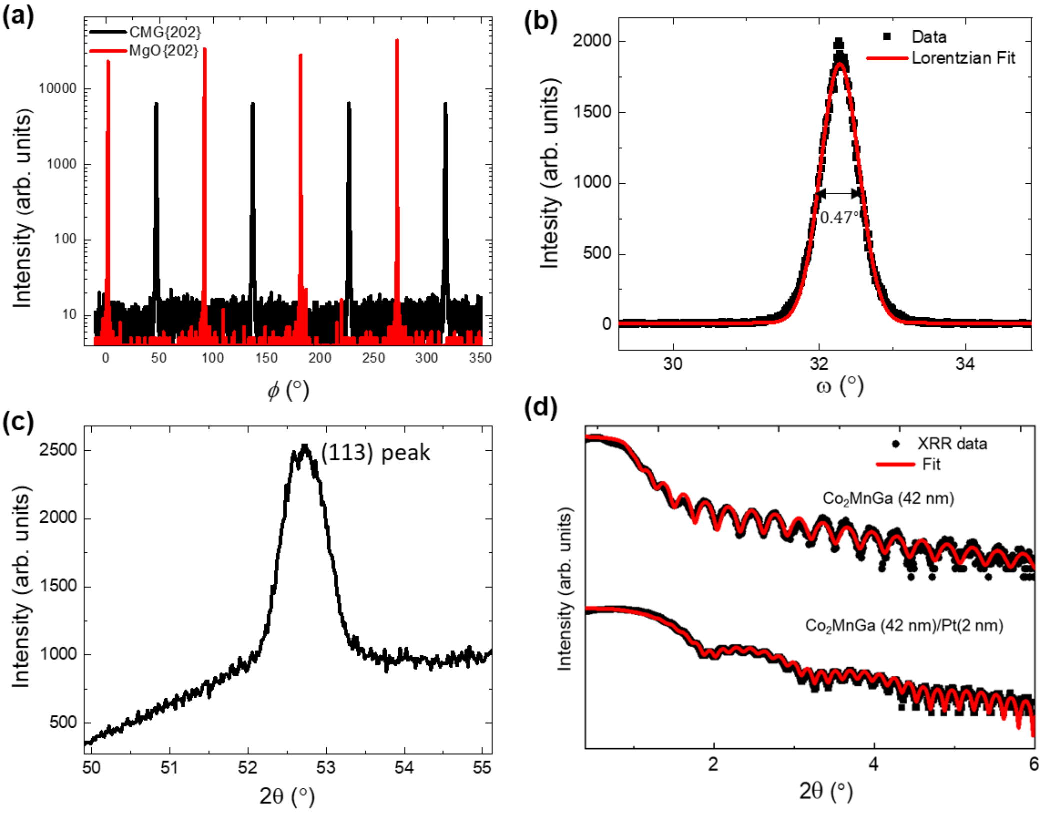

Figure 7.2: (a) ϕ-scan patterns of the {202} planes from the 42-nm-thick CMG film and the MgO substrate. (b) Rocking curve (ω-scan) of (004) reflection from 42-nm-thick CMG film. (c) (113) Bragg peak measured in symmetric non-coplanar geometry. (d) X-ray reflectivity pattern of the 42-nm-thick CMG film in the presence and absence of Pt layer, where the solid line represents the least-squares fit to the data.

Figure 7.2(d) depicts the XRR pattern of the CMG film capped by a Si protective layer and Pt spin sink layer. The emergence of thickness oscillations beyond the critical angle, extending up to 1° and beyond, signifies well-defined films and precise interfaces. Through a comparison of the experimental data (filled symbols) with the model curve derived using a modified Parratt formalism (solid line), we extract key structural parameters, including thickness, roughness, and density of the different layers. The obtained thickness and density exhibit a remarkable agreement, deviating by no more than 2% from the nominal values. Additionally, the determined roughness values for the substrate/film and film/capping layer interfaces are found to be 3.2 Å and 2.4 Å, respectively. We have also included tables (Tables 7.1 and 7.2) showing parameters obtained from the least-squares fitting of the XRR data for samples with and without Pt. The interfacial roughness in the presence of the Pt layer is approximately 0.43 nm, while in its absence, it is around 1.40 nm. Both values are significantly lower than the AFM-measured topographical roughness of the uncapped films. This indicates that the interfacial roughness of Co_2MnGa/Pt thin films are low and closely follows the Co_2MnGa surface topography, even at the ultrathin Pt thicknesses used in this study.

Table 7.1. The parameter values obtained from fitting XRR spectra for MgO Sub/Co_2MnGa/Pt thin films.

Layer	Thickness (nm)	Density (gm/cc)	Roughness (nm)
Pt	2	21.8	0.43
Co_2MnGa	42	7.84	0.62
MgO substrate		3.22	0.25

Table 7.2. The parameter values obtained from fitting XRR spectra for MgO Sub/Co_2MnGa/Si thin films.

Layer	Thickness (nm)	Density (gm/cc)	Roughness (nm)
Si	3	2.16	1.40
Co_2MnGa	42	7.86	0.24
MgO substrate		3.22	0.32

In Figure 7.3(a), we show typical in-plane and out-of-plane magnetization hysteresis loops for the 42-nm-thick CMG film measured at 300 K. The Co_2MnGa film is a soft magnet with an in-plane magnetic easy axis. The saturation magnetization and coercivity are found to be 803 ± 15 kA/m and 2.4 ± 0.6 mT, respectively. The Curie temperature is measured using SQUID magnetometry with an oven option where the magnetization is recorded with a constant in-plane field of 20 mT while warming up the sample, as shown in the Figure 7.3(b). The extracted Curie temperature is 720 ± 5 K, which is slightly higher than the bulk value indicating a small amount of disorder and/or off-stoichiometry in our films.

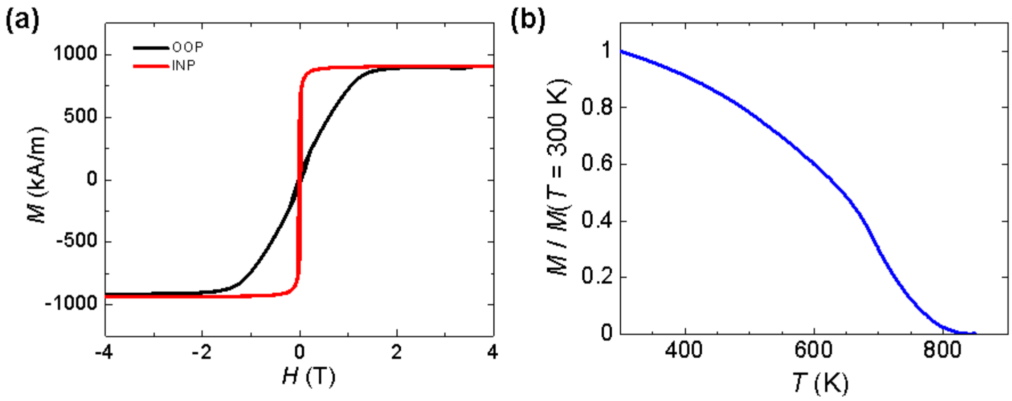

Figure 7.3: (a) In-plane (IP) and out-of-plane (OOP) hysteresis loops of CMG (42 nm) film. (b) The temperature dependence of magnetization for the same film.

Magnetization dynamics

A schematic of the MgO/Co_2MnGa (42 nm)/Pt (*t* nm) sample stack (CMG/Pt (*t*) hereafter) with the TR-MOKE measurement geometry is depicted in Figure 7.4(a). When a femtosecond (fs) laser pulse is incident on an ordered magnetic material, due to the excitation of electrons carrying spin angular momenta, the magnetization of the material is partially or fully lost within the sub-picosecond (sub-ps) timescale [35,274]. This phenomenon in the sub-ps timescale is called the ultrafast demagnetization [35]. Subsequently, electrons and spins start to relax. This relaxation occurs in two different timescales: the first one occurs in a few ps timescale when electrons and spins exchange their energy with lattice, called fast remagnetization, and the second one occurs in hundreds of ps timescale, known as slow relaxation, that corresponds to the energy transfer to the substrate or the surroundings. After fast relaxation, the lattice temperature changes, leading to a change in the magnetocrystalline/shape anisotropy of the system that acts as an effective field to trigger the damped precessional motion of the magnetization. Laser-induced time-resolved magnetization dynamics of CMG/Pt (t = 6 nm) heterostructure at pump fluence of 10 mJ/cm^2 and in-plane external magnetic field (H) of 290 mT is shown in Figure 7.4(b).

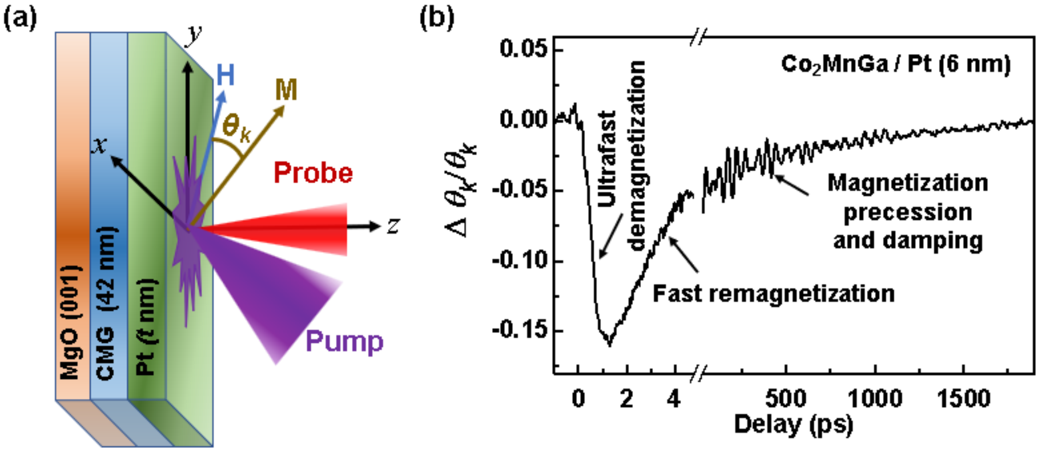

Figure 7.4: (a) Schematic of the sample structure and the experimental geometry. (b) Representative TR-MOKE trace for CMG/Pt(6 nm) sample at an in-plane bias magnetic field (H) of 290 mT and pump fluence of 10 mJ/cm^2 showing three temporal regimes.

Figure 7.5(a) shows the typical TR-MOKE signals at short delay time measured in CMG/Pt (1 nm) heterostructure at a pump fluence of 10 mJ/cm^2. The Kerr rotation signals show different behaviour with opposite signs when reversing the magnetic field. A small amount of nonmagnetic contribution in the transient Kerr rotation signals induces an antisymmetric difference between the reversed magnetization curves. The true ultrafast demagnetization curve is extracted by subtracting the Kerr rotation signals measured at opposite magnetic fields with equal magnitude (± 290 mT). Figure 7.5(b) shows the transient reflectivity and Kerr rotation signals at + 290 mT measured simultaneously in CMG/Pt (4 nm) at the same pump fluence. It is clear from the data that the Kerr rotation signal is much stronger than the transient reflectivity signal, implying negligible contribution of the nonmagnetic signal in the transient Kerr rotation signal. Nevertheless, even this negligible non-magnetic contribution is eliminated by subtracting the Kerr signals measured at opposite magnetic fields.

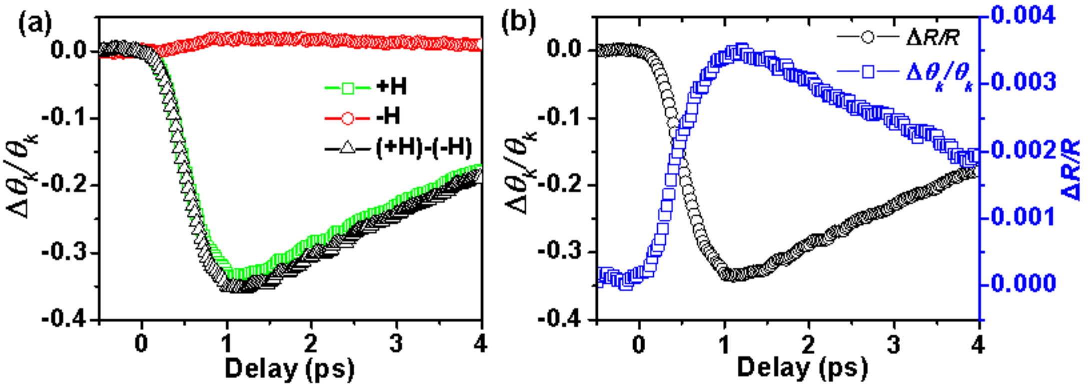

Figure 7.5: (a) Time-resolved Kerr rotation signals measured under opposite magnetic fields (green and red) of ±290 mT and the subtracted signal showing the true ultrafast demagnetization and fast remagnetization (black). (b) Time-resolved reflectivity and Kerr rotation signals under positive field (+290 mT) of CMG/Pt (1 nm) heterostructure at pump fluence of 10 mJ/cm^2.

The ultrafast demagnetization and fast remagnetization of CMG/Pt(t) heterostructures are shown in Figure 7.6(a). These traces correspond to subtracted time-resolved Kerr signals measured for magnetic fields of same strength but opposite sign in order to filter out nonmagnetic contributions, if present, in the Kerr signal. The following expression derived from the phenomenological three-temperature model (3TM) [50] is used to fit the experimental data and to further extract the ultrafast demagnetization time (τ_m) and the fast remagnetization time (τ_e):

$$\frac{-\Delta M_z}{M_z} = \left[\left\{\frac{A_1}{(t/\tau_0+1)^{\frac{1}{2}}} + \frac{A_1\tau_m - A_2\tau_e}{\tau_e - \tau_m} e^{-t/\tau_m} + \frac{A_2\tau_e - A_1\tau_e}{\tau_e - \tau_m} e^{-t/\tau_e}\right\} H(t) + A_3\delta(t)\right] \otimes G(t). \qquad (7.1)$$

Here, A_1 represents the value of the normalized magnetization after equilibrium between electron, spin and lattice systems has been re-established following the demagnetization; A_2 relates to the initial electron temperature rise and to the maximum magnetization quenching during ultrafast demagnetization; A_3 represents the magnitude of the state-filling effect during pump-probe temporal overlap, associated with a Dirac-delta function ($\delta(t)$). τ_0 is the timescale of heat diffusion. $H(t)$ and $G(t)$ are the Heaviside step function and Gaussian function, respectively. The change in Kerr rotation ($\Delta\theta_k$) for all samples is normalized by the total Kerr rotation (θ_k) and fitted with equation 7.1. Variation of the extracted τ_m and τ_e are shown in

Figure 7.6(b) and 7.6(c). The ultrafast demagnetization time τ_m is found to decrease monotonically from 471 ± 34 fs to 354 ± 14 fs with the increase of Pt thickness. A clear decreasing trend in the magnetization quenching is observed with increasing t that can be ascribed to the decrease in absorption of laser energy by the magnetic CMG film below the Pt overlayer. The variation of magnetic quenching is quantified by A_2 and the fast remagnetization state at equilibrium by A_1, both shown in Figure 7.6(d).

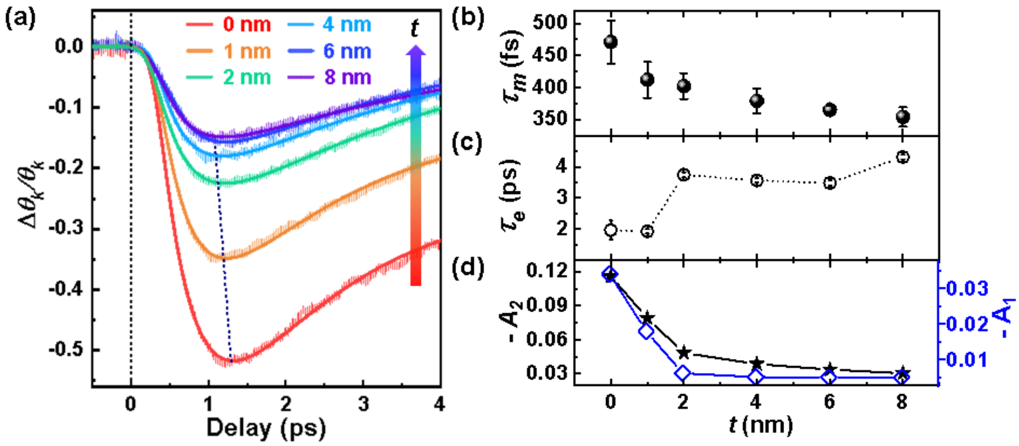

Figure 7.6: (a) Time-resolved Kerr rotation showing ultrafast demagnetization and fast remagnetization of CMG/Pt(t) heterostructures. Variation of (b) the ultrafast demagnetization time τ_m, (c) the remagnetization time τ_e, (d) $-A_1$(left axis) and $-A_2$ (right axis) with Pt thickness (t).

There are two predominant microscopic mechanisms responsible for the ultrafast demagnetization of magnetic materials. One is the SFS that includes Elliot-Yafet-like electron-phonon or electron defect scattering [48], Coulomb scattering [47], electron-magnon scattering [112], relativistic spin-flip scattering [49] etc. The second mechanism is based upon spin transport [51] due to laser-excited hot electrons. In the presence of good spin absorptive (or spin sink) material, here Pt, adjacent to CMG, and in combination with a spin-transparent CMG/Pt interface, a spin current generation from CMG to Pt is expected, thereby enhancing the ultrafast demagnetization rate of Pt, in accordance with our experimental observations.

Subsequently, we have studied the precessional dynamics including the damping and its variation with Pt thickness, as shown in Figure 7.7(a). Due to the relatively high thickness of CMG (higher than the optical penetration depth), excited spin-waves (SWs) propagate through the sample thickness, hence yielding perpendicular standing SW (PSSW) modes in addition to the uniform Kittel mode. To extract the effective Gilbert damping, it is necessary to find out the decay times of different dynamical modes of the precession and the effective magnetization. After eliminating the exponential background of slow relaxation, the precessional Kerr oscillation is fitted with the following expression to extract the decay times:

$$\theta_k = Ae^{-t/\tau}\sin(2\pi ft+\delta) + A_{\mathrm{PSSW}}e^{-t/\tau_{PSSW}}\sin(2\pi f_{\mathrm{PSSW}}t+\delta_{\mathrm{PSSW}}) \qquad (7.2)$$

Where τ and τ_{PSSW} are the decay times of uniform Kittel and PSSW modes with frequencies f, f_{PSSW} and amplitudes A, A_{PSSW}, respectively. Precessional dynamics for all samples are measured at different bias magnetic fields (*H*) ranging from 140 to 290 mT and the corresponding frequency values calculated from the FFT power spectra are plotted as a function of the applied bias magnetic field (H) (as shown in Figure 7.7(b) for *t* = 0, 1 and 6 nm). This allows to extract the effective magnetization (M_{eff}), Landé *g*-factor and the exchange stiffness constant (A_{ex}) using the theoretical expression given by [174]:

$$f = \frac{\gamma}{2\pi}\sqrt{\left(H+\frac{2A_{\mathrm{ex}}}{M_{eff}}\left(\frac{n\pi}{d}\right)^2\right)\left(H+M_{eff}+\frac{2A_{\mathrm{ex}}}{M_{eff}}\left(\frac{n\pi}{d}\right)^2\right)} \qquad (7.3)$$

where $\gamma = g\mu_B/\hbar$ is the gyromagnetic ratio ($\hbar = \frac{h}{2\pi}$, the reduced Planck constant), n is the order of PSSW mode and *d* is the thickness of the CMG film.

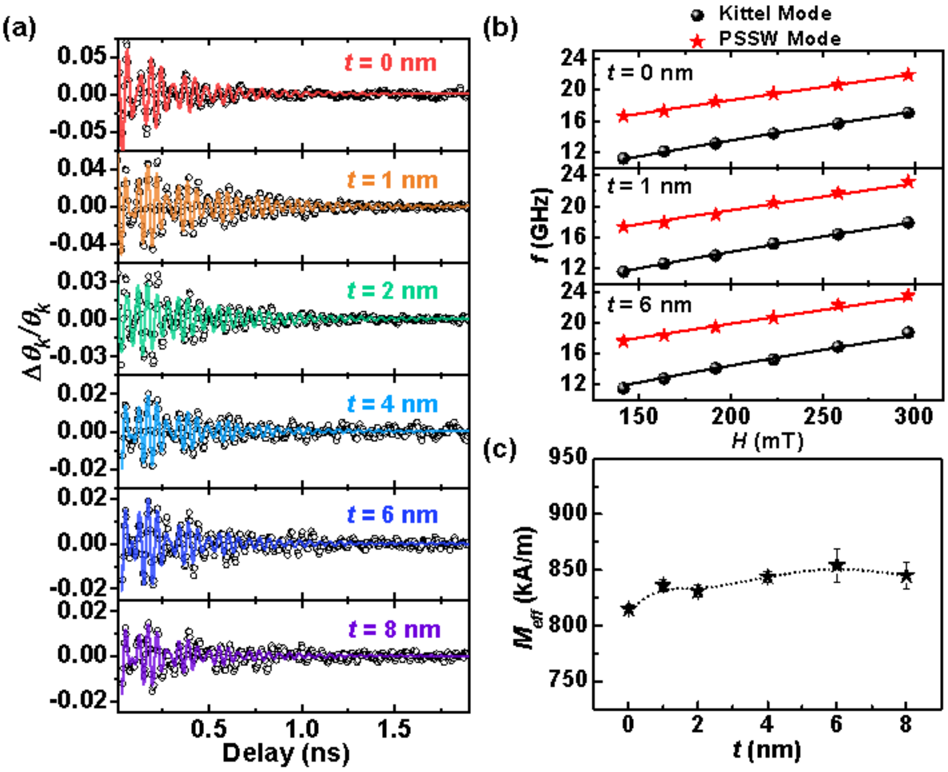

Figure 7.7: (a) Background subtracted time-resolved Kerr rotation showing the damped magnetization precession of CMG/Pt (*t*) heterostructures at a pump fluence of 10 mJ/cm^2 at an in-plane external bias magnetic field (*H*) of 290 mT. Symbols represent experimental data and solid lines represent theoretical fits using equation 7.2. (b) Precessional frequency (*f*) as a function of external magnetic field (*H*) for *t* = 0, 1, and 6 nm. Symbols represent extracted *f* from the FFT power spectra at different *H* values and solid lines represent fits using equation 7.3. (c) Variation of M_{eff} with *t*.

The uniform Kittel mode corresponds to $n = 0$, while $n = 1$ stands for the 1st order PSSW mode. The extracted M_{eff} as a function of t is shown in Figure 7.7(c). For almost all the film stacks, M_{eff} is found to be close to the saturation magnetization M_s, which indicates that the dead layer and the interface anisotropy are negligible in these heterostructures. A marginal enhancement in the g-factor (~ 2.02) for the CMG/Pt heterostructures is observed with respect to the bare CMG layer (1.95) [275]. Previous reports have demonstrated similar enhancement of the g-factor in ferromagnet/nonmagnet (FM/NM) heterostructures, attributed to a charge transfer mechanism from $5d$ to $3d$ electrons upon formation of the FM/NM interface, and a corresponding change of magnetic moment [276]. The value of A_{ex} is determined to be 10.4 ± 0.3 pJ/m from the fit of the PSSW mode, comparable to the exchange stiffness value obtained from FMR measurements on an 80-nm-thick CMG film [275].

Next, we have estimated both the effective damping coefficients α and α_{PSSW} corresponding to the Kittel and the PSSW mode using the following expression [134]:

$$\alpha = \frac{1}{\gamma\tau(H+M_{\mathrm{eff}}/2)} \tag{7.4}$$

In a standard FM/NM heterostructure, there are two dominant contributions to this effective magnetic damping. One is the inevitable local spin-flip scattering that causes energy dissipation within the FM itself [164], while another one is the energy dissipation from the FM to the adjacent NM layer, which is nonlocal (*e.g.*, due to so-called spin pumping) and controllable (via the NM thickness). The coherent magnetization precession of the FM results in an out-of-equilibrium spin accumulation at the FM/NM interface, which then dissipates gradually in the adjacent NM by generating a pure spin current, thereby enhancing the effective damping in the heterostructure. This mechanism is known as spin pumping [22]. The extracted damping coefficients corresponding to the Kittel mode (α) and the PSSW mode (α_{PSSW}) for different values of Pt thickness (t) are shown in Figure 7.8(a). In the presence of Pt, both α and α_{PSSW} are lower than for the bare CMG film. This may be due to the local modification of the spin-orbit interaction near the interface [277], and/or to spin polarization from the CMG/Pt interfacial density of states. However, enhancements in α and α_{PSSW} values are observed with the increase in Pt thickness (shown in blue and black shaded regions of Figure 7.8(a)), which supports the generation of pure spin currents through the CMG/Pt interface.

The flow of spin current through the interface is characterized by the intrinsic and effective spin-mixing conductance. The intrinsic spin-mixing conductance ($G_{\uparrow\downarrow}$) is the electronic conductance properties of the spin channels, when the NM thickness is much higher than the spin-diffusion length (λ). The effective spin-mixing conductance (G_{eff}) considers the spin backflow factor and it approaches asymptotically the intrinsic spin-mixing conductance ($G_{\uparrow\downarrow}$) with the increasing the NM layer's thickness beyond λ. Due to the significantly lower resistivity of Pt compared to Co_2MnGa, we applied the ballistic spin transport model, neglecting the resistivity of NM. In contrast to the ballistic method, which implies fast spin current transfer for $t \ll \lambda_{mfp}$ where λ_{mfp} represents the mean free path of Pt, the resistivity of Pt is taken into the calculation of $G_{\uparrow\downarrow}$ using the diffusion model, resulting in a higher estimation of spin-mixing conductance. So, in the ballistic spin-transport model, the damping is related to the intrinsic spin-mixing conductance as follows [271,272]:

$$\alpha = \alpha_0 + \frac{G_{\uparrow\downarrow}\left(1-e^{-\frac{2t}{\lambda}}\right)g\mu_B}{4\pi d M_{\text{eff}}} \tag{7.5}$$

Here, α_0 denotes the intrinsic Gilbert damping parameter in the absence of any NM, d is the FM thickness. In the presence of Pt, we have fitted α as a function of t using equation 7.6, as shown in Figure 7.8(c), while keeping α_0, $G_{\uparrow\downarrow}$ and λ as the fitting parameters. We found α_0 = 0.0100 ± 0.0004, $G_{\uparrow\downarrow} = (1.73 \pm 0.02) \times 10^{16}$ cm^{-2} and $\lambda = 2.9 \pm 0.2$ nm. Noteworthily, this value of $G_{\uparrow\downarrow}$ is found to be the highest known among the reported values for any FM/NM heterostructure.

Despite various anterior theoretical models [86], Zhang *et al.* first introduced the role of spin transport to the ultrafast demagnetization process in terms of the relation between demagnetization time (τ_m) and Gilbert damping (α). They demonstrated that for heterostructures and multilayers: a relationship of proportionality between τ_m and α indicates the dominant role of spin-flip scattering behind ultrafast demagnetization [91,278], while a proportional relationship between the ultrafast demagnetization rate, i.e. $\Delta(1/\tau_m) = (1/\tau_m)|_t - (1/\tau_m)|_{t=0}$) and modulation in Gilbert damping ($\Delta\alpha = \alpha - \alpha_0$; where α represents the Gilbert damping parameter in the presence of non-local effects such as spin pumping, and α_0 is the intrinsic Gilbert damping of the ferromagnetic system, free from extrinsic effects. α_0 is found to be 0.0100 ± 0.0004 from the fit of α vs. t using equation 7.5, as shown in Figure 7.8(b)) highlights the dominating role of spin currents via interfacial spin-chemical potential (μ_s) which is itself proportional to the spin accumulation at the interface [92]. Figure 7.8(c) clearly shows that $\Delta(1/\tau_m)$ vs. $\Delta\alpha$ for different t follows a proportional relationship, thus revealing the dominant role of interfacial spin transport in our system. This allows us to find the value of μ_s through the following expression [92]:

$$\Delta\frac{1}{\tau_m} = \frac{\mu_s}{\hbar}\Delta\alpha, \tag{7.6}$$

where ħ is the reduced Planck constant. In turn, the interfacial spin-chemical potential μ_s is found to be 60 ± 7 meV at the CMG/Pt interface.

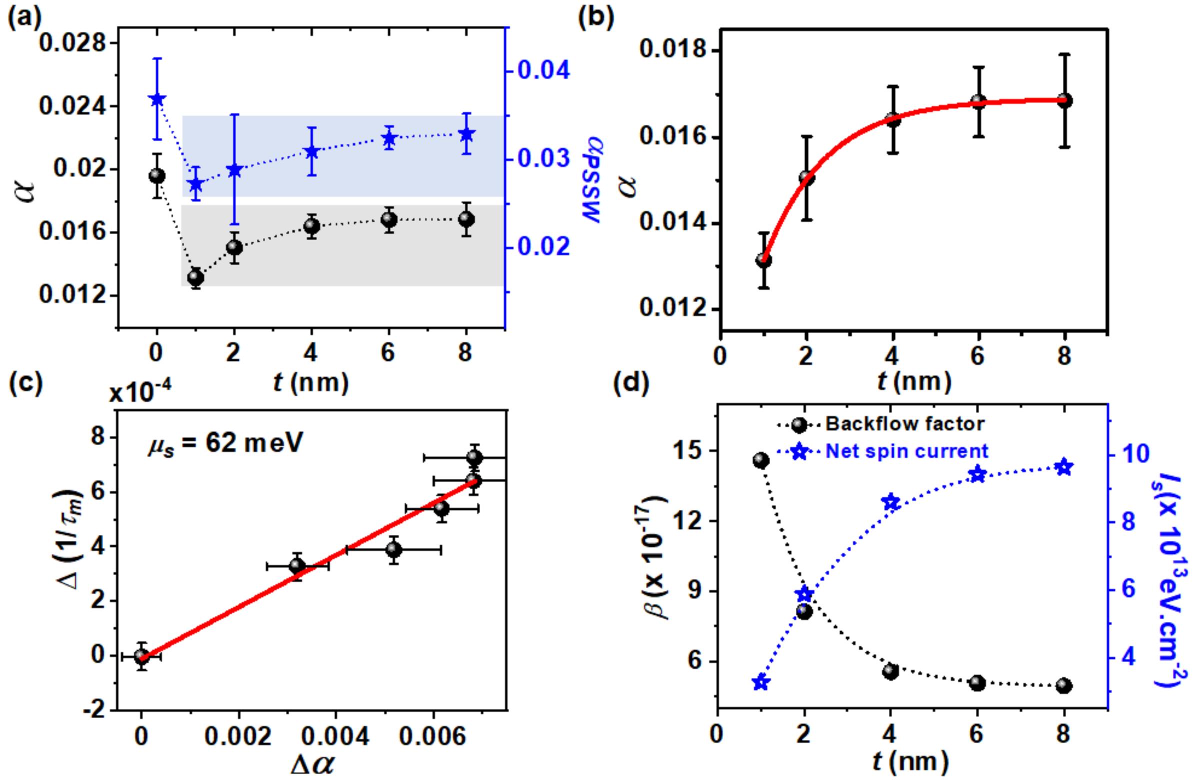

Figure 7.8: (a) Variation of damping coefficient (α) of Kittel mode (solid circular symbols) and PSSW mode (solid star symbols) with the Pt thickness, *t*. The in-plane external bias magnetic field (*H*) is 290 mT, and the pump fluence equal to 10 mJ/cm^2. Dashed lines are a guide to the eye. (b) Dependence of α as a function of Pt thickness, *t*. The solid line is a fit to equation 7.5. (c) Variation of the ultrafast demagnetization rate $\Delta(1/\tau_m)$ in fs^{-1} as a function of the modulation of effective Gilbert damping ($\Delta\alpha$) for CMG/Pt(*t*) heterostructures. (d) Variation of back-flow factor (β) and net spin current (I_s) with *t*.

The generated net spin current $\vec{I}_s$ consists of a pumped spin current $\vec{I}_s^{\text{pump}}$ from FM to NM and a spin backflow current $\vec{I}_s^{\text{back}}$ which returns into the FM after reflecting back from the outer surface of the NM [22,121]. The flow of spin angular momentum across the NM/FM interface is determined by the interplay between the I_s^{pump} and I_s^{back}. This spin backflow can be quantified by the spin backflow factor β:

$$\beta = \left(2\pi G_{\uparrow\downarrow}\sqrt{\frac{\varepsilon}{3}}\,tanh\left(\frac{t}{\lambda}\right)\right)^{-1} \tag{7.7}$$

Here, $\varepsilon\left(=\frac{Z_{Pt}e^2}{\hbar c}\right)$ is the spin-flip probability. For Pt, ε takes the value of 0.105 [279]. The dependence of the magnitude of net spin current, I_s, on β and interfacial μ_s follows [161]:

$$I_s = \mu_s/4\pi\beta. \tag{7.8}$$

The variations of β and I_s as a function of *t* are shown in Figure 7.8(d). The enhancement of *t* decreases the backflow probability, thus resulting in an enhanced net spin current.

According to the spin Hall magnetoresistance model [280], the pumped-out spin current from the FM is not fully transferred to the NM layer. This can be parameterized as the interfacial spin transparency (*T*) which is correlated with the magnitude of $G_{\uparrow\downarrow}$ by the following expression:

$$T = \frac{G_{\uparrow\downarrow}tanh\left(\frac{t}{2\lambda}\right)}{G_{\uparrow\downarrow}coth\left(\frac{t}{2\lambda}\right)+\frac{h}{2\lambda e^2\rho}} \tag{7.9}$$

Where ρ is the resistivity of the NM at room temperature. Taking our experimental value of ρ = 39.5 µΩ.cm for Pt, we obtain a sizeable value for the spin transparency *T* = 0.83 ± 0.01 using equation 7.9, comparable with $Co_2Fe_{0.4}Mn_{0.6}Si$/Pt interfaces [279].

The effective spin-mixing conductance (G_{eff}) takes care of the spin-backflow factor, thus depends on the Pt thickness (*t*) as follows:

$$G_{eff} = G_{\uparrow\downarrow}\left(1 - e^{-\frac{2t}{\lambda}}\right) \tag{7.10}$$

As t increases G_{eff} approaches the intrinsic spin-mixing conductance ($G_{\uparrow\downarrow}$) asymptotically in the regime of the negligible spin backflow current, as shown in Figure 7.9(a).

Finally, to directly examine any other possible interfacial effects that are affecting the damping in these heterostructures, we have introduced a Cu spacer layer between the CMG and Pt layers [281] to decouple the CMG/Pt interface and the ensuing effects like spin-memory loss and two-magnon scattering. Having very small SOC strength and spin-flip scattering probability, Cu exhibits a very long spin-diffusion length. Thus, the insertion of a thin Cu layer between CMG and Pt does not influence the spin-pumping-induced damping of CMG, while if other interfacial effects are present that will be noticeable in the modulation of damping. Therefore, to examine other interfacial effects, a Cu spacer layer of 2 nm thickness is introduced between CMG(42 nm) and Pt(8 nm) layers and magnetization precession is measured as shown in Figure 7.9(b). The corresponding α is found to be 0.017 which is approximately the same as that of CMG/Pt (8 nm) heterostructure. The invariance of α with the insertion of Cu spacer confirms that the CMG/Cu interface is transparent for spin-pumping and other possible interfacial effects for damping are negligible.

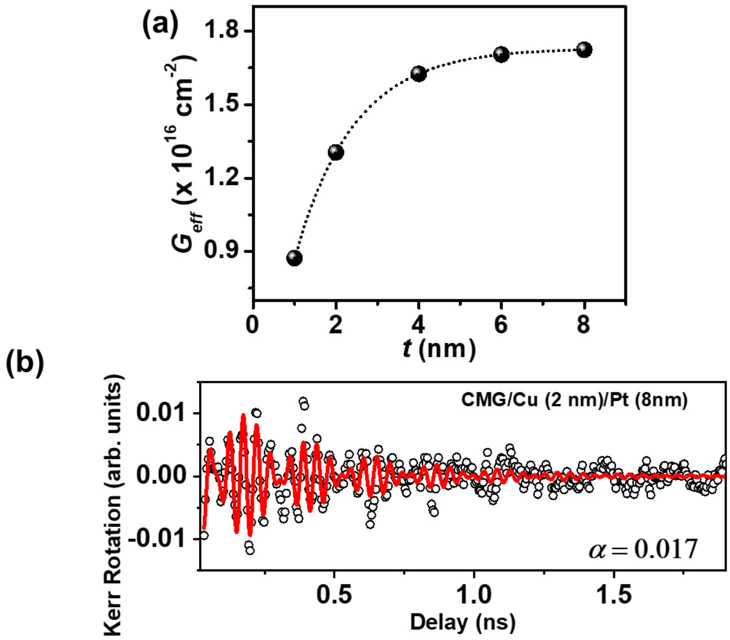

Figure 7.9: (a) Variation of the effective spin-mixing conductance ($\boldsymbol{G_{eff}}$) as a function of Pt thickness (t). (b) Background subtracted time-resolved Kerr rotation showing the damped magnetization precession of CMG/Cu(2 nm)/Pt(8 nm) heterostructures with a pump fluence of 10 mJ/cm^2 at an external bias magnetic field of 290 mT. Symbols represent experimental data points and the solid line represents fit using equation 7.2.

Below, and following our detailed investigation of the magnetization dynamics over time scales which cover several orders of magnitude, we put forward a schematic three stages process. After the laser excitation, both the majority and minority electrons are excited from *d* bands to *sp*-like conduction bands above the Fermi level. It is worth noting that a large difference in velocities or lifetimes of majority and minority spins affects the transport properties of the laser-induced hot electrons. Having a very short lifespan, minority spins are slowed down and within 100 fs decay to nonmobile *d* bands almost at the same position at which they were excited (Figure 7.10(a)). Conversely, the majority spins having higher velocities, along with longer lifetimes, leave the excited region immediately (after excitation with ~ 1 nm/fs velocity), resulting in the part of quenching of the net magnetization. Another part of quenching occurs due to the back flux of minority spins from NM. The electrons that escaped from the FM experience inelastic scattering in the NM and excite electrons that have a random velocity direction. A portion of these electrons forms a flux from NM to FM (Figure 7.10(b)). Majority spins continue to diffuse within FM while minority spins experience a significant deterioration in their interfacial transport. Consequently, the minority spins become trapped after reaching the interface, and contribute to the built-in interfacial spin accumulation; which one eventually relaxes over the electronic spin-relaxation time.

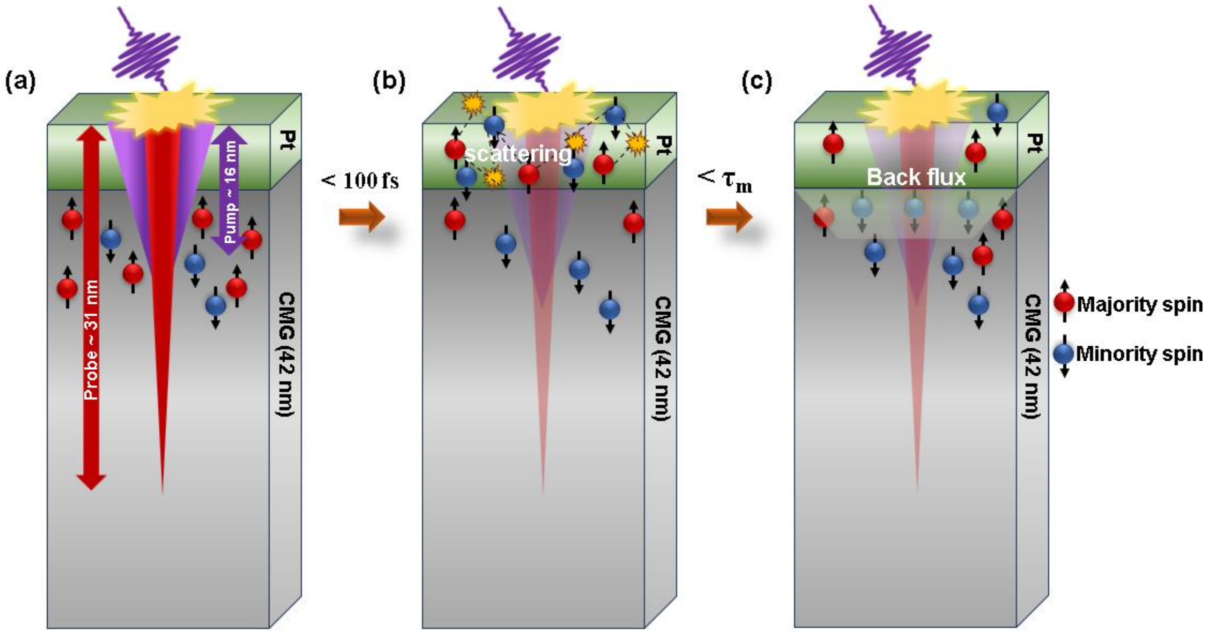

Figure 7.10: (a) Excitation of majority and minority spins within CMG after laser excitation. (b) Transmitted majority spins from CMG to Pt experience inelastic scattering and excite electrons in Pt that have a random velocity direction. (c) Following the ultrafast demagnetization process (with time constant τ_m), a fraction of electrons forms a back flux of spin polarized current from Pt to CMG where majority-spin electrons diffuse whereas minority-spin electrons face a decay in transmission and accumulate at the interface.

7.4 Conclusion

In summary, we have investigated the magnetization dynamics in magnetic Weyl semimetal, Co_2MnGa/Pt heterostructures using time-resolved magneto-optical Kerr effect magnetometry. Our observations show that the demagnetization time decreases and the damping coefficient increases exponentially with increasing Pt thickness, indicating the dominant role of spin transport. Employing a ballistic spin-transport model, we determined an ultrahigh intrinsic spin-mixing conductance in the Co_2MnGa/Pt heterostructure of $(1.73 \pm 0.02) \times 10^{16}$ cm^{-2}. Additionally, we demonstrated the variation of the spin backflow factor and net spin current with Pt thickness, estimating the interface spin transparency to be 0.83 ± 0.01. Overall, this study is a comprehensive investigation of the role of spin transport on femtosecond to nanosecond magnetization dynamics in a magnetic Weyl semimetal, establishing these materials as viable candidates for future spintronics devices. The use of materials, or more significantly of combinations of materials, in engineered heterostructures that efficiently generate and transfer spin current are crucial for improving magnetic data storage devices. From the femtosecond laser-induced spin dynamics, we observed high spin-mixing conductance and interfacial spin transparency in Co_2MnGa/Pt, along with the tuneable spin-transport-induced Gilbert damping and ultrafast demagnetization time of Co_2MnGa, make it an advantageous material for pure spin current-based devices and spintronics-photonic circuits. The spin-mixing conductance and interfacial spin transparency at the Co_2MnGa/Pt interface are significantly higher than those in widely used FM/NM heterostructures [136], facilitating efficient spin information transfer and proving Co_2MnGa to be an excellent pure spin current source with a robust spin pumping effect. The thickness-dependence of the Gilbert damping and ultrafast demagnetization time provide essential guidelines for selecting suitable external conditions for specific device applications. However, for spin-based device applications, these parameters can be further tuned by selecting NM materials with higher effective spin Hall angles, adjusting the fluence and irradiation time of laser pulses, and modifying the thickness of Co_2MnGa, indicating that this system does not represent the fundamental limit for tuning and optimization of these critical parameters. In contrast to previous studies that focused on the role of Weyl points on the ultrafast spin dynamics overlooking super-diffusive spin transport [282,283], our research underscores its significant impact on ultrafast spin dynamics, potentially opening avenues for spin-orbitronics devices based on super-diffusive spin transport in Weyl semimetals. Additionally, strategies such as applying electric fields, strain, or doping to induce diverse interfacial spin-orbit coupling effects may enable precise control over critical spin-transport parameters and ultrafast magnetization quenching in magnetic Weyl semimetal thin films.

CHAPTER 8

Magnetic Anisotropy Controlled Ultrafast Demagnetization in Heavy Metal/CoFeB Heterostructures with Varying CoFeB Thickness

8.1 Introduction

Ultrafast demagnetization [35], a sub-hundreds of femtosecond (fs) phenomena is a key in AOS that plays a crucial role in spintronics devices. A powerful optical laser pulse has the ability to disrupt the magnetic alignment within a magnetic substance in a fraction of a second. This phenomenon is called the ultrafast demagnetization. During this process, the magnetization of the magnetic material can be partially or completely extinguished, which is referred as the magnetic quenching, followed by its partial restoration upon cooling down from the temporary excited state. After the first experimental observation of ultrafast demagnetization by Beaurepaire *et al*. [35] in 1996, the scientific community continues to engage in intense debates regarding the actual microscopic mechanism responsible for this magnetization quenching. Based on the phenomenological 3TM by Beaurepaire *et al*., the excitation of the magnetic materials by a femtosecond laser pulse creates hot electrons and these hot electrons transfer energy to interconnected systems like spins and lattice, resulting in a rapid rise in spin temperature that causes demagnetization. In 1997, Hübner and Zhang [39] proposed that ultrafast demagnetization is a consequence of exchange interaction and SOC. Later, in 2000, they suggested that it is a collective effect arising from the interaction of the applied laser field and SOC in FM [40]. Subsequently, various models have demonstrated that the change in spin angular momentum is responsible for different types of SFS [47-49,112,113]. It is widely believed that the SOC strength determines the spin angular momentum transfer rate [48,131], speeding up the demagnetization rate. In contrast, in 2010, Battiato *et al*. [51] introduced a novel framework for optically induced SST and Malinowski *et al*. [50] first demonstrated experimentally that transfer of interlayer spin-angular momentum can accelerate the demagnetization process. Recent studies [161,284] have shown that not only the SOC of FM, the SOC of NM also significantly influences the demagnetization time (τ_m) in nonmagnet/ferromagnet (NM/FM) heterostructures. The presence of NM heavy metals creating an interface with transition metal FM alters the interfacial orbital angular momentum of the transition metal FM, resulting in an enhanced spin-orbit interaction, thereby increasing the PMA [285]. PMA is also present at the interfaces of transition metal FMs and nonmagnetic oxides such as MgO and AlO_x. This is due to the unique bonding interactions between the metal and oxygen ions at the interface. Notably, significant interface PMA has been reported in HM/CoFeB/MgO structures, which are fundamental to MTJs [286]. With the reduction in CoFeB thickness, the orientation of the magnetic easy axis shifts from IP to OOP [287]. Experimental evidence indicates that the adjacent NM underlayer on the opposite side of the CoFeB layer is crucial in influencing the strength of PMA [288,289]. Ta is still regarded as the best option for implementing high PMA in CoFeB/MgO structures. Although various studies [161,290] have been done on ultrafast demagnetization separately for PMA and in-plane magnetic anisotropy (IMA) samples, however there is a noticeable gap in the study of magnetic anisotropy dependent ultrafast demagnetization.

In this article, we have studied the ultrafast demagnetization of Ta (10 nm)/$Co_{20}Fe_{60}B_{20}$ (t)/MgO (2 nm)/Al_2O_3 (10 nm) by varying CoFeB thickness (t) to control the tic anisotropy from t = 1.3 - 3 nm with a transition thickness of 1.5 nm where the magnetization easy axis changes from OOP to IP orientation and studied the magnetic anisotropy controlled ultrafast demagnetization. A significant increase in magnetic quenching has been observed in the ultrafast demagnetization for OOP oriented samples compared to IP samples. This finding has been validated through measurements conducted on a different set of samples where Ta (5 nm)/Ru (20 nm)/Ta (5 nm) is used as a NM. In the latter case, OOP to IP transition thickness is changed to 1.7 nm because of the high surface quality. For both cases, the demagnetization time (τ_m) increases with the increase of CoFeB thickness. Different magnetization quenching and τ_m for different underlayer is due to the different bulk SOC of the NM. Therefore, one can optimize τ_m and magnetic quenching solely through the manipulation of the interfacial SOC, without altering the NM layer. This research will provide valuable insights for developing ultrafast operation of MTJs, STT-MRAM devices.

8.2 Experimental details

Sample Preparation:

The heterostructure stacks of Ta (10 nm)/$Co_{20}Fe_{60}B_{20}$ (t = 1.3, 1.4, 1.5, 1.8, 2, 3 nm)/MgO (2 nm)/Al_2O_3 (10 nm) and Ta (5 nm)/Ru (20 nm)/Ta (5 nm)/$Co_{20}Fe_{60}B_{20}$ (t = 1.2, 1.7, 3 nm)/MgO (2 nm)/Al_2O_3 (10 nm) for this study were deposited on top of Si/SiO_2 (700 nm) substrate using RF magnetron sputtering at a base pressure of ~10^{-8} Torr at room temperature. Here, Al_2O_3 is a capping layer that prevents the MgO and CoFeB layers from degradation with time. After deposition, the heterostructures were subjected to annealing at a temperature of 280°C under a perpendicular magnetic field of 600 mT in vacuum for an hour to ensure smooth interface with consistent distribution of magnetic properties [291]. For clarity, the heterostructures were described as Ta/CoFeB (*t*) and TRT/CoFeB (*t*) respectively throughout the manuscript.

Characterization:

The static magnetic hysteresis loops of the samples were measured using VSM associated with the PPMS system to ensure the CoFeB thickness dependent magnetic anisotropy. The layer thicknesses, interfacial roughness and SLD were investigated by XRR measurements.

The magnetization dynamics were studied using a TR-MOKE magnetometer based on a two-colour non-collinear pump-probe technique [34]. The TR-MOKE consists of a femtosecond amplified laser with a wavelength of 800 nm, having a pulse width of ~ 35 fs and a repetition rate of 1 kHz. A beam splitter is used to split the laser beam into two parts. One part of the fundamental laser beam is fed into the SHG and after frequency doubling (λ = 400 nm) we obtain the pump beam corresponding to a photon energy of 3.1 eV which is used to excite the sample. Another part of the fundamental beam (λ = 800 nm) of 1.55 eV photon energy is heavily attenuated which is used as the probe beam to detect the transient Kerr rotation. The pump beam is obliquely incident on the sample (~ 45° surface normal) and focused to a spot size of 300 μm. The probe beam is incident normally on the sample and focused to a spot size of 100 μm. The probe spot is carefully placed at the centre of the pump spot to probe the dynamics from a uniformly excited volume. The pump beam is chopped at a frequency of 373 Hz using an optical chopper and the back-reflected probe beam is collected in a dual photodetector assembly using a polarized beam splitter that captured the reflectivity and Kerr rotation signal separately and simultaneously as a function of the delay time between pump and probe beams. During the course of the measurement, the pump and probe fluence were kept constant at 10 mJ/cm^2 and 1 mJ/cm^2, respectively, and a significant external magnetic field of 3 kOe is applied almost parallel to the sample plane. The data points from the experiment are collected at a time interval of 25 fs, guaranteeing accurate determination of τ_m. The experiments are carried out in ambient conditions and at room temperature.

8.3 Results and discussions

Static Characterization:

We conducted measurements of the IP hysteresis loop utilizing VSM at ambient temperature for Ta/CoFeB (*t*) and TRT/CoFeB (*t*), and the results of Ta/CoFeB (*t*) are shown in Figure 8.1(a). It is evident from the figure that an increase in the CoFeB thickness results in an increment in the squareness of the hysteresis loop, with the transition thickness from OOP to IP magnetization being 1.5 nm for Ta/CoFeB (*t*) samples.

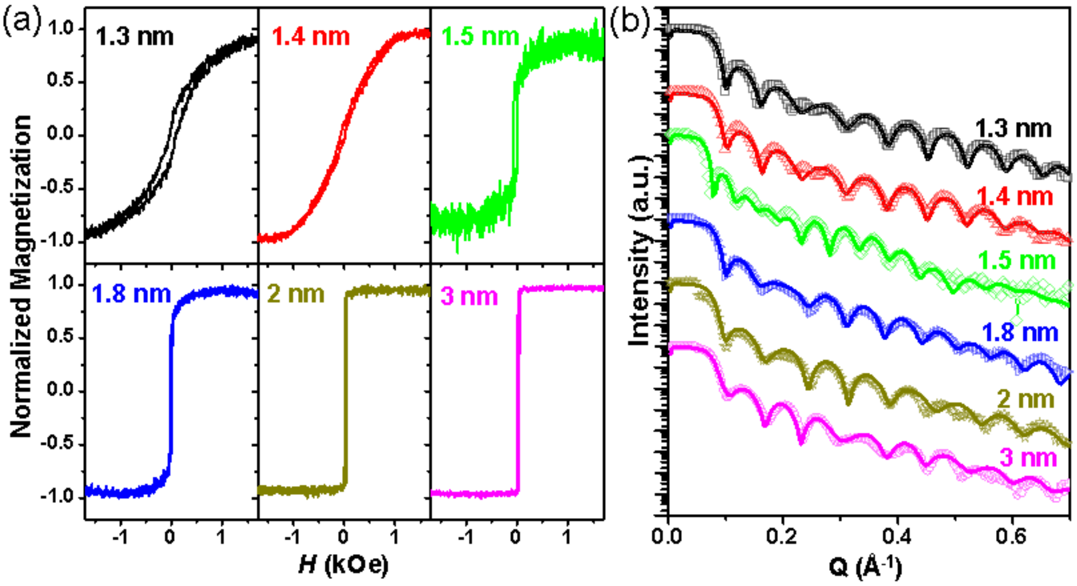

Figure 8.1: (a) In-plane magnetic hysteresis loops and (b) XRR spectra from Ta/CoFeB (*t*) heterostructures. In (b) coloured symbols represent the experimental data points and the solid lines are the theoretical fits. The thickness of CoFeB is shown next to each spectrum.

Figure 8.1(b) shows the XRR spectra of Ta/CoFeB (*t*) heterostructures measured using a 1.54 Å Cu-Kα x-ray source. The XRR spectra display distinct oscillations up to a scattering vector of 0.7 Å^{-1}, indicating uniform deposition of the films. The 'Reflex' software is used to analyze the XRR spectra from where the thickness, roughness and SLD of the different layers have been extracted. The SLD is directly related to the electron density of the material. The layer thickness values derived from the fits are observed to be in close proximity to their nominal thickness values. The values of interfacial roughness and SLD derived from the fits are presented in Table 8.1.

Table 8.1: Parameters obtained from the XRR analysis of Ta/CoFeB (*t*)/MgO heterostructures.

Heterostructure	**Layer**	**Thickness (nm)**	**Roughness (nm)**	**SLD (10^{-5}Å^{-2})**
Ta/CoFeB (1.3 nm)/MgO	MgO	2.05	0.9	3.08
	CoFeB	1.3	0.2	4.84
	Ta	8.4	0.35	10.3
	Sub	-	0.27	1.82
Ta/CoFeB (1.4 nm)/MgO	MgO	2.04	0.6	3.4
	CoFeB	1.4	0.2	4.65
	Ta	8.4	0.35	10.29
	Sub	-	0.27	1.82
Ta/CoFeB (1.5 nm)/MgO	MgO	2	0.4	2.48
	CoFeB	1.5	0.3	5.11
	Ta	9.9	0.7	7.14
	Sub	-	0.5	1.89
Ta/CoFeB (1.8 nm)/MgO	MgO	2.05	0.32	3.4
	CoFeB	1.8	0.45	5.87
	Ta	84.5	0.4	10.59
	Sub	-	0.7	1.82
Ta/CoFeB (2 nm)/MgO	MgO	2.05	0.8	3.08
	CoFeB	2	0.45	5.04
	Ta	8.14	0.37	9.46
	Sub	-	0.3	3.22
Ta/CoFeB (3 nm)/MgO	MgO	2.04	0.8	3.08
	CoFeB	2.98	0.45	5.66
	Ta	8.44	0.35	10.3
	Sub	-	0.27	1.82

In-plane magnetic hysteresis loops of TRT/CoFeB (*t*)/MgO for three CoFeB thicknesses are shown in Figure 8.2: one with high PMA (*t* = 1.2 nm), one at the transition thickness (*t* = 1.7 nm) and another one with an IP easy axis (*t* = 3 nm).

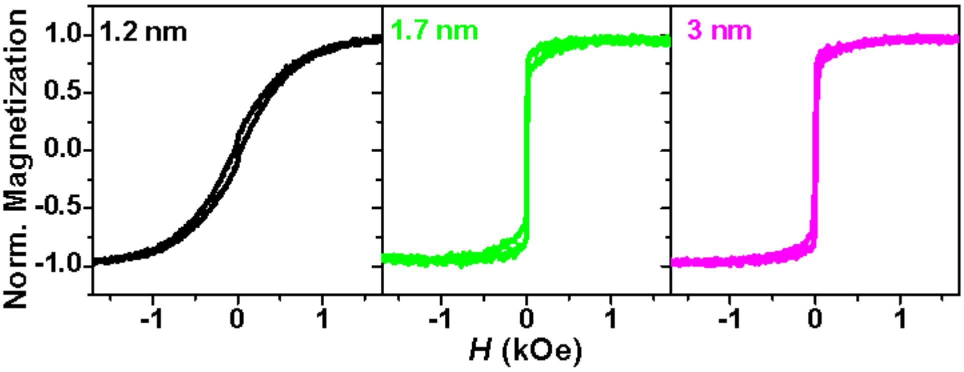

Figure 8.2: In-plane magnetic hysteresis loop for Sub/Ta (5 nm)/Ru (20 nm)/Ta (5 nm)/CoFeB (*t*)/MgO (2 nm)/AlO (10 nm) heterostructures. The thickness of CoFeB is shown in each graph.

Laser-induced ultrafast demagnetization:

Figure 8.3(a) depicts the schematic representation of the sample structure and the experimental geometry used in TR-MOKE measurements. Figure 8.3(b) shows the typical TR-MOKE signal at ultrafast timescale measured in Ta/CoFeB (1.3 nm) with the applied IP magnetic field of 3 kOe by reversing the magnetization direction (green and red symbols in Figure 8.3(b)) at a fixed pump fluence of 10 mJ/cm^2. The strength of the applied magnetic field is strong enough to align the magnetization of all samples along the x-direction. However, a minor nonmagnetic contribution blends into the transient MOKE signals, causing a slight asymmetric variation in the reversed TR-MOKE traces. The true ultrafast demagnetization signal (black symbols in Figure 8.3(b)) is obtained by taking half of the subtracted the time-resolved Kerr rotation signals recorded at opposite magnetic fields with equal strength.

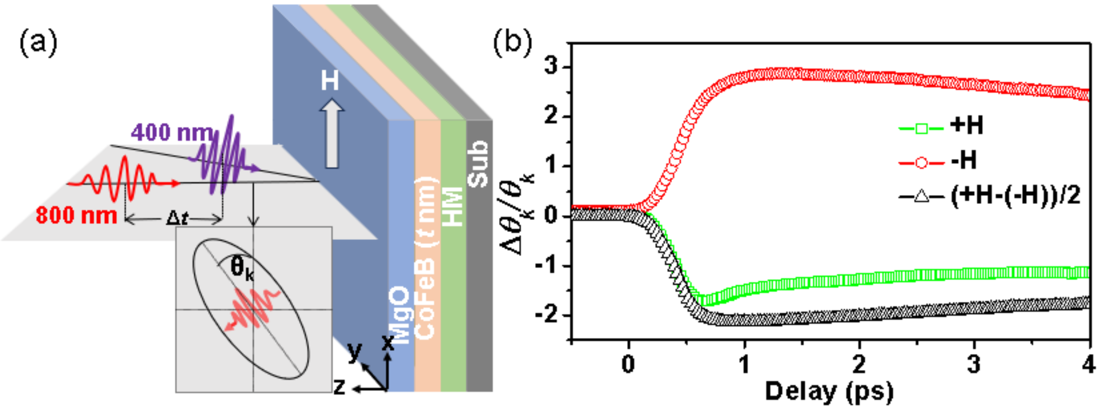

Figure 8.3: (a) Schematic of the TR-MOKE experiment. A pump pulse of 400 nm wavelength excites the heterostructure film, magnetized along the x-axis. The subsequent time evolution of magnetization is monitored by a time-delayed probe pulse by detecting the Kerr rotation of the reflected beam from the sample. (b) Time-resolved Kerr rotation signals measured under opposite magnetic fields (green and red symbols) of ± 3 kOe and half of the subtracted signal showing the true ultrafast demagnetization and fast remagnetization (black symbol) of Ta/CoFeB (1.3 nm) heterostructure at a pump fluence of 10 mJ/cm^2 is shown.

Figure 8.4(a) shows the time-resolved reflectivity data for Ta/CoFeB (t) at a fixed pump fluence of 10 mJ/cm^2. There has been minimal variation in the reflectivity amplitude of the samples with the variation of the CoFeB thickness. This indicates the similar absorption of photon energy for all samples. Figure 8.4(b) shows the laser induced ultrafast demagnetization and fast remagnetization process for the Ta/CoFeB (t nm) heterostructures measured under an IP magnetic field of 3 kOe and at a fixed pump fluence of 10 mJ/cm^2. The expression obtained from the phenomenological 3TM [50]. describes well the ultrafast demagnetization and the fast remagnetization process as follows:

$$\frac{-\Delta\theta_k}{\theta_k} = \left[\left\{\frac{A_1}{(t/\tau_0+1)^{\frac{1}{2}}} + \frac{A_1\tau_m - A_2\tau_e}{\tau_e-\tau_m}e^{-t/\tau_m} + \frac{A_2\tau_e - A_1\tau_e}{\tau_e-\tau_m}e^{-t/\tau_e}\right\}H(t) + A_3\delta(t)\right]\otimes G(t). \tag{8.1}$$

The above expression is derived from the concept that a magnetic system consists of three interconnected subsystems: electron, spin and lattice. According to the 3TM, when the system is excited by a femtosecond laser, the temperature of the electronic system rapidly rises, causing the hot electrons to occupy energy levels above the Fermi level. These hot electrons then stimulate the spin degrees of freedom through electron-magnon interaction, leading to an immediate decrease in the magnetization. Over time, the energy distribution among the three subsystems facilitates a quick recovery of the diminished magnetization. In equation 8.1, A_1 represents the post equilibrium magnetization value after equilibration of different subsystems: spin, electron and lattice. A_2 signifies the maximum magnetization quenching during ultrafast demagnetization and A_3 denotes the state filling from the temporal overlap of pump-probe, expressed by a Dirac delta function ($\delta(t)$). τ_0 represents the cooling time of heat diffusion. $H(t)$ and $G(t)$ are the Heaviside step function and Gaussian laser pulse, respectively. The ultrafast demagnetization time is represented by τ_m and the fast remagnetization time is described by τ_e illustrating the timescale of electron-phonon interaction. The temporal modification of the Kerr rotation ($\Delta\theta_k$) for all the measurements is normalized against the total Kerr rotation (θ_k) and then fitted with equation 8.1.

The factors influencing fs magnetization dynamics of a FM can be categorized into two groups: intrinsic factors which are dependent on the materials used and extrinsic factors which are dependent on experimental conditions like external magnetic field strength, field orientation and pump fluence. In our case, extrinsic factors remain constant throughout the study, exerting no influence on the dynamics. So only the intrinsic factors are responsible for the modulation in dynamics. Intrinsic factors encompass two distinct contributions. The first contribution is solely reliant on the FM material, which exhibits varying scattering probabilities and SOC strength depending on the material and thickness. The second contribution arises from the SST, which occurs due to the presence of a NM layer adjacent to the FM, facilitating the transfer of spin-angular momentum from the FM to the NM. The SOC strength of the NM materials, along with the spin accumulation at the interface, is crucial for the demagnetization of these heterostructures. One of our earlier studies showed that the spin accumulation at the interface is dependent upon the thickness of the NM layer [161]. The uniform thickness of Ta across all samples assures identical transport of spin current in a direction perpendicular to the interface. In the IMA thickness regime ($t \geq 1.5$ nm), an increase in the thickness of CoFeB may lead to a rise in Elliott-Yafet-like SFS events due to the increase in number of atoms. This phenomenon results in a prolonged duration for the local dissipation of spin angular momentum, along with the transport of spin from the CoFeB to the Ta.

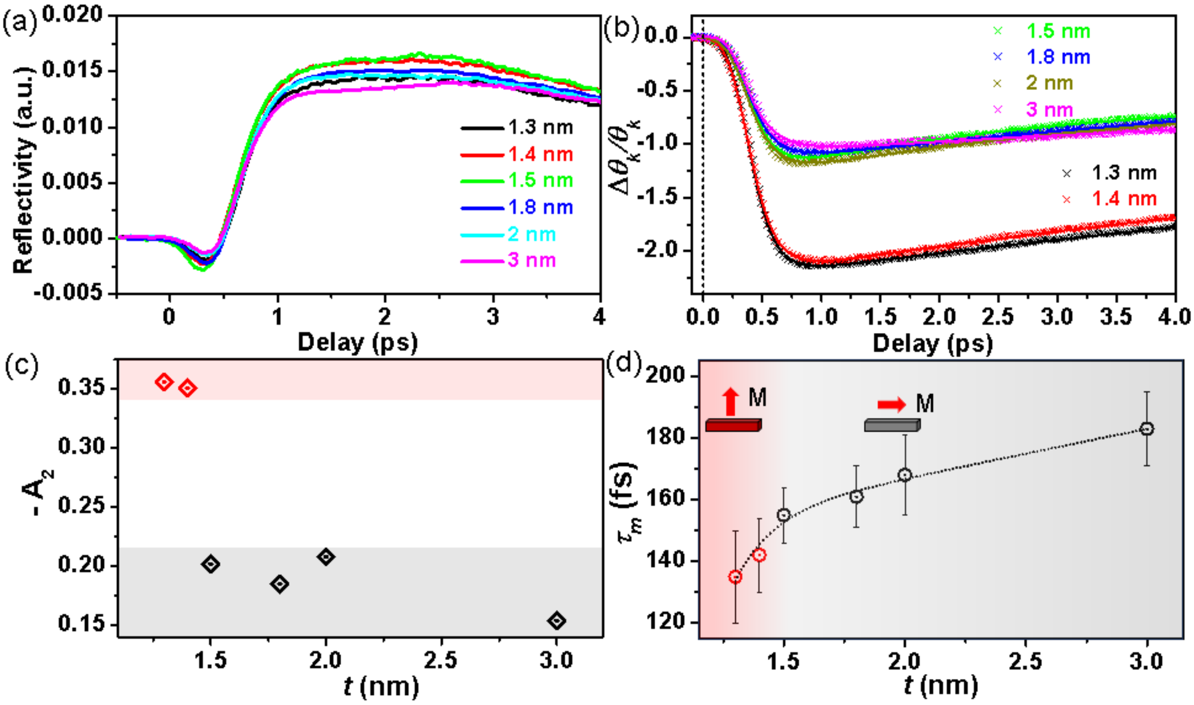

Figure 8.4: Time-resolved (a) reflectivity and (b) Kerr rotation showing ultrafast demagnetization and fast relaxation, in Ta/CoFeB (t) heterostructures. (c) Maximum magnetic quenching ($-A_2$) in PMA samples (red symbols) and IMA samples (black symbols) as a function of t. Maximum quenching is two times more in PMA samples as opposed to IMA samples. (d) Evolution of demagnetization time (τ_m) with CoFeB thickness (t nm). Red symbols and black symbols represent PMA and IMA samples, respectively.

Through both experimental methods and the first principles density-functional-theory calculations, Okabayashi *et al*. [285] have demonstrated that the interfacial orbital magnetic moments of FM in FM/NM structures exhibit anisotropy which promotes the PMA for thinner samples. The perpendicular component of the orbital moment ($m_{orb}^{\perp}$) is greater than the in-plane component ($m_{orb}^{\parallel}$). Conversely, these moments are isotropic in thicker IMA samples. The atomic sites of the FM demonstrate an overall positive energy, thereby validating the PMA driven by orbital momentum. The PMA energy can be expressed as [292-294]:

$$\Delta E_{PMA} = \frac{G}{H}\frac{\xi}{4\mu_B}(m_{orb}^{\perp} - m_{orb}^{\parallel}) \tag{8.2}$$

Where $G/H$are the band structure coefficients and $\xi$is the spin-orbit coupling parameter.

On the other hand, Boeglin *et al.* [295] have shown by distinguishing the orbital and spin moments in ultrafast dynamics that the reduction of the orbital momentum occurs more rapidly than the reduction of spin momentum. Furthermore, the attenuation of the orbital moment is greater than that of the spin moment. The above observation may explain our observation of significant quenching of magnetization in PMA samples ($t < 1.5$ nm), quantifiable by the fitting parameter A_2, as shown in Figure 8.4(c). Additionally, it highlights the accelerated ultrafast demagnetization time, as depicted in Figure 8.4(d), observed in PMA samples as opposed to the IMA samples.

Another set of heterostructures, TRT/CoFeB (t nm) is measured to verify the observation and ascertain whether the high quenching and faster demagnetization are salient characteristics of PMA samples or not. In this heterostructure, PMA to IMA transition thickness of CoFeB is 1.7 nm because of high surface quality. Three samples were analyzed: one with high PMA ($t = 1.2$ nm), one at the transition thickness ($t = 1.7$ nm) and another one with IMA ($t = 3$ nm). The time-resolved Kerr rotation signals showing the ultrafast demagnetization with fast remagnetization for TRT/CoFeB (t nm) fitted with equation 8.1 is shown in Figure 8.5(a).

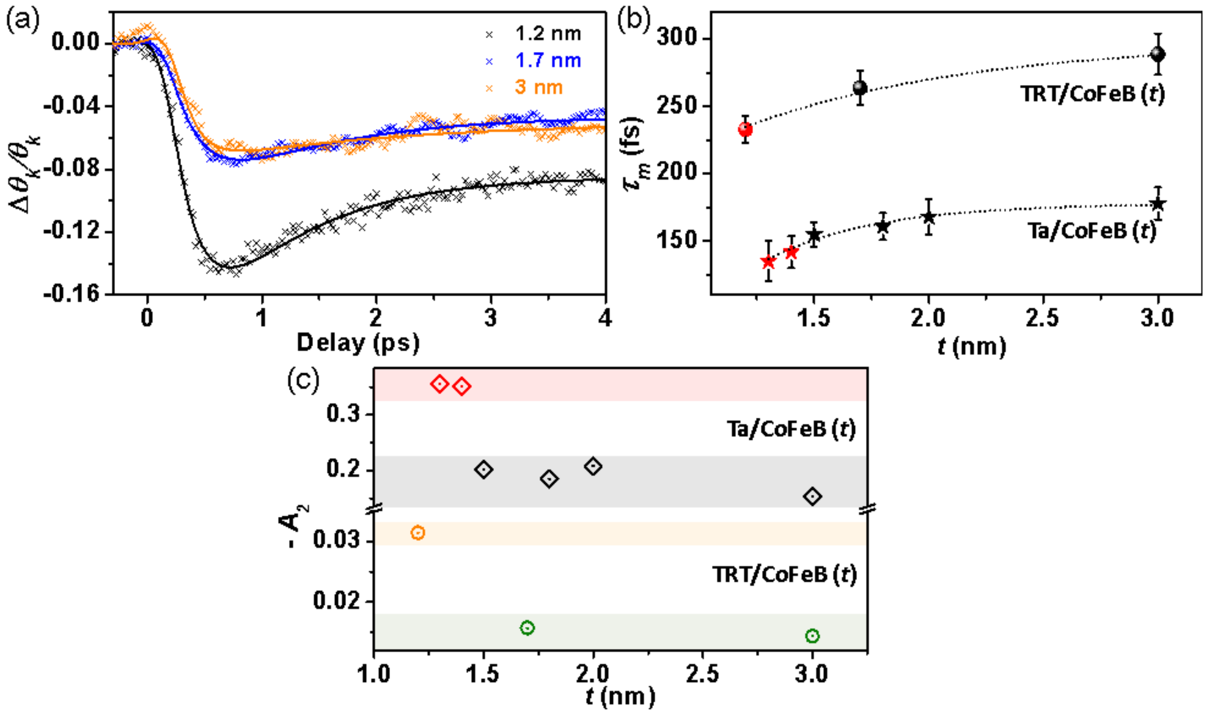

Figure 8.5: (a) Time-resolved Kerr rotation showing ultrafast demagnetization and fast relaxation in TRT/CoFeB (t) heterostructures. (b) Variation of demagnetization time (τ_m) with CoFeB thickness (t nm) in TRT/CoFeB and Ta/CoFeB (t) heterostructures. Red symbols and black symbols represent PMA and IMA samples, respectively. (c) Maximum magnetic quenching ($-A_2$) as a function of t for Ta/CoFeB (t) (square symbols, where red and black symbols indicate PMA and IMA samples, respectively) and TRT/CoFeB (t) (circular symbols, where orange and green symbols indicate PMA and IMA samples, respectively).

The consistent findings validate the origin of the higher quenching and faster demagnetization in PMA samples. In Figure 8.5(b), τ_m of these three heterostructures is plotted against t (nm), keeping Ta/CoFeB (t nm) as a reference for proper comparison. Maximum magnetic quenching is also illustrated in Figure 8.5(c) for comparative analysis of TRT/CoFeB (t) and Ta/CoFeB (t). The increase in τ_m by ~158% and decrease in magnetic quenching by one orders of magnitude for TRT/CoFeB as opposed to Ta/CoFeB (*t*) can be attributed to the comparatively weaker SOC strengths of TRT in comparison with Ta [284].

8.4 Conclusion

In summary, we have conducted a thorough investigation into the ultrafast demagnetization process by manipulating the magnetic anisotropy in Ta/CoFeB (*t*)/MgO and TRT/CoFeB (*t*)/MgO thin film heterostructures. Our approach involved the utilization of all-optical time-resolved magneto-optical Kerr effect magnetometry. We observed a significant magnetization quenching with faster demagnetization in heterostructures exhibiting PMA. Remarkably, for PMA samples the magnetization quenching is twice as that for IMA samples with slightly accelerated demagnetization. This additional quenching is shown to be not a result of difference in absorption of energy as validated through the time-resolved reflectivity data. The observed increase in magnetization quenching in PMA samples may be attributed to the anisotropic orbital magnetic moments in CoFeB responsible for PMA combined with the spin transport mechanism, which is a common mechanism in NM/FM heterostructures. In IMA samples, the longer demagnetization time with the increase of CoFeB thickness can be attributed to the local dissipation of spin-angular momentum by spin-flip scattering in conjunction with spin transport. Furthermore, a much slower demagnetization by about ~ 158% and drastic decrease in magnetization quenching by an order of magnitude in TRT/CoFeB (*t*) as opposed to Ta/CoFeB (*t*) can be attributed to much weaker bulk SOC strength of TRT than Ta. The results presented here will be useful for future PMR, MTJs, STT MARM devices.

CHAPTER 9

Summary and future perspective

9.1 Summary

In summary, we have explored the dynamics of magnetization across various spintronic materials, spanning timescales from femtoseconds to nanoseconds. Our investigation encompassed a range of phenomena, including ultrafast demagnetization, fast relaxation, and slow relaxation accompanied by magnetization precession and damping, within FM thin films, FM alloys, HM/FM heterostructures, and TMDs/FM heterostructures. The samples utilized in this research were fabricated using RF/DC magnetron sputtering, ion beam sputtering, and the pulsed reverse electrodeposition technique. Initial characterizations of these samples were conducted through XRD, XRR, AFM, and Raman spectroscopy. The static magnetic properties were assessed using static-MOKE and VSM. Additionally, we employed a custom-designed noncollinear time-resolved MOKE magnetometer to investigate the magnetization dynamics over the femtosecond to nanosecond timescale.

In this thesis, we investigated the ultrafast demagnetization and damping in β-Ta/CoFeB thin film heterostructures by using all-optical TR-MOKE magnetometry. The study involved systematically varying the thicknesses of both Ta and CoFeB. Our experimental results revealed a direct correlation between the ultrafast demagnetization rate and the modulation of damping, with interface spin transport identified as the prevailing mechanism for both processes. Notably, at higher thicknesses of β-Ta ($t \geq 7$ nm), the spin accumulation coefficient was found to be ~ 0.24 eV, approximately 1.8 times less than its value in the lower thickness regime ($t < 7$ nm). These findings have significant implications for the development of ultra-high-speed spin-orbitronic devices.

Soft magnetic materials with higher resistivity and moderate anisotropy field are potential core materials for high-frequency integrated magnetic passives, making them suitable for on-chip power supply devices. We have investigated the ultrafast magnetization dynamics of electrodeposited cobalt phosphorus (CoP) alloy, focusing on the in-plane magnetic orientation (φ) dependence. The precession frequency analysis reveals a dominant two-fold anisotropy along with a moderate four-fold anisotropy, while the Gilbert damping coefficient exhibits a four-fold anisotropy with respect to φ. Interestingly, the ultrafast demagnetization is observed to be nearly isotropic across different values of φ. It is hypothesized that the SOC significantly influences these anisotropic precessional dynamics, although the role of anisotropic SOC in ultrafast spin-flip scattering processes under highly non-equilibrium conditions appears to be negligible.

TMDs have attracted significant attention due to their strong SOC and the distinct layer number dependence in relation to spin–valley coupling. This presents the potential to manipulate the spin degree of freedom of the FM in thin film heterostructures and could be of interest for future spin-based devices. In this study, we have experimentally shown the odd–even layer dependence of WS_2 nanolayers through measurements of ultrafast magnetization dynamics in WS_2/Co_3FeB thin film heterostructures conducted through time-resolved Kerr magnetometry. The fluence dependent magnetic damping (α) indicates the presence of broken symmetry and the prevalence of intra- and interband scattering for even and odd layers of WS_2, respectively. The longer demagnetization time, τ_m, in 3 and 5 layers of WS_2 suggests an interplay between spin–orbit and spin-valley coupling arise as a result of broken symmetry. Conversely, the shorter τ_m in even layers in relation to the bare FM layer implies the existence of spin transport. By analyzing τ_m and α, we have identified the primary mechanisms of ultrafast demagnetization, which transition from spin transport to spin-flip scattering for even layers of WS_2 with increasing fluence. A comprehension of the two-dimensional material and its dependence on odd–even layer at ultrashort time scales offers valuable insights for the development of spin-based devices for the next-generation.

Magnetic Weyl semimetals are gaining recognition as a novel category of material systems for spintronics, attributed to their fundamental topological characteristics and the significant interaction between topology and magnetism. This interaction leads to the emergence of unique electronic states and spin-orbital effects. We have examined the ultrafast magnetization dynamics of the Weyl semimetal Heusler ferromagnet Co_2MnGa. The research focuses on ultrafast demagnetization and precessional dynamics associated with the Kittel and PSSW modes of Co_2MnGa, in conjunction with platinum (Pt) thin films of varying thicknesses. We ascertain the exchange stiffness constant of Co_2MnGa and provide comprehensive insights into spin transport at the Co_2MnGa/Pt interface. By analyzing the modulation of Gilbert damping in Co_2MnGa as a function of Pt thickness, we derive a remarkably high intrinsic spin-mixing conductance, $G_{\uparrow\downarrow} = 1.73 \times 10^{16}$ cm^{-2} for the interface, and determine the spin diffusion length of Pt to be 2.9 ± 0.2 nm. The interfacial spin transparency is observed to achieve a significant value of ~ 83% in the ideal spin-sink regime, indicating the substantial potential of this heterostructure for applications in spin-orbitronics and devices that depend on ultrafast magnetization dynamics.

The impact of magnetic anisotropy on laser-induced ultrafast demagnetization is investigated in Ta/CoFeB (*t*)/MgO heterostructures. A decrease in CoFeB thickness results in a change in the magnetic easy axis from IP to OOP, leading to a doubling of magnetic quenching. It is observed that demagnetization occurs more rapidly in OOP-oriented samples compared to those at the transition thickness from OOP to IP and the IP samples. This phenomenon is attributed to the anisotropic interfacial orbital magnetic moment of CoFeB driven PMA in OOP samples combined with the super-diffusive spin transport through NM/FM interface. In in-IMA samples, the observed increase in demagnetization time with greater CoFeB thickness can be explained by the local dissipation of spin-angular momentum, which occurs due to spin-flip scattering alongside spin transport mechanisms. Similar measurements in TRT/CoFeB (t)/MgO heterostructures confirm these results. The significantly increased quenching rate by a factor of 10 and approximately 158% faster ultrafast demagnetization in Ta/CoFeB (t)/MgO in comparison to TRT/CoFeB (t)/MgO may be attributed to the higher SOC of the heavy metal, Ta, relative to TRT. These findings provide valuable insights for the advancement of perpendicular magnetic recording, magnetic random-access memory, and future spintronics devices.

9.2 Future perspective

The impact of spintronics is increasing significantly day by day. With conventional semiconductor devices reaching their limits of a few nm, there is a growing need for faster and more efficient devices in smaller sizes at a lower cost. Researchers and device designers have no choice but to turn to spin-based devices to meet these demands. Enhancing current technology and developing new technologies are essential to meet the demands of the device market. Progress in materials science, lithography, device miniaturization, and device manufacturing are crucial to keep up with the pace of innovation. Hence, a comprehensive scientific comprehension of ultrafast spin dynamics and manipulation of various spin-related phenomena in ferromagnetic thin films is a key component of contemporary magnetism studies. Ultrafast demagnetization stands out as a fundamental process in ultrafast spin dynamics. Despite numerous attempts to elucidate the mechanisms driving this phenomenon, several inquiries still linger. Both spin-flip scattering and spin current transport have been identified as factors influencing the demagnetization of a magnetic material. Our recent research, along with other literature, indicates that in thin film heterostructures of potentially significant NM/FM or TMD/FM (with an even number of TMD layers), spin current transport plays a crucial role in ultrafast demagnetization. Conversely, in TMD/FM thin film heterostructures with an odd number of TMD layers, SFS is shown to be the dominant factor. However, further extensive experimental and theoretical studies on various materials are necessary to explore the coexistence and quantitative contribution of these mechanisms to the demagnetization process.

In this doctoral thesis, we have established a correlation between ultrafast demagnetization time and the Gilbert damping parameter to elucidate the primary microscopic mechanism driving the ultrafast demagnetization phenomenon. This integration of phenomena across a wide temporal spectrum can also be applied to various materials, facilitating a comprehensive understanding of ultrafast magnetization dynamics. A significant emerging subfield within spintronics, known as spin-orbitronics, has arisen, concentrating on the effective generation, transport, and application of pure spin current. This subfield has significantly influenced the advancement of next-generation memory and storage technologies. In this research, we have employed the spin pumping effect to produce pure spin current in non-magnetic/ferromagnetic thin film heterostructures and have elucidated the importance of the interface in the efficient transfer of pure spin current for device applications. The efficiency of spin current transport is characterized by interfacial spin transparency, which is influenced by both intrinsic and extrinsic factors, including electronic band structure mismatches and interfacial defects. Furthermore, we have demonstrated that the spin-chemical potential at the interface is contingent upon the thickness of the non-magnetic layer. Nevertheless, numerous other heterostructure combinations remain unexplored regarding their interfacial spin transparency, spin-mixing conductance, and spin-chemical potential values. Additionally, the impact of various deposition conditions, such as annealing temperature, argon pressure, and material doping, on interfacial spin transparency, spin-mixing conductance, and spin-chemical potential is still underrepresented in the literature, representing vital areas for future research.

Research in magnetic memory and storage devices has been ignited by the laser-induced modification of magnetic thin films and heterostructures. This technique enables the manipulation and reversal of both static and dynamic magnetic parameters by means of rapid heating and cooling processes. The TR-MOKE technique is capable of examining magnetocaloric effects, ultrafast demagnetization time, fast remagnetization time, and Gilbert damping parameter at ambient temperature. Furthermore, dynamic parameters in various thin film heterostructures can be investigated by adjusting penetration depth using different laser wavelengths. The study explores the impact of the PMA on the ultrafast demagnetization of NM/FM heterostructures. The control of ultrafast spin dynamics can be achieved through the application of strain or electric field at the NM/FM interface, potentially leading to the development of electric field or strain-controlled ultrafast memory devices through material engineering.

REFERENCES

[1] G. E. Moore, IEEE Solid-State Circuits Society Newsletter **11**, 33 (2006).

[2] Nature Nanotechnology **12**, 1105 (2017).

[3] M. N. Baibich, J. M. Broto, A. Fert, F. N. Van Dau, F. Petroff, P. Etienne, G. Creuzet, A. Friederich, and J. Chazelas, Physical Review Letters **61**, 2472 (1988).

[4] G. Binasch, P. Grünberg, F. Saurenbach, and W. Zinn, Physical Review B **39**, 4828 (1989).

[5] G. A. Prinz, Science **282**, 1660 (1998).

[6] A. Hubert and R. Schäfer, *Magnetic Domains: The Analysis of Magnetic Microstructures* (Springer, 1998).

[7] S. O. Mbam, S. E. Nwonu, O. A. Orelaja, U. S. Nwigwe, and X.-F. Gou, Materials Research Express **6**, 122001 (2019).

[8] P. Poulopoulos and K. Baberschke, Journal of Physics: Condensed Matter **11**, 9495 (1999).

[9] K. M. Krishnan, (Oxford University Press, 2016).

[10] P. Aich, C. Meneghini, and L. Tortora, Materials **16**, 7331 (2023).

[11] P. Sheng, B. Wang, and R. Li, Journal of Semiconductors **39**, 011006 (2018).

[12] Y. Tserkovnyak, A. Brataas, and G. E. W. Bauer, Physical Review Letters **88**, 117601 (2002).

[13] J. Sinova, S. O. Valenzuela, J. Wunderlich, C. H. Back, and T. Jungwirth, Reviews of Modern Physics **87**, 1213 (2015).

[14] E. Saitoh, M. Ueda, H. Miyajima, and G. Tatara, Applied Physics Letters **88** (2006).

[15] A. K. Chaurasiya, C. Banerjee, S. Pan, S. Sahoo, S. Choudhury, J. Sinha, and A. Barman, Sci Rep **6**, 32592 (2016).

[16] W. Lin, M. Hehn, L. Chaput, B. Negulescu, S. Andrieu, F. Montaigne, and S. Mangin, Nature Communications **3**, 744 (2012).

[17] J. C. Sánchez, L. Vila, G. Desfonds, S. Gambarelli, J. P. Attané, J. M. De Teresa, C. Magén, and A. Fert, Nat Commun **4**, 2944 (2013).

[18] K. Shen, G. Vignale, and R. Raimondi, Physical Review Letters **112**, 096601 (2014).

[19] A. Hoffmann, physica status solidi c **4**, 4236 (2007).

[20] S. A. Wolf, D. D. Awschalom, R. A. Buhrman, J. M. Daughton, S. von Molnár, M. L. Roukes, A. Y. Chtchelkanova, and D. M. Treger, Science **294**, 1488 (2001).

[21] A. Brataas, Y. Tserkovnyak, G. E. W. Bauer, and B. I. Halperin, Physical Review B **66**, 060404 (2002).

[22] Y. Tserkovnyak, A. Brataas, and G. E. W. Bauer, Phys. Rev. B **66**, 224403 (2002).

[23] K. Ando, S. Takahashi, J. Ieda, H. Kurebayashi, T. Trypiniotis, C. H. Barnes, S. Maekawa, and E. Saitoh, Nat Mater **10**, 655 (2011).

[24] G. Schmidt, D. Ferrand, L. Molenkamp, A. Filip, and B. J. Wees, Physical Review B **62** (2000).

[25] J.-S. Kim, G. Kim, J. Jung, K. Jung, J. Cho, W.-Y. Kim, and C.-Y. You, Scientific Reports **12**, 4549 (2022).

[26] G. Nahrwold, J. Scholtyssek, S. Motl-Ziegler, O. Albrecht, U. Merkt, and G. Meier, Journal of Applied Physics **108**, 013907 (2010).

[27] A. Soumyanarayanan, N. Reyren, A. Fert, and C. Panagopoulos, Nature **539**, 509 (2016).

[28] C.-F. Pai, Y. Ou, L. H. Vilela-Leão, D. C. Ralph, and R. A. Buhrman, Physical Review B **92**, 064426 (2015).

[29] J. C. Rojas-Sánchez *et al.*, Phys Rev Lett **112**, 106602 (2014).

[30] N. Nakajima *et al.*, Physical Review Letters **81**, 5229 (1998).

[31] V. P. Amin and M. D. Stiles, Physical Review B **94**, 104420 (2016).

[32] M. J. Hurben and C. E. Patton, Journal of Applied Physics **83**, 4344 (1998).

[33] K. Nagata, S. Y. Matsushita, X.-C. Pan, K.-K. Huynh, and K. Tanigaki, Physical Review Materials **5**, 024208 (2021).

[34] A. Barman and J. Sinha, in *Spin Dynamics and Damping in Ferromagnetic Thin Films and Nanostructures*, edited by A. Barman, and J. Sinha (Springer International Publishing, Cham, 2018), pp. 13.

[35] E. Beaurepaire, J. C. Merle, A. Daunois, and J. Y. Bigot, Phys. Rev. Lett. **76**, 4250 (1996).

[36] J. Hohlfeld, E. Matthias, R. Knorren, and K. H. Bennemann, Physical Review Letters **78**, 4861 (1997).
[37] B. Koopmans, M. van Kampen, J. T. Kohlhepp, and W. J. M. de Jonge, Physical Review Letters **85**, 844 (2000).
[38] F. Dalla Longa, J. T. Kohlhepp, W. J. M. De Jonge, and B. Koopmans, Phys. Rev. B **75**, 224431 (2007).
[39] W. Hubner and G. Zhang, Physical Review B **58** (1997).
[40] G. P. Zhang and W. Hübner, Physical Review Letters **85**, 3025 (2000).
[41] E. Beaurepaire, G. M. Turner, S. M. Harrel, M. C. Beard, J.-Y. Bigot, and C. A. Schmuttenmaer, Applied Physics Letters **84**, 3465 (2004).
[42] J. Stöhr, and H. C. Siegmann, 2006).
[43] V. P. Zhukov and E. V. Chulkov, Physics-Uspekhi **52**, 105 (2009).
[44] E. Carpene, E. Mancini, C. Dallera, M. Brenna, E. Puppin, and S. De Silvestri, Physical Review B **78**, 174422 (2008).
[45] R. J. Elliott, Physical Review **96**, 266 (1954).
[46] Y. Yafet, in *Solid State Physics*, edited by F. Seitz, and D. Turnbull (Academic Press, 1963), pp. 1.
[47] M. Krauß, T. Roth, S. Alebrand, D. Steil, M. Cinchetti, M. Aeschlimann, and H. C. Schneider, Phys. Rev. B **80**, 180407(R) (2009).
[48] B. Koopmans, G. Malinowski, F. Dalla Longa, D. Steiauf, M. Fähnle, T. Roth, M. Cinchetti, and M. Aeschlimann, Nat. Mater. **9**, 259 (2010).
[49] J.-Y. Bigot, M. Vomir, and E. Beaurepaire, Nat. Phys. **5**, 515 (2009).
[50] G. Malinowski, F. Dalla Longa, J. H. H. Rietjens, P. V. Paluskar, R. Huijink, H. J. M. Swagten, and B. Koopmans, Nat. Phys. **4**, 855 (2008).
[51] M. Battiato, K. Carva, and P. M. Oppeneer, Phys. Rev. Lett. **105**, 027203 (2010).
[52] M. Hofherr *et al.*, Science Advances **6**, eaay8717 (2020).
[53] C. Dornes *et al.*, Nature **565**, 209 (2019).
[54] T. L. Gilbert, IEEE Transactions on Magnetics **40**, 3443 (2004).
[55] L. D. Landau and E. M. Lifshitz, 1935).
[56] G. T.L., Physical Review D **100**, 1243 (1955).
[57] C. Kittel, Physical Review **73**, 155 (1948).
[58] F. Bloch, Zeitschrift für Physik **61**, 206 (1930).
[59] B. Hillebrands and K. Ounadjela, 2002).
[60] C. Herring and C. Kittel, Physical Review **81**, 869 (1951).
[61] B. Heinrich, in *Ultrathin Magnetic Structures III: Fundamentals of Nanomagnetism*, edited by J. A. C. Bland, and B. Heinrich (Springer Berlin Heidelberg, Berlin, Heidelberg, 2005), pp. 143.
[62] P. Krivosik, N. Mo, S. Kalarickal, and C. E. Patton, Journal of Applied Physics **101**, 083901 (2007).
[63] B. Heinrich, J. F. Cochran, and K. Myrtle, Journal of Applied Physics **53**, 2092 (1982).
[64] B. Sahoo, K. Roy, P. Gupta, A. Mishra, B. Satpati, B. B. Singh, and S. Bedanta, Advanced Quantum Technologies **4**, 2000146 (2021).
[65] J. O. Rantschler, R. D. McMichael, A. Castillo, A. J. Shapiro, W. F. Egelhoff, B. B. Maranville, D. Pulugurtha, A. P. Chen, and L. M. Connors, Journal of Applied Physics **101**, 033911 (2007).
[66] A. Krysztofik, S. Özoğlu, R. D. McMichael, and E. Coy, Scientific Reports **11**, 14011 (2021).
[67] A. K. Chaurasiya, A. Kumar, R. Gupta, S. Chaudhary, P. K. Muduli, and A. Barman, Physical Review B **99**, 035402 (2019).
[68] C. Kittel and A. H. Mitchell, Physical Review **101**, 1611 (1956).
[69] J. Kuneš and V. Kamberský, Physical Review B **65**, 212411 (2002).
[70] V. Kamberský, Physical Review B **76**, 134416 (2007).
[71] K. Gilmore, Y. U. Idzerda, and M. D. Stiles, Physical Review Letters **99**, 027204 (2007).
[72] B. Heinrich, R. Urban, and G. Woltersdorf, Journal of Applied Physics **91**, 7523 (2002).
[73] H. Suhl, IEEE Transactions on Magnetics **34**, 1834 (1998).
[74] S. Qiao, W. Yan, S. Nie, J. Zhao, and X. Zhang, AIP Advances **5**, 087170 (2015).
[75] M. I. Dyakonov and V. I. Perel, Physics Letters A **35**, 459 (1971).
[76] V. M. Edelstein, Solid State Communications **73**, 233 (1990).

[77] O. Gomonay, K. Yamamoto, and J. Sinova, Journal of Physics D: Applied Physics **51**, 264004 (2018).
[78] H. H. a. G. Dunifer, J. Physique (Paris) **C8** (1988).
[79] L. Berger, Physical Review B **54**, 9353 (1996).
[80] Y. Tserkovnyak, A. Brataas, G. E. W. Bauer, and B. I. Halperin, Reviews of Modern Physics **77**, 1375 (2005).
[81] B. Heinrich, J. F. Cochran, and R. Hasegawa, Journal of Applied Physics **57**, 3690 (1985).
[82] J. Lindner, K. Lenz, E. Kosubek, K. Baberschke, D. Spoddig, R. Meckenstock, J. Pelzl, Z. Frait, and D. L. Mills, Physical Review B **68**, 060102 (2003).
[83] L. Zhu, L. Zhu, D. C. Ralph, and R. A. Buhrman, Physical Review Applied **13**, 034038 (2020).
[84] T. Valet and A. Fert, Physical Review B **48**, 7099 (1993).
[85] K. Gupta, R. J. H. Wesselink, R. Liu, Z. Yuan, and P. J. Kelly, Physical Review Letters **124**, 087702 (2020).
[86] B. Koopmans, J. J. M. Ruigrok, F. DallaLonga, and W. J. M. de Jonge, Phys. Rev. Lett. **95**, 267207 (2005).
[87] M. Djordjevic and M. Münzenberg, Physical Review B **75**, 012404 (2007).
[88] J. Walowski, G. Müller, M. Djordjevic, M. Münzenberg, M. Kläui, C. A. F. Vaz, and J. A. C. Bland, Physical Review Letters **101**, 237401 (2008).
[89] I. Radu, G. Woltersdorf, M. Kiessling, A. Melnikov, U. Bovensiepen, J. U. Thiele, and C. H. Back, Phys Rev Lett **102**, 117201 (2009).
[90] E. G. Tveten, A. Brataas, and Y. Tserkovnyak, Physical Review B **92**, 180412 (2015).
[91] W. Zhang, W. He, X.-Q. Zhang, Z.-H. Cheng, J. Teng, and M. Fähnle, Phys. Rev. B **96**, 220415 (2017).
[92] W. Zhang, Q. Liu, Z. Yuan, K. Xia, W. He, Q.-f. Zhan, X.-q. Zhang, and Z.-h. Cheng, Phys. Rev. B **100**, 104412 (2019).
[93] J. Kerr, The London, Edinburgh, and Dublin Philosophical Magazine and Journal of Science **3**, 321 (1877).
[94] M. Faraday, Philosophical Transactions of the Royal Society of London **136**, 1 (1846).
[95] Z. Q. Qiu and S. D. Bader, Review of Scientific Instruments **71**, 1243 (2000).
[96] S. Swann, Physics in Technology **19**, 67 (1988).
[97] J. E. Mahan, 2000).
[98] H. Jagodzinski, Berichte der Bunsengesellschaft für physikalische Chemie **79**, 553 (1975).
[99] W. H. Bragg and W. L. Bragg, Proceedings of the Royal Society of London. Series A, Containing Papers of a Mathematical and Physical Character **88**, 428 (1913).
[100] L. G. Parratt, Physical Review **95**, 359 (1954).
[101] E. Meyer, Progress in Surface Science **41**, 3 (1992).
[102] A. Barman and A. Haldar, in *Solid State Physics*, edited by R. E. Camley, and R. L. Stamps (Academic Press, 2014), pp. 1.
[103] Operator's Manual, Libra Ultrafast Amplifier Laser System, Coherent, California.
[104] Operator's Manual: Vitesse Diode Pumped Mode-Locked Ti: Sapphire Laser, Coherent, California. .
[105] Operator's Manual, Evolution-15/30 High Energy High Average Power Q Switched Laser System, Coherent, California. .
[106] Operator’s Manual, SDG Elite-Synchronization and Delay Generator, Coherent, California.
[107] G. Ju, A. V. Nurmikko, R. F. C. Farrow, R. F. Marks, M. J. Carey, and B. A. Gurney, Physical Review Letters **82**, 3705 (1999).
[108] C. D. Stanciu, F. Hansteen, A. V. Kimel, A. Kirilyuk, A. Tsukamoto, A. Itoh, and T. Rasing, Phys. Rev. Lett. **99**, 047601 (2007).
[109] C. Banerjee, N. Teichert, K. E. Siewierska, Z. Gercsi, G. Y. P. Atcheson, P. Stamenov, K. Rode, J. M. D. Coey, and J. Besbas, Nature Communications **11**, 4444 (2020).
[110] M. Dąbrowski *et al.*, Nano Letters **21**, 9210 (2021).
[111] W. Hübner and G. P. Zhang, Physical Review B **58**, R5920 (1998).

[112] G. P. Zhang, W. Hübner, G. Lefkidis, Y. Bai, and T. F. George, Nat. Phys. **5**, 499 (2009).
[113] R. Mondal, M. Berritta, K. Carva, and P. M. Oppeneer, Physical Review B **91**, 174415 (2015).
[114] C. Illg, M. Haag, and M. Fähnle, Physical Review B **88**, 214404 (2013).
[115] Y. Tserkovnyak, E. M. Hankiewicz, and G. Vignale, Physical Review B **79**, 094415 (2009).
[116] S. A. Bender, R. A. Duine, and Y. Tserkovnyak, Physical Review Letters **108**, 246601 (2012).
[117] N. Bergeard, M. Hehn, S. Mangin, G. Lengaigne, F. Montaigne, M. L. M. Lalieu, B. Koopmans, and G. Malinowski, Physical Review Letters **117**, 147203 (2016).
[118] E. Turgut *et al.*, Phys Rev Lett **110**, 197201 (2013).
[119] D. Rudolf *et al.*, Nature Communications **3**, 1037 (2012).
[120] S. Azzawi, A. Ganguly, M. Tokaç, R. M. Rowan-Robinson, J. Sinha, A. T. Hindmarch, A. Barman, and D. Atkinson, Physical Review B **93**, 054402 (2016).
[121] S. N. Panda, S. Mondal, J. Sinha, S. Choudhury, and A. Barman, Sci. Adv. **5**, eaav7200 (2019).
[122] M. Fähnle, J. Seib, and C. Illg, Physical Review B **82**, 144405 (2010).
[123] M. Fähnle and C. Illg, Journal of Physics: Condensed Matter **23**, 493201 (2011).
[124] M. Cecot *et al.*, Scientific Reports **7**, 968 (2017).
[125] F. Riente, S. Mendisch, L. Gnoli, V. Ahrens, M. R. Roch, and M. Becherer, AIP Advances **10**, 125229 (2020).
[126] J. Colin, G. Abadias, A. Michel, and C. Jaouen, Acta Materialia **126**, 481 (2017).
[127] J. Shaw, H. Nembach, T. Silva, S. Russek, R. Geiss, C. Jones, N. Clark, T. Leo, and D. Smith, Phys. Rev. B **80** (2009).
[128] S. N. Panda, S. Majumder, S. Choudhury, A. Bhattacharya, S. Sinha, and A. Barman, Nanoscale **13**, 13709 (2021).
[129] M. van Kampen, C. Jozsa, J. T. Kohlhepp, P. LeClair, L. Lagae, W. J. M. de Jonge, and B. Koopmans, Phys. Rev. Lett. **88**, 227201 (2002).
[130] A. J. Schellekens, W. Verhoeven, T. N. Vader, and B. Koopmans, Applied Physics Letters **102**, 252408 (2013).
[131] K. C. Kuiper, T. Roth, A. J. Schellekens, O. Schmitt, B. Koopmans, M. Cinchetti, and M. Aeschlimann, Applied Physics Letters **105**, 202402 (2014).
[132] S. U. Jen, Y. D. Yao, Y. T. Chen, J. M. Wu, C. C. Lee, T. L. Tsai, and Y. C. Chang, Journal of Applied Physics **99**, 053701 (2006).
[133] H. C. Yuan *et al.*, Applied Physics Letters **105**, 072413 (2014).
[134] J. Walowski, M. D. Kaufmann, B. Lenk, C. Hamann, J. McCord, and M. Münzenberg, J. Phys. D: Appl. Phys. **41**, 164016 (2008).
[135] H. Song, K.-D. Lee, C.-Y. You, S.-H. Yang, S. Parkin, B.-G. Park, J.-W. Sohn, J.-I. Hong, and S.-C. Shin, Applied Physics Express **8**, 053002 (2015).
[136] S. N. Panda, S. Majumder, A. Bhattacharyya, S. Dutta, S. Choudhury, and A. Barman, ACS Appl. Mater. Interfaces **13**, 20875 (2021).
[137] K. Gilmore, Y. U. Idzerda, and M. D. Stiles, Journal of Applied Physics **103**, 07D303 (2008).
[138] E. Montoya, P. Omelchenko, C. Coutts, N. R. Lee-Hone, R. Hübner, D. Broun, B. Heinrich, and E. Girt, Physical Review B **94**, 054416 (2016).
[139] M.-H. Nguyen, D. C. Ralph, and R. A. Buhrman, Physical Review Letters **116**, 126601 (2016).
[140] N. Singh, P. Elliott, J. K. Dewhurst, and S. Sharma, Physical Review B **103**, 134402 (2021).
[141] N. Tancogne-Dejean, F. G. Eich, and A. Rubio, Journal of Chemical Theory and Computation **16**, 1007 (2020).
[142] K. Krieger, J. K. Dewhurst, P. Elliott, S. Sharma, and E. K. Gross, J Chem Theory Comput **11**, 4870 (2015).
[143] C. Ó. Mathúna, N. Wang, S. Kulkarni, and S. Roy, IEEE Transactions on Power Electronics **27**, 4799 (2012).
[144] N. Wang, T. O'Donnell, S. Roy, M. Brunet, P. McCloskey, and S. C. O'Mathuna, Journal of Magnetism and Magnetic Materials **290-291**, 1347 (2005).
[145] D. Apalkov *et al.*, ACM J. Emerg. Technol. Comput. Syst. **9**, 13:1 (2013).
[146] S. X. Wang, N. X. Sun, M. Yamaguchi, and S. Yabukami, Nature **407**, 150 (2000).
[147] V. Korenivski, Journal of Magnetism and Magnetic Materials **215-216**, 800 (2000).
[148] S. Roy, P. McCloskey, B. Jamieson, T. O'Donnell, and D. Gardner, 2011).
[149] S. Roy *et al.*, Journal of Magnetism and Magnetic Materials **290-291**, 1524 (2005).

[150] J. Riveiro and M. Sanchez-Trujillo, IEEE Transactions on Magnetics **16**, 1426 (1980).
[151] J. Riveiro and G. Rivero, IEEE Transactions on Magnetics **17**, 3082 (1981).
[152] J. M. Riveiro, Journal of Magnetism and Magnetic Materials **27**, 119 (1982).
[153] L. Pérez, Ó. de Abril, M. C. Sánchez, C. Aroca, E. López, and P. Sánchez, Journal of Magnetism and Magnetic Materials **215-216**, 337 (2000).
[154] I. Lucas, L. Perez, C. Aroca, P. Sánchez, E. López, and M. C. Sánchez, Journal of Magnetism and Magnetic Materials **290-291**, 1513 (2005).
[155] P. McCloskey, B. Jamieson, T. O'Donnell, D. Gardner, M. A. Morris, and S. Roy, Journal of Magnetism and Magnetic Materials **320**, 2509 (2008).
[156] P. McCloskey, B. Jamieson, T. O'Donnell, D. Gardner, M. A. Morris, and S. Roy, Journal of Magnetism and Magnetic Materials **322**, 1536 (2010).
[157] P. McCloskey, T. O'Donnell, B. Jamieson, D. Gardner, M. A. Morris, and S. Roy, in *Handbook of Nanoelectrochemistry: Electrochemical Synthesis Methods, Properties and Characterization Techniques*, edited by M. Aliofkhazraei, and A. S. H. Makhlouf (Springer International Publishing, Cham, 2016), pp. 1.
[158] M. S. Safavi and F. C. Walsh, Surface and Coatings Technology **422**, 127564 (2021).
[159] A. Samanta, G. Gubbiotti, and S. Roy, Physical Review B **107**, 214449 (2023).
[160] U. Bovensiepen, Nature Physics **5**, 461 (2009).
[161] S. Dutta, S. Narayan Panda, J. Sinha, S. Choudhury, and A. Barman, ACS Appl. Nano Mater. **5**, 17995 (2022).
[162] S. Mondal, A. Talapatra, J. Arout Chelvane, J. R. Mohanty, and A. Barman, Physical Review B **100**, 054436 (2019).
[163] in *Collected Papers of L.D. Landau*, edited by D. Ter Haar (Pergamon, 1965), pp. 101.
[164] P. He, X. Ma, J. W. Zhang, H. B. Zhao, G. Lüpke, Z. Shi, and S. M. Zhou, Phys. Rev. Lett. **110**, 077203 (2013).
[165] K. Lenz, H. Wende, W. Kuch, K. Baberschke, K. Nagy, and A. Jánossy, Physical Review B **73**, 144424 (2006).
[166] T. Gerrits, H. A. M. van den Berg, J. Hohlfeld, L. Bär, and T. Rasing, Nature **418**, 509 (2002).
[167] H. Xia *et al.*, Physical Review B **104**, 024404 (2021).
[168] S. Kulkarni and S. Roy, Journal of Magnetism and Magnetic Materials **322**, 1592 (2010).
[169] D. Mallick, K. Paul, T. Maity, and S. Roy, Journal of Applied Physics **125**, 023902 (2019).
[170] Xingguang Zhang, X. Ke, and H. Zhu, Chemistry (Weinheim an der Bergstrasse, Germany) **18**, 8048 (2012).
[171] X. Yuan *et al.*, Nanoscale Res Lett **8**, 478 (2013).
[172] K. J. Roe, M. W. Dashiell, J. Kolodzey, P. Boucaud, and J. M. Lourtioz, Journal of Vacuum Science & Technology B: Microelectronics and Nanometer Structures Processing, Measurement, and Phenomena **17**, 1301 (1999).
[173] C. Pakpum, IOP Conference Series: Materials Science and Engineering **213**, 012023 (2017).
[174] A. Barman, V. V. Kruglyak, R. J. Hicken, A. Kundrotaite, and M. Rahman, Appl. Phys. Lett. **82**, 3065 (2003).
[175] S. P. Vernon, S. M. Lindsay, and M. B. Stearns, Physical Review B **29**, 4439 (1984).
[176] K. Lee, J. Cho, C.-K. Lee, J. Kim, C.-Y. You, M. Byun, and J.-S. Kim, Journal of Magnetism and Magnetic Materials **512**, 167057 (2020).
[177] C. Eyrich *et al.*, Physical Review B **90**, 235408 (2014).
[178] D. Steiauf, J. Seib, and M. Fähnle, Physical Review B **78**, 020410(R) (2008).
[179] K. Gilmore, M. D. Stiles, J. Seib, D. Steiauf, and M. Fähnle, Physical Review B **81**, 174414 (2010).
[180] Y. Li *et al.*, Physical Review Letters **122**, 117203 (2019).
[181] N. Leroux, A. De Riz, D. Sanz-Hernández, D. Marković, A. Mizrahi, and J. Grollier, Neuromorphic Computing and Engineering **2**, 034002 (2022).
[182] P. Tengdin *et al.*, Science Advances **4**, eaap9744 (2018).
[183] W. You *et al.*, Physical Review Letters **121**, 077204 (2018).
[184] E. Turgut *et al.*, Physical Review B **94**, 220408 (2016).
[185] A. B. Schmidt *et al.*, Physical Review Letters **105**, 197401 (2010).

[186] S. Husain, R. Gupta, A. Kumar, P. Kumar, N. Behera, R. Brucas, S. Chaudhary, and P. Svedlindh, Applied Physics Reviews **7**, 041312 (2020).
[187] Z. Wu *et al.*, Nature Communications **7**, 12955 (2016).
[188] H. Lee *et al.*, ACS Applied Materials & Interfaces **11**, 31543 (2019).
[189] P. Sarangapani, J. Charles, and T. Kubis, Physical Review Applied **17**, 024005 (2022).
[190] A. F. Morpurgo, Nature Physics **9**, 532 (2013).
[191] Y. Liu, Y. Gao, S. Zhang, J. He, J. Yu, and Z. Liu, Nano Research **12**, 2695 (2019).
[192] M. Yamamoto, Y. Shimazaki, I. V. Borzenets, and S. Tarucha, Journal of the Physical Society of Japan **84**, 121006 (2015).
[193] K. F. Mak, K. L. McGill, J. Park, and P. L. McEuen, Science **344**, 1489 (2014).
[194] D. Xiao, G.-B. Liu, W. Feng, X. Xu, and W. Yao, Physical Review Letters **108**, 196802 (2012).
[195] S. Wu *et al.*, Nature Physics **9**, 149 (2013).
[196] Y. Ye *et al.*, Nature Nanotechnology **11**, 598 (2016).
[197] G. Aivazian *et al.*, Nature Physics **11**, 148 (2015).
[198] G. Berghäuser *et al.*, Nature Communications **9**, 971 (2018).
[199] D. W. Latzke *et al.*, Physical Review B **91**, 235202 (2015).
[200] G. Wu, Y. Ren, X. He, Y. Zhang, H. Xue, Z. Ji, Q. Y. Jin, and Z. Zhang, Physical Review Applied **13**, 024027 (2020).
[201] W.-T. Lu and Z. Yuan, Physical Review B **104**, 214404 (2021).
[202] W. Yao, D. Xiao, and Q. Niu, Physical Review B **77**, 235406 (2008).
[203] S. Husain *et al.*, Physical Review B **105**, 064422 (2022).
[204] Interfacial charge transfer is essential for AOS. Linearly polarized excitation should generate a coherent superposition of excitons in both K valleys. Electron hopping from TMD to FM is only allowed when the spin orientation of the electrons in TMD is the same as that of lowest-energy unoccupied conduction band. Immediately after optical excitation and before demagnetization the transfer of electrons from TMD with spin parallel to the FM will begin, leaving the electrons with spin opposite to that of the FM in the other K valley. However, there will be an imbalance of the remaining electrons in the K valleys. The transfer of the remaining electrons will induce remagnetization of the FM. The initial charge transfer for one of the valleys is expected to begin from few fs to sub-hundreds of fs timescale, before the demagnetization of the FM.
[205] M. Dąbrowski, S. Guo, M. Strungaru, P. S. Keatley, F. Withers, E. J. G. Santos, and R. J. Hicken, Nature Communications **13**, 5976 (2022).
[206] A. S. Sethulekshmi, J. S. Jayan, A. Saritha, and K. Joseph, Journal of Alloys and Compounds **876**, 160107 (2021).
[207] S. Husain, A. Kumar, P. Kumar, A. Kumar, V. Barwal, N. Behera, S. Choudhary, P. Svedlindh, and S. Chaudhary, Physical Review B **98**, 180404 (2018).
[208] S. E. Kim *et al.*, Nature **597**, 660 (2021).
[209] S. Mondal, Y. Lin, D. Polley, C. Su, A. Zettl, S. Salahuddin, and J. Bokor, ACS Nano **16**, 9620 (2022).
[210] A. Capua, S.-h. Yang, T. Phung, and S. S. P. Parkin, Physical Review B **92**, 224402 (2015).
[211] Y. Sun *et al.*, Physical Review Letters **111**, 106601 (2013).
[212] Y. Fan *et al.*, Physical Review B **89**, 094428 (2014).
[213] X. Ma, L. Ma, P. He, H. B. Zhao, S. M. Zhou, and G. Lüpke, Physical Review B **91**, 014438 (2015).
[214] Y. Jiang, S. Chen, W. Zheng, B. Zheng, and A. Pan, Light Sci Appl **10**, 72 (2021).
[215] S. Mondal and A. Barman, Physical Review Applied **10**, 054037 (2018).
[216] A. Okada *et al.*, Proceedings of the National Academy of Sciences **114**, 3815 (2017).
[217] A. Kumar, F. Pan, S. Husain, S. Akansel, R. Brucas, L. Bergqvist, S. Chaudhary, and P. Svedlindh, Physical Review B **96**, 224425 (2017).
[218] B. Khodadadi *et al.*, Physical Review Letters **124**, 157201 (2020).
[219] A. T. Costa and R. B. Muniz, Physical Review B **92**, 014419 (2015).
[220] V. Kamberský, Canadian Journal of Physics **48**, 2906 (1970).
[221] Y. H. Park, H. C. Koo, K. H. Kim, H. j. Kim, J. Chang, S. H. Han, and H. Kim, IEEE Transactions on Magnetics **46**, 1562 (2010).
[222] A. Eschenlohr *et al.*, Nature Materials **12**, 332 (2013).

[223] B. Teso, S. Kravenkit, K. Sorn-in, A. Kaewrawang, A. Kruesubthaworn, A. Siritaratiwat, T. Mewes, C. K. A. Mewes, and C. Surawanitkun, Applied Surface Science **472**, 36 (2019).
[224] J. C. W. Song, M. S. Rudner, C. M. Marcus, and L. S. Levitov, Nano Lett. **11**, 4688 (2011).
[225] M. Massicotte, G. Soavi, A. Principi, and K.-J. Tielrooij, Nanoscale **13**, 8376 (2021).
[226] Q. Cui, Y. Zhu, J. Liang, P. Cui, and H. Yang, Physical Review B **103**, 085421 (2021).
[227] B. Q. Lv *et al.*, Phys. Rev. X **5**, 031013 (2015).
[228] Y. Sun, S.-C. Wu, and B. Yan, Phys. Rev. B **92**, 115428 (2015).
[229] X. Wan, A. M. Turner, A. Vishwanath, and S. Y. Savrasov, Phys. Rev. B **83**, 205101 (2011).
[230] A. A. Burkov and L. Balents, Phys. Rev. Lett. **107**, 127205 (2011).
[231] G. Xu, H. Weng, Z. Wang, X. Dai, and Z. Fang, Phys. Rev. Lett. **107**, 186806 (2011).
[232] M. N. Ali *et al.*, Nature **514**, 205 (2014).
[233] L. X. Yang *et al.*, Nat. Phys. **11**, 728 (2015).
[234] S.-M. Huang *et al.*, Nat. Commun. **6**, 7373 (2015).
[235] A. A. Soluyanov, D. Gresch, Z. Wang, Q. Wu, M. Troyer, X. Dai, and B. A. Bernevig, Nature **527**, 495 (2015).
[236] H. Weng, C. Fang, Z. Fang, B. A. Bernevig, and X. Dai, Phys. Rev. X **5**, 011029 (2015).
[237] Z. Wang, M. G. Vergniory, S. Kushwaha, M. Hirschberger, E. V. Chulkov, A. Ernst, N. P. Ong, R. J. Cava, and B. A. Bernevig, Phys. Rev. Lett. **117**, 236401 (2016).
[238] B. Yan and C. Felser, Ann. Rev. Conden. Matt. Phys. **8**, 337 (2017).
[239] H. Weyl, Proceedings of the National Academy of Sciences of the United States of America **15 4**, 323 (1929).
[240] S. A. Parameswaran, T. Grover, D. A. Abanin, D. A. Pesin, and A. Vishwanath, Phys. Rev. X **4**, 031035 (2014).
[241] Y. Baum, E. Berg, S. A. Parameswaran, and A. Stern, Phys. Rev. X **5**, 041046 (2015).
[242] C. Shekhar *et al.*, Nat. Phys. **11**, 645 (2015).
[243] F. Arnold *et al.*, Nat. Commun. **7**, 11615 (2016).
[244] J. Xiong, S. K. Kushwaha, T. Liang, J. W. Krizan, M. Hirschberger, W. Wang, R. J. Cava, and N. P. Ong, Science **350**, 413 (2015).
[245] D. T. Son and B. Z. Spivak, Phys. Rev. B **88**, 104412 (2013).
[246] X. Huang *et al.*, Phys. Rev. X **5**, 031023 (2015).
[247] A. A. Burkov, Phys. Rev. Lett. **113**, 187202 (2014).
[248] N. Nagaosa, J. Sinova, S. Onoda, A. H. MacDonald, and N. P. Ong, Rev. Mod. Phys. **82**, 1539 (2010).
[249] J. Noky, J. Gayles, C. Felser, and Y. Sun, Phys. Rev. B **97**, 220405 (2018).
[250] S. N. Guin *et al.*, NPG Asia Mater. **11**, 16 (2019).
[251] G. E. Volovik, in *Quantum Analogues: From Phase Transitions to Black Holes and Cosmology*, edited by W. G. Unruh, and R. Schützhold (Springer Berlin Heidelberg, Berlin, Heidelberg, 2007), pp. 31.
[252] Y. Sun, Y. Zhang, C. Felser, and B. Yan, Phys. Rev. Lett. **117**, 146403 (2016).
[253] H.-x. Liu, Y. Honda, T. Taira, K.-i. Matsuda, M. Arita, T. Uemura, and M. Yamamoto, Appl. Phys. Lett. **101** (2012).
[254] A. Boehnke *et al.*, Nat. Commun. **8**, 1626 (2017).
[255] B. Balke, S. Ouardi, T. Graf, J. Barth, C. G. F. Blum, G. H. Fecher, A. Shkabko, A. Weidenkaff, and C. Felser, Solid State Commun. **150**, 529 (2010).
[256] D. Kurebayashi and K. Nomura, Sci. Rep. **9**, 5365 (2019).
[257] K. Tang, Z. Wen, Y.-C. Lau, H. Sukegawa, T. Seki, and S. Mitani, Appl. Phys. Lett. **118** (2021).
[258] I. Belopolski *et al.*, arXiv preprint arXiv:1712.09992 (2017).
[259] A. Sakai *et al.*, Nat. Phys. **14**, 1119 (2018).
[260] H. Reichlova *et al.*, Appl. Phys. Lett. **113** (2018).
[261] K. Manna *et al.*, Phys. Rev. X **8**, 041045 (2018).
[262] Q. Wang, Z. Wen, T. Kubota, T. Seki, and K. Takanashi, Appl. Phys. Lett. **115** (2019).
[263] A. Markou *et al.*, Phys. Rev. B **100**, 054422 (2019).
[264] Y. Zhang, Y. Yin, G. Dubuis, T. Butler, N. V. Medhekar, and S. Granville, npj Quant. Mater. **6**, 17 (2021).
[265] G. Bierhance *et al.*, Appl. Phys. Lett. (2021).

[266] J. Hawecker *et al.*, Appl. Phys. Lett. **120** (2022).
[267] L. Tomarchio, S. Mou, L. Mosesso, A. Markou, E. Lesne, C. Felser, and S. Lupi, ACS Appl. Elect. Mater. **5**, 1437 (2023).
[268] S. A. Ryan *et al.*, Sci. Adv. **9**, eadi1428 (2023).
[269] A. Kirilyuk, A. V. Kimel, and T. Rasing, Rev. Mod. Phys. **82**, 2731 (2010).
[270] S. Dutta, A. Samanta, S. N. Panda, S. Roy, and A. Barman, J. Mater. Sci. **58**, 14817 (2023).
[271] J. Foros, G. Woltersdorf, B. Heinrich, and A. Brataas, J. Appl. Phys. **97** (2005).
[272] J. Borge and I. V. Tokatly, Phys. Rev. B **96**, 115445 (2017).
[273] L. J. Zhu and J. H. Zhao, Sci. Rep. **7**, 42931 (2017).
[274] S. R. Tauchert *et al.*, Nature **602**, 73 (2022).
[275] P. Swekis *et al.*, Nanomater. **11**, 251 (2021).
[276] J. S. Lee, E. Vescovo, C. C. Kao, J. M. Beaujour, A. D. Kent, H. Jang, J. Y. Kim, J. H. Park, and J. H. Shim, Phys. Rev. B **80**, 180403 (2009).
[277] N. Behera, S. Chaudhary, and D. K. Pandya, Sci. Rep. **6**, 19488 (2016).
[278] S. Dutta, S. Husain, P. Kumar, N. K. Gupta, S. Chaudhary, P. Svedlindh, and A. Barman, Nanoscale **16**, 4105 (2024).
[279] K. Dutta, S. N. Panda, T. Seki, S. Pan, K. Takanashi, and A. Barman, Adv. Quant. Tech. **5**, 2200033 (2022).
[280] Y.-T. Chen, S. Takahashi, H. Nakayama, M. Althammer, S. T. B. Goennenwein, E. Saitoh, and G. E. W. Bauer, Phys. Rev. B **87**, 144411 (2013).
[281] W. Zhang, W. Han, X. Jiang, S.-H. Yang, and S. S. P. Parkin, Nat. Phys. **11**, 496 (2015).
[282] X. Lu *et al.*, Nat. Commun. **15**, 2410 (2024).
[283] C. P. Weber, J. Appl. Phys. **129** (2021).
[284] S. N. Panda, B. Rana, Y. Otani, and A. Barman, Advanced Quantum Technologies **5**, 2200016 (2022).
[285] J. Okabayashi, Y. Miura, and H. Munekata, Scientific Reports **8**, 8303 (2018).
[286] S. Ikeda *et al.*, Nature Materials **9**, 721 (2010).
[287] J. Sinha *et al.*, Applied Physics Letters **102** (2013).
[288] D. C. Worledge *et al.*, Applied Physics Letters **98** (2011).
[289] T. Liu, J. W. Cai, and L. Sun, AIP Advances **2** (2012).
[290] S. Pan, F. Ganss, S. Panda, G. Sellge, C. Banerjee, J. Sinha, O. Hellwig, and A. Barman, Journal of Materials Science **57**, 6212 (2022).
[291] Y. Liu, L. Hao, and J. Cao, AIP Advances **6** (2016).
[292] B. Dieny and M. Chshiev, Reviews of Modern Physics **89**, 025008 (2017).
[293] P. Bruno, Physical Review B **39**, 865 (1989).
[294] A. Manchon *et al.*, Journal of Applied Physics **104** (2008).
[295] C. Boeglin, E. Beaurepaire, V. Halté, V. López-Flores, C. Stamm, N. Pontius, H. A. Dürr, and J. Y. Bigot, Nature **465**, 458 (2010).